MATERIALS FOR ADAPTIVE STRUCTURAL ACOUSTIC CONTROL

Period February 1, 1996 to January 31, 1997

Final Report

VOLUME II

OFFICE OF NAVAL RESEARCH
Contract No.: N00014-92-J-1510

DTIC QUALITY INSPECTED 4

L. Eric Cross

PENNSTATE
1855

19970520 047

THE MATERIALS RESEARCH LABORATORY
UNIVERSITY PARK, PA

OMB No. 0704-0188

1. AGENCY USE ONLY (Leave blank)	2. REPORT DATE 4/14/97	3. REPORT TYPE AND DATES COVERED FINAL REPORT 2/1/96-1/31/97

4. TITLE AND SUBTITLE

MATERIALS FOR ADAPTIVE STRUCTURAL ACOUSTIC CONTROL

5. FUNDING NUMBERS

ONR CONTRACT NO:
N00014-92-J-1510

6. AUTHOR(S)

L. ERIC CROSS

7. PERFORMING ORGANIZATION NAME(S) AND ADDRESS(ES)

MATERIALS RESEARCH LABORATORY
THE PENNSYLVANIA STATE UNIVERSITY
UNIVERSITY PARK, PA 16802-4800

8. PERFORMING ORGANIZATION REPORT NUMBER

9. SPONSORING/MONITORING AGENCY NAME(S) AND ADDRESS(ES)

OFFICE OF NAVAL RESEARCH   GERALD T. SMITH
CODE 1513:NRJ   OFFICE OF NAVAL RESEARCH RES.
800 NORTH QUINCY STREET   536 SOUTH CLARK STREET, RM 286
ARLINGTON, VA 22217-5660   CHICAGO, ILLINOIS 60606-1588

10. SPONSORING/MONITORING AGENCY REPORT NUMBER

REP.

11. SUPPLEMENTARY NOTES

12a. DISTRIBUTION/AVAILABILITY STATEMENT

12b. DISTRIBUTION CODE

13. ABSTRACT (Maximum 200 words)

SEE FOLLOWING TWO PAGES.

14. SUBJECT TERMS

15. NUMBER OF PAGES

16. PRICE CODE

17. SECURITY CLASSIFICATION OF REPORT	18. SECURITY CLASSIFICATION OF THIS PAGE	19. SECURITY CLASSIFICATION OF ABSTRACT	20. LIMITATION OF ABSTRACT

NSN 7540-01-280-5500

Standard Form 298 (Rev 2-89)
Prescribed by ANSI Std 239-18
298-102

GENERAL INSTRUCTIONS FOR COMPLETING SF 298

The Report Documentation Page (RDP) is used in announcing and cataloging reports. It is important that this information be consistent with the rest of the report, particularly the cover and title page. Instructions for filling in each block of the form follow. It is important to *stay within the lines* to meet *optical scanning requirements.*

Block 1. Agency Use Only *(Leave blank).*

Block 2. Report Date. Full publication date including day, month, and year, if available (e.g. 1 Jan 88). Must cite at least the year.

Block 3. Type of Report and Dates Covered. State whether report is interim, final, etc. If applicable, enter inclusive report dates (e.g. 10 Jun 87 - 30 Jun 88).

Block 4. Title and Subtitle. A title is taken from the part of the report that provides the most meaningful and complete information. When a report is prepared in more than one volume, repeat the primary title, add volume number, and include subtitle for the specific volume. On classified documents enter the title classification in parentheses.

Block 5. Funding Numbers. To include contract and grant numbers; may include program element number(s), project number(s), task number(s), and work unit number(s). Use the following labels:

C	-	Contract	PR	-	Project
G	-	Grant	TA	-	Task
PE	-	Program Element	WU	-	Work Unit Accession No.

Block 6. Author(s). Name(s) of person(s) responsible for writing the report, performing the research, or credited with the content of the report. If editor or compiler, this should follow the name(s).

Block 7. Performing Organization Name(s) and Address(es). Self-explanatory.

Block 8. Performing Organization Report Number. Enter the unique alphanumeric report number(s) assigned by the organization performing the report.

Block 9. Sponsoring/Monitoring Agency Name(s) and Address(es). Self-explanatory.

Block 10. Sponsoring/Monitoring Agency Report Number. *(If known)*

Block 11. Supplementary Notes. Enter information not included elsewhere such as: Prepared in cooperation with...; Trans. of...; To be published in.... When a report is revised, include a statement whether the new report supersedes or supplements the older report.

Block 12a. Distribution/Availability Statement. Denotes public availability or limitations. Cite any availability to the public. Enter additional limitations or special markings in all capitals (e.g. NOFORN, REL, ITAR).

DOD - See DoDD 5230.24, "Distribution Statements on Technical Documents."
DOE - See authorities.
NASA - See Handbook NHB 2200.2.
NTIS - Leave blank.

Block 12b. Distribution Code.

DOD - Leave blank.
DOE - Enter DOE distribution categories from the Standard Distribution for Unclassified Scientific and Technical Reports.
NASA - Leave blank.
NTIS - Leave blank.

Block 13. Abstract. Include a brief *(Maximum 200 words)* factual summary of the most significant information contained in the report.

Block 14. Subject Terms. Keywords or phrases identifying major subjects in the report.

Block 15. Number of Pages. Enter the total number of pages.

Block 16. Price Code. Enter appropriate price code *(NTIS only).*

Blocks 17. - 19. Security Classifications. Self-explanatory. Enter U.S. Security Classification in accordance with U.S. Security Regulations (i.e., UNCLASSIFIED). If form contains classified information, stamp classification on the top and bottom of the page.

Block 20. Limitation of Abstract. This block must be completed to assign a limitation to the abstract. Enter either UL (unlimited) or SAR (same as report). An entry in this block is necessary if the abstract is to be limited. If blank, the abstract is assumed to be unlimited.

ABSTRACT

This report documents work carried out largely over the fifth and final year of the ONR sponsored University Research Initiative (URI) entitled "Materials for Adaptive Structural Acoustic Control." This program has continued to foster the successful development of new electroceramic single crystal and composite material combinations for both sensing and actuation functions in adaptive structural systems.

For the classical perovskite relaxor, dielectrics typified by lead magnesium niobate, continuing studies of properties in the temperature region above the dielectric maximum T_m have added strong additional support to the superparaelectric/spin glass model for the behavior developed earlier in the IMRL. The most exciting and important discovery of the year has been the ultra high strain capability of relaxor ferroelectric single crystal actuators. For crystal in the lead zinc niobate:lead titanate (PZN;PT) solid solution system, at compositions in the rhombohedral phase close to the morphotropic phase boundary to the tetragonal ferroelectric phase at 9 mole % PT in PZN, crystals cut and poled along the 001 cube axis exhibit massive field induced quasi linear anhysteretic strains up to 0.6%. For this poling d_{33} values up to 2,300 pC/N and coupling coefficients k_{33} of 94% have been achieved and it was the original hypothesis that these extreme numbers must be largely due to extrinsic domain wall motion. Now however it is very clear that the exact equivalence of the effect of an 001 oriented E field on the $111, \bar{1}11, 1\bar{1}1, \text{and} \bar{1}\bar{1}1$ rhombohedral domains precludes this field from driving domain wall motion so that quite contrary to our earlier expectation the polarization and associated strain phenomena are purely intrinsic. At higher field levels there is an obvious step in both polarization and strain into an induced tetragonal phase which gives total reproducible induced strains up to 1.7%. Clearly the PZN:PT crystals represent a major breakthrough into a completely new regimen for piezoelectric actuation and sensing.

For antiferroelectric:ferroelectric switching compositions in the lead lanthanum zirconated titanate stannate family, new experimental studies have proven that the induced polarization P_3 and the strain x_{33} onset at different field levels. A new domain re-orientation model has been invoked to explain this startlingly unusual behavior. Both barium and strontium additives have also been explored to control hysteresis between forward and backward switching with good success. As well as being interesting for transduction we believe these compositions are sure to be important for energy storage dielectrics.

In composite sensing it is pleasing to report that the moonie flextensional patent has now been licensed to the Input:Output Corporation who have successfully fabricated and sold more than 80,000 moonie sensors. Work is continuing on the cymbal type modification of the moonie with focus now on array structures for large area panels. This topic is transitioning to a joint study between the IMRL and Penn State's ARL, on a new MURI initiative. For the very small hollow PZT spheres produced by blowing, the emphasis has been upon both poling and driving from outer surface electrodes, and exploring both by experiment and by finite element theoretical methods, the resonant mode structures which can be induced. Studies of the 2:2 composite structures confirm the very high effective hydrostatic sensitivity and are permitting closer consonance between measurement and theoretical analysis.

Actuation studies have been dominated by the initial exploration of the fantastic strain capability of the relaxor ferroelectric MPB single crystals. Obviously the induced strains are on order of magnitude larger than for conventional PZT ceramics, but the blocking force has

not yet been determined. It is expected that d_{31} will also be large and anhysteritic in these crystals, as spontaneous strain depends on Q_{44} which is a pure shear constant. The d_{15} however may be significantly more complex as an E_1 field will certainly drive domain walls in these E_3 poled crystals.

Reliability studies of conventional actuators are continuing with emphasis on using acoustic emission to explore and separate domain wall motion and crack propagation. Most earlier studies were indeterminate and difficult to interpret, recently for these strongly piezoelectric samples we have shown that electrical noise in the power supply induces very strong mechanical noise in the sample giving high spurious emission counts. New studies using a long time constant filter in the supply have permitted clear and effective separation. Over the last few years there has been a strong re-awakening of interest in bimorph type transducer amplifiers with new concepts like rainbow, cerambow and thunder appearing. Under our ONR program with Virginia Polytechnic it has been necessary to sort out the conflicting claims for these 'morph' types and these data are included for completeness. We have also begun serious study of the large electrostriction in the soft polyurethane elastomers where it has been necessary to derive new techniques to measure strain with ultra low constraint on the films.

Processing studies now involved both single crystal flux growth and a wide range of powder and ceramic processing. Current needs for integrity and better mechanical properties are driving new needs for fine grained PZT piezoceramics and new processing is permitting retention of excellent properties down to submicron grain sizes.

From the wide range of thin ferroelectric film activities in the laboratory, only those which refer to the thicker films being produced on silicon for MEMS devices are included.

MATERIALS FOR ADAPTIVE STRUCTURAL ACOUSTIC CONTROL

Period February 1, 1996 to January 31, 1997

Final Report

VOLUME II

OFFICE OF NAVAL RESEARCH
Contract No.: N00014-92-J-1510

L. Eric Cross

TABLE OF CONTENTS

APPENDICES

VOLUME I

General Summary Papers

1. Cross, L.E., "Ferroelectric Materials for Electromechanical Transducer Applications." *Mat. Chem. Phys* **43**, 108-115 (1996).

2. Cross, L.E., "Ferroelectric Ceramics: Materials and Application Issues." *Ceramic Transactions* **68**, 15-55 (1996).

3. Li. S., J.A. Eastman, Z. Li, C.M. Foster, R.E. Newnham, and L.E. Cross, " Size Effects in Ferroelectrics." *Phys. Lett. A* **212**, 341 (1996).

4. Li, Shaoping, J.A. Eastman, R.E. Newnham, and L.E. Cross, "Susceptibility of Nanostructured Ferroelectrics." *Japanese J. Appl. Physics* **35** (Part 2) [No. 4B], L502-L504 (1996).

5. Newnham, R.E., Chapter: Crystal Chemistry and Crystal Physics, in <u>Innovative Ideas in Ceramics and Materials Curricula</u>, edited by T. Stoebe and W. Huebner. Published by the *American Ceramic Society*, pp. 65-72 (1996).

6. Uchino, K., "New Applications of Photostriction." *Innovations in Mater. Res.* **1** (1), 11-22 (1996).

7. Aburatani, H. and K. Uchino, "Acoustic Emission (AE) Measurement Technique in Piezoelectric Ceramics." *Jpn. J. Appl. Phys.* **35** (2) [4B], L516-L518 (1996).

Materials Studies

8. Choi, S., J.M. Jung, and A.S. Bhalla, "Dielectric, Pyroelectric and Piezoelectric Properties of Calcium-Modified Lead Magnesium Tantalate-Lead Titanate Ceramics." *Ferroelectric Letters* **21**, 27-33 (1996).

9. Alberta, E. and A.S. Bhalla, "Preparation of Phase Pure Perovskite Lead Indium Niobate Ceramic." *Mater. Lett.* **29**, 127-129 (1996).

10. Zhang, Q.M., J. Zhao, T.R. Shrout, and L.E. Cross, "The Effect of Ferroelastic Coupling in Controlling the Abnormal Aging Behavior in Lead Magnesium Niobate-Lead Titanate Relaxor Ferroelectrics." *J. Mater. Res.* **12** (7), (1997).

11. Alberta, E., A.S. Bhalla, and T. Takenaka, "Piezoelectric, elastic and Dielectric Constants for Ceramics in the Solids Solution: $xPbZrO_3$ - $(1-x-z)Pb(Zn_{1/3}Nb_{2/3})$ O_3 - $zPbTiO_3$." *Ferroelectrics* **188**, 109-124 (1996).

12. Zhang, Q.M. and J. Zhao, "Polarization Responses in Lead Magnesium Niobate Based Relaxor Ferroelectrics." *Applied Physics Letters* (submitted).

13. Müeller, V. and Q.M. Zhang, "Nonlinearity and Scaling Behavior in Donor Doped Lead Zirconate Titanate Piezoceramic." *Physics Review Letters* (submitted).

14. Zhang, Q.M., J. Zhao, K. Uchino, and J. Zheng, "Change of the Weak-Field Properties of $Pb(ZrTi)O_3$ Piezoceramics with Compressive Uniaxial Stresses and Its Links to the Effect of Dopants on the Stability of the Polarizations in the Materials." *J. Mat. Res.* **12**, 226 (1997).

15. Markowski, K., S.-E. Park, S. Yoshikawa, and L.E. Cross, "The Effect of Compositional Variations in the Lead Lanthanum Zirconate Stannate Titanate System on Electrical Properties." *J. Amer. Ceram.* **79** (12), 3297-3304 (1996).

16. Park, S.-E., K. Markowski, S. Yoshikawa, and L.E. Cross, "The Effect of Barium and Strontium Additions in the Lead Lanthanum Zirconate Stannate Titanate System on Electrical Properties." *J. Amer. Ceram.* **80** (2), 407-412 (1997).

VOLUME II

17. Yoshikawa, S., K. Markowski, S.-E. Park, M.-J. Pan, and L.E. Cross, "Antiferroelectric-to-Ferroelectric Phase Switching Lead Lanthanum Zirconate Stannate Titanate (PLZST) Ceramics." *SPIE Proceedings* **IV** (1997).

18. Blue, C.T., J.C. Hicks, S.-E. Park, S. Yoshikawa, and L.E. Cross, "In-situ X-ray Diffraction Study of the Antiferroelectric-Ferroelectric Phase Transition in PLSnZT." *Applied Physics Letter* **68** (21), 2942-2944 (1996).

19. Pan, M.-J., S.-E. Park, K. Markowski, and S. Yoshikawa, "Antiferroelectric-to-Ferroelectric PLZST Ceramics-II: The Effect of Pre-Stress Conditions on the Strain Behavior." Submitted *Proceedings of IEEE International Symposium on the Applications of Ferroelectrics*, Rutgers University, East Brunswick, New Jersey (August 1996).

20. M.-J. Pan, Markowski, K., S.-E. Park, S. Yoshikawa, and L.E. Cross. "Antiferroelectric-to Ferroelectric PLZSnT Ceramics-I: Structure, Compositional Modification and Electric Properties." Submitted *Proceedings of IEEE International Symposium on the Applications of Ferroelectrics*, Rutgers University, East Brunswick, New Jersey (August 1996).

Materials Studies–continued

21. Lopath, P.D., K.K. Shung, S.-E. Park, and T.R. Shrout, "Ultrasonic Transducers Using Piezoelectric Single Crystals Perovskites." Submitted *Proceedings of IEEE International Symposium on the Applications of Ferroelectrics*, Rutgers University, East Brunswick, New Jersey (August 1996).

22. Park, S.-E. and T.R. Shrout, "Characteristics of Relaxor-Based Piezoelectric Single Crystals for Ultrasonic Transducers." Proceedings of 1996 IEEE Ultrasonics Symposium, San Antonio, Texas (November 1996).

23. Park, S.-E., P.D. Lopath, K.K. Shung, and T.R. Shrout, "Relaxor-Based Single Crystal Materials for Ultrasonic Transducer Applications." Proceedings on SPIE's International Symposium on Medical Imaging, Newport Beach, California (February 1997).

24. Lopath, P.D., S.-E. Park, K.K. Shung, and T.R. Shrout, "$Pb(Zn_{1/3}Nb_{2/3})O_3/PbTiO_3$ Single Crystal Piezoelectrics for Ultrasonic Transducers." Proceedings on SPIE's International Symposium on Medical Imaging, Newport Beach, California (February 1997).

25. Park, S.-E. and T.R. Shrout, "Relaxor Based Ferroelectric Single Crystals for Electro-Mechanical Actuators." *Innovations in Materials Research* (accepted).

26. Park, S.-E. and T.R. Shrout, "Characteristics of Relaxor-Based Piezoelectric Single Crystals for Ultrasonic Transducers," *IEEE Trans. on Ultrasonics, Ferroelectric and Frequency Control Special Issue on Ultrasonic Transducers* (to be published).

27. Jin, B., R. Guo, and A.S. Bhalla, "Piezoelectric Properties and Equivalent Circuits of Ferroelectric Relaxor Single Crystals."

28. Mulvihill, M.L., K. Uchino, Z. Li, and W. Cao, "In-situ Observation of the Domain Configurations during the Phase Transitions in Barium Titanate." *Phil. Mag. B.* **74** (1), 25-36 (1996).

29. Mulvihill, M.L., L.E. Cross, and K. Uchino, "Dynamic Motion of the Domain Configuration in Relaxor Ferroelectric Single Crystals as a Function of Temperature and Electric Field." *Ferroelectrics* **186**, 325-328 (1996).

30. Sundar, V. and R.E. Newnham, "Conversion Method Measurements of Electrostriction Coefficients in Low-K Dielectrics." *Mat. Res. Bull.* **31** (5), 545-554 (1996).

31. Sundar, V., J.-F., Li, D. Viehland, and R.E. Newnham, "Interferometric Evaluation of Electrostriction Coefficients." *Mat. Res. Bull.* **31** (5), 555-563 91996).

Materials Studies–continued

32. Sundar, V., N. Kim, C. Randall, R. Yimnirun, and R.E. Newnham, "The Effect of Doping and Grain Size on Electrostriction in $PbZr_{0.52}Ti_{0.48}O_3$." Submitted *Proceedings of IEEE International Symposium on the Applications of Ferroelectrics*, Rutgers University, East Brunswick, New Jersey (August 1996).

33. Erdei, S., L. Galambos, I. Tanaka, L. Hesselik, F.W. Ainger, L.E. Cross, and R.S. Feigelson, "Segregation and Inhomogenities in Photorefractive SBN Fibers." *SPIE Proceedings V–Photorefractive Fiber and Crystal Devices: Materials, Optical Properties, and Applications II*, **2849**, 168-173 (1996).

34. Li, Shaoping, J.A. Eastman, J.M. Vertrone, R.E. Newnham, and L.E. Cross, "Coherent Coupling in Ferroelectric Superlattices." (1996).

35. Su, J., Q.M. Zhang, and R.Y. Ting, "Space Charge Enhanced Electromechanical Response in Thin Film Polyurethane Elastomers." *Applied Physics Letters* (submitted).

36. Zhang, Q.M., J. Su, and C.-H. Kim, "An Experimental Investigation of Electromechanical Responses in a Polyurethane Elastomer." *J. Appl. Phys.* **81** (6), 2770 (1997).

VOLUME III

37. Su, J., Q.M. Zhang, C.H. Kim, R.Y. Ting, and R. Capps, "Effects of Transitional Phenomena on the Electric Field Induced Strain-Electrostrictive Response of a Segmented Polyurethane Elastomer." *J. Appl. Polymer Sci.* (accepted).

Composite Sensors

38. Fernandez, J.F., A. Dogan, Q.M. Zhang, J.F. Tressler, and R.E. Newnham, "Hollow Piezoelectric Composites, Sensors and Actuators." *A: Physical* **51** (2,3), 183-192 (1996).

39. Fernandez, J.F., A. Dogan, Q.M. Zhang, and R.E. Newnham, "Piezoelectric Composites with Enclosed Hollow Spaces." Proceedings 4th Euroceramics Conference, *Electroceramics* **5**, 39-46 (1996).

40. Fernandez, J.F., A. Dogan, J.T. Fielding, K. Uchino, and R.E. Newnham, "Temperature Dependence of New Design Ceramic-Metal Piezocomposites Actuators." Proceeding 4th Euroceramics Conference, *Electroceramics* **5**, 133-138 (1996).

Composite Sensors–continued

41. Newnham, R.E., "Composite Sensors and Actuators," <u>Disordered Materials</u>, edited by G. Milton, K. Godlen, G. Grimmett, and P. Sen, Springer-Verlag, NY (accepted January 1997).

42. Tressler, J.F. and R.E. Newnham, "Doubly Resonant Cymbal Transducers, *IEEE Transactions of UFFC*, Special Issue on Transducers (accepted 1996).

43. Tressler, J.F., W. Cao, K. Uchino, and R.E. Newnham, "Ceramic Metal Composite Transducers for Underwater Acoustic Applications." Submitted *Proceedings of IEEE International Symposium on the Applications of Ferroelectrics*, Rutgers University, East Brunswick, New Jersey (August 1996).

44. Alkoy, S., A. Dogan, A.C. Hladky, J.K. Cochran, and R.E. Newnham, "Vibration Modes of PZT Hollow Sphere Transducers." Submitted *Proceedings of IEEE International Symposium on the Applications of Ferroelectrics*, Rutgers University, East Brunswick, New Jersey (August 1996).

45. Alkoy, S., A. Dogan, A.C. Hladky, and R.E. Newnham, "Miniature Piezoelectric Hollow Sphere Transducers (BBs)." 1996 Proceeding of IEEE International Frequency Control Symposium, pp. 586-594, Honolulu, Hawaii (1996).

46. Alkoy, S., A. Dogan, A.C. Hladky, and R.E. Newnham, "Piezoelectric Hollow Spheres." 1996 Proceeding 3rd Turkish Ceramic Society Meeting., Eds. V. Günay, H. Mandel, S. Ozgen. Istanbul, Turkey (October 1996).

47. Koc, B., A. Dogan, J.F. Fernandez, R.E. Newnham, and K. Uchino, "Accelerometer Application of the Modified Moonie (Cymbal) Transducer." *J. App. Phys.* **35**, 65-67 (1996).

VOLUME IV

48. Kumar, S., A. Bhalla, and L.E. Cross, "Underwater Acoustic Absorption by Collocated Smart Materials." *Ferroelectric Letters* **21**, 11-16 (1996).

49. Geng, X. and Q.M. Zhang, "Evaluation of Piezocomposites for Ultrasonic Transducer Applications–Influence of the Unit Cell Dimensions and the Properties of Constituents the Performance of 2-2 Piezocomposites." *IEEE Transactions of UFFC* (accepted).

50. Zhang, Q.M. and X. Geng, "Acoustic Properties of the Interface of a Uniform Medium-2-2 Piezocomposite and the Field Distributions in the Composite." *J. Appl. Phys.* (accepted).

51. Park, S.-E., and T.R. Shrout, "Ultrahigh Strain and Piezoelectric Behavior in Relaxor Based Ferroelectric Single Crystals."

52. Uchino, K. and S. Takahashi, "Multilayer Ceramic Actuators." *Current Opinion, Ceramic, Composites and Intergrowths*, p. 98-705 (1996).

53. Zheng, J., S. Takahashi, S. Yoshikawa, and K. Uchino, "Heat Generation in Multilayer Piezoelectric Actuators." *J. Amer. Ceram.* **79** (12), 3193-3198 (1996).

54. Dogan, A., J.F. Fernandez, K. Uchino, and R.E. Newnham, "New Piezoelectric Composite Actuator Designs for Displacement Amplification." *Proceeding Euroceramic Conference, Electroceramics* (5), 127-132 (1995) (in press).

VOLUME V

55. Poosanaas, P., A. Dogan., A.V. Prasadarao, S. Komarneni, and K. Uchino, "Photostriction of Sol-Gel Processed PLZT Ceramics." *J. Electroceramics* (1996) (in press).

56. Uchino, K., "Reliability of Ceramic Actuators." Submitted *Proceedings of IEEE International Symposium on the Applications of Ferroelectrics*, Rutgers University, East Brunswick, New Jersey (August 1996).

57. Uchino, K., "High Electromechanical Coupling Piezoelectrics-How High Energy Conversion Rate is Possible?-." *Proceeding MRS 1996* (1996) (in press).

58. Uchino, K., "Recent Developments in Ceramic Actuators-Comparison Among USA, Japan and Europe."

59. Xu, B., Q.M. Zhang, V.D. Kugel, Q. M. Wang, and L.E. Cross, "Optimization of Bimorph Based Double Amplifier Actuator under Quasistatic Situation." Submitted *Proceedings of IEEE International Symposium on the Applications of Ferroelectrics*, Rutgers University, East Brunswick, New Jersey (August 1996).

60. Kugel, V.D., S. Chandran, and L.E. Cross, "Caterpillar-Type Piezoelectric d_{33} Bimorph Transducer." *Appl. Phys. Lett.* **69** (14), 2021-2023 (1996).

61. Kugel, V.D., Q.M. Zhang, B. Xu, Q.-M. Wang, S. Chandran, and L.E. Cross, "Behavior of Piezoelectric Actuators under High Electric Field." Submitted *Proceedings of IEEE International Symposium on the Applications of Ferroelectrics*, Rutgers University, East Brunswick, New Jersey (August 1996).

62. Kugel, V.D., B. Xu, Q.M. Zhang, and L.E. Cross, "Bimorph-Based Piezoelectric Air Acoustic Transducer Model." *Sensors and Actuators A* (submitted 1996).

Actuator Studies–continued

63. Chandran, S., V.D. Kugel, and L.E. Cross, "CRESCENT: A Novel Piezoelectric Bending Actuator." *Proceeding SPIE's 4th Annual Symposium on Smart Structures* accepted 1997).

64. Kugel, V.D., S. Chandran, and L.E. Cross, "A Comparative Analysis of Piezoelectric Bending-Mode Actuators." Submitted *SPIE Proceedings*, Smart Structures and Materials: Smart Materials Technologies, 3040, 70-80 (1997).

65. Wang, Q.M., B. Xu, V.D. Kugel, and L.E. Cross, "Characteristics of Shear Mode Piezoelectric Actuators," Submitted *Proceedings of IEEE International Symposium on the Applications of Ferroelectrics*, Rutgers University, East Brunswick, New Jersey (August 1996).

Integration Studies

66. Elissalde, C., L.E. Cross, and C.A. Randall, "Structural-Property Relations in a Reduced and Internally Biased Oxide Wafer (RAINBOW) Actuator Material." *J. Amer. Ceram.* **79** (8), 2041-2048 (1996).

67. Xu. B., Q.M. Zhang, V.D. Kugel, Q. Wang, and L.E. Cross, "Optimization of Bimorph Based Double Amplifier Transducer under Quasistatic Conditions." Submitted *Proceedings of IEEE International Symposium on the Applications of Ferroelectrics*, Rutgers University, East Brunswick, New Jersey (August 1996).

68. Xu, B., Q. M. Zhang, V.D. Kugel, and L.E. Cross, "Piezoelectric Air Transducer for Active Noise Control." *Proceeding SPIE, Smart Structures and Integrated Systems* **271** (7), 388 (1996).

VOLUME VI

69. Chandran, S., V.D. Kugel, and L.E. Cross, "Characterization of the Linear and Non-Linear Dynamic Performance of RAINBOW Actuator." Submitted *Proceedings of IEEE International Symposium on the Applications of Ferroelectrics*, Rutgers University, East Brunswick, New Jersey (August 1996).

70. Wang, H., Q.M. Zhang, L.E. Cross, and C.M. Trottier, "Tailoring Material Properties by Structure Design–Radially Poled Piezoelectric Cylindrical Tube." *Ferroelectrics* **173**, 181-189 (1995).

Processing Studies

71. Park, S.-E., M. Mulvihill, P.D. Lopath, M. Zipparo, and T.R. Shrout, "Crystal Growth and Ferroelectric Related Properties of (1-x) Pb $(A_{1/3}Nb_{1/3})O_3$ - $xPbTiO_3(A=Zn^{2+}$, $Mg^{2+})$." Submitted *Proceedings of IEEE International Symposium on the Applications of Ferroelectrics*, Rutgers University, East Brunswick, New Jersey (August 1996).

72. Mulvihill, M., S.-E. Park, G. Risch, Z. Li, K. Uchino, and T.R. Shrout, "The Role of Processing Variables in the Flux Growth of PZN-PT Relaxor Ferroelectric Single Crystals." *Jpn. J. Appl. Phys.* **35** (Pt. 1; No. 7), 3984-3990 (1996).

73. Pan, M.-J., S.-E. Park, C.W. Park, K.A. Markowski, S. Yoshikawa, and C. Randall, "Superoxidation and Electrochemical Reactions during Switching in $Pb(Zr,Ti)O_3$ Ceramics." *J. Amer. Ceram.* **79** (11), 2971-2974 (1996).

74. Park, S.-E., M.L. Mulvihill, G. Risch, and T.R. Shrout, "The Effect of Growth Condition on Dielectric Properties of $Pb(Zn_{1/3}Nb_{2/3})O_3$ Crystal." *Jpn. J. Appl. Phys.* **36** (1) (1997).

75. Yoshikawa, Y. and K. Uchino, "Chemical Preparation of Lead-Containing Niobate Powders." *J. Amer. Ceram.* **79** (9), 2417-2421 (1996).

76. Ravindrathan, P., V. Srikanth, S. Komarneni, and A.S. Bhalla, "Processing of $Pb(Zn_{1/3}Nb_{2/3})O_3$: Ceramics at High Pressure." *Ferroelectrics* **188**, 135-141 (1996).

77. Ravindrathan, P., S. Komarneni, A.S. Bhalla, and R. Roy, "Low Temperature Chemical Routes to Smart Materials." *Ferroelectrics* **188**, 125-133 (1996).

78. Alberta, E.F. and A.S. Bhalla, "A Processing and Electrical Property Investigation of the Solid Solution: (x) $Pb(In_{1/2}Nb_{1/2})O_3$ - $(1-x)Pb(Sc_{1/2}Ta_{1/2})O_3$." *Ferroelectrics* **188**, 95-107 (1996).

Thin Film Ferroelectrics

79. Chen, H.D., K.R. Udayakumar, C.J. Gaskey, and L.E. Cross, "Fabrication and Electrical Properties of Lead Zirconate Titanate Thick Films." *J. Amer. Ceram.* **79** (8), 2189-2192 (1996).

80. Chen, H.D., K.K. Li, C.J. Gaskey, and L.E. Cross, "Thickness-Dependent Electrical Properties in Lanthanum-Doped PZT Thick Films." *Mat. Res. Soc. Symp. Proc.* **433**, 325-332 (1996).

81. Ravichandran, D., R. Meyer, Jr., R. Roy, R. Guo, A.S. Bhalla, and L.E. Cross, "Sol-Gel Synthesis of $Ba(Mg_{1/3}Ta_{2/3})O_3$: Phase Pure Powder and Thin Films." *Mat. Res. Bull.* **31** (7), 817-825 (1996).

82. Ravichandran, D., K. Yamakawa, R. Roy, A.S. Bhalla, S. Trolier-McKinstry, R. Guo, and L.E. Cross, "The Effect of Annealing Temperature on the Formation of $SrBi_2Ta_2O_9$ (SBT) Thin Films." Submitted *Proceedings of IEEE International Symposium on the Applications of Ferroelectrics*, Rutgers University, East Brunswick, New Jersey (August 1996).

Instrumentation

83. Su, J., P. Moses, and Q.M. Zhang, "A Bimorph Based Dilatometer for Field Induced Strain Measurement in Soft and Tin Free Standing Polymer Films." *Reviews of Scientific Instruments* (submitted).

MATERIALS STUDIES

(continued)

APPENDIX 16

Effect on Electrical Properties of Barium and Strontium Additions in the Lead Lanthanum Zirconate Stannate Titanate System

Seung-Eek Park,[*] Kelley Markowski, Shoko Yoshikawa,[*] and L. Eric Cross[*]

Materials Research Laboratory, The Pennsylvania State University, University Park, Pennsylvania 16802

The effect of barium (Ba) and strontium (Sr) additions on the electrical properties of lead lanthanum zirconate stannate titanate (PLZST) ceramics and their electrically induced phase change behavior was examined. Sr additions decreased both the ferroelectric (FE) ↔ antiferroelectric (AFE) transition temperature (T_{AFE-FE}) and the temperature of the maximum dielectric constant (T_{MAX}). This indicates that Sr additions stabilize the AFE phase. Along with B-site modifications Sr additions can be used to decrease the switching field and hysteresis. Ba additions caused the temperature range of the AFE phase to narrow by increasing T_{AFE-FE} and decreasing T_{MAX}. This behavior indicates an ability to lower the switching field and suppress hysteresis. Using a combination of both A-site and B-site modifications it is possible to tailor the properties (for example, switching field, hysteresis, and operating temperature range) of this group of phase change materials to meet the requirements of specific applications.

I. Introduction

IN 1965 Berlincourt *et al.*[1] established the ternary phase diagram for the PLZST family of ceramics. This phase diagram included the stability regions for the antiferroelectric (AFE) and ferroelectric (FE) phases as well as their symmetries, for example, $FE_{R(HT)}$ (ferroelectric rhombohedral, high temperature), $FE_{R(LT)}$ (ferroelectric rhombohedral, low temperature), $AFE_{(T)}$ (antiferroelectric, tetragonal), and $AFE_{(O)}$ (antiferroelectric, orthorhombic). The phase most studied has been the $AFE_{(T)}$ phase because of its ability to be readily switched to its neighboring $FE_{R(LT)}$ phase with the application of an electric field. This transition is accompanied with a large change in volume associated with high longitudinal strain. This material, therefore, has been investigated for applications including charge storage capacitors[1,2] and high strain transducers and actuators.[3–5]

High strains of up to 0.5% have been reported for this material.[6] However, this amount of strain is not achieved at the AFE–FE phase switching field but rather at fields much higher than the switching field. After switching occurs, the strain continues to increase with the subsequent application of higher electric fields. Therefore, low switching fields are a prerequisite to obtaining high strain. The hysteresis (the difference in the forward and backward switching fields) that accompanies the AFE–FE transition should also be decreased to avoid the large temperature change caused by self heat generation.

Variations in PLZST compositions were previously investigated and reported.[6] Both Ti:Sn and Zr:Sn ratio variations were considered. On decreasing the Ti:Sn ratio along a line perpendicular to the morphotropic phase boundary (MPB) in the phase diagram ("A" compositions shown in Fig. 1) the following conclusions were made: the switching field increased with an associated decrease in the FE–AFE transition temperature; the dielectric maxima peak became more diffuse; and the room-temperature dielectric constant decreased. Regardless of the Ti:Sn ratio: 0.2% strain was realized at the switching field; strain continued to increase with increasing field after phase switching; the hysteresis remained constant at 25 kV/cm along with T_{MAX}. Increasing the Zr:Sn ratio along the MPB ("B" compositions in Fig. 1): the hysteresis increased with an increase in T_{MAX}; the switching field decreased with an increase in the AFE–FE transition temperature; the strain at the switching field remained nearly constant at approximately 0.16%; the dielectric maximum increased; the dielectric maximum peak also became sharper.

Based on this research, variations within the PLZST system were found to modify either switching field or hysteresis. However, a modification producing the desired decrease in both switching field and hysteresis was not possible. These variations at best produced a sample with lowered switching field and constant hysteresis (Ti/Sn ratio modifications). Therefore, A-site modifications based on tolerance factor considerations and phase stability were evaluated. The tolerance factor can be described for perovskites with the general formula ABX_3 by

$$t = (R_A + R_X)/(\sqrt{2})(R_B + R_X)$$

where R_A is the radius of A, R_B the radius of B, and R_X the radius of X. When $t > 1$ the FE phase is stabilized, and when $t < 1$ the AFE phase is stabilized.[7] For Pb-based compounds, however, only trends need to be considered because of the high polarizability of the Pb. Both Ba and Sr were considered as A-site additions in this study, Ba being an FE stabilizer and Sr being an AFE stabilizer, both potentially lowering T_{MAX} and subsequently suppressing hysteresis.

In this study, compositional modifications on the A-site were investigated. Additions of Ba and Sr were evaluated in both the AFE and FE regions of the PLZST phase diagram. Polarization, strain, and dielectric properties were measured. The effect of these additions is also discussed on the basis of tolerance factor, with respect to ionic size.
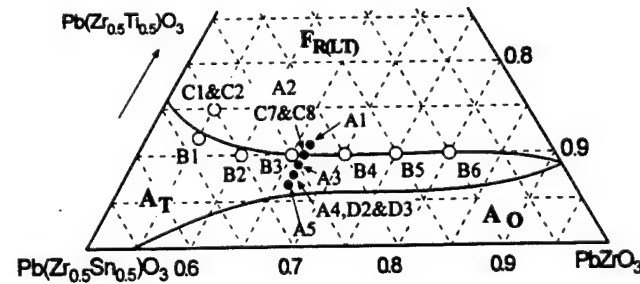

Fig. 1. PLZST phase diagram[1] and investigated compositions.

Table I. PLZST Compositions with Ba and Sr Additions

	Composition	Comments
C1	$(Pb_{0.93}Sr_{0.05}La_{0.02})(Zr_{0.55}Ti_{0.15}Sn_{0.30})_{0.995}O_3$	In Fe region of phase diagram
C2	$(Pb_{0.93}Ba_{0.05}La_{0.02})(Zr_{0.55}Ti_{0.15}Sn_{0.30})_{0.995}O_3$	
C7	$(Pb_{0.93}Sr_{0.05}La_{0.02})(Zr_{0.66}Ti_{0.10}Sn_{0.24})_{0.995}O_3$	On the MPB
C8	$(Pb_{0.93}Ba_{0.05}La_{0.02})(Zr_{0.66}Ti_{0.10}Sn_{0.24})_{0.995}O_3$	
A2[6]	$(Pb_{0.98}La_{0.02})(Zr_{0.66}Ti_{0.10}Sn_{0.24})_{0.995}O_3$	
D3	$(Pb_{0.88}Ba_{0.10}La_{0.02})(Zr_{0.66}Ti_{0.08}Sn_{0.26})_{0.995}O_3$	10% Ba, Zr:Ti:Sn 66:8:26, in AFE region of phase diagram
D2	$(Pb_{0.93}Ba_{0.05}La_{0.02})(Zr_{0.66}Ti_{0.08}Sn_{0.26})_{0.995}O_3$	5% Ba, Zr:Ti:Sn 66:8:26
A4[6]	$(Pb_{0.98}La_{0.02})(Zr_{0.66}Ti_{0.08}Sn_{0.26})_{0.995}O_3$	0% Ba, Zr:Ti:Sn 66:8:26

II. Experimental Procedure

(1) Sample Preparation

The compositions discussed in this paper were prepared according to the formulas presented in Table I. Polycrystalline ceramic materials investigated in this study were prepared by solid-state reaction, using the appropriate amounts of reagent-grade raw materials of lead carbonate $(2PbCO_3 \cdot Pb(OH)_2)$ (Hammond Lead Products, Inc., Hammond, IN), lanthanum oxide $(La_2O_3$, Alpha Products Co., Danvers, MA), zirconium dioxide $(ZrO_2$, Harshaw Chemical Co., Cleveland, OH), titanium dioxide $(TiO_2$, Whitaker, Clark and Daniels Co., Plainfield, NJ), and tin oxide $(SnO_2$, Alpha, Ward Hill, MA). The chemical purity of each was greater than 99%. Barium and strontium additions were made using the appropriate amounts of strontium carbonate $(SrCO_3$, Alpha, Ward Hill, MA) and barium carbonate $(BaCO_3$, J. T. Baker Chemical Co., Phillipsburg, NJ), respectively. The sintering process was carried out in a lead-rich environment in order to minimize lead volatilization. To further enhance densification and increase the electric field where dielectric breakdown occurs, the sintered specimens were hot isostatically pressed for 2 h at 1200°C in an air atmosphere under a pressure of 20 MPa. Disk samples were then prepared by polishing with silicon carbide and alumina polishing powders to achieve flat and parallel surfaces onto which gold was sputtered as an electrode.

(2) Characterization Techniques

(A) Phase and Microstructure: Calcined and sintered powders were examined by X-ray diffraction to ensure phase purity and to identify the crystal structure. Typically the samples showed a single phase within the detection limit of XRD (<2%).

(B) Dielectric Properties: Multifrequency impedance analyzers (Hewlett-Packard 4274A and 4275A LCR meters) were used in conjunction with a computer-controlled temperature chamber (Delta Design Inc., Model MK 2300) to measure capacitance as a function of temperature and frequency. Capacitance was converted to dielectric permittivity using the sample

geometry and permittivity of air. Measurements were taken from 100 Hz to 100 kHz at temperatures from $-150°$ to 250°C.

(C) Polarization and Strain: High field measurements included polarization and strain hysteresis using a computer-controlled modified Sawyer Tower system with a National Instruments Input Output card and linear variable displacement transducer (LVDT) sensor driven by a lock-in amplifier (Stanford Research Systems, Model SR830), respectively. The voltage was supplied using a Trek 609C-6 high-voltage dc amplifier. Through the LVDT sensor the strain of the samples can be measured with the application of an applied field. Electric fields as high as ~100 kV/cm were applied using an amplified sine waveform at 0.2 Hz. During testing the samples were submerged in Fluorinert (FC-40, 3M, St. Paul, MN), an insulating liquid, to prevent arcing.

III. Results and Discussion

(1) Sr Additions

(A) In the Ferroelectric Region: Additions of Sr^{2+} in the FE region of the PLZST phase diagram demonstrated that 5% Sr^{2+} additions (composition C1) produced samples that were AFE at room temperature even though compositionally located in the FE region of the phase diagram. The polarization and strain behavior are shown in Fig. 2. The switching field, polarization, and strain data are summarized in Table II. This AFE behavior at room temperature showed that Sr additions induce a shift in the AFE_{Tet}–FE_{Rhom} phase boundary upward toward the $Pb(Zr_{0.5}Ti_{0.5})O_3$ composition. This shift indicates a more stable room-temperature AFE phase associated with the decrease of both T_{FE-AFE} and T_{MAX}. The stabilization of the AFE phase produced higher switching fields with less hysteresis. Additions of Sr^{2+} also produced a decrease in the maximum dielectric constant and more diffuse dielectric constant behavior as a function of temperature. Dielectric data are shown in Fig. 3.

This decrease in T_{FE-AFE} can be described by tolerance factor considerations. Sr is smaller than Pb (1.27 and 1.32 Å, respectively) and thereby decreases the tolerance factor upon substitution, decreasing the space in which the B-site cation is allowed
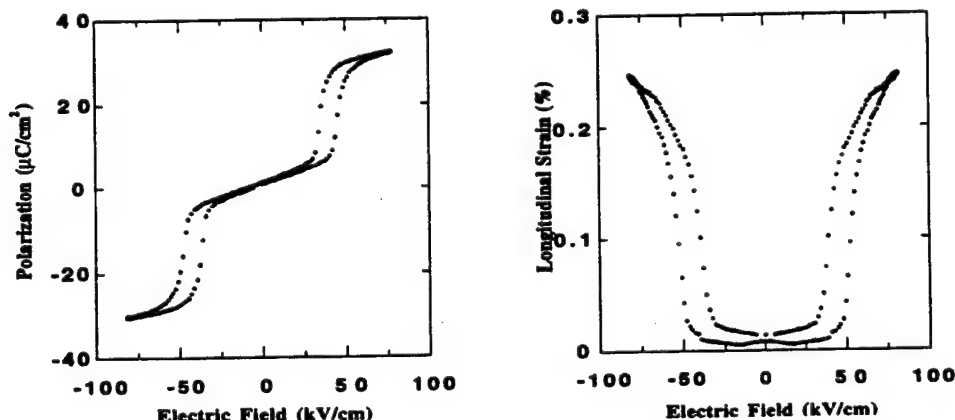

Fig. 2. Electrically induced polarization and strain for composition C1.

Table II. Summary of Electric-Field-Induced Polarization and Strain for Ba- and Sr-Modified Compositions[†]

| | Electric-field induced polarization and strain | | | | | | | |
| | At switching field | | | | At maximum applied field | | | |
Sample	E_{AF} (kV/cm)	$\Delta E' = E_{AF} - E_{FA}$ (kV/cm)	P_s (μC/cm²)	S_3 (%)	E_{app}	P_{app} (μC/cm²)	S_3 (%)	Comments
C1	50	10	23	0.17	79	34	0.25	5% Sr
C2	FE				90	35	0.18	5% Ba
C7	No switching occurred (max field 100 kV/cm)							5% Sr
C8 (25°C)	FE				63	32	0.28	5% Ba
C8 (70°C)	24	13	15	0.19	75	32	0.32	5% Ba
A2[6]	37	25	32	0.18	111	38	0.42	0% Ba
D3	27	10	26	0.17	54	29	0.27	10% Ba
D2	39	23	24	0.20	92	34	0.34	5% Ba
A4[6]	71	25	32	0.16	133	41	0.48	0% Ba

[†]E_{AF} = field for antiferroelectric–ferroelectric phase switching (forward switching). E_{FA} = field for ferroelectric–antiferroelectric phase switching (backward switching). ΔE = difference between the E_{AF} and E_{FA}.

to "rattle." This in turn decreases the polarizability facilitating a decrease in the Curie point. Initially, the Curie point corresponds to the ferroelectric phase transition temperature, in this system, T_{FE-AFE}. Therefore, T_{FE-AFE} will decrease with Sr additions. Sr additions also decreased the T_{MAX}, indicating further stabilization of the paraelectric phase along with the antiferroelectric phase. This decrease in T_{MAX} can further be correlated to the narrow hysteresis found with Sr additions in comparison to compositions without Sr. Dielectric data in Fig. 3 also show the dielectric constant ($K \sim 1000$, 1 kHz) of virgin samples (no exposure to an electric field) to be lower than those of samples exposed to their switching field ($K \sim 1300$, 1 kHz). This behavior can be attributed to the AFE domain preferred orientation after exposure to an electric field.

(B) On the Morphotropic Phase Boundary: Additions of 5% Sr in the AFE region of the phase diagram (composition C7) also caused a decrease in T_{FE-AFE}, which produced a highly stable AFE phase that could not be switched at an applied field of 100 kV/cm at room temperature. The polarization behavior is shown in Fig. 4. Compositionally C7 has the same Zr:Ti:Sn ratio (66:10:24) as composition A2, which was AFE with a switching field of 37 kV/cm. The addition of Sr compared to composition A2 produced a significantly higher switching field and more stable room-temperature AFE. These results are shown in Table II. Through analysis of the dielectric data it is
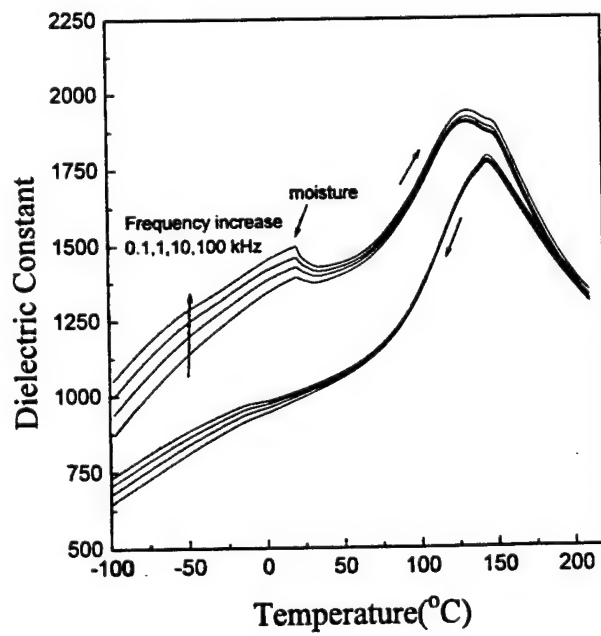

Fig. 4. Polarization vs electric field for composition C7.

found that an FE–AFE transition exists below −50°C, producing a highly stable room-temperature AFE phase.

Additions of Sr brought a decrease in both T_{MAX} (contributing to a decrease in hysteresis) and a decrease in T_{FE-AFE} (contributing to a higher switching field). As shown in our previous work[6] variations in the Zr:Sn ratio produce the same behavior; therefore, Sr additions alone have limited benefits. The increase in switching field caused by Sr additions is the limiting factor when considering this modification. However, a combination of varied Ti:Sn ratio (producing variations in the T_{FE-AFE}, AFE stability, and hence switching field, while maintaining a constant hysteresis and constant T_{MAX}) can be used in conjunction with A-site modifications (which alter the T_{MAX}) to further engineer the properties of PLZST ceramics. Figure 5 shows the composition region which can be modified by Sr^{2+} in the PLZST phase diagram, considering a shift in the AFE_{Tet}–FE_{Rhom} phase boundary upward toward the $Pb(Zr_{0.5}Ti_{0.5})O_3$ composition.

Fig. 3. Temperature dependence of dielectric constant for the composition C1; (heating) E-field exposed sample and (cooling) virgin sample.
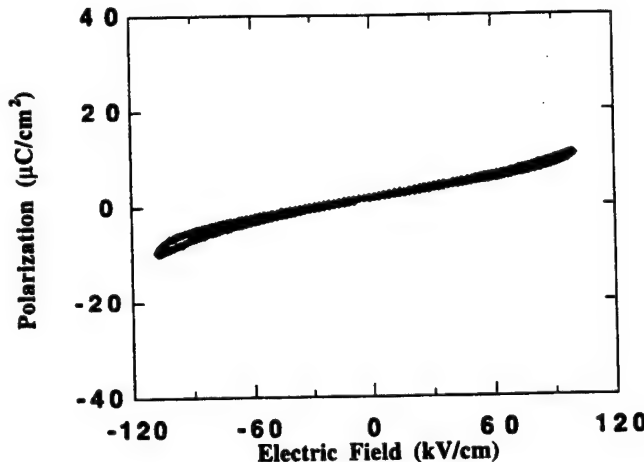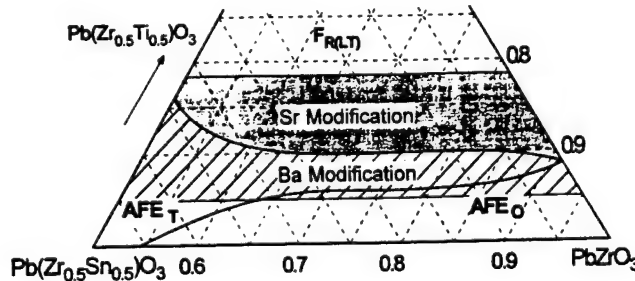

Fig. 5. Schematic of possible compositional regions for Ba and Sr additions.
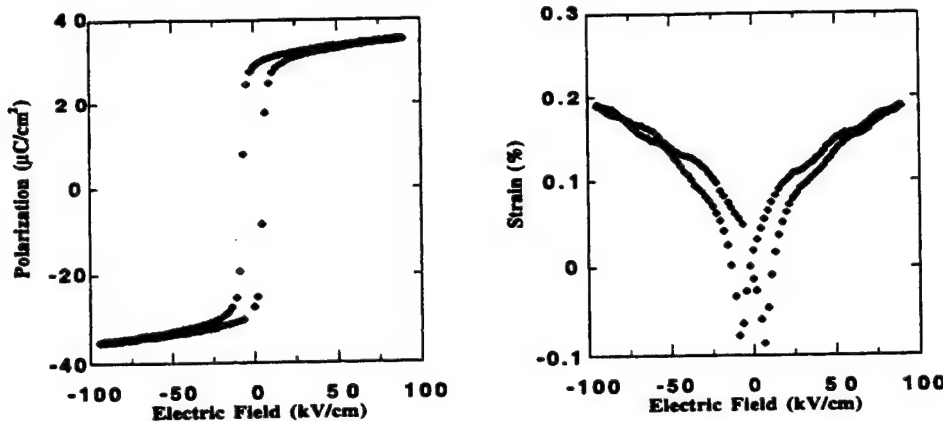
Fig. 6. Electrically induced polarization and strain for composition C2.

(2) Ba Additions

(A) In the FE Region: Preliminary results regarding 5% Ba additions in the FE region (composition C2) showed FE behavior at room temperature. The polarization and strain behavior are shown in Fig. 6 and summarized in Table II. This behavior was anticipated because Ba is an FE stabilizer. With respect to tolerance factor considerations Ba is larger than Pb (1.48 and 1.32 Å, respectively), therefore stabilizing the FE phase, increasing the space that the B-site cation can "rattle." The Curie temperature, T_C (which can be correlated to T_{FE-AFE}), should increase with Ba additions. Dielectric data in Fig. 7 showed a transition from FE to PE without any AFE stable temperature range. This figure showed the dielectric constant of virgin samples to be higher than those of samples exposed to an E-field (poled); this behavior indicates the presence of an FE phase. We can infer from these data that this modification decreases T_{MAX} and increases T_{FE-AFE} effectively overlapping and obscuring the AFE phase region altogether. This behavior indicates that Ba additions decrease the temperature range of the AFE phase which brings about the desirable properties of low switching field and suppressed hysteresis. To confirm this behavior a Ba-modified composition near the MPB was chosen.

(B) On the MPB: Results regarding 5% Ba additions (composition C8) indicated FE behavior at room temperature although the composition is located in the AFE region of the phase diagram near the MPB. The room-temperature FE behavior was anticipated because of the large size of the Ba ions being incorporated into the PLZST structure. For the same PLZST composition (A2) without Ba the T_{FE-AFE} was approximately $-30°C$. Dielectric data in Fig. 8 show an abrupt FE-AFE transition at 40°C for poled samples (on heating) with a diffuse AFE-FE transition for virgin samples (on cooling). This indicates the phase switching from FE to AFE at 40°C. This finding confirms that Ba additions increase the T_{FE-AFE}. It is also interesting to note the exchange of higher dielectric constant curve from the virgin to poled sample at 40°C. These behaviors can also be ascribed to the transition of poled FE phase into subsequent AFE phase. As previously demonstrated by compositions C1 and C2, AFE compositions tend to have a higher dielectric constant for samples that have been exposed to an electric field large enough to achieve phase switching to FE, while for FE compositions exposed to an electric field (poled) the opposite is true. The polarization and strain data at both 25° and 70°C are shown in Fig. 9 and summarized in Table II. FE and AFE behaviors are found at 25° and 70°C, respectively. This behavior is consistent with the previous results showing a phase transition at 40°C.

These results indicate that the Ba addition shifted the AFE_{Tet}–FE_{Rhom} phase boundary downward toward the $PbZrO_3$–$PbSnO_3$ binary line because 5% Ba^{2+} additions stabilize the FE phase in
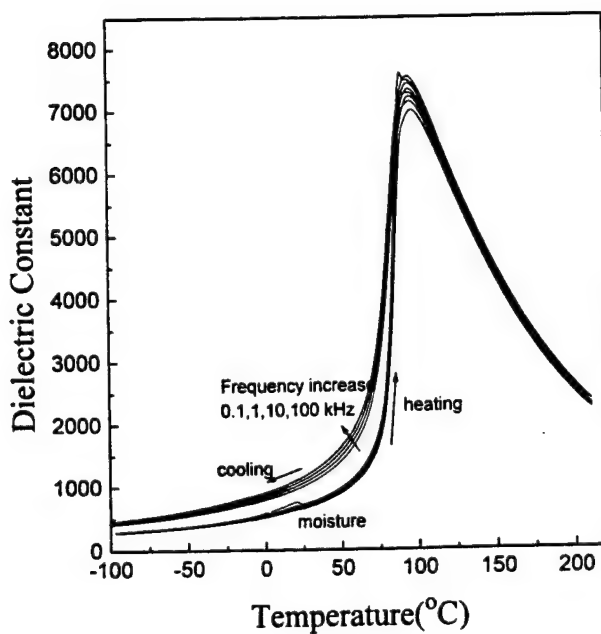

Fig. 7. Temperature dependence of dielectric constant for the composition C2; (heating) poled sample and (cooling) virgin sample.
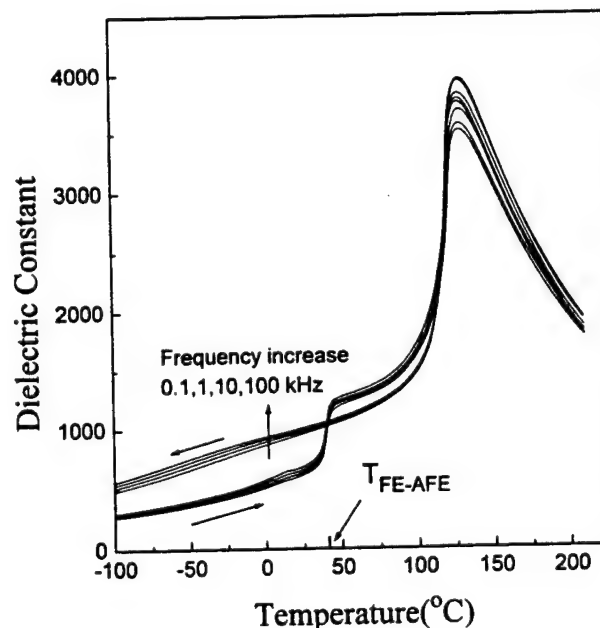

Fig. 8. Temperature dependence of dielectric constant for the composition C8; (heating) poled sample and cooling (virgin sample).
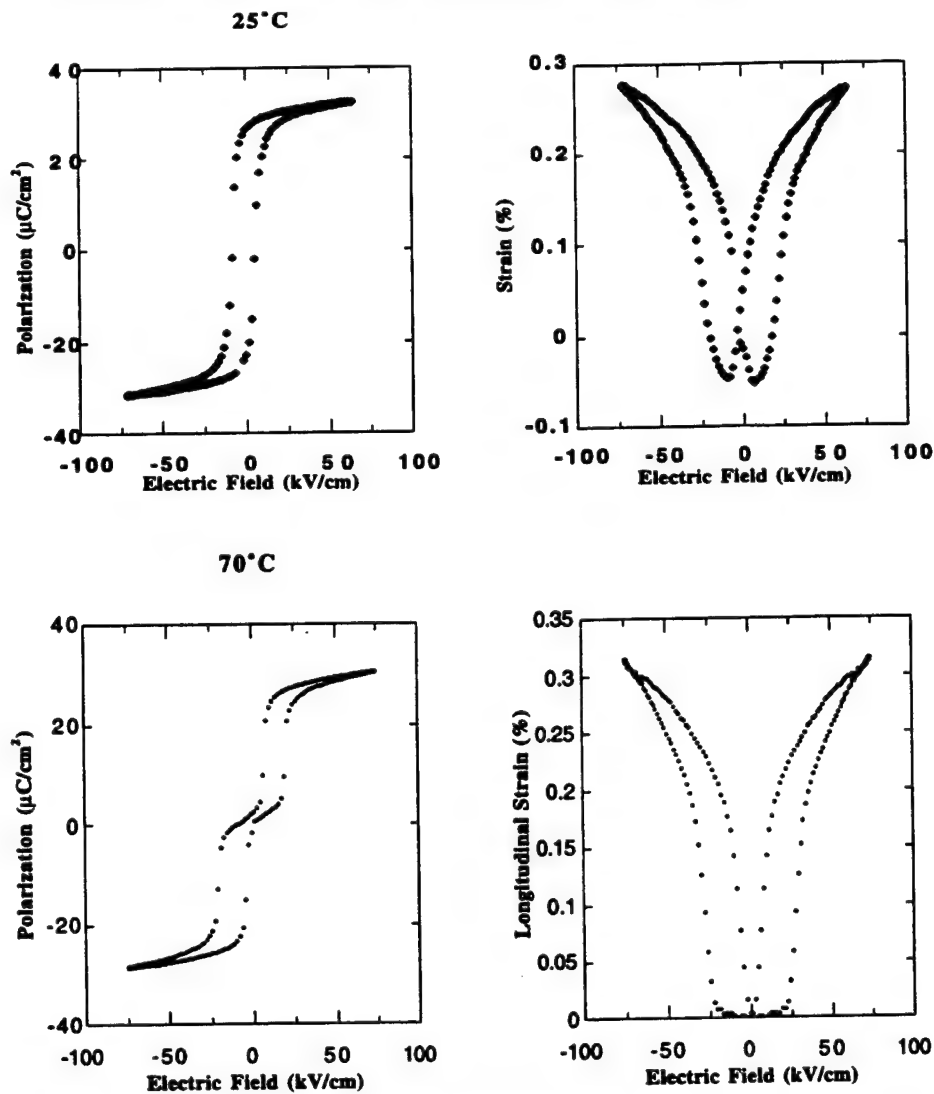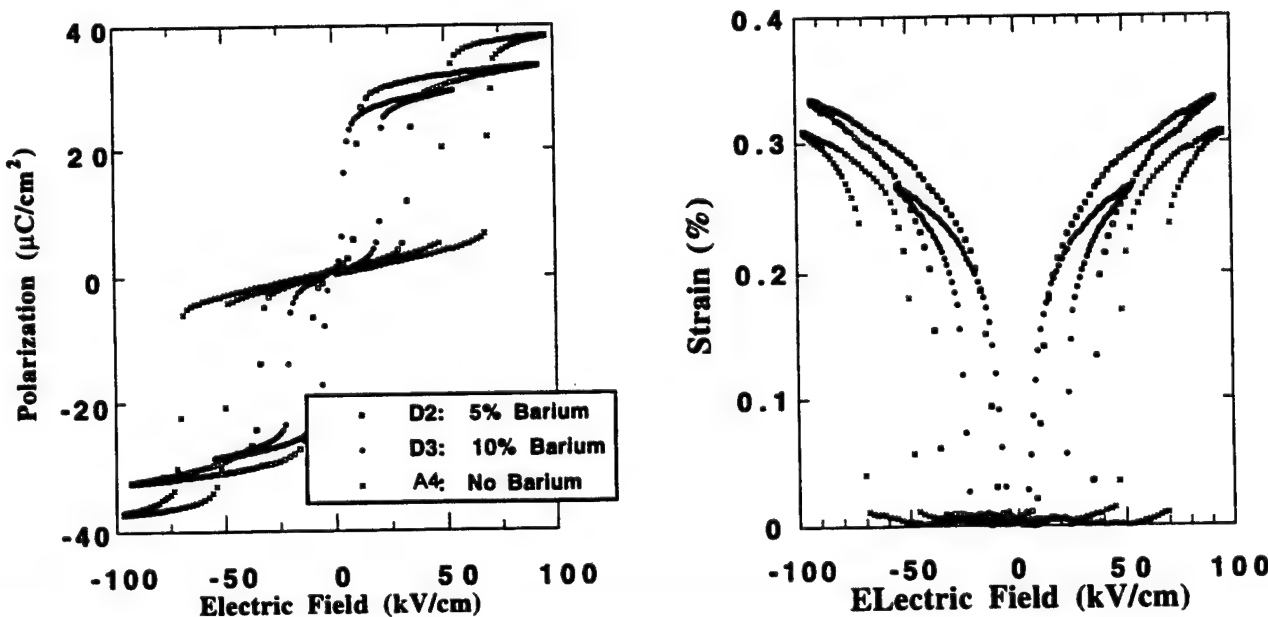
25°C

70°C

Fig. 9.   Electrically induced polarization and strain for composition C8, 25° and 70°C.

Fig. 10.   Electrically induced polarization and strain for compositions D2, D3, and B4.

the AFE region of the PLZST phase diagram. Therefore, Ba^{2+} additions should be considered in the AFE region as shown in Fig. 5.

(C) Comparison of 0%, 5%, and 10% Ba Addition in AFE Region: As discussed previously, Ba^{2+} additions tend to stabilize the FE phase. These results, however, were based on compositions relatively near the MPB and FE region. To more clearly address the effect of the Ba^{2+} additions and to magnify its effect, 10% Ba^{2+} additions deep within the AFE region were considered. The compositions considered were D2 with 5% Ba, D3 with 10% Ba, and A4[6] with no Ba, all with the same Zr:Ti:Sn ratio of 66:08:26. These compositions are shown in Fig. 1.

Table II and Fig. 10 show the comparison of the polarization and strain induced by application of an E-field for the compositions A4, D2, and D3. Increased Ba^{2+} content clearly lowered switching field, and decreased hysteresis. It is important to note that the maximum strain is a function of sample quality (density, second phase, etc.) and associated maximum electric field rather than composition in this case. The dielectric data are shown in Fig. 11. These data showed a decreased T_{MAX} (associated with decreased hysteresis), increased K_{MAX}, and increased T_{FE-AFE} (associated with decreased switching field) with increased Ba^{2+} content.

Through the compositional analysis of both A- and B-site modifications it is possible to consider the requirements of a specific application and tailor the properties of the phase change material. For example, A-site modification with Ba^{2+} decreases both hysteresis and switching field at room temperature, at the expense of narrower operating temperature range. The switching field and hysteresis will also be as a function of the operating temperature and microstructure. This dependence will be discussed in future work.

IV. Conclusions

Additions of Sr can be used along with Ti:Sn ratio changes to modify the properties of phase change ceramics, for example decreasing hysteresis. Sr additions have limited merit because they cause increases in the switching field and therefore increases in the field necessary to obtain maximum strain levels. Ti:Sn ratio changes can be used to lower the switching field and Sr additions can be used to suppress hysteresis.

Ba additions proved to be a FE phase stabilizer lowering the T_{MAX} and increasing the T_{FE-AFE}. These additions lowered both the amount of hysteresis and the switching field. It should be noted, however, that these changes also make the AFE temperature range smaller. Ideally, with respect to applications, a balance should be maintained between switching field, hysteresis, and operating temperature range.
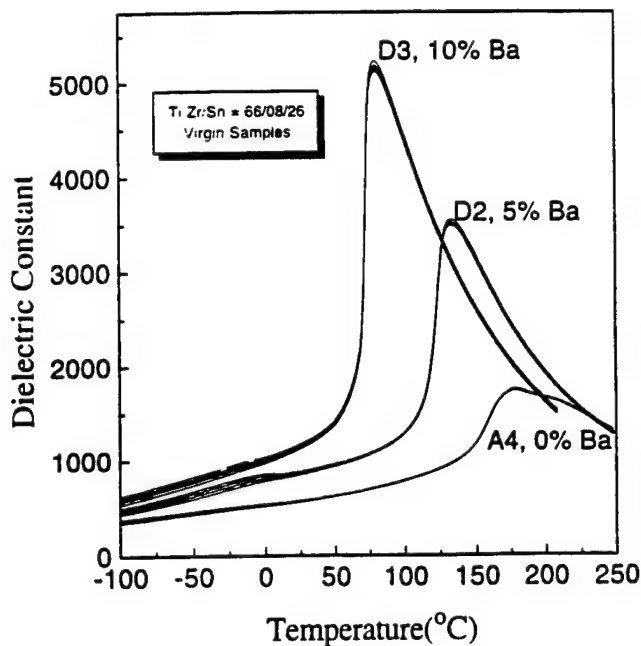

Fig. 11.   Temperature dependence of dielectric constant for the composition A4, D2, and D3; (cooling) virgin sample.

References
[1]D. Berlincourt, H. H. A. Krueger, and B. Jaffe, "Stability of Phases in Modified Lead Zirconate with Variation in Pressure, Electric Field, Temperature and Composition," *J. Phys. Chem. Solids*, **25**, 659–74 (1964).
[2]B. Jaffe, "Antiferroelectric Ceramics with Field-Enforced Transitions: A New Nonlinear Circuit Element," *Proc. IRE*, **49** [8] 1264–67 (1961).
[3]K. Uchino and S. Nomura, "Electrostriction in PZT-Family Antiferroelectrics," *Ferroelectrics*, **50**, 191–96 (1983).
[4]A. Furuta, K.-Y. Oh, and K. Uchino, "Shape Memory Ceramics and Their Application to Latching Relays," *Sens. Mater.*, **3,4**, 205–15 (1992).
[5]W. Y. Pan, Q. Zhang, A. Bhalla, and L. E. Cross, "Field-Forced Antiferroelectric-to-Ferroelectric Switching in Modified Lead Zirconate Titanate Ceramics," *J. Am. Ceram. Soc.*, **72** [4] 571–78 (1989).
[6]K. Markowski, S.-E. Park, S. Yoshikawa, and L. E. Cross, "The Effect of Compositional Variations in the Lead Lanthanum Zirconate Stannate Titanate System on Electrical Properties," *J. Am. Ceram. Soc.*, **79** [12] 3297–304 (1996).
[7]K. J. Rao and C. N. R. Rao, *Phase Transitions in Solids: An Approach to the Study of the Chemistry and Physics of Solids*. McGraw-Hill, New York, 1978. □

APPENDIX 17

Antiferroelectric-to-Ferroelectric Phase Switching Lead Lanthanum Zirconate Stannate Titanate (PLZST) Ceramics

Shoko Yoshikawa[a] , Kelley Markowski[b] , Seung-Eek Park,
Ming-Jen Pan, L. Eric Cross

Materials Research Laboratory, The Pennsylvania State University,
University Park, PA 16802

ABSTRACT

Electric field induced antiferroelectric (AFE) to ferroelectric (FE) phase transformations are accompanied by large strain and significant hysteresis. The properties of these materials can be tailored to fit specific applications such as high strain actuators and charge capacitors. As an attempt to reduce hysteresis, Barium and Strontium A-site substitution of the phase transformation behavior of $(Pb_{0.98-\delta}La_{0.02}A_\delta)(Zr_xSn_yTi_z)O_3$ (A=Ba, Sr) ceramics have been investigated. The ceramic samples in this study produced 0.2% to 0.3% strain level. Barium proved to be a strong FE stabilizer with decreasing both switching field and hysteresis, while Strontium proved to be a strong AFE stabilizer. Some practical data, including temperature stability and current requirements, are also to be discussed.

Keywords: lead zirconate stannate titanate ceramics, antiferroelectric-to-ferroelectric phase switching ceramics, field induced strain, field induced polarization

1. INTRODUCTION

Lead zirconate ($PbZrO_3$) and lead titanate ($PbTiO_3$) form a complete solid-solution series (lead zirconate titanate, or PZT) of great technological importance. It is used in various Zr:Ti ratios and with numerous dopants to manufacture a vast array of electronic and electromechanical devices.

The effects of pressure-enforced ferroelectric (FE) to antiferroelectric (AFE) in modified $PbZrO_3$ was originally studied by Berlincourt et al. for an application of shock-actuated power supplies[1,2]. The relatively recent work on the same ceramics are published from Sandia National Laboratories[3,4].

Triaxial phase diagram introducing lead stannate ($PbSnO_3$) for both Niobium (Nb) and Lanthanum (La) doped system have been developed from the large amount of compositional study pursued at Clevite Corporation[1,2] in 1960s.

(a) Shoko Yoshikawa: Correspondence: e-mail: sxy3@psuvm.psu.edu; Phone: (814) 863-1096; Fax: (814) 865-2326
(b) Kelley Markowski: Current address: Materials Systems Inc., Littleton, MA 01460

Our interest in these families of materials lies in their ability to produce large strain at the electric (E)-field induced tetragonal AFE (AFE$_T$) to rhombohedral FE transformation (FE$_R$)[5,6]. Depending on the compositional adjustments, the materials can exhibit shape memory effect as described by Uchino, et al.[7].

Our compositions, unlike the above example of FE-to-AFE transformation to release energy upon application of pressure, start from AFE$_T$ phase and switches to FE phase upon application of E-field. For actuator application, it is, therefore, important to optimize the compositions to exhibit following characteristics:

1. Larger strain, thus larger displacement,
2. Lower hysteresis, thus less heat generation, and
3. Lower switching field, thus less E-field requirement.

We have shown previously[8,9] that the B-site compositional modification controls switching field, though hysteresis behavior has little influence.

The objective in this study, therefore, is to attempt to produce compositions with less hysteresis without sacrificing too much strain while maintaining relatively low switching E-field. A-site modifications were accomplished by the addition of Ba and Sr.

2. EXPERIMENTAL PROCEDURE

2.1 Sample preparation

The five compositions described as A, A1, A2, B, and C in Table 1 were prepared according to the formula. Figure 1 shows the location of these compositions in the PLZST ternary phase diagram. Polycrystalline ceramic materials investigated in this study were prepared by solid state reaction, using the appropriate amount of reagent grade raw materials of lead carbonate ($PbCO_3$), lanthanum oxide (La_2O_3), zirconium dioxide (ZrO_2), titanium dioxide (TiO_2), and tin oxide (SnO_2). The chemical purity of each of the raw materials was greater than 99%. Barium and strontium additions were made using the appropriate amounts of strontium carbonate ($SrCO_3$) and barium carbonate ($BaCO_3$), respectively. The sintering process was carried out in a lead rich environment in order to minimize lead volatilization. To further enhance densification and increase the electric field where dielectric breakdown occurs, the sintered specimens were hot isostatically pressed for 2 hours at 1200°C in an air atmosphere under a pressure of 20MPa. Disk samples were then prepared by polishing with silicon carbide and alumina polishing powders to achieve a flat and parallel surface onto which gold was sputtered as an electrode.

Table 1.   PLZT compositions.

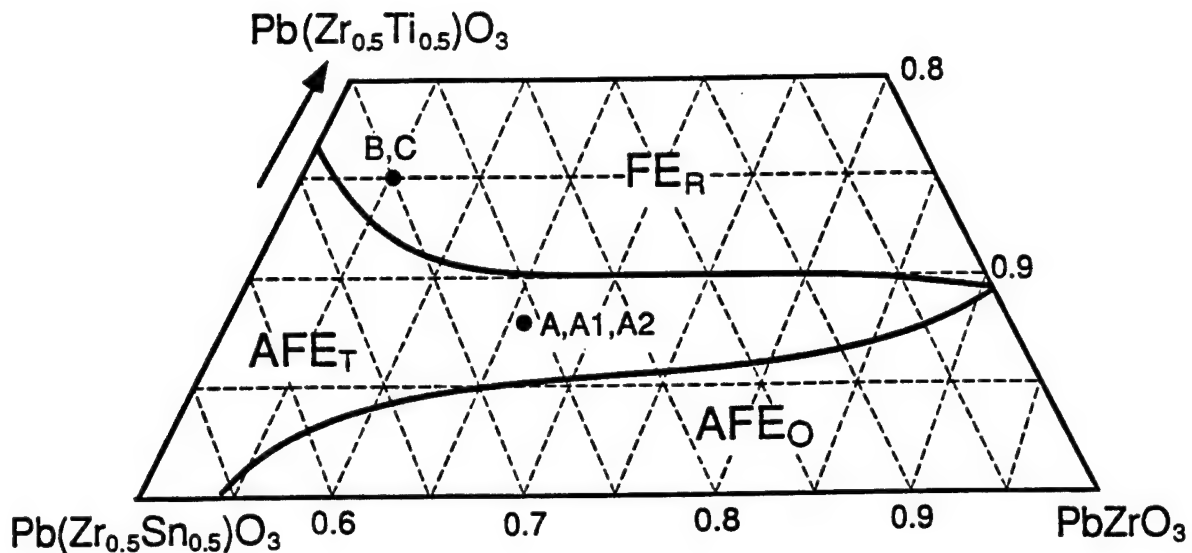|	COMPOSITION	Comments
A	$(Pb_{0.88}La_{0.02})(Zr_{0.66}Ti_{0.26})_{0.995}O_3$	0% Ba, Zr:Ti:Sn 66:8:26
A1	$(Pb_{0.93}Ba_{0.05}La_{0.02})(Zr_{0.66}Ti_{0.08}Sn_{0.26})_{0.995}O_3$	5%Ba,Sr:Ti:Sn 66:8:26
A2	$(Pb_{0.88}Ba_{0.10}La_{0.02})(Zr_{0.66}Ti_{0.08}Sn_{0.26})_{0.995}O_3$	10%Ba,Zr:Ti:Sn 66:8:26
B	$(Pb_{0.93}Sr_{0.05}La_{0.02})(Zr_{0.55}Ti_{0.15}Sn_{0.30})_{0.995}O_3$	5% Sr, FE region of phase diagram
C	$(Pb_{0.93}Ba_{0.05}La_{0.02})(Zr_{0.55}Ti_{0.15}Sn_{0.30})_{0.995}O_3$	5% Ba, FE region of phase diagram

Figure 1:   PLZST phase diagram and investigated compositions.

2.2   Characterization techniques

(a)   Phase and microstructure

Calcined and sintered powders were examined by x-ray diffraction to insure phase purity and to identify the crystal structure. Typically, the samples showed a single phase within the detection limit of XRD (< 2%).

(b)   Dielectric properties

Multifrequency meters (Hewlett Packard 4274A and 4275A LCR meters) were used in conjunction with a computer controlled temperature chamber (Delta Design Inc., Model MK 2300) to measure capacitance as a function of temperature and frequency. Capacitance was converted to dielectric permittivity using the sample geometry and permittivity of air. Measurements were taken from 100 Hz to 100 kHz at temperatures from -150°C to 250°C.

(c)   Polarization and strain

High field measurements included polarization and strain hysteresis using a computer controlled modified Sawyer Tower system with a National Instruments Input Output card and linear variable displacement transducer (LVDT) sensor driven by a lock in amplifier (Stanford Research Systems, Model SR830). The voltage was supplied using a Trek 609C-6 high voltage DC amplifier. Through the LVDT sensor the strain of the samples can be measured with the applications of an applied field. Electric fields as high as ~ 100kV/cm were applied using an amplified sine waveform at 0.2 Hz. During testing the samples were submerged in Fluorinert (FC-40, 3M), an insulating liquid, to prevent arcing.

3.   RESULTS AND DISCUSSION

3.1   A-Site Modification

A-site modifications were based on tolerance factor, which can be described for perovskites with the general formula ABX_3 by:

$$t = (R_A + R_X) / (\sqrt 2) (R_B + R_X)$$

where R_A = radius of A, R_B = radius of B and R_X = radius of X. Ba^{2+} (1.48Å) is larger than Pb^{2+} (1.32Å), and Sr^{2+} (1.27Å) is smaller than Pb^{2+}. When t > 1 the FE phase is stabilized when t < 1 the AFE phase is stabilized[10]. For Pb based compounds, however, only trends need to be considered because of the high polarizability of the Pb. Both Ba and Sr were considered as A-site additions only in this study. Ba being a FE stabilizer and Sr being a AFE stabilizer both potentially lowering T_{max} and subsequently suppressing hysteresis.

Figure 2 shows E-field induced polarization (a) and strains (b) for compositions A, A1, and A2. As anticipated, increased Ba^{2+} content clearly lowered switching field, and decreased hysteresis. It is important to note that the maximum strain is a function of applied electric field after the switching. The dielectric data is shown in Figure 3. This data showed a decrease T_{max} (associated with decreased hysteresis), increased K_{max} and increased T_{FE-AFE} (associated with decreased switching field) with increased Ba^{2+} content, though T_{FE-AFE} is not obvious in virgin sample. This also indicates that the operating temperature range is narrower as Ba^{2+} content increased (to be discussed below).

Figures 4 to 7 show the results of compositions B and C. The original location of the composition is in rhombohedral ferroelectric region (FE_R); therefore, the composition without Ba or Sr addition is ferroelectric. As anticipated from Sr being AFE stabilizer, as sintered composition B with 5% Sr addition showed antiferroelectric, and underwent AFE-to-FE transformation upon application of E-field (Figure 4). The switching field was approximately 50 kV/cm, and hysteresis was relatively small.

On the contrary, the same composition with Ba^{2+} addition instead of Sr^{2+} showed stable ferroelectric behavior, as shown in Figure 6. Dielectric data in Figure 7 showed a transition from FE to PE (paraelectric) without any AFE stable temperature range. It is determined from the fact that the cooling run (sample depoled by exposing temperature above T_{max}) showing higher dielectric constant than heating (E-field exposed sample) run, unlike the data in Figure 5.

3.2.   Temperature stability

Low field dielectric data, as discussed above, are important tools to determine temperature stability of each composition without actually measuring the strain in different temperature conditions. At very low temperature all of the compositions discussed in this study are ferroelectric. There are temperature regions in which compositions show AFE phase, which can be transformed to FE by E-field. Above T_{max}, the phase is PE so that only electrostrictive strain behavior can be observed.

General temperature behavior of this family of ceramics is shown in Figure 8 of temperature and E-field phase diagram. The shaded areas describe hysteresis. As the figure indicates, it is possible to decrease hysteresis by operating at a higher temperature, though strain level will be reduced.

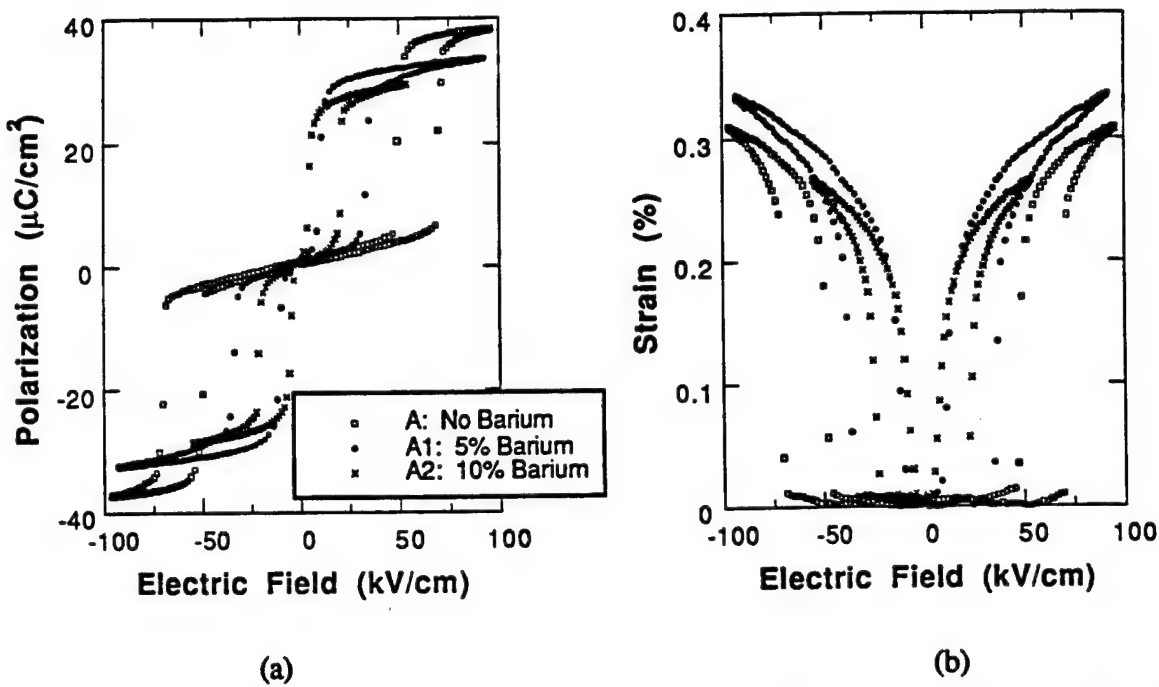(a)   (b)

Figure 2:   Electrically induced polarization (a) and strain (b) for compositions A, A1, and A2.
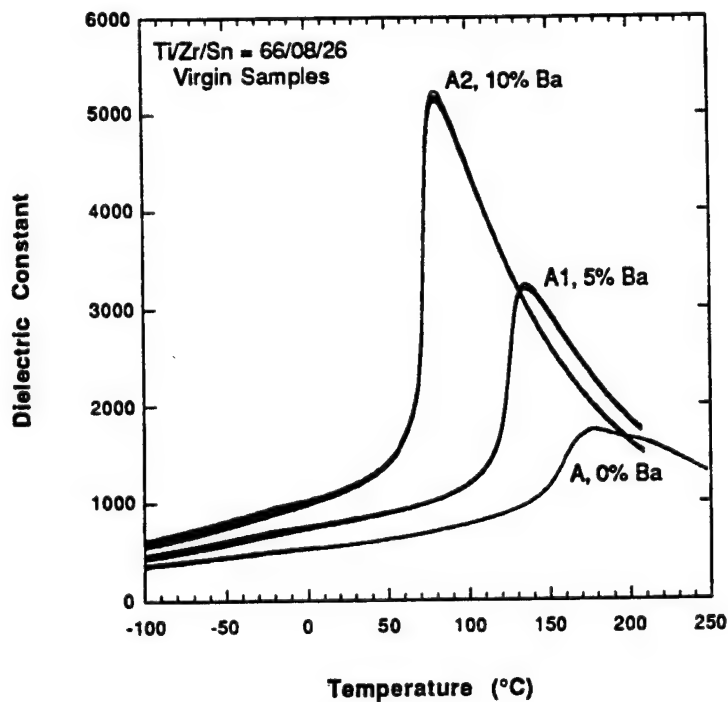

Figure 3:   Temperature dependence of dielectric constant for the compositions A, A1, and A2; (cooling)
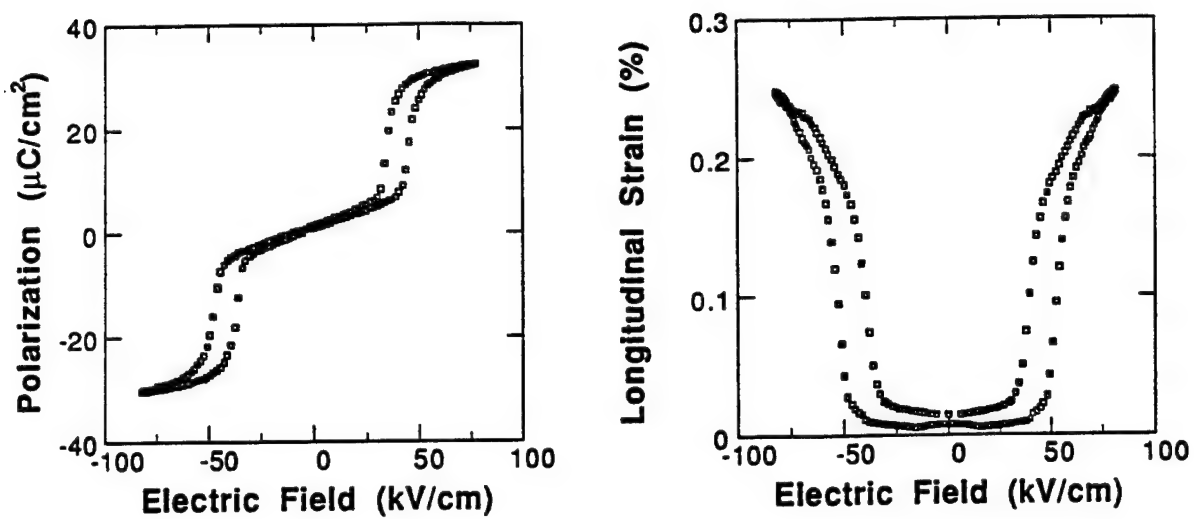   virgin sample.

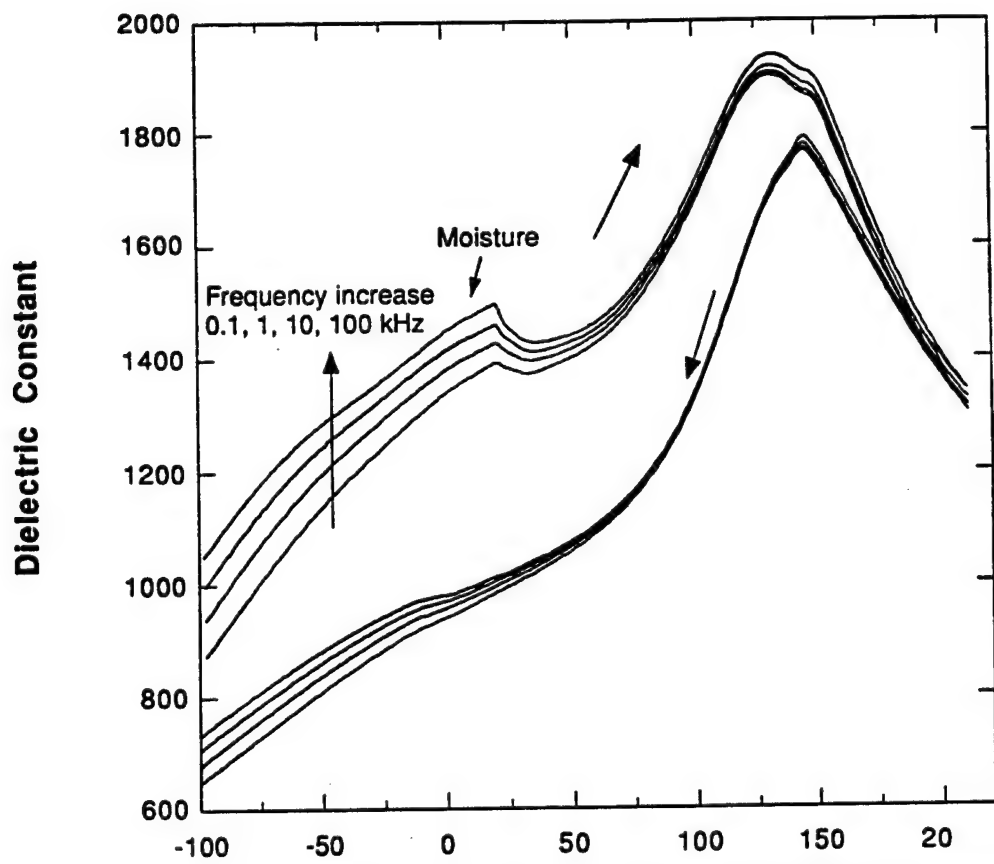Figure 4:   Electrically induced polarization and strain for composition B.

Figure 5:   Temperature dependence of dielectric constant for the composition B; poled sample, heating first, then cooling
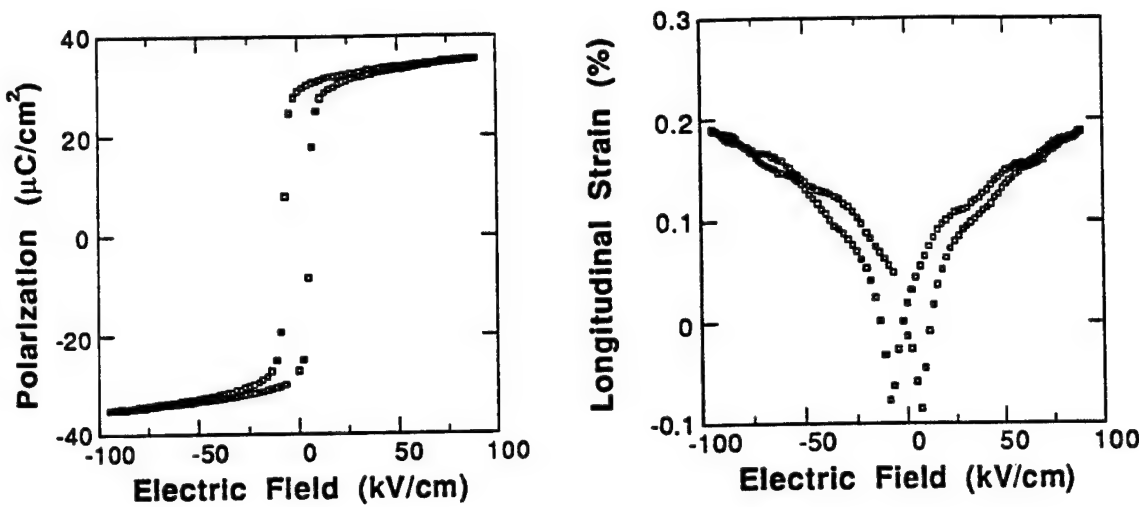
Figure 6:   Electrically induced polarization and strain for composition C.
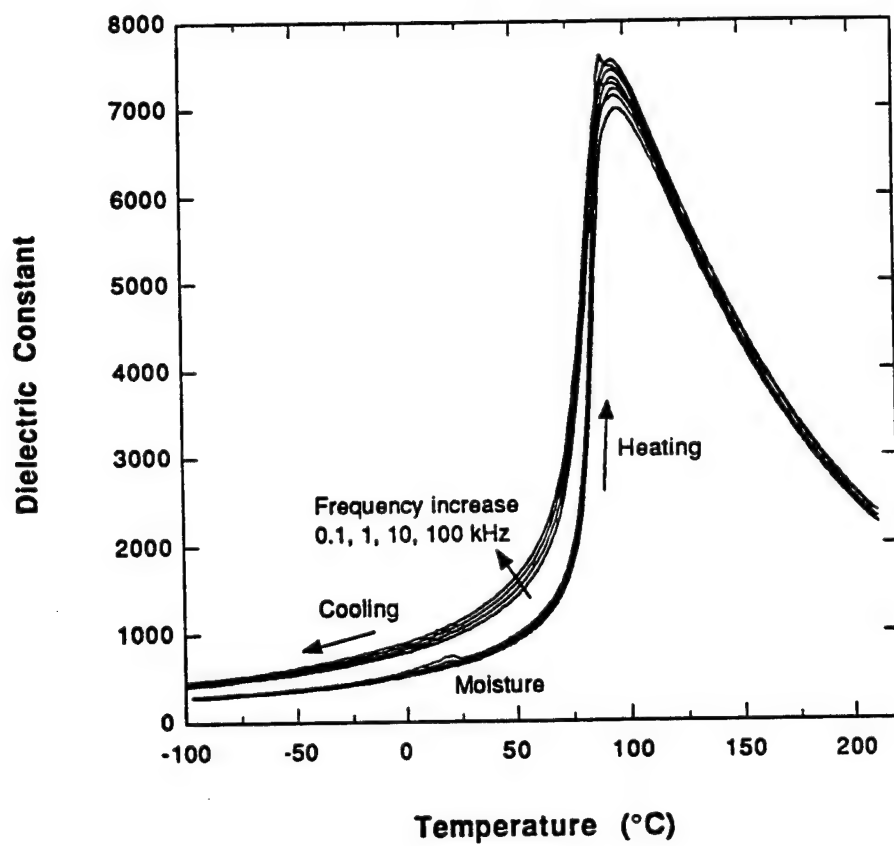

Figure 7:   Temperature dependence of dielectric constant for the composition C; poled sample, heating
first, then cooling

The above study of A-site modification showed that it is possible to decrease hysteresis and switching field at room temperature with, unfortunately, narrowing AFE temperature range. It is, therefore, critical to determine optimum composition based upon the requirements of a specific application and tailor the properties of the phase change materials.
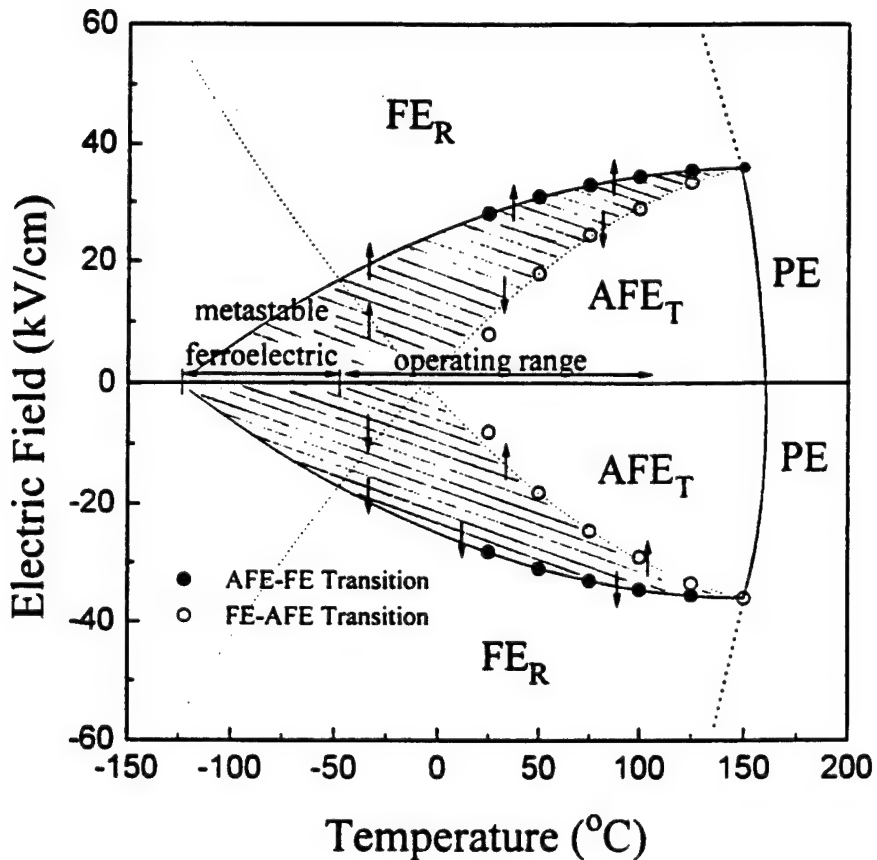

Figure 8: Temperature-electric field phase diagram. Shaded area indicates hysteresis.

3.3. Current requirement

Previous study[5] on compositional modification on the B-site also showed high field dielectric constants and loss by using DC bias field. As sharp increase and decrease in polarization hysteresis loop indicate, charge requirement to drive these ceramics as actuators can be quite high. Figure 9 shows the AC current required when one of the samples undergoes a phase transition from AFE-FE and subsequent switching back into the AFE phase by increasing and decreasing E-field. These measurements were completed at a low frequency (0.2 Hz) and represent relatively low current requirements. The current required at a higher frequency would be substantially higher and should be taken into account when the operating circuit for this material is designed. Current is lost in the time required to complete a measurement cycle (5 sec in this case), which accounts for the lack of symmetry in Figure 9.
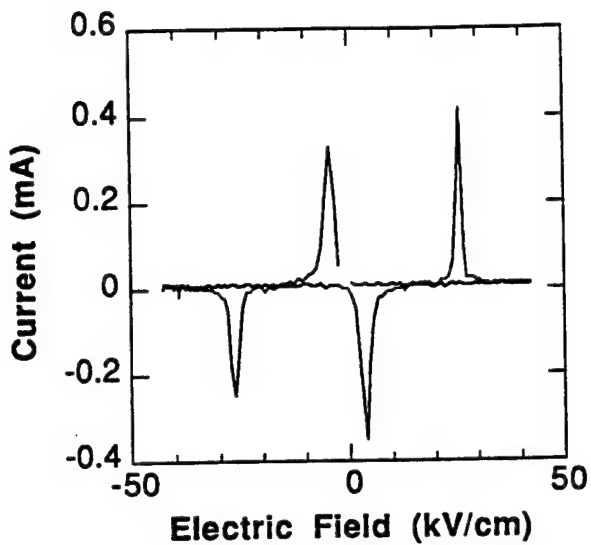
Figure 9:   Current requirements on phase switching (0.2 Hz).

4.   CONCLUSIONS

A-site compositional modification can be used along with B-site Ti:Sn ratio changes to modify the properties of phase switching ceramics, for example decreasing hysteresis. Sr additions have limited merit alone because they cause increases in the switching field and, therefore, increases in the field necessary to obtain maximum strain levels. Sr addition, however, suppressed hysteresis.

Ba additions proved to be a FE phase stabilizer, lowering both the amount of hysteresis and the switching field. It should be noted, however, that these changes also make the AFE temperature range smaller. The operation temperature and current requirement for this family of ceramics were also summarized. Ideally, with respect to application, a balance should be maintained between switching field, hysteresis and operating temperature range.

ACKNOWLEDGEMENTS

REFERENCES

1. D. Berlincourt, H.H.A. Krueger, and B. Jaffe, "Stability of Phases in Modified Lead Zirconate with Variation in Pressure, Electric Field, Temperature, and Composition," *J. Phys. Chem. Solids*, Vol. 25, 659–674 (1964).

2. B. Jaffe, "Antiferroelectric Ceramics with Field-Enforced Transitions: A New Nonlinear Circuit Element," *The Proceedings of the IRE*, Vol. 49[8], 1264–1267 (1961).

3. D.H. Zeuch, S.T. Montgomery, J.D. Keck, "Hydrostatic and triaxial compression experiments on unpoled PZT 95/5-2Nb ceramic: The effects of shear stress on the F_{R1} to A_O polymorphic phase transformation," *J. Mater. Res.*, 7, pp. 3314–3332 (1992).

4. D.H. Zeuch, S.T. Montgomery, J.D. Keck, "Further observation on the effect of nonhydrostatic compression on F_{R1} to A_O polymorphic phase transformation in niobium doped, lead-zirconate-titanate ceramic," *J. Mater. Res.*, 9, pp. 1322–1327 (1994).

5. K. Uchino and S. Nomura, "Electrostriction in PZT-Family Antiferroelectrics," *Ferroelectrics*, Vol. 50, 191–196 (1983).

6. W.Y. Pan, Q. Zhang, A. Bhalla, and L.E. Cross, "Field-Forced Antiferroelectric-to-Ferroelectric Switching in Modified Lead Zirconate Titanate Ceramics," *J. Am. Ceram. Soc.*, Vol.[4], 571–578 (1989).

7. A. Furuta, K-Y Oh, and K. Uchino, "Shape Memory Ceramics and Their Application to Latching Relays," *Sensors and Materials*, 3.4, 205–215 (1992).

8. S. Yoshikawa, N. Kim, T. Shrout, Q. Zhang, P. Moses, L.E Cross, "Field-Induced Lead Zirconate Titanate Stannate Antiferroelectric-to-Ferroelectric Phase Switching Ceramics, SPIE North American Conference on Smart Structure and Materials, *SPIE* Vol. 2441, p. 223–232.

9. K. Markowski, S-E. Park, S. Yoshikawa, L.E. Cross, "The Effect of Compositional Variations in the Lead Lanthanum Zirconate Stannate Titanate System on Electrical Properties," to be published in J. *Am. Ceram. Soc.*

10. K.J. Rao, C.N.R. Rao, Phase Transition in Soleds: An approach to the Study of the Chemistry and Physics of Solids," McGraw-Hill, New York (1978).

APPENDIX 18

In situ x-ray diffraction study of the antiferroelectric–ferroelectric phase transition in PLSnZT

C. T. Blue and J. C. Hicks
Materials Research Branch, Code 525, NCCOSC/RDT&E Division, San Diego, California 92152-5000

S.-E. Park, S. Yoshikawa, and L. E. Cross
Materials Research Laboratory, The Pennsylvania State University, University Park, Pennsylvania 16802

In situ x-ray diffraction studies were performed on the PLSnZT antiferroelectric–ferroelectric phase switching ceramic and polycrystalline powder. The crystallography of both the antiferroelectic and electric-field-induced ferroelectric phases were determined for the approximate composition of $Pb_{0.98}La_{0.02}(Zr_{0.55}Sn_{0.33}Ti_{0.12})_{0.995}O_3$. A preferred antiferroelectric domain structure has been identified and possible mechanisms responsible for the domain structure are presented. A single tetragonal phase has been identified for the room temperature zero-field antiferroelectric material with unit cell dimensions $a = 4.107$ Å and $c = 4.081$ Å. An electric field-induced structure developing at the antiferroelectric–ferroelectric switching field has also been observed and determined to be of rhombohedral symmetry with $a = 4.105$ Å and $\theta = 89.85°$ indicating a volume increase of 0.49% for the tetragonal–rhombohedral transition. © *1996 American Institute of Physics.* [S0003-6951(96)00121-0]

The La modified Pb(Ti,Zr,Sn)O$_3$ family of antiferroelectrics has displayed extremely high electric-field-induced longitudinal and volume strains. Several compositions close to the morphotropic phase boundary between the antiferroelectric and ferroelectric phases have been reported to exhibit longitudinal strains as high as 0.8%.[1-3] It has also been recently shown that compositions of Pb(Ti,Zr,Sn)O$_3$ similar to those studied in this work gave strains ~0.2% at the phase switching and up to 0.5% at the maximum applied field.[4] The transition between the two phases can be driven by temperature change, mechanical stress or electric field. Although it has been the assertion of several groups in the field that the antiferroelectric (AFE) phase is a tetragonal perovskite and the electric-field-induced ferroelectric (FE) phase is a rhombohedral perovskite crystal structure, much of this assertion is based on early free-energy calculations[5] and transmission electron microscopy observations of the two phases in which the subsequent FE phase has been induced by means other than an electric field[6] (i.e. compositionally, thermally). However, a direct observation of the microstructures in the AFE and subsequent electric-field-induced FE phases with x-ray diffraction has been difficult.[7] It is the aim of this work to study the crystal structures of the AFE and field-induced FE phases by making direct *in situ* x-ray diffraction measurements as a function of applied electric field.

The PLSnZT samples were prepared using the procedure described in reference 4. In the present study, we will present crystallography results for samples with the composition Pb$_{0.98}$La$_{0.02}$(Zr$_{0.55}$Sn$_{0.33}$Ti$_{0.12}$)$_{0.995}$O$_3$. The longitudinal strain and polarization vs electric field characteristics of all samples studied were measured prior to x-ray characterization using a LVDT (linear variable differential transformer) and modified Sawyer–Tower circuit as described in Ref. 4. Such characterized samples were then formed into capacitors. Ag 1 μm base electrodes and thin 500 to 1000 Å Al counterelectrodes were deposited at room temperature on ceramic samples to form such capacitors. The thin Al counterelectrode helped to

minimize the attenuation of x rays during the *in situ* x-ray diffraction measurements. A thick Ag guard ring electrode was added to protect the Al counterelectrode during surface breakdown. The dielectric constant as a function of temperature was measured at 1 kHz using an HP LCR meter with a sample hot stage. Laboratory x-ray diffraction spectra were taken at room temperature with a Rigaku rotating anode x-ray diffractometer using nickel-filtered copper $K\alpha$ radiation. Diffraction peaks due to the $K\alpha_2$ line are approximately 40% of the intensity of the difffraction peaks due to the $K\alpha_1$ line. The diffractometer is equipped with a sample holder attachment designed so as to allow both dc and ac polarization measurements on ceramic samples formed into capacitors. X-ray diffraction scan parameters include a step size of 0.002° and a counting time per step of 1 s. Polarization vs electric field data on these capacitors measured using the conventional Sawyer–Tower circuit were collected on a HP digital scope interfaced to a PC. *In situ* x-ray diffraction data as a function of electric field were collected on a PC interfaced to the Rigaku system. Identification and modelling of the observed crystal structures was accomplished with the help of several programs included in "X-ray Powder Programmes on IBM Compatible PC" written by M. Calligaris and S. Geremia, U. Trieste. Unit cell parameters for all observed structures were determined using the standard relation for quadratic forms $1/d^2$ for tetragonal and rhombohedral symmetry with further refinement of the cell parameters performed using the least squares refinement program "XLAT."

In the present work, the crystallography as a function of electric field of a PLSnZT ceramic with an approximate composition of Pb$_{0.98}$La$_{0.02}$(Zr$_{0.55}$Sn$_{0.33}$Ti$_{0.12}$)$_{0.995}$O$_3$ was studied using *in situ* x-ray diffraction. The PbZrO$_3$–PbTiO$_3$–PbSnO$_3$ phase diagram in Fig. 1 shows the proximity of the studied composition to the morphotropic antiferroelectric–ferroelectric (AFE-FE) phase boundary. Figure 2(a) displays the polarization as a function of electric field hysteresis loop for the studied composition. The ce-
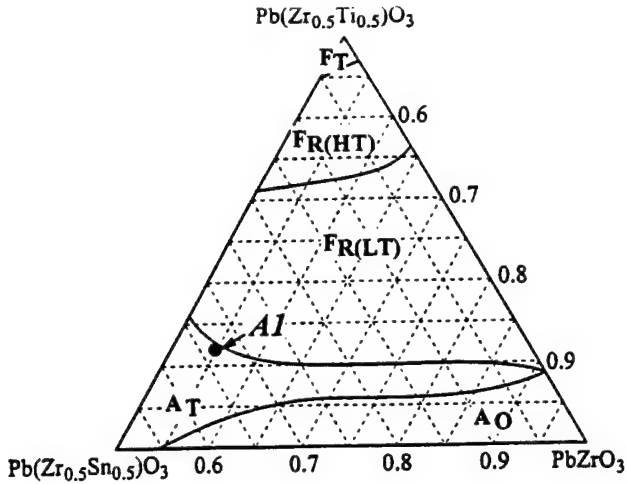
FIG. 1. Ternary phase diagram of the Zr-rich side of the $PbZrO_3 - PbTiO_3 - PbSnO_3$ system and the approximate composition studied in this work. (Taken after Pan et al.—see reference 2 and reference 5.)

ramic sample dimensions measured $d=13$ mm and $t=0.3$ mm. As can be observed from the plot, the switching field from the antiferroelectric to ferroelectric state is ~ 26 kV/cm. The macroscopic longitudinal strain vs electric field is plot-
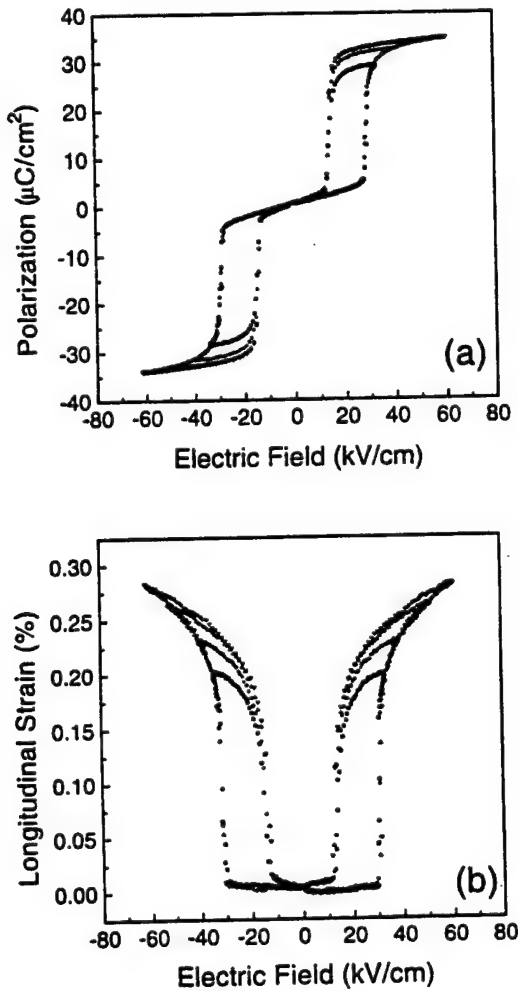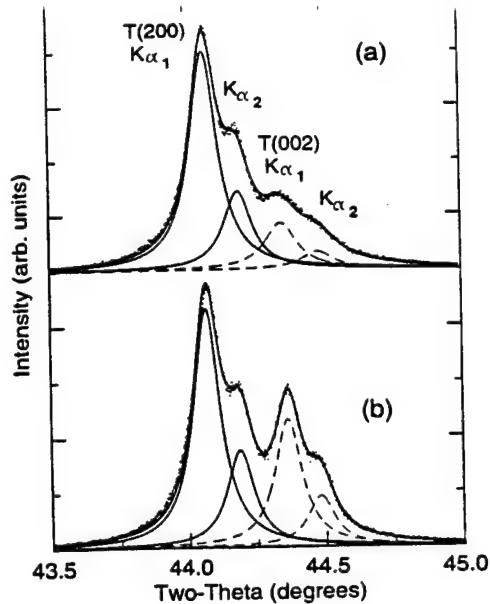

FIG. 3. $\theta - 2\theta$ x-ray diffraction scan showing the (200) and (002) diffraction peaks for the tetragonal phase at room temperature and zero-field for both (a) the ceramic sintered sample and (b) that same ceramic sample after having been ground to a fine-grain powder.

ted for the same sample in Figure 2(b) exhibiting a strain of 0.28% at a field of 60 kV/cm. As expected, only negligible longitudinal strain is observed for fields below the ferroelectric switching field and a large strain and spontaneous polarization develops upon the transformation to the ferroelectric state.

A full powder $\theta - 2\theta$ x-ray diffraction spectrum of the

FIG. 2. (a) Polarization vs electric field (P vs E) hysteresis loop for the composition studied in this work and (b) longitudinal strain as a function of electric field for the same sample.
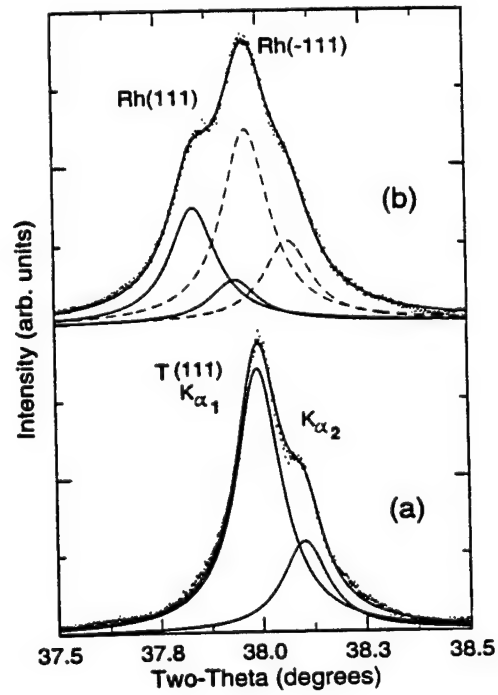

FIG. 4. Room temperature $\theta - 2\theta$ x-ray diffraction spectrum for PLSnZT ceramic sample at (a) $E_{appl}=0$ and (b) $E_{appl}=E_{AFE-FE}=26$ kV/cm showing the zero-field AFE line profile fit with a single tetragonal structure and the electric-field-induced FE spectrum fit to a single rhombohedral structure.

Blue et al.   2943

PLSnZT ceramic at room temperature and zero electric field (not shown) was taken and could be fit fully to a single tetragonal phase with cell parameters $a=4.107$ Å and $c=4.081$ Å. All observed fundamental reflections could be indexed to this single primitive perovskite cell. As expected, superstructure reflections could not be observed in the conventional x-ray diffraction patterns.[6] Therefore, structures for AFE and FE phases are compared on the basis of their primitive perovskite cells. $(00l)$ peaks were barely detectable in the ceramic indicating a preferred domain structure for the tetragonal antiferroelectric zero-field phase. Figure 3 is an x-ray diffraction $\theta - 2\theta$ scan showing the (200) and (002) peaks for the tetragonal phase at room temperature and zero-field for both the previously E-field exposed ceramic sintered sample [Fig. 3(a)] and that same ceramic sample after having been ground to a fine-grain powder [Fig. 3(b)]. The line through the data is the fit of a sum of the four Lorentzians each shown with a full width at half-maximum (FWHM) of approximately 0.07°. In all the fits, the Lorentzian representing the $K\alpha_2$ diffraction peak was fixed at approximately 40% of the intensity of the $K\alpha_1$ diffraction peak. As can be seen from the figure, the (002) peak in the case of the ceramic is much reduced in intensity from that in the powder. This is no doubt due to a preferred AFE tetragonal phase domain structure in which ~2/3 of the grains for the tetragonal phase have aligned with the c-axis planes tilted out of the plane of the sample. It is obvious that the E-field exposure which induces the phase switching is responsible for this preferred domain structure. This preferred orientation would then be mechanically clamped in the tetragonal AFE phase. Figure 4 displays room temperature $\theta - 2\theta$ x-ray diffraction spectra for the ceramic sample at: (a) zero applied field $E_{appl}=0$ and (b) the antiferroelectric–ferroelectric switching field $E_{appl}=E_{AFE-FE}\sim26$ kV/cm. As mentioned earlier, the room temperature zero-field antiferroelectric x-ray diffraction spectrum could fit fully with a single tetragonal phase with $a=4.107$ Å and $c=4.081$ Å. Only the (111) peak for the tetragonal structure is shown. The dark line through the data is a fit of the sum of two Lorentzians ($K_{\alpha 1}$ and $K_{\alpha 2}$ with FWHM~0.07°), the positions of which were determined from the (200) and (002) profile analysis. Upon application of the applied field, $E_{appl}=E_{AFE-FE}$, the (111) tetragonal diffraction line profile changes dramatically as can be seen in (b). The resultant profile in (b) could be fit fully to the (111) and (−111) peaks of a rhombohedral structure with $a=4.105$ Å and $\theta=89.85°$, demonstrating a complete phase transition from the tetragonal to the rhombohedral phase. This results in a volume strain of 0.49% for this transition, which is clearly an upper limit for any macroscopic observation of volume and longitudinal strains.

Based on these results, it is impossible to predict macroscopic strains, but we can merely predict upper limits, since the distribution of grain orientation is not known. Rocking curve measurements are currently in progress in an attempt to measure this distribution and predict macroscopic strains. All peaks investigated in the full $\theta - 2\theta:10°-70°$ spectrum

displayed changes consistent with a single tetragonal structure converting to a rhombohedral structure. However, all of the diffraction peaks other than the (111) are best fit with a combination of a tetragonal and a rhomboedral lattice implying only partial transitions for these grains. This should not be surprising as the interaction of the dipole associated with the perovskite structure and the applied electric field can be dramatically less for planes where the dipole is not perfectly aligned with the field as it is for the (111) plane. While the observed changes in the spectrum and therefore the occurrence of the rhombohedral structure is correlated to the occurrence of the ferroelectric state, the relative amounts of the two relevant crystal structures cannot be determined beyond E_{AFE-FE} and throughout the strain vs electric field hysteresis curve because of the difficulties in maintaining electric fields above E_{AFE-FE} over the x-ray diffracted surface thickness of the ceramic.

Using *in situ* x-ray diffraction, direct observations of the microstructures in the AFE and subsequent electric-field-induced FE phases of the $Pb_{0.98}La_{0.02}(Zr_{0.55}Sn_{0.33}Ti_{0.12})_{0.995}O_3$ ceramic have been made. A single tetragonal phase has been identified for the room temperature zero-field antiferroelectric phase. An electric-field-induced structure developing at the antiferroelectric–ferroelectric switching field has also been observed and determined to be of rhombohedral symmetry with $a=4.105$ Å and $\theta=89.85°$ with the occurrence of the rhombohedral structure correlated to the ferroelectric phase. The relative population of the two possible structures throughout the polarization and/or strain hysteresis loop, however, has not yet been completely determined. Currently, similar *in situ* x-ray diffraction studies are being performed on room temperature FE materials that undergo a temperature increase induced FE–AFE phase transition. This study should allow for a more quantitative analysis of the relative population of the AFE tetragonal and FE rhombohedral structures throughout the FE–AFE phase transition.

[1] W. Pan, Q. Zhang, A. Bhalla, and L. E. Cross, J. Am. Ceram. Soc. 72, 571 (1989).
[2] W. Y. Pan, C. Q. Dam, Q. M. Zhang, and L. E. Cross, J. Appl. Phys. 66, 6014 (1989).
[3] W. Pan, W. Y. Gu, and L. E. Cross, Ferroelectrics 99, 195 (1989).
[4] S. Yoshikawa, N. Kim, T. Shrout, Q. Zhang, P. Moses, and L. E. Cross, Proc. SPIE 2441, 223 (1995).
[5] D. Berlincourt, IEEE Trans. Sonics Ultrason. SU-13, 116 (1966).
[6] J. S. Speck, M. De Graef, A. P. Wilkinson, A. K. Cheetham, and D. R. Clarke, J. Appl. Phys. 73, 7261 (1993). Clarke, J. Appl. Phys. 73, 7261 (1993).
[7] L. Shebanov, M. Kusnetsov, and A. Sternberg, J. Appl. Phys. 76, 4301 (1994).

APPENDIX 19

Antiferroelectric-to-Ferroelectric Phase Switching PLSnZT Ceramics-II. The Effect of Pre-Stress Conditions on the Strain Behavior

M.-J. Pan, S.-E. Park, K.A. Markowski, S. Yoshikawa, and L.E. Cross

Materials Research Laboratory
The Pennsylvania State University
University Park, PA 16802 USA

Abstract—Actuators used for large strain applications are typically placed in pre-stressed conditions to maintain their integrity during service. It is therefore important to understand the characteristics of the materials under mechanical stress. In this study the effects of pre-stresses in lead lanthanum stannate zirconate titanate (PLSnZT) were examined, with an emphasis on the phase transformation behavior. The pre-stress was applied on a thin ring-shaped sample using a stress bolt assembly. It was found that the performance of PLSnZT is very sensitive to pre-stresses along the electric field direction. Specifically, the displacement decreased by 50% from its stress-free value as soon as a small pre-stress (3MPa) was applied. Subsequent stressing produced contradicting results in the two compositions investigated. One showed continuous decrease in strain upon stressing and the other, surprisingly, showed the opposite. These observations were discussed and possible explanations were given.

I. Introduction

In 1965 Berlincourt [1] established the ternary phase diagram for the lead lanthanum stannate zirconate titanate (PLSnZT) system, as shown in Fig. 1. In this family of ceramics, the phase most studied has been the antiferroelectric tetragonal (AFE_{tet}) phase because of its ability to be readily switched to its neighboring ferroelectric rhombohedral (FE_{rh}) phase with the application of an electric field. This phase transition is accompanied with a large change in volume associated with high longitudinal strain (in the field direction). Previous studies reported strain as high as 0.85% [2,3], although other crystallographic analyses based on x-ray diffraction have shown that 0.5% is the maximum strain possible for an ideal single crystal in this system [4,5]. This PLSnZT family of ceramics, therefore, has been widely investigated for actuators applications.

Actuator materials are often used under large mechanical load. In addition, actuators used for large strain applications are typically placed in pre-stressed conditions to maintain their integrity during service. Therefore, it is important to understand the characteristics of the materials under external stress. Previous studies have focused on the piezoelectric properties of various ferroelectric properties under uni-axial stress [6,7,8,9]. Unlike piezoelectric materials which only involve ferroelectric domain reorientation, antiferroelectric materials undergo a phase transition prior to any domain movement. Up to this time, little is known regarding the performance of antiferroelectric materials under stress, especially how the stress would affect the phase transformation and subsequent piezoelectric behavior.

This report investigates the behavior of PLSnZT ceramics under pre-stress. Two different compositions in the AFE_{tet} region ($(Pb_{0.98}La_{0.02})(Sn_{0.33}Zr_{0.55}Ti_{0.12})_{0.995}O_3$, or B1, and $(Pb_{0.98}La_{0.02})(Sn_{0.24}Zr_{0.66}Ti_{0.10})_{0.995}O_3$, or A2) were chosen for this study. Their locations are shown in the PLSnZT ternary phase diagram in Fig. 1. Fig. 2 shows the longitudinal, transverse, and volume strain of composition B1. As expected, the increase in volume associated with the phase transition from the AFE_{tet} to FE_{rh} structure is clearly observed.
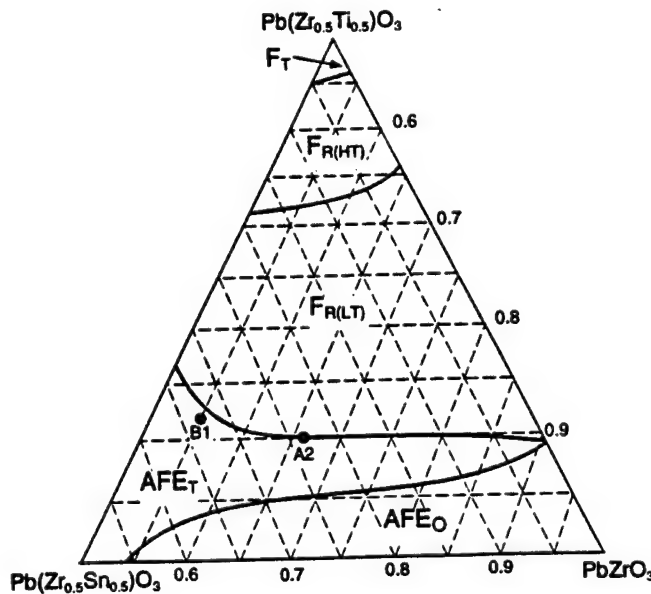
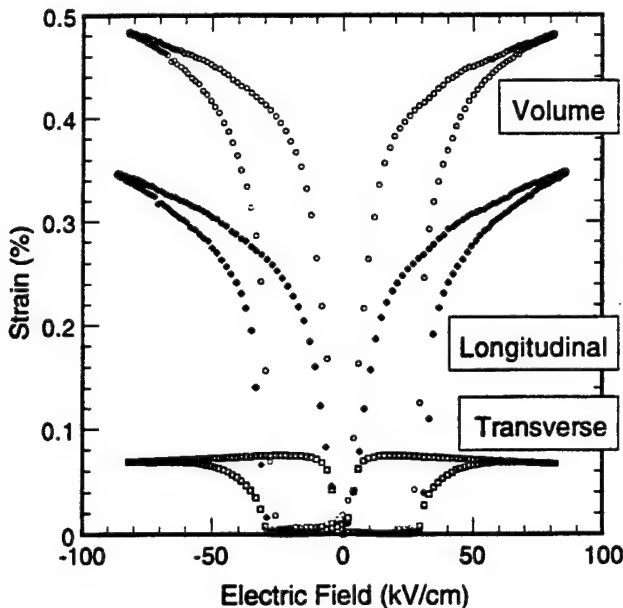Fig. 1   PLSnZT phase diagram showing compositions A2 and B1.

Fig. 2 Field-induced longitudinal, transverse, and volume strain for composition B1.

II. EXPERIMENTAL PROCEDURE

A. Sample Preparation

Polycrystalline samples were made by solid state reactions using reagent grade raw powders. Calcined powders were examined by x-ray diffraction (XRD) to insure phase purity and to identify crystal structure. Typical samples showed a single phase within the detection limit of XRD. Ceramic pellets were sintered in a lead-rich environment to suppress lead volatilization. Sintered pellets were ground and polished to achieve flat and parallel surfaces onto which gold electrodes were sputtered.
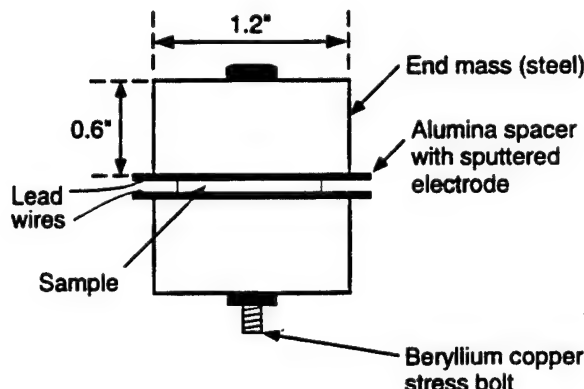

Fig. 3 The Stress Bolt Assembly

B. Characterization

(a) Applying Pre-Stress

Pre-stresses were applied to the samples using the stress bolt assembly, as shown in Fig. 3. This test apparatus was chosen because it closely resembles the setup in real-life service for transducer applications. A typical sample was approximately 22 mm in outer diameter, 12 mm in inner diameter, and 500μm in thickness. The magnitude of stress on the samples was monitored by measuring the change in bolt length. By drawing a free body diagram of the sample cross section, one can easily determine the relationship between the change in bolt length and pre-stress.

(b) Polarization and Strain

The polarization and strain under high electric field was measured using an integrated, computer-controlled system. Electric field as high as 60 kV/cm was applied to the sample using a high voltage amplifier (Trek 609C-6, Trek Incorporated, Medina, New York). All measurements were conducted at 0.2Hz. During measurement, samples were immersed in Fluorinert™ (FC-40, 3M, St. Paul, Minnesota), an insulating liquid, to prevent arcing. Polarization induced by the applied field was measured by using the modified Sawyer-Tower circuit. In the meantime, strain in the field direction was monitored by a linear variable displacement transformer (LVDT) driven by a lock-in device (Model SR830, Stanford Research Systems). The stress bolt assembly was placed between a fixed frame and the LVDT. As the samples deform under the applied electric field, the bolt elongates correspondingly. Note that the stress on the samples increase slightly during measurement due to the constraint of the stress bolt.

III. RESULTS AND DISCUSSION

Various pre-stress levels from 3 MPa to 15 MPa were applied. During the measurements, the pre-stressed sample deforms under the applied electric field and that displacement is measured by the change in bolt length. The results of composition A2 are shown in Fig. 4. As shown in the figure, the strain decreased by almost 50% when a small stress of only 3 MPa was applied, comparing to the strain in the free state. On the other hand, the polarization under stress is only slightly lower than its free state, indicating that the AFE-to-FE switching is complete. Subsequently, an increase in pre-stress further decreases the overall strain with little change in polarization. Apparently, there is a decoupling between the polarization and strain behavior. This decoupling has been observed before (under stress-free condition) and may be associated with the incommensuration of the AFE phase [10]. There has also been evidence suggesting that the AFE-to-FE phase switching involves multiple steps [11].

These results can be explained by considering the AFE-to-FE switching process. When the switching field is reached, the energy state requires the AFE-to-FE transition to occur. As most of the polarization change results from the switching
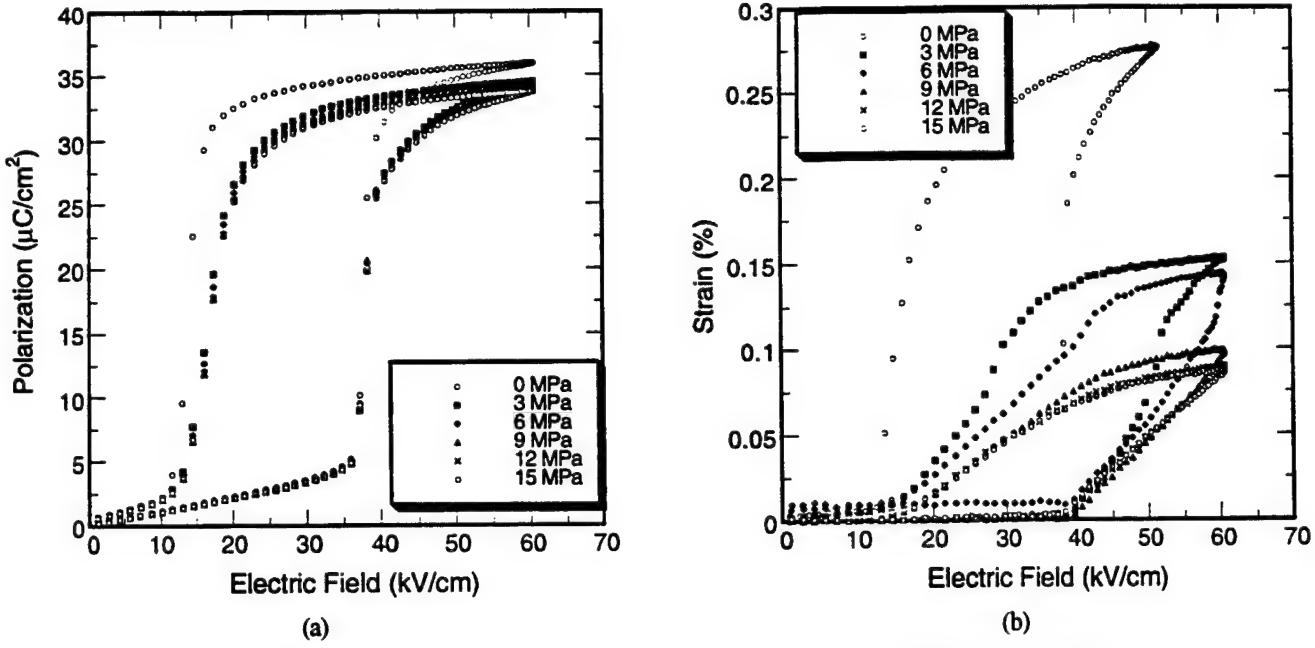
Fig. 4 (a) Polarization and (b) strain behaviors of composition A2 under various pre-stresses.

of polarization vectors (from antiparallel to parallel), the polarization values stayed almost unchanged. This stress, however, will impede the subsequent ferroelectric behavior in the following aspects.

(1) Decreased strain values: The piezoelectric effect is impeded by the pre-stress.

(2) Decreased slope in the strain-electric field curve: Under higher pre-stress, it takes higher electric field to reach a specific strain.

(3) Change in strain-electric field slope during the application of electric field: The change in slope indicates that multiple steps might be involved in the AFE-to-FE switching behavior.

(4) Increased back-switching field: The pre-stress forces the FE phase to switch back early, as the AFE phase has smaller volume.

From these observations, it was found that composition A2 is very "soft" and its ferroelectric and piezoelectric activities are easily impeded by external load.

Surprisingly, the strain of composition B1 under pre-stress, as shown in Fig. 5, exhibited very different behavior. Although the strain decreased by 50% when only 3 MPa was applied, subsequent stressing increased the generated strain. Since the polarization values remained almost the same, the phase switching process was complete. Obviously, the ferroelectric state of composition B1 behaved very differently from that of A2. To take extra caution, the measurements were repeated to confirm the results. The discrepancy between the behaviors of the two compositions, however, remained.

Efforts were made to explain this discrepancy. One possible explanation is whether the ferroelectric phase is "soft" or "hard." In the past, it has been observed that "soft" materials showed a monotonic decrease in d_{33} values with

increasing stress while "hard" materials first showed an increase (with maximum d_{33} occurring between 50 and 150 MPa, depending on the composition) and then decrease [6,7,8]. Nevertheless, no reasons were given for these observations, nor can we determine the "hardness" of the ferroelectric states of these two compositions. In addition, the literature data were often taken under different conditions, typically using resonance method and under low electric field.

Although the above argument about the ferroelectric and piezoelectric activities after phase switching can partially explained the experimental results, there is another possible cause for such a discrepancy. Careful examination of the setup suggested that the friction and clamping at the sample/spacer interfaces are the most likely source for such a difference. In our measurement, sample thickness was kept at below 500μm because of the high field (>50kV/cm) needed for the compositions to fully switch. The thickness/width ratio is much less than 2, the ratio preferred to minimize the clamping effect [12]. As a result, the friction/clamping at the interfaces might interact with generated strain, both longitudinal and transverse, and hence affect ceramic performance in various ways. This speculation, however, is hard to confirm since the roughness of the surfaces is difficult to characterize.

There are other issues regarding the stress bolt measurement, such as torque on the sample, parallelism of sample, and difficulty in bolt length measurement. Moreover, the applied pre-stress changes during measurement as the generated strain stretches the stress bolt further. For a typical sample, the pre-stress can increase by as much as 5%. Apparently, our results of the stress bolt measurement is a combination of all the above.
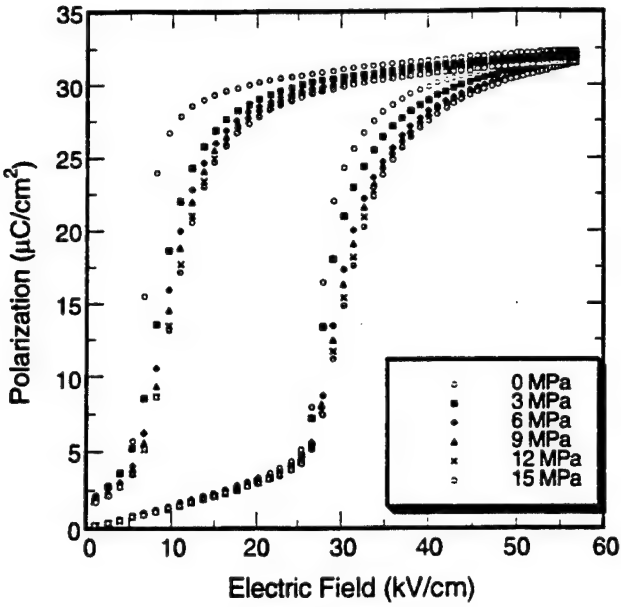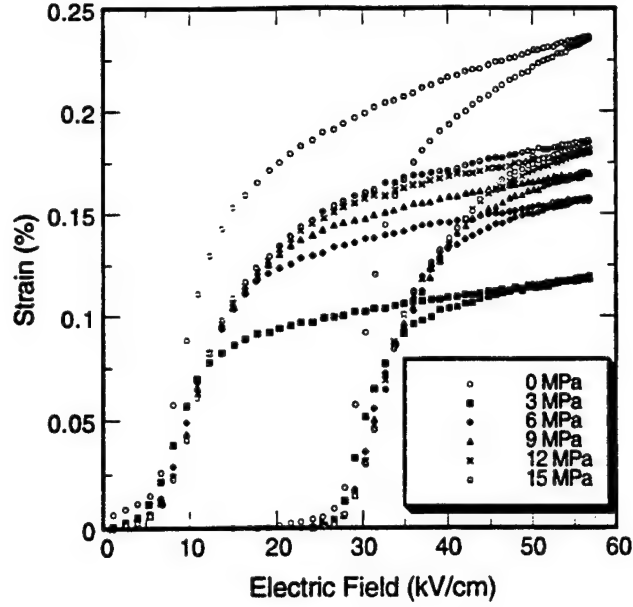
Fig. 5 (a) Polarization and (b) strain behaviors of composition B1 under various pre-stresses.

As many factors might affect the measurements, our results need to be confirmed by other methods. One possible solution is using multilayer actuators where the sample height/width ratio can be larger than 2 (to minimize clamping effects). This, however, would require intensive effort in sample preparation for each new composition and also one has to consider all other materials involved such as metal electrodes and polymer adhesive. Another possibility is using bar-shaped samples with height/width ratio >2 and monitor the strain using strain gauges. Again, it would require very high voltage to drive the sample and hence the power supply has to be adequate.

IV. CONCLUSIONS

The effects of pre-stress on the polarization and strain behaviors of two different PLSnZT ceramics were examined. The pre-stress was applied using a stress bolt assembly and monitored by measuring the bolt length. It was found that the displacements (in the field direction) of both compositions decreased by 50% from their stress-free values as soon as a small pre-stress (3 MPa) was applied. Subsequent stressing produced contradicting results in the two materials. One showed continuous decrease in strain upon stressing and the other, surprisingly, showed the opposite. It was speculated that the different behaviors might depend on whether a material is "soft" or "hard." The most likely cause, however, is the sample geometry used in this study and the corresponding clamping effect at contact surfaces. Other issues were also discussed and alternative measurements to confirm the experimental results were suggested.

REFERENCES

[1] D.Berlincourt, "Transducers Using Forced Transitions between Ferroelectric and Antiferroelectric States," IEEE Transactions on Sonics and Ultrasonics, Vol. SU-13 [4] 116-125 (1966).

[2] W. Pan, Q. Zhang, A. Bhalla, and L.E. Cross, "Field-Forced Antiferroelectric-to-Ferroelectric Switching in Modified Lead Zirconate Titanate Stannate Ceramics," J. Am. Ceram. Soc., 72 [4] 571-78 (1989).

[3] W.Y. Pan, C.Q. Dam, Q.M. Zhang, and L.E. Cross, "Large Displacement Transducers Based on Electric Field Forced Phase Transition in the Tetragonal $(Pb_{0.97}La_{0.02})(Ti,Zr,Sn)O_3$ Family of Ceramics," J. Appl. Phys., 66 [12] 6014-23 (1989).

[4] C.T. Blue, J.C. Hicks, S.-E. Park, S. Yoshikawa, and L.E. Cross, "In situ X-Ray Diffraction Study of the Antiferroelectric-ferroelectric Phase Transition in PLSnZT," Appl. Phys. Lett., 68 [21] 2942-44 (1996).

[5] L. Shebanov, M. Kusnetsov, and A. Sternberg, "Electric Field-Induced Antiferroelectric-to-Ferroelectric Phase Transition in Lead Zirconate Titanate Stannate Ceramics Modified with Lanthanum," J. Appl. Phys., 76 [7] 4301-4 (1994).

[6] H.H. Krueger, "Stress Sensitivity of Piezoelectric Ceramics: Part 1. Sensitivity to Compressive Stress Parallel to the Polar Axis," J. Acoust. Soc. Am., 42 [3] 636-645 (1967).

[7] S.W. Meeks and R.W. Timme, "Effects of One-Dimensional Stress on Piezoelectric Ceramics," J. Appl. Phys., 46 [10] 4334-38 (1975).

[8] T. Inoue and S. Takahashi, "Measurements for Piezoelectric Ceramic Properties Applied Compressive Stress Parallel to the Polar Axis," Trans. IECE Japan, vol. E69, 1180-1187 (1986).

[9] M. Kondo, K. Ohya, and S. Shimizu, "Effects of One-Dimensional Compressive Stress on the Properties of Multilayer Piezoelectric Ceramic Actuator," IEEE ISAF90 pp.530-534.

[10] D. Vieland, D. Forst, Z. Xu, and J.-F. Li, "Incommensurately Modulated Polar Structures in Antiferroelectric Sn-Modified Lead Zirconate Titanate: The Modulated Structure and Its Influence on Electrically Induced Polarizations and Strains," J. Am. Ceram. Soc., 78 [8] 2101-12 (1995).

[11] S.-E. Park, M.-J. Pan, K.A. Markowski, S. Yoshikawa, and L.E. Cross, "E-Field Induced Phase Transition of Antiferroelectric Lead Lanthanum Zirconate Titanate Stannate (PLZTS) Ceramics," unpublished work.

[12] J.C. Conway, An Investigation of the Stress Distribution in a Circular cylinder under Static Compressive Load for Varying Boundary Conditions. M.S. Thesis, The Pennsylvania State University, 1963.

APPENDIX 20

Antiferroelectric-to-Ferroelectric Phase Switching PLSnZT Ceramics- I. Structure, Compositional Modification and Electrical Properties

M.-J. Pan, K.A. Markowski, S.-E. Park, S. Yoshikawa, and L.E. Cross

Materials Research Laboratory
The Pennsylvania State University
University Park, PA 16802 USA

Abstract—Electric field induced antiferroelectric-to-ferroelectric (AFE-FE) phase transformation is usually accompanied by large strain, which is attractive for actuator applications. In this study, the AFE-FE switching of lead lanthanum stannate zirconate titanate (PLSnZT) was investigated and efforts were made to find high strain compositions with low switching field and hysteresis. Compositional modifications on both the A- and B-site were attempted in order to modify material properties. The B-site modifications were completed through manipulation of the Ti:Sn and Zr:Sn ratios. On the other hand, the A-site modifications were accomplished by the addition of Ba and Sr. It was demonstrated that one can tailor material properties to fit specific application requirements through compositional modifications.

I. INTRODUCTION

Lead lanthanum stannate zirconate titanate (PLSnZT) family of ceramics was first investigated by Berlincourt [1] and has been widely studied since then. It was established that the antiferroelectric tetragonal (AFE_{tet}) phase can be readily switched to ferroelectric rhombohedral (FE_{rh}) phase with the application of an electric field. This antiferroelectric-to-ferroelectric (AFE-FE) phase transition is accompanied by a large volume strain, which is a result of the larger FE_{rh} cell as compared to the AFE_{tet}. In particular, the high longitudinal strain (in the electric field direction) has been of interest for high performance actuators and transducers. Previous studies reported strain as high as 0.85% [2,3], although other crystallographic analyses based on x-ray diffraction have shown that 0.5% is the maximum strain possible for an ideal single crystal in this system [4,5]. For polycrystalline samples, strain of 0.2% should be readily achievable at the AFE-FE switching field.

For the actuator application of AFE ceramics, it is desirable to have low switching field coupled with high strain. In addition, large hysteresis is an undesirable characteristic as the generated heat is difficult to dissipate in an encapsulated environment during service. In this study, efforts were made to search for compositions with both low switching field and

small hysteresis. Compositional modifications on both the A-site and B-site ions in the PLSnZT family of ceramics were investigated. B-site variations include changes in the Ti:Sn and Zr:Sn ratios near the antiferroelectric tetragonal (AFE_{tet}) ferroelectric rhombohedral (FE_{rh}) morphotropic phase boundary (MPB). Based on ionic size and tolerance factor considerations, A-site modifications were attempted by substituting Ba^{2+} or Sr^{2+} ions to stabilize FE or AFE phases, respectively. The influence of these modifications on strain, switching field and hysteresis, are examined.

II. EXPERIMENTAL PROCEDURE

A. Sample Preparation

The compositions used in this study are shown in Fig. 1. Polycrystalline ceramic materials investigated in this study were prepared by solid state reaction, using the appropriate amounts of reagent grade raw materials. Calcined powders were examined by X-ray diffraction (XRD) to insure phase purity and to identify the crystal structure. Typically, the samples showed a tetragonal structure within the detection limit of XRD. The sintering process was carried out in a lead rich environment in order to minimize lead volatilization. After sintering the samples showed about 2% weight loss. The samples were pale yellow after sintering and remained this color throughout processing. Disk samples (with diameter 11mm and thickness 0.3mm) were then prepared by polishing with silicon carbide and alumina polishing powders to achieve flat and parallel surfaces onto which gold was sputtered.

B. Characterization Techniques

High-field measurements included polarization and strain hysteresis using a computer-controlled modified Sawyer Tower circuit and a linear variable displacement transformer (LVDT) driven by a lock-in amplifier (Stanford Research Systems, Model SR830). The voltage was supplied using a Trek 609C-6 high voltage DC amplifier. Through the LVDT, the strain of the samples can be measured with the application of an applied field. Electric fields as high as ~100 kV/cm were applied using an amplified sine waveform at 0.2 Hz. During testing the samples were submerged in Fluorinert (FC-40, 3M, St. Paul, MN), an insulating liquid, to prevent arcing.
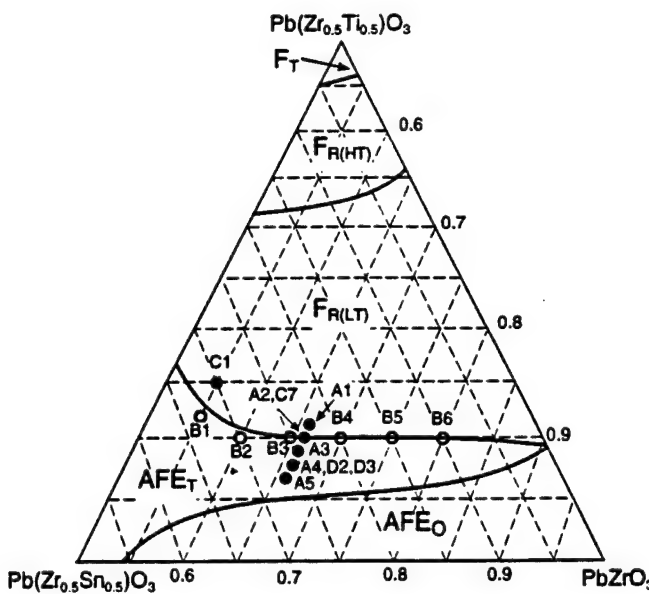
Fig. 1 PLSnZT ternary phase diagram

III. B-SITE VARIATIONS

A. Effects of Varying the Ti:Sn Ratio

Compositions A1 to A5 with varying Ti:Sn ratios i.e. moving compositionally perpendicular to the AFE_{tet}-FE_{rh} MPB, were evaluated. These compositions are shown on the PLSnZT phase diagram in Fig. 1.

The polarization and strain behaviors for these compositions are shown in Fig. 2. At the switching field, the longitudinal strain was between 0.16 to 0.18% for all compositions. This strain is reasonable for polycrystalline samples, considering X-ray investigations showed 0.5% to be

the maximum strain attainable for single crystals [4,5]. The maximum longitudinal strain is a function of the maximum field applied and typically fell between 0.4% and 0.5%.

The switching field increased as the compositions moved further from the MPB, i.e. deeper into the AFE region with increased Sn^+ content. This can be attributed to a material with a more stable room temperature AFE phase existing deep within the AFE region. This phase requires a higher field to switch to its FE phase. The polarization curves demonstrate this AFE stabilization, i.e. the polarization curve for composition A1 exhibits only slight AFE characteristic resembling a pinched single hysteresis, with a low switching field; while A5 shows strong AFE behavior and distinct double hysteresis behavior with a high switching field. The switching field, however, increased as the compositions moved further from the MPB. It is important to note that although the maximum strain for composition A3 appears very high, this sample was exposed to a significantly higher maximum field than the others. This ability to withstand the application of a high electric field may be attributed to high sample density, rather than being compositionally founded.

It is also interesting to note that although the AFE-FE switching field varies for different compositions, the amount of hysteresis remained nearly constant at ~25kV/cm.

B. Effects of Varying the Zr:Sn Ratio

The compositions B1 to B6 were located along the AFE_{tet}-FE_{rh} MPB with varied Zr:Sn ratio. These compositions are shown in Fig. 1. All compositions demonstrated AFE behavior at room temperature with the exception of the composition with the highest Zr content (Composition B6, Zr:Ti:Sn:: 80:10:10), which exhibited FE behavior.

The polarization and strain data are shown in Fig. 3. At the switching field the B Compositions produced approximately 0.16% strain regardless of composition and exhibited increasing strain with increased electric field after the phase transition. Changes in switching field and
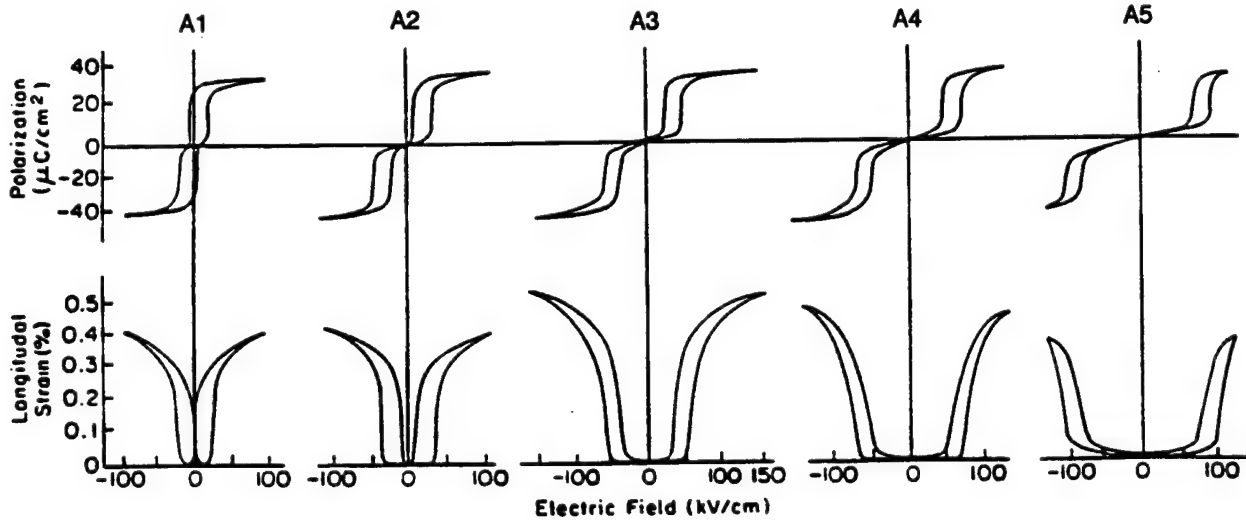

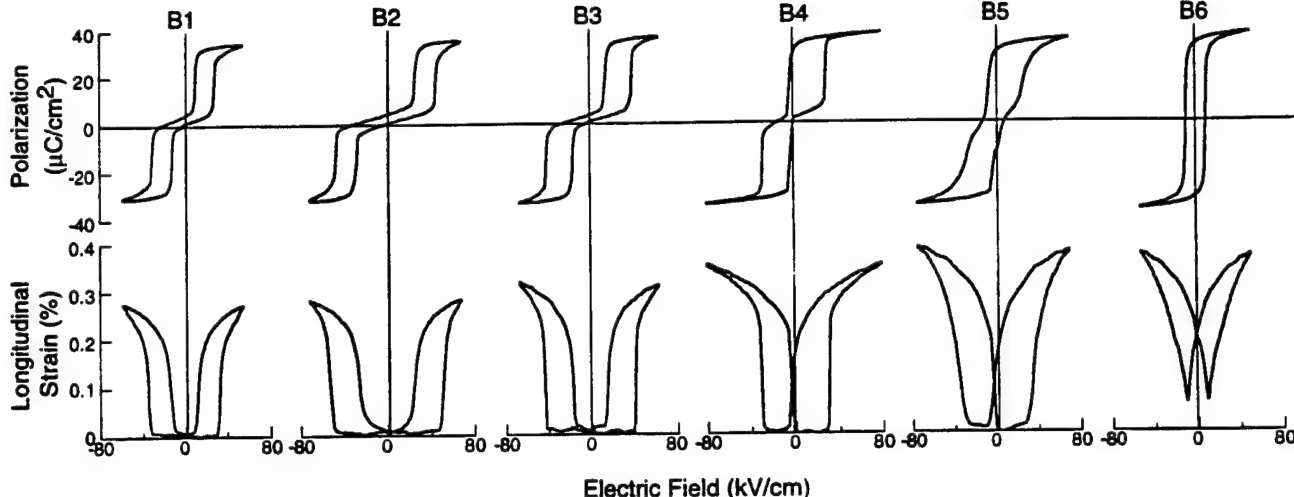Fig. 2 Polarization and strain of A compositions

Fig. 3 Polarization and strain of B compositions

hysteresis, however, were observed as a function of Zr:Sn variation. The switching field tended to decrease with increasing Zr content, i.e. moving left to right along the MPB. B1 exhibited consistently anomalous behavior, possibly due to its elevated Ti content with respect to the other compositions. The hysteresis increased for the AFE samples B2 to B5. Composition B1, which exhibited the lowest amount of hysteresis has been excluded from this discussion due to its elevated Ti content.

C. Discussion

From the above results, it was obvious that although one can modify the switching field and hysteresis with B-site variations, it is not possible to produce the desired decrease in both switching field and hysteresis. These variations at best produce compositions with lowered switching field and constant hysteresis (Ti:Sn ratio variation). Therefore, one has to resort to A-site doping to achieve the desired properties.

IV. A-SITE MODIFICATIONS

In this section, A-site modifications based on tolerance factor consideration and phase stability were investigated. The tolerance factor (t) for perovskites can be described with the general formula ABO_3 by:

$$t = \frac{R_A + R_O}{\sqrt{2}(R_B + R_O)}$$

where R_A = radius of A
 R_B = radius of B
 R_O = radius of O.

In general, when t > 1 the FE phase is stabilized and when t < 1 the AFE phase is stabilized [6]. For Pb based compounds, however, only trends need to be considered

because of the high polarizability of the Pb. Both Ba and Sr were considered as A-site additions in this study due to their valence. Ba being a FE stabilizer and Sr being a AFE stabilizer both potentially lowering dielectric maximum and subsequently suppressing hysteresis. In this section, additions of 5% Ba and 5% Sr were evaluated in both the AFE and FE regions of the PLSnZT phase diagram. The compositions are shown in Fig. 1.

A. Sr Additions

Additions of Sr in the FE region of the PLSnZT demonstrated that 5% Sr^{4+} additions (composition C1) produced samples that were AFE at room temperature even though compositionally located in the FE region of the phase diagram. The polarization and strain behaviors are shown in Fig. 4. This AFE behavior at room temperature showed that Sr additions induce a shift in the AFE_{tet}-FE_{rh} phase boundary upward towards the $Pb(Zr_{0.5}Ti_{0.5})O_3$ composition. This shift indicates a more stable room temperature AFE phase. The stabilization of the AFE phase also produced higher switching fields with less hysteresis. Apparently, to produce desired properties, one could move farther into the FE region to reduce the switching field while suppressing the hysteresis.

When 5% Sr is added to a composition on MPB, the ceramic became strongly antiferroelectric. Composition C7 (Fig. 1) could not be switched at an applied field of 100kV/cm at room temperature. Note that composition C7 has the same Zr:Ti:Sn ratio (66:10:24) as composition A2, which switches at 37 kV/cm. These results suggest that Sr is an effective AFE stabilizer.

B. Ba Additions

Results regarding 5% Ba addition in the AFE region (composition D2) showed improved AFE behavior at room temperature. The polarization and strain of D2 are shown in Fig. 5. Both the switching field and hysteresis of
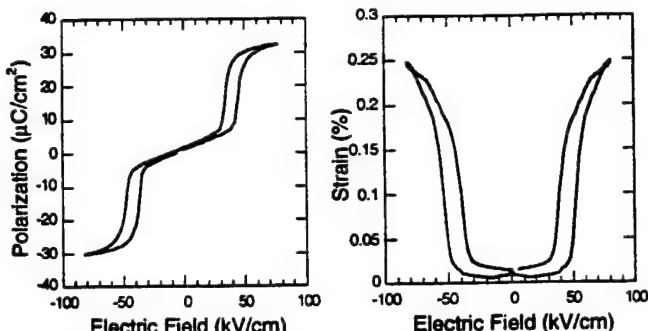
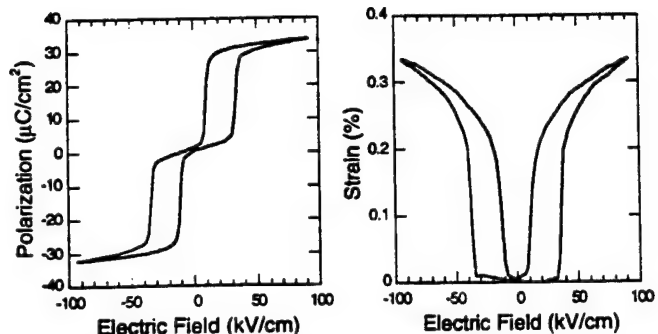Fig. 4 Polarization and strain of composition C1

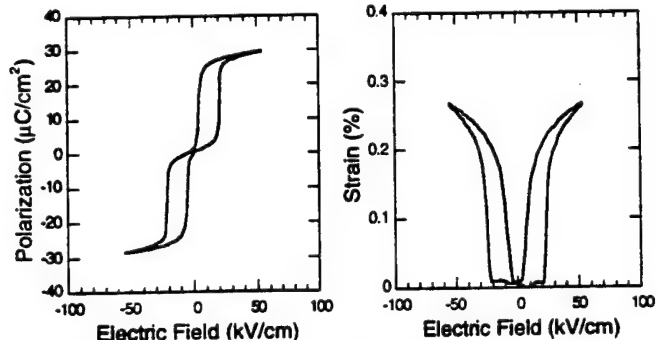
Fig. 5 Polarization and strain of composition D2

Fig. 6 Polarization and strain of composition D3

composition D2 decreased comparing to composition A4, which has the same Zr:Ti:Sn ratio (66:8:26). The switching field and hysteresis decreased from 71 and 25 kV/cm to 39 and 23 kV/cm, respectively. These results indicate that the Ba addition shifted the AFE_{tet}-FE_{rh} phase boundary downward toward the $PbZrO_3$-$PbSnO_3$ binary line. In other words, Ba appeared to be a strong FE stabilizer. To magnify the effect of Ba addition, 10% Ba (composition D3) was added. As anticipated, the switching field and hysteresis of D3 is further reduced, as shown in Fig. 6. In fact, they dropped to 27 and 15 kV/cm respectively.

C. Discussion

Although Sr and Ba modifications produced very favorable results, one should be aware of the operating temperature range of these modified compositions. Although Ba additions decrease hysteresis and switching field, the temperature range of their AFE behavior is quite narrow. Unfortunately, due to limited space, those results are not presented here. In addition, the field-induced strain is usually slightly inferior to that without Ba/Sr.

V. CONCLUSIONS

The effect of compositional modifications on the phase switching behavior of PLSnZT ceramics was examined. For B-site variations, the effect of varying Zr:Sn and Ti:Sn ratios near the AFE_{tet}-FE_{rh} MPB was reported. It was found that on decreasing the Ti:Sn ratio (top to bottom) along a line perpendicular to the MPB, the switching field increased and the hysteresis remained constant at 25kV/cm. On the other hand, increasing the Zr:Sn ratio (left to right) along the MPB caused the switching field to decrease and the hysteresis to increase. Apparently, these variations at best produce compositions with lowered switching field and constant hysteresis (Ti:Sn ratio variation). A-site modifications were accomplished by the addition of Ba and Sr. Ba proved to be a strong FE stabilizer and Sr, a strong AFE stabilizer. Both dopants suppress hysteresis successfully. In particular, Ba can effectively reduce both switching field and hysteresis with a small sacrifice in strain. In all cases, approximate 0.2%

strain was realized at the switching field regardless of the composition. Through the compositional analysis of both A- and B-site modifications, it is possible to consider the requirements of a specific application and tailor the properties of the phase switching material.

REFERENCES

[1] D.Berlincourt, "Transducers Using Forced Transitions between Ferroelectric and Antiferroelectric States," IEEE Transactions on Sonics and Ultrasonics, Vol. SU-13 [4] 116-125 (1966).

[2] W. Pan, Q. Zhang, A. Bhalla, and L.E. Cross, "Field-Forced Antiferroelectric-to-Ferroelectric Switching in Modified Lead Zirconate Titanate Stannate Ceramics," J. Am. Ceram. Soc., 72 [4] 571-78 (1989).

[3] W.Y. Pan, C.Q. Dam, Q.M. Zhang, and L.E. Cross, "Large Displacement Transducers Based on Electric Field Forced Phase Transition in the Tetragonal $(Pb_{0.97}La_{0.02})(Ti,Zr,Sn)O_3$ Family of Ceramics," J. Appl. Phys., 66 [12] 6014-23 (1989).

[4] C.T. Blue, J.C. Hicks, S.-E. Park, S. Yoshikawa, and L.E. Cross, "In situ X-Ray Diffraction Study of the Antiferroelectric-ferroelectric Phase Transition in PLSnZT," Appl. Phys. Lett., 68 [21] 2942-44 (1996).

[5] L. Shebanov, M. Kusnetsov, and A. Sternberg, "Electric Field-Induced Antiferroelectric-to-Ferroelectric Phase Transition in Lead Zirconate Titanate Stannate Ceramics Modified with Lanthanum," J. Appl. Phys., 76 [7] 4301-4 (1994).

[6] K.J. Roa and C.N.R. Roa. Phase Transitions in Solids: An Approach to the Study of the Chemistry and Physics of Solids, McGraw-Hill, New York, 1978.

APPENDIX 21

Ultrasonic Transducers Using Piezoelectric Single Crystal Perovskites

Patrick D. Lopath[1], Seung-Eek Park[2], K. Kirk Shung[1] and T.R. Shrout[2]
The Whitaker Center for Medical Ultrasonic Transducer Engineering
[1]Bioengineering Department
[2]Materials Research Laboratory
The Pennsylvania State University
University Park, Pennsylvania 16802

Abstract- Solid solutions of the relaxor-based $Pb(Zn_{1/3}Nb_{2/3})O_3$ (PZN) and $Pb(Mg_{1/3}Nb_{2/3})O_3$ (PMN) systems with $PbTiO_3$ (PT) have been grown in single crystal form. The piezoelectric and dielectric properties of several compositions are reported along various crystallographic directions. The piezoelectric transducer model developed by Kimholtz, Leedom and Matthaei (KLM) was employed to study the behavior of these materials as ultrasonic resonators. Extremely high piezoelectric coupling coefficients ($k_{33} > 94\%$) and a range of dielectric constants (3000-5000) have been observed in these systems on the rhombohedral side of the morphotropic phase boundary (MPB). Relatively low dielectric constants (~1000) and high thickness mode coupling ($kt > 63\%$) were observed as typical of tetragonal formulations. The ability to tailor the dielectric and piezoelectric constants with composition and crystal orientation allows the design of very large bandwidth ultrasonic transducers for applications ranging from medical diagnostic imaging to high frequency single element ultrasound backscatter microscopy.

I. Introduction

With the state of the art in ultrasonic imaging accelerating with the electronics industry, often it is the transducer which remains as a bottleneck to increased image resolution. Lead zirconate titanate (PZT), the industry standard transducer material, has served the medical diagnostic field well for many years; however, its limited ability to convert electrical to mechanical energy over a broad bandwidth, (measured as the square of k_{ij}, the coupling constant of the utilized mode) limits a PZT transducer's broad-band performance as well as its sensitivity. Broad bandwidth is the key to short pulse length in time (and space) and thus the key to increased axial resolution, while sensitivity defines a transducer's ability to detect and convert low level acoustic pulses.

High piezoelectric activity was reported in single crystal relaxor based materials as early as 1981 by Kuwata et al. [1,2] and in 1989 by Shrout et al. [3] for a morphotropic phase boundary (MPB) compositions of the PZN/PT and PMN/PT systems receptively. Piezoelectric coefficients, d_{33}, greater than 1500 pC/N were observed in the PMN/PT system. Only very recently, however, has the ultrasonic community, led by Toshiba [4], begun to move these solid solutions out of the laboratory and into the domain of medical devices. The unique piezoelectric and dielectric

properties of these novel materials allows the design of very sensitive, broad-band transducers and transducer arrays. The obvious advantage of these materials is in the 2.5 - 7.5MHz diagnostic imaging range. The recent interest in the use of ultrasonic backscatter microscopy (UBM) [5,6] has also prompted an investigation into the use of these single crystal materials to increase the resolution of these systems as well. Using the one dimensional simulation of the KLM model, theoretical designs using single crystal materials have been investigated and optimized to the limits of current fabrication technology.

Relying on modern dicing technology, fabrication studies en route to composite transducers with single crystal materials are underway. Evaluation includes vibrational modal analysis of bar shaped resonators parallel to the [100] and [110] crystallographic directions, as well as dicing feasibility using an industry standard Kulicke and Soffa 782 wafer dicing saw.

II. Material Properties

Ultrasonic transducer design begins with the piezoelectric material. Careful consideration of the material properties needed for a specific application will lead to a more effective transducer. Before the introduction of these single crystal materials to the ultrasonic community, material selection was limited, for the most part, to the proper choice of a particular PZT, hard or soft. The various PZTs are achieved through donor or acceptor doping of the ceramic. The k_{33} mode coupling in these systems is generally limited to ~75% for Navy Type VI or PZT-5H. With the introduction of single crystal materials with coupling coefficients over 94% and high dielectric constants, vastly improved designs are now possible.

A. Materials Selection

The relaxor based single crystal materials do not rely on a MPB, as do polycrystalline ceramics, to achieve their enhanced piezoelectric and dielectric properties. Instead it appears that orientation direction plays a major role [7]. While the materials investigated in this work lie near the
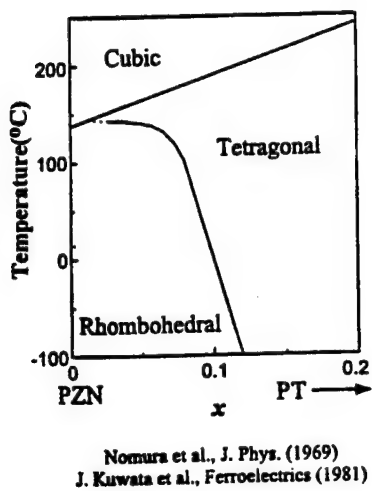
Fig 1. PZN/PT Phase diagram showing the MPB.

MPB (fig.1) [1,8] at 9.0-9.5% PT in PZN/PT, (~35% PT in PMN/PT), the highest k_{33} mode coupling observed to date appears in the rhombohedral phase at around 8% PT for PZN/PT. As stated in [1], poling along the <001> family yields a maximum piezoelectric response. In a rhombohedral crystal one might expect the [111] direction to allow for maximum polarization since it is the true polarization axis in rhombohedral symmetry, however Park and Shrout [7] showed that a lack of domain stability in [111] is responsible for much lower coupling along the [111] axis. Relevant parameters are summarized in Table I.

B. Transducer Design - Arrays

Once the ideal polarization axis is defined, one must consider the geometry of the ultrasonic device to be fabricated. An acoustic array uses a different geometry, and thus a different vibrational mode, than a single element transducer or, for that matter, a k_{33} test sample. Consider first an array which consists of many tall, narrow elements. Each
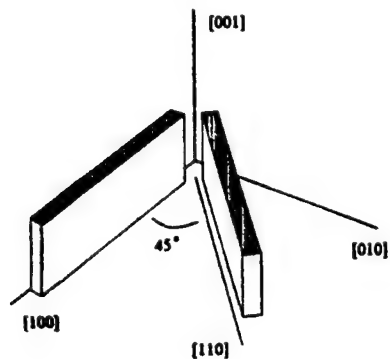

Fig 2. Resonant samples prepared. Axes are parallel to the <001> family.

element utilizes a partially clamped k_{33} mode of vibration. A true k_{33} mode would be a rod poled through the long axis and driven parallel to the poling direction. The rod is not laterally clamped in any direction. An array element, however, is laterally clamped in the elevation direction. This geometry tends to reduce the coupling coefficient from the ideal k_{33}. The tall, narrow geometry also mandates a small surface area, and thus a low capacitance, which leads to a large electrical impedance and an electrical mismatch to standard 50 Ω transmit and receive electronics. The need to increase the capacitance of each element forces the designer to look for high dielectric constant materials. In these relaxor based systems, both a high k_{33} and a large free dielectric constant are found on the rhombohedral side of the MPB. However the large coupling coefficients leads to a low clamped, or high frequency, dielectric constants with respect to soft PZTs. The result of this lower clamped relative permittivity can be seen in the simulated pulse echo response in fig. 3.

While the <001> family is defined as the poling direction for an array element, it is now left to define a dicing direction along the surface of the crystal which will provide the optimum performance. Given crystal symmetry with the <001> family every 90 degrees, the [100] and [110] (45 degrees from <001>) directions have been investigated. Dicing parallel to the [100] axis yields three distinct modes, with the thickness or clamped k_{33} mode along the poling axis (at 880 KHz in the test sample of fig. 2) being the dominant mode. The low frequency mode at 228 KHz is the k_{31} mode, with the bar resonating in the length dimension perpendicular to the poling direction. The center mode has been attributed to a flexural length mode. The frequency constants (Nt measured in MHz*mm) of the present modes are such that it is fairly easy to move undesired modes and harmonics out of the main thickness mode to allow accurate measurement and efficient operation. The drop in k_{33} to what we call k_{bar} (for the clamped k_{33} or 'bar' mode) is minimal, from 94% to 90%.

Dicing parallel to the [110] direction yields a more confusing picture. There is not a dominant mode present. The frequency constants of the various modes result in modal overlap in samples cut to approximate array dimensions, bleeding energy between modes and making accurate measurement and efficient operation impossible.

TABLE I
COUPLING AND FREQUENCY CONSTANTS FOR RELAXOR BASED SINGLE CRYSTALS AND PZT 5-H

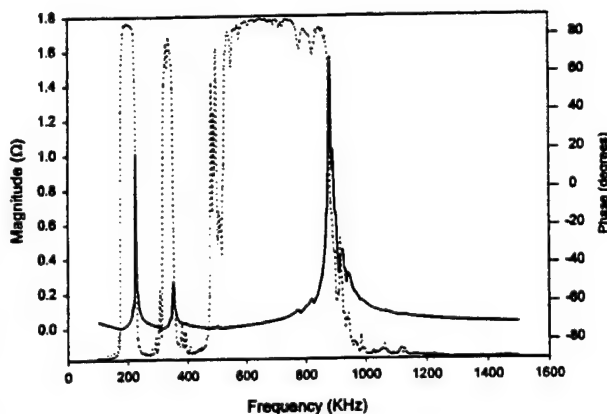| Material	Poling	Mode	Nt	k_{ij}	ε_r^T
PZT 5-H	N/A	k_{33}	1.75	0.73	3640
PZN8%PT	<001>	k_t	2.07	0.47	4530
PZN9.5%PT	<001>	k_t	1.967	0.54	1550
PMN30%PT	<001>	k_t	2.368	0.57	4740
PMN35%PT	<001>	k_{33}	1.714	0.93	4540

Fig 2. Impedance plot for a <001> poled and [100] aligned PZN 8% PT k_{bar} sample. The k_{bar} mode is the highest frequency mode present. The low frequency mode is k_{31}.

Up to this point we have defined the characteristics needed for an array element: A rhombohedral composition, poled parallel to <001> and diced, parallel to [100], to dimensions defined by the frequency constants to achieve a pure thickness vibrational mode over the final bandwidth of the transducer. It will be seen later that these single crystal materials can yield very wide bandwidth devices, so care must be taken when dimensioning the final transducer to avoid exciting unwanted modes.

C. Transducer Design - Single Elements

Transducer design for an applications such as ultrasound backscatter microscopy (UBM) has requirements different than design for arrays. Since impedance of the piezoelectric resonator varies inversely with capacitance as in (1),

$$Z = \frac{1}{j\omega C} \qquad (1)$$

at high frequencies, large area, high frequency, single element transducers suffer from the opposite problem than array elements; they become very low impedance, and again offer a poor match to the 50Ω driving electronics. As before, a large coupling coefficient is desired to achieve a wide bandwidth. However, these elements operate in a true clamped thickness, or k_t, mode. Due to insufficient anisotropy in rhombohedral crystals, compositions with PT content below the MPB tend to have very efficient k_{33}, but k_t only comparable to PZT.

Compositions above the MPB have low free dielectric constants characteristic of tetragonal materials such as PT. In this tetragonal configuration, the crystal is very anisotropic with the polar axis at [001]. The large anisotropy yields high k_t values, since very little energy is coupled into the lateral

directions as evident from (2) where k_p is the planar coupling coefficient.

$$k_{33} \cong k_t^2 + k_p^2 - k_p^2 k_t^2 \qquad (2)$$

Evaluation of PZN/PT crystals at 11% PT show k_t over 63% in comparison to PZT Navy Type VI at k_t of only 52%.

II. Transducer Simulation

The second step in the design of a transducer is to optimize the required transducer response. For example, a Doppler transducer has different bandwidth requirements than an imaging transducer. Our goal herein is to construct very high resolution imaging transducers. Design was done using the KLM model [9] employed via an ABCD parameter approach encoded in MathCad [10].

The pulse/echo waveform in fig. 3 simulates a 93% bandwidth subdiced array element with a center frequency of 5MHz. The bandwidth was measured at the -6dB points in the spectrum. This simulation predicts results for an array fabricated from PZN 8% PT poled in <001> and diced parallel to [001]. A fairly low impedance backing was simulated (6 MRayl) and a 2 layer matching scheme as described by Desilets et al. was used to achieve a maximally flat response [11]. An optimized array design of the same geometry constructed of Navy type VI PZT 5-H displays only a 67% bandwidth. Note the slightly lower insertion loss present in the PZT element. This is due to the higher clamped capacitance of the PZT element due to it higher clamped dielectric constant.

III. Transducer Fabrication

Fabrication studies have primarily concentrated on easier to construct single element acoustic devices. To take
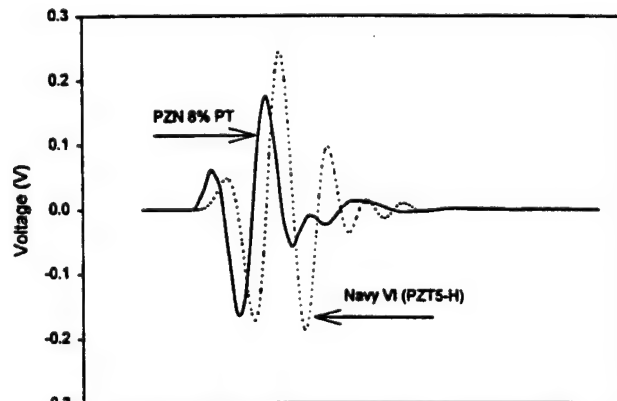

Fig. 3. Simulated pulse/echo response of a 93% bandwidth PZN 8% PT array element at 5MHz compared to a 67 % bandwidth PZT element of similar design.

advantage of the anomolously high partially clamped k_{33} (k_{bar}) displayed by these materials, composites with 2-2 connectivity were also constructed (fig. 4). Transducer fabrication from an as grown single crystal begins with orientation using x-ray diffraction. Once a reference face parallel to the (001) plane is polished into the crystal, the crystal can be sliced parallel to the reference face to approximately 500μm. These slices are then selected on the basis of quality and an appropriate diameter circle is turned at high speed on a lathe using a diamond cutting tool. This disc is then lapped flat and the surface crystallographic alignment is measured, again with x-ray diffraction, and marked. Kerfs are cut into the material parallel to [100] using standard dicing technology (Kulicke and Soffa 782 wafer dicing saw). The problem of dicing a novel material is not one to be overlooked. While the principles of dicing required for polycrystalline ceramics is a useful reference point, these relaxor based single crystals do not dice in the same manner as PZTs. In order to avoid excess surface chipping and kerf blowout, we found the need for much higher spindle speeds and much slower feed rates than necessary for PZT. Figure 4 shows a composite of PMN35%PT and Hysol 2038/3404 epoxy. The dicing was achieved at a spindle speed of 40K RPM and a material feed rate of 0.15 mm/sec. The kerfs are 27μm wide and 140μm deep at 72μm center to center spacing. The cuts were made with a 3-6μm grit diamond impregnated nickel blade. A layer of polymer over the cut surface may help to reduce surface chipping on future devices. Engineered acoustic backing and matching layers can then be added per simulation results.
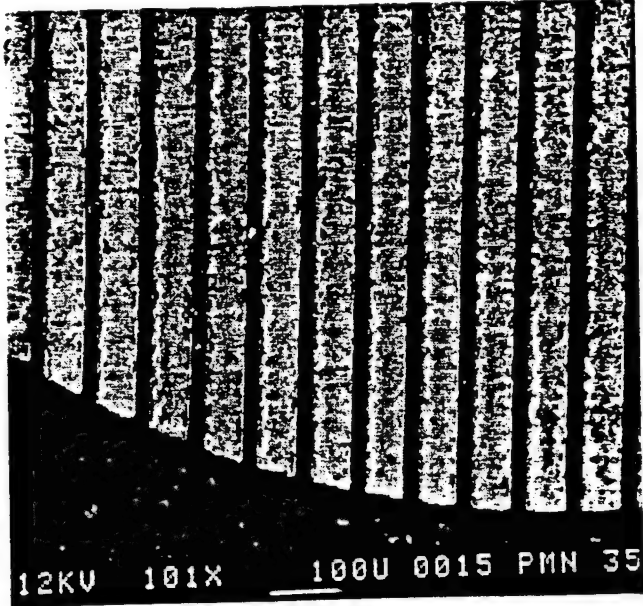

12KU 101X 100U 0015 PMN 35

Fig 4. PMN 35% PT / Hysol 2038 composite.

IV. Conclusion

We have shown that these single crystal perovskites offer the possibility of extremely broad bandwidth devices. A transducer's overall performance is, to some extent, a function of the piezoelectric coupling coefficient and the clamped dielectric constant of the active material. With these properties varying with composition and crystallographic axis, much research remains to optimize these parameters for the two solid solution systems presented. Currently, extremely high piezoelectric coupling coefficients and favorable dielectric constants are available via a number of compositions and crystal cuts. Although fabrication techniques differ from standard PZT, precision diced composites and arrays are feasible with these single crystal materials.

References

[1] Jun Kuwata. Kenji Uchino, and Shoichiro Nomura. "Phase Transitions in the $Pb(Zn_{1/3}Nb_{2/3})O_3$-$PbTiO_3$ System." *Ferroelectrics*, vol. 37, pp. 579-582. 1981.

[2] Jun Kuwata. Kenji Uchino, and Shoichiro Nomura. "Dielectric and Piezoelectric Properties of $0.91Pb(Zn_{1/3}Nb_{2/3})O_3$ - $0.09PbTiO3$ Single Crystals." *Japanese Journal of Applied Physics*, vol. 21, no. 9, pp. 1298-1302. September, 1982.

[3] S.W. Choi. T. R. Shrout, "Morphtropic Phase Boundry in $Pb(Mg_{1/3}Nb_{2/3})O_3$ $PbTiO_3$ System," *Materials Letters*, vol. 8, no. 6-7, pp. 253-255 July, 1989.

[4] U.S. Patent Number 5402791, "Piezoelectric Single Crystal. Ultrasonic Probe, and Array-Type Ultrasonic Probe" Toshiba, April, 1995.

[5] D. H. Turnbull, et al., "A 40-100 MHz B-Scan Ultrasound Backscatter Microscope for Skin Imaging," *Ultrasound in Med. & Biol.*, vol. 21, no. 1, pp. 79-88, 1995.

[6] F. Stuart Foster. et al., "Principles and Applications of Ultrasound Backscatter Microscopy," *IEEE Trans. on Ultrasonic, Ferroelectrics and Frequency Control*, vol. 40, no. 5, pp. 608-616, September. 1993.

[7] Seung-Eek Park, Thomas R. Shrout, "Characteristics of Relaxor-Based Piezoelectric Materials for Ultrasonic Transducers," in press *IEEE Trans. on Ultrasonics. Ferroelectric and Frequency Control Special Issue on Ultrasonic Transducers*, 1996.

[8] Shoichiro Nomura. Takashi Takahashi, Yuji Yokomizo. "Frreoelectric Properties in the System $Pb(Zn_{1/3}Nb_{2/3})O_3$-$PbTiO_3$," *J. Phys. Soc. Japan*, vol. 27, pp. 262, 1969.

[9] R. Krimholtz. D. A. Leedom. and D. L. Matthaei, "New Equivalent Circuits for Elementary Piezoelectric Transducers," *Electr. Let.*, vol. 6, pp 398-399, July 1971.

[10] M.J. Zipparo. K. K. Shung, T. R. Shrout, "High Frequency Properties of Fine Grain PZT," *Proc. IEEE Ultrasonic Syposium*, vol. 1, pp. 601-604, November; 1995.

[11] C. S. Desilets. J. D. Fraser, and G. S. Kino, "The Design of Efficient Broad-Band Piezoelectric Transducers," *IEEE Trans. on Sonics and Ultrasonics.*, vol. 25,no. 3, pp 115-25, May 1978.

[12] Bernard Jaffe, William R. Cook, Jr, and Hans Jaffe, <u>Piezoelectric Ceramics</u>. R.A.N. Publishers (1971).

[13] T. R. Shrout, J. Fielding,"Relaxor Ferroelectric Materials". Proc. IEEE Ultrasonics Symposium ,1990.

[14] K. K. Shung, "General Engineering Principles In Diagnostic Ultrasound," *IEEE Eng. Med. Biol. Magazine*, pp 7-13, Dec 1987.

[15] W. A. Smith, "Piezocomposite Materials for Acoustical Imaging Transducers", *Proc. International Symposium on Acoustical Imaging*, 1994.

APPENDIX 22

Characteristics of Relaxor-Based Piezoelectric Single crystals for Ultrasonic Transducers

Seung-Eek Park and Thomas R. Shrout

Whitaker Center for Ultrasonic Imaging, The Pennsylvania State University
University Park, PA 16802

Abstract - For ultrasonic transducers, piezoelectric ceramics offer a range of dielectric constants ($K \sim 1000$-5000), large piezoelectric coefficients ($d_{ij} \sim 200$-$700 pC/N$), and high electromechanical coupling ($k_T \cong 50\%$, $k_{33} \cong 75\%$). For several decades, the material of choice has been polycrystalline ceramics based on the solid solution $Pb(Zr_{1-x},Ti_x)O_3$ (PZT), compositionally engineered near the morphotropic phase boundary (MPB). The search for alternative MPB systems has led researchers to revisit relaxor-based materials with the general formula, $Pb(B_1,B_2)O_3$ ($B_1:Zn^{2+}$, Mg^{2+}, Sc^{3+}, Ni^{2+}..., $B_2:Nb^{5+}$, Ta^{5+}...). There are some claims of superior dielectric and piezoelectric performance compared to that of PZT materials. However, when the properties are examined relative to transition temperature (Tc), these differences are not significant. In the single crystal form, however, Relaxor-PT materials, represented by $Pb(Zn_{1/3}Nb_{2/3})O_3$ - $PbTiO_3$ (PZN-PT), $Pb(Mg_{1/3}Nb_{2/3})O_3$ - $PbTiO_3$ (PMN-PT) have been found to exhibit longitudinal coupling coefficients (k_{33})>90%, thickness coupling (k_T)>63%, dielectric constants ranging from 1000 to 5000 with low dielectric loss <1%, and exceptional piezoelectric coefficients d_{33}>2000pC/N, the later promising for high energy density actuators. For single crystal piezoelectrics to become the next generation material of ultrasonic transducers, further investigation in crystal growth. device fabrication and testing are required.

INTRODUCTION

Innovations in transducer design continues to be the driving force for the development of new piezoelectric materials. Electromechanical coupling (k_{ij}), dielectric constant (K) and acoustic impedance (Z) are the most important parameters which determine the performance of an ultrasonic imaging system. Material characteristics associated with the design of imaging devices have been reviewed by Gururaja [1] and Smith [2]. Piezoelectric ceramics are currently the material of choice offering relatively high coupling, a wide range of dielectric constants, and low dielectric loss. These merits translate into transducer performance in the form of relatively high sensitivity, broad bandwidth and minimal thermal heating. Two approaches have been taken to couple
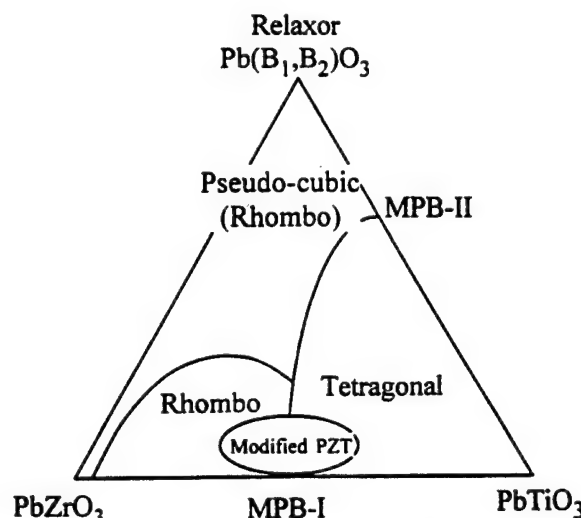

Figure 1 Ternary diagram depicting MPBs in PZT and Relaxor-PT systems for piezoelectric ceramics [27].

acoustic energy from high acoustic impedance (Z=30-36 MRayls) piezoelectric ceramics to the human body(Z=1.5 Mrayls); (1) multiple quarter wavelength matching layers and/or (2) lower impedance composite comprised of piezoelectric ceramic with a passive polymer. Although the properties can be tailored to meet various device requirements, it is the volume ratio of the piezoelectric ceramic and its inherent properties that are critical to transducer performance.

$Pb(Zr_{1-x},Ti_x)O_3$ (PZT) ceramics have been the mainstay for high performance transducer applications. Compositionally, PZT ceramics lie near the morphotropic phase boundary (MPB) between the tetragonal and rhombohedral phases, as depicted in Figure 1. MPB compositions have anomalously high dielectric and piezoelectric properties as a result of enhanced polarizability arising from the coupling between two equivalent energy states, i.e. the tetragonal and rhombohedral phases. allowing optimum domain reorientation during the poling process. Further modifications using acceptor and donar dopants give us the wide range of piezoelectric compositions we have today. An excellent review on piezoelectric ceramics including both modified and undoped PZT ceramics is

Table 1 Morphotropic Phase Boundaries in perovskite $Pb(B_1B_2)O_3$-PT systems

Binary System	PT content on MPB	T_c (T_cs of end compounds)	Ref
$(1-x) Pb(Zn_{1/3}Nb_{2/3})O_3 - x PbTiO_3$ (PZN-PT)	$x \cong 0.09$	~ 180°C (140 °C- 490°C)	28
$(1-x) Pb(Mg_{1/3}Nb_{2/3})O_3 - x PbTiO_3$ (PMN-PT)	$x \cong 0.33$	~ 150°C (-10°C - 490°C)	29,30
$(1-x) Pb(Mg_{1/3}Ta_{2/3})O_3 - x PbTiO_3$ (PMT-PT)	$x \cong 0.38$	~ 80°C (-98°C - 490°C)	8
$(1-x) Pb(Ni_{1/3}Nb_{2/3})O_3 - x PbTiO_3$ (PNN-PT)	$x \cong 0.40$	~ 170°C (-120°C - 490°C)	30
$(1-x) Pb(Co_{1/3}Nb_{2/3})O_3 - x PbTiO_3$ (PCN-PT)	$x \cong 0.38$	~ 250°C (-98°C - 490°C)	31
$(1-x) Pb(Sc_{1/2}Ta_{1/2})O_3 - x PbTiO_3$ (PSN-PT)	$x \cong 0.45$	~ 205°C (26°C - 490°C)	32
$(1-x) Pb(Sc_{1/2}Nb_{1/2})O_3 - x PbTiO_3$ (PST-PT)	$x \cong 0.43$	~ 250°C (90°C - 490°C)	33,34
$(1-x) Pb(Fe_{1/2}Nb_{1/2})O_3 - x PbTiO_3$ (PFN-PT)	$x \cong 0.07$	~ 140°C (110°C - 490°C)	8
$(1-x) Pb(Yb_{1/2}Nb_{1/2})O_3 - x PbTiO_3$ (PYN-PT)	$x \cong 0.50$	~ 360°C (280°C - 490°C)	8
$(1-x) Pb(In_{1/2}Nb_{1/2})O_3 - x PbTiO_3$ (PIN-PT)	$x \cong 0.37$	~ 320°C (90°C - 490°C)	35
$(1-x) Pb(Mg_{1/2}W_{1/2})O_3 - x PbTiO_3$ (PMW-PT)	$x \cong 0.55$	~ 60°C (39°C - 490°C)	36
$(1-x) Pb(Co_{1/2}W_{1/2})O_3 - x PbTiO_3$ (PCW-PT)	$x \cong 0.45$	~ 310°C (32°C - 490°C)	37
$(1-x) PbZrO_3 - x PbTiO_3$ (PZT)	$x \cong 0.48$	~ 360°C (230°C - 490°C)	3

given by Jaffe, Cook, and Jaffe [3], published in 1971.

RELAXOR-BASED PIEZOELECTRICS

The search for alternative MPB systems other than that found in PZT have led researchers to investigate relaxor-based ferroelectrics and their solid solution with $PbTiO_3$ (PT). Lead based relaxor materials, discovered by Soviet researchers [4,5] in 1950s, are complex perovskites with the general formula $Pb(B_1B_2)O_3$, ($B_1=Mg^{2+}$, Zn^{2+}, Ni^{2+}, Sc^{3+} ...., $B_2=Nb^{5+}$, Ta^{5+}, W^{6+} ...). Characteristic of relaxors is a broad and frequency dispersive dielectric maxima [6]. These relaxor materials and their solid solutions with $PbTiO_3$ have been compiled by Landolt-Börnstein [7] with numerous MPB systems reported.

Early investigations of Relaxor-PT ceramics in the 60s and 70s were plagued with inadequate process controls resulting in piezoelectric ceramics of marginal interest. With the advent of the columbite precursor method and an overall better understanding of perovskite-pyrochlore phase relationship and corresponding structure-property relationships, a renewed interest in the Relaxor-PT MPB systems came about. The wide range of Relaxor-PT MPB systems have been recently reviewed, including relevant dielectric and piezoelectric properties [8].

Several of the Relaxor-PT systems are summarized in Table 1 and schematically shown in the $PbZrO_3$–$PbTiO_3$–$Pb(B_1B_2)O_3$ ternary system in Figure 1. In contrast to the PZT system, the amount of PT associated with Relaxor-PT MPB is in general less than that for PZT varying from 7% for PFN-PT to 50 mole% for PYN-PT. In PZT, the MPB is relatively insensitive to temperature. However, in

Relaxor-PT systems, the MPB compositions are strongly temperature dependent.

In recent articles on Relaxor-PT compositions, including new MPB systems, e.g. PYN-PT [8], modified PSN-PT [9], and materials processed using hot pressing [10], there are claims of compositions with superior dielectric and piezoelectric properties compared to that of PZT ceramics. As reported in Table 2, these claims appear to be valid, with Relaxor-PT ceramics* offering relatively high dielectric constants (K_S), large piezoelectric coefficients (d_{ij}), and superior electromechanical coupling coefficients (k_{ij}). In the following section, however, it will be shown that such claims are misleading and must be analyzed with respect to the ferroelectric materials transition temperature. This temperature

Figure 2 Piezoelectric coefficient (d_{33}) as a function of transition temperature (T_c) for piezoelectric ceramics, including PZT, modified PZTs, and Relaxor-PT systems. Data were compiled from references, commercial brochures and internal investigations.

---

* The term "relaxor ferroelectric" is used herein to represent all complex perovskite $Pb(B_1B_2)O_3$ systems. In actuality, relaxor dielectric behavior only occurs for those systems which possess short range chemical ordering as classified by Randall et al. [24] In general, however, classical relaxor behavior occurs within certain compositional limits for all $Pb(B_1B_2)O_3$ -PT systems.

Table 2 Reported Dielectric and Piezoelectric Properties for selected PZT and Relaxor Binary Systems

Form	Materials	k_P	k_t*	k_{33}	d_{33} (pC/N)	K_3'	T_C (°C)	Ref.
Ceramics (poly-crystalline)	**PZT-MPB Composition**							
	PZT 53/47	0.52		0.67	220	~800	360	36
	Modified PZTs							
	PZT-4 (Navy I)	0.58	0.51	0.70	289	1200	330	39
	PZT-8 (Navy III)	0.50	0.44	0.70	220	1000	300	39
	PZT-5 (Navy II)	0.60	0.49	0.70	400	2000	360	39
	PZT 5H (Navy VI)	0.65	0.50	0.75	590	3500	190	39
	Relaxor-PT MPB Compositions							
	0.7PMN-0.3PT	0.50			670	5000	145	29
	0.67PMN-0.33PT	0.63		0.73	690	5000	160	29
	0.60PMN-0.40PZT(40/60)	0.50			-	2370	170	40
	0.55PST-0.45PT	0.61		0.73	655		205	32
	0.575PSN-0.425PT	0.66	0.55	0.74	389	1550	260	9
	0.575PSN-0.425PT (1%Nb doped)	0.69	0.52	0.76	504	2540	248	9
	0.575PSN-0.425PT (2% Sc doped)	0.63	0.53	0.72	359	1480	260	9
	0.58PSN-0.42PT	0.71	0.56	0.77	450		260	41
	0.5PNN-0.5PZT(35/65)	0.45	-		370		150	42
	0.87PZN-0.05BT-0.08PT	0.52	0.49		640	5200	150	43
Single Crystals	95PZN-5PT			0.86	~1500	4000	160	44
	91PZN-9PT			0.92	~1500		190	18,19
	89PZN-11PT			0.92	620	1000	200	44
	70PMN-30PT				~1500	4000	150	20
	60PMN-40PT				~1500		170	20

designated by T_C, is the temperature at which the material transforms from the prototypical non-ferroelectric to ferroelectric phase being associated with a spontaneous polarization and large dielectric anomaly. The importance of this transition temperature with respect to transducer fabrication, piezoelectric activity, etc., will also be discussed.

COMPOSITIONAL ENGINEERING OF PIEZOELECTRIC CERAMICS

Among the important material parameters mentioned previously, electromechanical coupling (k_{ij}), dielectric constant (K) and associated piezoelectric coefficient (d_{ij}) are the key parameters to be compositionaly engineered. In general, the piezoelectric properties of a ferroelectric ceramic can be expressed using the simplistic term,

$$d_{ij} \sim 2Q_{ij}K\varepsilon_0 P_i \qquad (1)$$

where d_{ij} is the piezoelectric coefficient, P_i the remnant polarization on poling, K the dielectric constant, ε_0 the permittivity of free space, and Q_{ij} the electrostriction coefficient. Since both Q_{ij} and P_i exhibit little dependence on composition or temperature below T_C in ferroelectric ceramics such as PZT, the piezoelectric coefficient d_{ij} and dielectric constant K are interrelated,

i.e., a ceramic with high piezoelectric coefficient also exhibits a large dielectric constant. To achieve a high dielectric constant or piezoelectric coefficient, MPB-based ceramics are further engineered by compositionaly adjusting the Curie temperature (T_C) downward relative
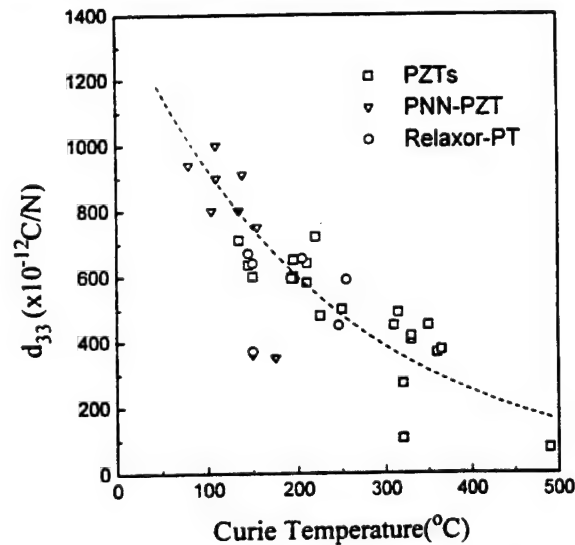

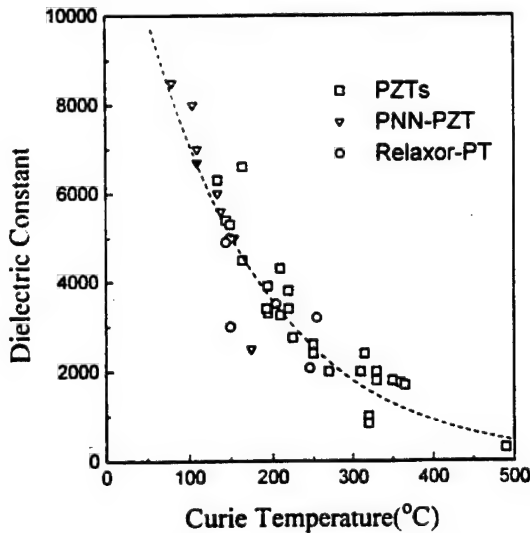Figure 3 Dielectric Constant (K) as a function of transition temperature (T_c) for piezoelectric ceramics, including PZT, modified PZTs, and Relaxor-PT systems. Data were compiled from references, commercial brochures and internal investigations.

Figure 4 Longitudinal coupling coefficient (k₃₃) as a function of transition temperature (T_c) for piezoelectric ceramics, including PZT, modified PZTs, and Relaxor-PT systems. Data were compiled from references, commercial brochures and internal investigations.

to room temperature. The effect of transition temperature (T_C) on the dielectric and piezoelectric properties is clearly evident in Figures 2 and 3. As shown, the room temperature values of both d_ij and K are plotted as a function of T_C for a variety of modified PZT ceramics, including Relaxor-PT systems, rather than a tabulation of properties, the methodology frequently available in company brochures, review articles, etc. To achieve both

Figure 5 Thickness coupling coefficient (k_T) as a function of transition temperature (T_c) for piezoelectric ceramics, including PZT, modified PZTs, and Relaxor-PT systems. Data were compiled from references, commercial brochures and internal investigations.
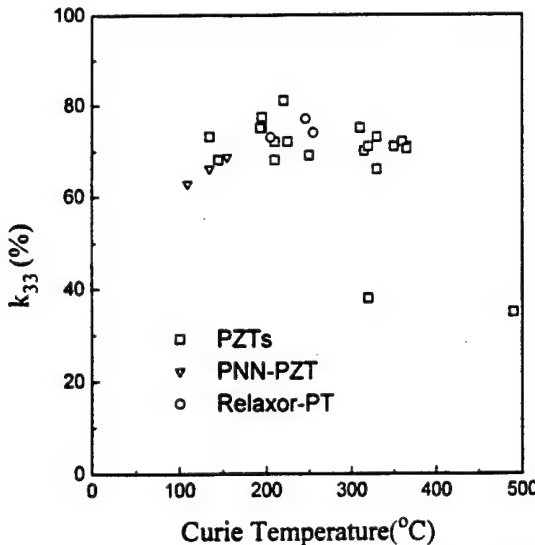
high dielectric constant and corresponding piezoelectrically "soft" materials generally used in ultrasonic imaging. requires materials with relatively low T_C. However, high piezoelectric coefficients and dielectric constants with correspondingly low T_Cs come with the expense of more temperature dependent properties. and less polarization stability, i.e. aging and loss of piezoelectric activity. As a general rule of thumb, piezoelectric materials can be safely used to approximately 1/2 T_C, without significant reduction in piezoelectric activity. This can restrict the working range of the device or limit fabrication techniques. During the fabrication process of transducers. the piezoelectric material may experience excessive temperature due to cutting/dicing, polymer curing, or the attachment of acoustic matching/backing materials. Therefore, not only must the dielectric and piezoelectric properties of a transducer material be considered, but also their T_C.

Electromechanical coupling factor (k_ij) is often referred to as the key material parameter for transducer design because it measures the true strength of the piezoelectric interaction once the elastic and dielectric response of the medium are normalized [11,12]. In addition, high coupling factor corresponds to a broad bandwidth response. which offers better axial resolution, deeper penetration, and most importantly, a degree of engineering freedom with the potential of operating the transducer at a narrow frequency regime for enhanced sensitivity.

Electromechanical coupling factor, piezoelectric coefficient and dielectric constant are interrelated by following equation.

$$k_{ij}^2 = \frac{d_{ij}^2}{K\varepsilon_0 s_{ij}} \qquad (2)$$

where d_ij is the piezoelectric coefficient, K the dielectric constant, ε_0 the permittivity of free space. and s_ij the elastic compliance. The question arises. since both d_ij and K are strongly dependent on T_C, what is the dependence of coupling k_ij? Figure 4 presents room temperature values of k₃₃ (longitudinal coupling) as a function of T_C. Important for high frequency ultrasound back scattered microscopy (UBM) and single element transducers. k_T (thickness) coupling values are given in Figure 5. As observed for both coupling coefficients, no relationship with T_c was evident. It is noted that the most widely used material in the ultrasonic imaging industry has a Tc ~ 210°C owing to the materials relatively high dielectric constant and coupling coefficient with providing good temperature stability.

In summarizing the observations presented above, the dielectric and piezoelectric properties of piezoelectric ceramics are strongly related to the transition temperature T_C. Upon direct comparison, *no one type of material.*
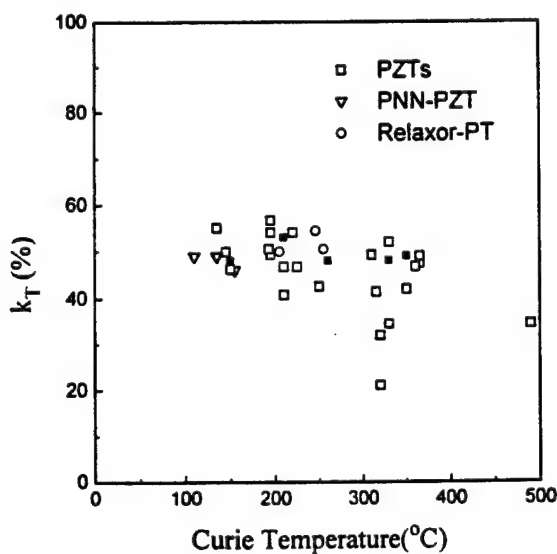
Table 3 Dielectric and Piezoelectric Properties of $Pb(A_{1/3}Nb_{2/3})O_3$ -$PbTiO_3$ crystals (A=Zn, Mg) from this work.

Longitudinal mode

Crystal	Cut	Tmax (°C)	Dielectric Constant (Loss)	Coup-ling	s_{33}^D (× 10^{-12} m^2/N)	d_{33} (pC/N)	Nt (Hz m)
PZN	001	~140	3600 (0.008)	0.852	13.2	1100	1521
PZN-8%PT	001	~165	4200 (0.012)	0.938	15.5	2070	1401
PZN-9.5%PT	001	~176	1400 (0.004)	0.894	15.5	1600*	1403
PMN-30%PT	001	~150	2890 (0.014)	0.808	11.6	730	1608
PMN-35%PT	001	~160	3100 (0.014)	0.923	10.2	1240	1730

* values determined by Berlincourt d_{33} meter.

Table 3 Continue.

Thickness mode

Crystal	Cut	Coupling	K_3^t	Loss	Qm	Nt (Hz m)
PZN	001	0.493	2730	0.013	40	2056
PZN-8%PT	001	0.481	4450	0.017	39	1831
PZN-9.5%PT	001	0.541	1550	0.024	31	1967
PZN-11%PT	001	0.638	890	0.024	17	1576
PMN-30% PT	001	0.568	4740	0.014	44	2368
PMN-35%PT	001	0.541	4540	0.031	35	2305

whether PZT-based or Relaxor-PT, offer significant advantages in overall transducer performance. *The question arises, are there opportunities for new piezoelectric materials with enhanced properties?*

To answer the question above, one must look to the single crystal form of piezoelectric materials, the topic of the following section.

SINGLE CRYSTAL PIEZOELECTRIC MATERIALS

Single crystal piezoelectrics such as quartz (SiO_2), lithium niobate ($LiNbO_3$), and the analogue lithium tantalate ($LiTaO_3$) are widely employed in specific applications that include oscillators, surface acoustic wave (SAW) devices, and in optics. In contrast to PZT ceramics, these single crystals offer inferior dielectric and piezoelectric properties. However, the single crystal form of high performance PZTs has been the research interest for many materials scientists. Attempts to grow single crystals of PZTs have been made by numerous researchers, resulting in crystallites too small to allow adequate property measurements [13,14,15,16,17]. Though Relaxor-PT ceramics were not shown to offer enhanced dielectric and piezoelectric properties comparable to PZT ceramics of similar T_Cs, they can be readily grown in single crystal form. This key distinction was first realized by Nomura and co-workers for the PZN and PZN-PT systems [18,19]. Following this ground-breaking work, single crystal growth of PMN-PT[20] and PSN-PT[21], etc., followed. In general, most $Pb(B_1,B_2)O_3$-PT crystals can be grown by high temperature solution growth using Pb-based fluxes.

Dielectric and piezoelectric properties for several $Pb(B_1B_2)O_3$-PT crystals are reported and compared to their polycrystalline counterparts in Table 2. As presented, piezoelectric coefficients and coupling coefficients are significantly higher, with d_{33} and k_{33} values greater than 1500 pC/N and 90%, respectively, found for MPB compositions in both the PZN-PT (x-0.09) and PMN-PT (x=0.35) systems. Though the Curie temperature (T_c) of these materials are relatively low < 200°C, the significance of these values becomes evident by directly comparing their values in relation to T_c in Figures 2~5.

Although ultra high coupling and piezoelectric properties of the PZN-PT system, first reported in 1981 and later in the PMN-PT system (1989), have been known for several years, their potential for high performance bio-medical ultrasound transducer and related devices has only been recognized recently. Serious efforts on the development of $Pb(B_1B_2)O_3$-PT crystals for high performance transducers includes investigations at Toshiba Co. and at the Pennsylvania State University.

Merits of the single crystal form itself include the possibility of "optimum" crystallographic cuts as analogous in the 35.25° rotated Y-cut in quartz crystals for a zero temperature coefficient of resonance, and X-cut in $LiTaO_3$ or 128° rotated Y cut in LiNbO3 crystals for
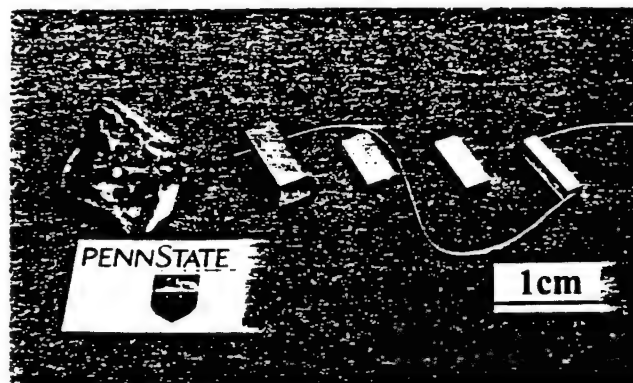

Figure 6 Sequence of sample preparation based on IEEE standards (PZN-9.5%PT (001) cuts). From left, as grown crystal, oriented sample using Laue back reflection camera, cut and polished sample, k_{31} sample electroded gold sputtering, and k_{33} sample.
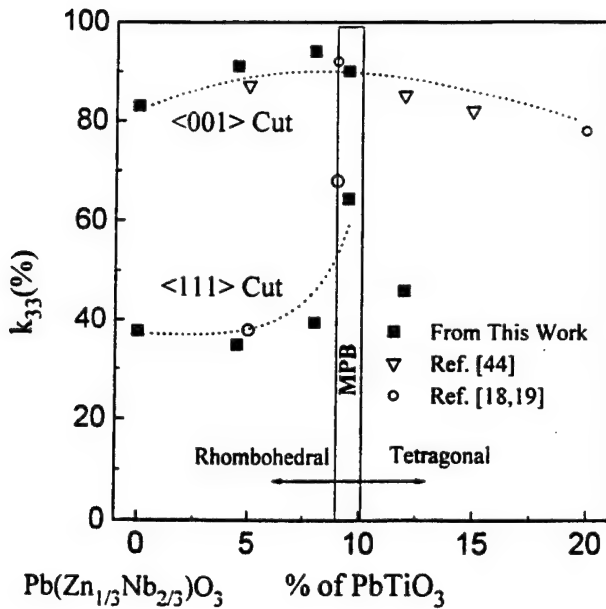
Figure 7 k_{33} as a function of composition and orientation in crystals of PZN-PT.

starting with an as-grown PZN-9.5%PT crystal.

Dielectric. piezoelectric. and electromechanical coupling coefficients for the various crystals are reported in Table 3. Parameters relevant to transducer designs, including dielectric loss, frequency constant (N), elastic compliance (s_{ij}), mechanical Q etc.. are also reported.

As reported in table 3. large coupling coefficients (k_{33}) and large piezoelectric coefficients (d_{33}) were found for PZN-PT crystals with MPB compositions, as previously reported by Kuwata [19]. Electromechanical coupling (k_{ij}) and piezoelectric coefficients (d_{ij}) equal to and larger than MPB crystal compositions were found for domain engineered rhombohedral crystals[#] as shown in Figure 7. Both pure PZN and PZN-8%PT crystals were found to possess high k_{33} values of ~85% and 94%, respectively, for (001) crystal cuts. Low values of dielectric loss < 1%. significantly less than their polycrystalline counterparts, should also be noted. The role of domains and their stability on the dielectric and piezoelectric properties of single crystals is the topic of further investigation. and further details is beyond the scope of this work.

As previously reported and given in figure 7, large values of k_{33} are also found in the tetragonal region (PT>10%) and, as reported in table 3, a value of 63% k_T was detected for the PZN-11%PT. High thickness coupling may be associated with the large anisotropy of the tetragonal crystals.

The dielectric constant was also found to be dependent on the crystal symmetry. Tetragonal crystals exhibited dielectric constants on the order of less than 1000 being significantly lower than rhombohedral crystals (3000~5000). Lower dielectric constants are also associated with both increased anisotropy and T_c. With similar coupling coefficients, the range of dielectric constants found in the PZN-PT system offer the flexibility in designing transducers with equivalent electrical impedance for a wide range of frequency and geometry.

optimum conditions including surface acoustic speed and coupling [22]. Another advantage of the single crystal form lies in terms of microstructural issues associated with polycrystalline ceramics. including grain size, porosity, etc. These can be also ignored removing scaling limitations. particularly relevant to high frequency transducers.

As stated above, the merits of using single crystals for high performance transducers is clearly evident, but few systematic studies have yet to be made. In the following section. preliminary results based on the author's ongoing investigation are presented.

CRYSTAL STRUCTURAL PROPERTY RELATIONSHIPS

Commonalties inherent to Relaxor-PT systems have been discussed in reviews by Shrout [23] and Randall [24]. Based on these commonalties. our research was limited to two representative systems of PZN-PT and PMN-PT. Though PMN-PT MPB crystals exhibit piezoelectric properties comparable with PZN-PT, more focus was given to the PZN system owing to its relatively lower PT content for MPB. This allows more uniform crystal growth of these solid solution materials. Details of crystal growth for these systems are given in references [25,26]. Compositions investigated include the rhombohedral PZN end member. MPB compositions (PT ≅ 9%) and tetragonal phases (> 10% PT).

High quality crystals (maximum size 1×1×1 cm) grown using PbO-based fluxes were characterized and samples prepared in accordance with IEEE standards. Figure 6. shows an example of the sequence of sample preparation

SUMMARY

The single crystal form of Relaxor-PT materials offers the possibility of dramatic improvements in transducer performance. Electromechanical coupling coefficients greater than 90% with non-MPB compositions as well as MPB compositions enables degree of freedom in designing transducers with broad bandwidth and/or improved sensitivity. A range of dielectric constants from ~1000 to 5000 in the PZN-PT system offers designers dielectrics for optimum electrical impedance matching. Ultrahigh piezoelectric strain coefficient d_{33}>2000pC/N clearly warrants further investigations in relation to high

[#] Rhombohedral crystals oriented and poled along pseudocubic <001> direction. Crystallographically. polarization direction of rhombohedral crystal is pseudocubic <111> direction.

energy density actuators. Microstructurally, single crystal transducers are not limited by grain size or porosity, offering high performance at very high frequencies.

Though clearly promising, the commercialization and growth of single crystals must be demonstrated and anticipated difficulties in fabrication and processing such as dicing, attaching matching layers and etc., must be overcome if single crystal piezoelectrics are to become piezoelectric materials for the next generation of ultrasound transducers.

REFERENCES

[1] T. R. Gururaja, "Piezoelectrics for Medical Ultrasonic Imaging", *American Ceramic Society Bulletin*, vol. 73, no. 5, pp. 50-55, May 1994.

[2] W. A. Smith, "New Opportunities in Ultrasonic Transducers emerging from Innovations in Piezoelectric Materials," 1992 SPIE International Symposium, July 21-22, 1992.

[3] B. Jaffe, W. R. Cook, Jr., and H. Jaffe. *Piezoelectric Ceramics*, London and New York: Academic Press, 1971.

[4] G. A. Smolenskii, V. A. Isupov, A. I. Agranovskaya, and N. N. Kainik, "New Ferroelectrics of Complex Composition. IV," *Soviet Physics - Solid State*, vol. 2 no. 11, pp. 2651-2654, May 1961.

[5] G. A. Smolenskii, V. A. Isupov, A. I. Agranovskaya, S. B. Popov, "Ferroelectrics with Diffuse Phase Transitions", *Soviet Physics - Solid State*, vol. 2, no. 11, pp. 2584-2594, May 1961.

[6] L. E. Cross, "Relaxor Ferroelectrics," *Ferroelectrics*, vol. 76, pp. 241-267, 1987.

[7] Landolt-Börnstein, *Ferroelectric and Antiferro-electric Substances*, vol. 19, Group III, Berlin: Springe Verlag, 1981.

[8] Y. Yamashita, "Pb(B'B")O$_3$-PbTiO$_3$ Materials," *The 7th US-Japan Study Seminar on Dielectric and Piezoelectric Ceramics*, Tukuba, 1995, pp. 181-185.

[9] Y. Yamashita, "Improved Ferroelectric Properties of Niobium-Doped Pb[(Sc$_{1/2}$Nb$_{1/2}$)Ti]O$_3$ Ceramics Material," *Japanese Journal of Applied Physics*, vol. 32, pp. 5036-5040, Nov. 1993.

[10] N. Kim, *Grain Size Effect on the Dielectric and Piezoelectric Properties in Compositions which are near the Morphotropic Phase Boundary of Lead Zirconate-Titanate Based Ceramics*, Ph. D. Thesis, Pennsylvania State University, 1994.

[11] J. F. Nye, *Physical Properties of Crystals*. Oxford University Press. Oxford: Clarendon Press, 1957.

[12] D. A. Berlincourt, D. R. Curran and H. Jaffe, *Piezoelectric and Peizomagnetic Materials and Their Function in Transducers*. New York: Academic Press, 1964, p169 in Physical Acoustics, Volume 1A, edited by W. P. Mason.

[13]. S. Fushimi and T. Ikeda, "Phase Equilibrium in the System PbO-TiO$_2$-ZrO$_2$," *Journal of the American Ceramic Society*, vol. 50, no. 3, pp. 129-132, March 1967.

[14] V. A. Kuznetzov, "Crystallization of Titaium, Zirconium and Hafnium Oxies and Some Titanate and Zirconate Compounds under Hydrothermal Conditions," *Journal of Crystal Growth*, vol. 34, pp. 405 - 410, 1968.

[15] R. Clarke and R. W. Whatmore, "The Growth and Characterization of PbZr$_x$Ti$_{1-x}$O$_3$ Single Crystals," *Journal of Crystal Growth*, vol. 33, pp. 29-38, 1976.

[16] T. Hatanaka and H. Hasegawa, "Dielectric Properties of Pb(Zr$_x$Ti$_{1-x}$)O$_3$ Single Crystals Including Monoclinic Zirconia," *Japanese Journal of Applied Physics*, vol. 34, pp. 5446-5448, Sept. 1995.

[17] K. Yanagisawa, H. Kanai, and Y. Yamashita, "Hydrothermal Crystal Growth of Lanthanum-Modified Lead Zirconate Titanate," *Japanese Journal of Applied Physics*, vol. 34, pp. 536-538 Sept. 1995.

[18] J. Kuwata, K. Uchino, and S. Nomura, "Phase Transitions in the Pb(Zn$_{1/3}$Nb$_{2/3}$)O$_3$ -PbTiO$_3$ System," *Ferroelectrics*, vol. 37, pp. 579-582, 1981.

[19] J. Kuwata, K. Uchino, and S. Nomura, "Dielectric and Piezoelectric Properties of 0.91Pb(Zn$_{1/3}$Nb$_{2/3}$)O$_3$ - 0.09PbTiO$_3$ Single Crystals," *Japanese Journal of Applied Physics*, vol. 21, no. 9, pp. 1298-1302, Sept. 1982.

[20] T. R. Shrout, Z. P. Chang, N. Kim, and S. Markgraf, "Dielectric Behavior of Single Crystals near the (1-x)Pb(Mg$_{1/3}$Nb$_{2/3}$)O$_3$ - (x) PbTiO$_3$ Morphotropic Phase Boundary," *Ferroelectric Letters*, vol. 12, pp. 63-69, 1990.

[21] V. G. Smotorakov, I. P. Raevskii, M. A. Malitskaya, S. M. Zaitsev, Y. M Popov, and N. A. Strekneva, "Preparation and Properties of Single Crystals of Pb$_2$ScNbO$_6$," *Inorganic Materials*, vol. 19, pp. 105-108, 1983.

[22] J. M. Herbert, *Ferroelectric Transducers and Sensors*, London and New York: Gordon and Breach Science Publishers, 1982.

[23]. T. R. Shrout and J. Fielding, Jr., "Relaxor Ferroelectric Materials," *in Proceedings of the 1990 IEEE Ultrasonics Symposium*, 1990, pp. 711-715.

[24] C. A. Randall, A. S. Bhalla, T. R. Shrout, and L. E. Cross, "Classification and Consequences of Complex Lead Perovskite Ferroelectrics with regard to B-site

Cation Order," *Journal of Materials Research*, vol. 5, no. 4, pp. 829-834, 1990.

[25]. M. L. Mulvihill, S.-E. Park, G. Risch, Z. Li, K. Uchino, T. R. Shrout, "The Role of Processing Variables in the Flux Growth of Lead Zinc Niobate-Lead Titanate Relaxor Ferroelectric Single Crystals," *Japanese Journal of Applied Physics*, vol. 35, no. 7, pp. 51-57, July 1996.

[26] S.-E. Park, M. L. Mulvihill, G. Risch, and T. R. Shrout, "The Effect of Growth Condition on Dielectric Properties of $Pb(Zn_{1/3}Nb_{2/3})O_3$ Crystal," *Japanese Journal of Applied Physics*, in review.

[27] Y. Yamashita, "Large Electromechanical Coupling Factors in Perovskite Binary Material System," *Japanese Journal of Applied Physics*, vol. 33, Pt. 1[9B], pp. 5328-5331, 1994.

[28] S. Nomura, "Ferroelectric Properties in the System $Pb(Zn_{1/3}Nb_{2/3})O_3$ -$PbTiO_3$," *Journal of Physical Society of Japan*, vol. 27, p. 262, 1969.

[29] S. W. Choi, T. R. Shrout, S. J. Jang, and A. S. Bhalla, "Dielectric and Pyroelectric Properties in the $Pb(Mg_{1/3}Nb_{2/3})O_3$ -$PbTiO_3$ system," *Ferroelectrics*, vol. 100, 29-38, 1989.

[30] H. Banno et al., in *Proceedings of the 1st Meeting on Ferroelectric Materials and Their Applications*, 1975, F-14, p. 339.

[31] T. Kudo, T. Yazaski, F. Naito, and S. Sugaya, "Dielectric and Piezoelectric Properties of $Pb(Co_{1/3}Nb_{2/3})O_3$-$PbTiO_3$ -$PbZrO_3$ Solid Solution Ceramics," *Journal of American Ceramic Society*, vol. 53, pp. 326-328, June 1970.

[32] J. F. Wang, J. R. Giniewicz, and A. S. Bhalla, "Soft Piezoelectric $(1-x)Pb(Sc_{1/2}Ta_{1/2})O_3$ - $xPbTiO_3$ Ceramics with High Coupling Factors and Low Qm," *Ferroelectric Letters*, vol. 16, pp. 113-118, 1993.

[33] V. J. Jonson, M. W. Valenta, J. E. Dougherty, R. M. Douglass and J. W. Meadows, "$Pb(Sc_{0.5}Nb_{0.5})_xO_3$, Perovskite-Type Ferroelectric Solid Solutions Possessing Relatively Large Spontaneous Polarizations," *Journal of Physical Chemistry in Solids*, vol. 24, pp. 85-93, 1963.

[34] V. J. Tennery, K. W. Hang, R. E. Novak, "Ferroelectric and Structural Properties of the $Pb(Sc_{1/2}Nb_{1/2})_{1-x}Ti_xO_3$ System, *Journal of American Ceramic Society*, vol. 51, pp. 671-674, Dec. 1968.

[35] U. Kodama, M. Osada, O. Kumon, and T. Nishimoto, "Piezoelectric Properties and Phase Transition of $PbIn_{1/2}Nb_{1/2}O_3$-$PbTiO_3$ Solid Solution Ceramics," *American Ceramics Society Bulletin*, vol. 48, no. 12, pp. 1122 - 1124, 1969.

[36] A. I. Zaslavskii and M. F. Bryzhina, "An X-ray Structural Investigation of the Antiferroelectric Pb_2MgWO_6 and the System of Solid Solutions Pb_2MgWO_6 - $PbTiO_3$," *Soviet Physics-Crystallography*, vol. 7, no. 5, pp. 577-583, 1963.

[37] V. A. Isupov and L. P. Belous, "Phase Transition in the Antiferroelectric $PbCo_{0.5}W_{0.5}O_3$ and $PbCo_{0.5}W_{0.5}O_3$ - $PbTiO_3$ Solid Solutions," *Soviet Physics-Crystallography*, vol. 16, no. 1, pp. 129 - 133, 1971.

[38] D. A. Berlincourt, C. Cmolik, and H. Jaffe, "Piezoelectric Properties of Polycrystalline Lead Titanate Zirconate Compositions," *Proceedings of the IRE*, vol. 48, pp. 220 -229, 1960.

[39] H. Jaffe and D. A. Berlincourt, "Piezoelectric Transducer Materials," *Proceedings of IEEE*, vol. 53 no. 10, pp. 1372-1386, 1965.

[40] H. Ouchi, K. Nagano, and S. Hayakawa, "Piezoelectric Properties of $Pb(Mn_{1/3}Nb_{2/3})O_3$ -$PbZrO_3$ Solid Solution Ceramics," *Journal of American Ceramic Society*, vol. 48, no. 12, pp. 630-635, 1965.

[41] Y. Yamashita, "Piezoelectric Properties of Niobium-Doped $[Pb(Sc_{1/2}Nb_{1/2})_{1-x}Ti_x]O_3$ Ceramics Material near the Morphotropic Phase Boundary," *Japanese Journal of Applied Physics*, vol. 33, no. 8, pp. 4562 -4656, August 1994.

[42] S. T. Chung, K. Nagata, and H. Igarashi, "Piezoelectric and Dielectric Properties of $Pb(Ni_{1/3}Nb_{2/3})O_3$ -$Pb(Zn_{1/3}Nb_{2/3})O_3$ -$PbTiO_3$," *Ferroelectrics*, vol. 94, pp. 243-247, 1989.

[43] S. Baumler, "The Dielectric and Piezoelectric Properties of PZN:PT:BT Ceramics," M. S. Thesis, The Pennsylvania State University, 1986.

[44] T. R. Shrout, unpublished work.

APPENDIX 23

Relaxor-based single crystal materials
for ultrasonic transducer applications

Seung-Eek Park[a], Patrick D. Lopath[b], Kirk K. Shung[b], and Thomas R. Shrout[a]

[a] Materials Research Laboratory, The Pennsylvania State University, University Park, PA 16802
[b] Department of Bioengineering, The Pennsylvania State University

ABSTRACT

Relaxor ferroelectric single crystals of $Pb(Zn_{1/3}Nb_{2/3})O_3$ (PZN), $Pb(Mg_{1/3}Nb_{2/3})O_3$ (PMN) and their solid solutions with normal ferroelectric $PbTiO_3$ (PT) were investigated for ultrasonic transducer applications. Crystals offer adjustable properties not only by compositional tailoring but also by domain state engineering associated with different crystallographic orientation, which is not achievable in polycrystalline materials. Longitudinal coupling coefficients (k_{33}) as high as 94 % and dielectric constants (K_3^T) in the range of 3500-6000 were achieved with low dielectric loss (<1%) using <001> oriented rhombohedral crystals of (1-x)PZN-xPT and (1-y)PMN-yPT, where x<0. 09 and y<0. 35. Dicing direction as well as poling direction were critical for high coupling under laterally clamped condition. Dicing parallel to the (001) yields 90% of laterally clamped coupling (k_{bar}) out of 94% longitudinal coupling (k_{33}) for PZN-8%PT. On the other hand, samples diced parallel to (110) exhibited no dominant mode present. Thickness coupling (k_T) as high as 64% and low dielectric constant (K_3^T) < 600 with low loss (<1%) could be achieved using tetragonal crystals of (1-x)PZN-xPT and (1-y)PMN-yPT, where x>0. 1 and y>0. 4. The performance gains associated with these ultra-high coupling coefficients and range of dielectric constants are evident in relation to broader bandwidth and electrical impedance matching. Specifically, rhombohedral crystals offer the possibility of extremely broad bandwidth devices for transducer arrays and tetragonal crystals for single element transducers. Transducer simulation was performed using the KLM model. The pulse/echo response simulated a 124% bandwidth subdiced array element with a center frequency of 10 MHz. An optimized array design of the same geometry constructed of PZT 5H displays a 87% bandwidth.

Keywords: relaxor ferroelectrics, single crystal, crystal orientation, bandwidth, impedance matching.

1. INTRODUCTION

Piezoelectric ceramics are currently the material of choice for ultrasonic transducer applications offering relatively high coupling (k_{ij}), a wide range of dielectric constants (K), and low dielectric loss. These merits translate into transducer performance in the form of relatively high sensitivity, broad bandwidth, impedance matching and minimal thermal heating. Among piezoelectric ceramics, $Pb(Zr_{1-x},Ti_x)O_3$ (PZT) ceramics have been the mainstay for high performance transducer applications. Compositionally, PZT ceramics lie near the morphotropic phase boundary (MPB) between the tetragonal and rhombohedral phases, as depicted in Figure 1. MPB compositions have anomalously high dielectric and piezoelectric properties as a result of enhanced polarizability arising from the coupling between two equivalent energy states, i. e. the tetragonal and rhombohedral phases, allowing optimum domain reorientation during the poling process. Further modifications using acceptor and donor dopants give us the wide range of piezoelectric compositions we have today. Alternative MPB systems can be found in relaxor-based ferroelectrics and their solid solutions with $PbTiO_3$ (PT). Lead based relaxor materials are complex perovskites with the general formula $Pb(B_1B_2)O_3$, ($B_1=Mg^{2+}$, Zn^{2+}, Ni^{2+}, Sc^{3+} . . . , $B_2=Nb^{5+}$, Ta^{5+}, W^{6+} . . .). Characteristic of relaxors is a broad and frequency dispersive dielectric maxima.[1]

Dielectric and piezoelectric properties for selected PZT's and relaxors-PT systems are summarized in table 1. Some relaxor-PT compositions such as modified $Pb(Sc_{1/2}Nb_{1/2})O_3$ - $PbTiO_3$ (PSN-PT) seem to possess superior dielectric and piezoelectric properties compared to that of PZT ceramics. However, if being analyzed with respect to the ferroelectric transition temperature designated by Tc (the temperature at which the material transforms from the prototypical non-ferroelectric to ferroelectric phase being associated with a spontaneous polarization and large dielectric anomaly) no one type of ceramic offers significant advantages in overall transducer performance. Enhanced piezoelectric activity of MPB-based ceramics by compositionaly adjusting the Curie temperature (Tc) downward relative to room temperature comes with the expense of more temperature dependent properties, and less polarization stability, i.e. aging and loss of piezoelectric activity.

Park 1/3

Table 1 Reported Dielectric and Piezoelectric Properties for selected PZT and Relaxor Binary Systems

Form	Materials	k_P	k_t*	k_{33}	d_{33} (pC/N)	K_3^J	Tc (°C)	Ref.
Ceramics (poly-crystalline)	**PZT-MPB Composition**							
	PZT 53/47	0.52		0.67	220	~800	360	3
	Modified PZTs							
	PZT-4 (Navy I)	0.58	0.51	0.70	289	1200	330	4
	PZT-8 (Navy III)	0.50	0.44	0.70	220	1000	300	4
	PZT-5 (Navy II)	0.60	0.49	0.70	400	2000	360	4
	PZT 5H (Navy VI)	0.65	0.50	0.75	590	3500	190	4
	Relaxor-PT MPB Compositions							
	0.7PMN-0.3PT	0.50			670	5000	145	5
	0.67PMN-0.33PT	0.63		0.73	690	5000	160	5
	0.60PMN-0.40PZT(40/60)	0.50			-	2370	170	6
	0.55PST-0.45PT	0.61		0.73	655	4000	205	7
	0.575PSN-0.425PT	0.66	0.55	0.74	389	1550	260	8
	0.575PSN-0.425PT (1%Nb doped)	0.69	0.52	0.76	504	2540	248	8
	0.575PSN-0.425PT (2% Sc doped)	0.63	0.53	0.72	359	1480	260	8
	0.58PSN-0.42PT	0.71	0.56	0.77	450	2200	260	9
	0.5PNN-0.5PZT(35/65)	0.45	-		370		150	10
	0.87PZN-0.05BT-0.08PT	0.52	0.49		640	5200	150	11
Single Crystals	95PZN-5PT			0.86	~1500	4000	160	12
	91PZN-9PT			0.92	~1500	2200	190	13,14
	89PZN-11PT			0.92	620	1000	200	12
	70PMN-30PT				~1500	4000	150	15
	60PMN-40PT				~1500		170	15

* Reported coupling factors often do not follow the simplistic equation, $k_{33}^2 \sim k_p^2 + k_T^2 - k_p^2 * k_T^2$. Based on the difficulties in accurately determining k_T, the confirmation of values should be made.

Further details on the relationship between dielectric/piezoelectric properties and Curie temperature (Tc) can be found in the article by S.-E. Park et al.[2]

Though Relaxor-PT ceramics do not offer enhanced dielectric and piezoelectric properties comparable to PZT ceramics of similar T_CS, it is the single crystal form of relaxor-PT's that exhibits ultrahigh piezoelectric properties not currently available with piezoelectric MPB ceramics. This key distinction was first realized by Nomura and co-workers[13,14] for MPB compositions of $Pb(Zn_{1/3}Nb_{2/3})O_3$ - $PbTiO_3$ (PZN-PT) systems with d_{33} and k_{33} values of 1500 pC/N and 90%, respectively, followed by the crystal growth of $Pb(Mg_{1/3}Nb_{2/3})O_3$ - $PbTiO_3$ (PMN-PT)[15] and $Pb(Sc_{1/2}Nb_{1/2})O_3$ - $PbTiO_3$ (PSN-PT)[16]. In general, most $Pb(B_1,B_2)O_3$-PT crystals can be grown by high temperature solution growth using Pb-based fluxes. Distinctly increased dielectric and piezoelectric properties of $Pb(B_1,B_2)O_3$-PT crystals are compared with ceramics in table 1. Though clearly attractive, few systematic studies have followed.

Merits of the single crystal form itself include the possibility of "optimum" crystallographic cuts as analogous in AT and BT cuts in quartz crystals for a zero temperature coefficient of resonance, and X-cut in $LiTaO_3$ or 128° rotated Y cut in $LiNbO_3$ crystals for optimum conditions including surface acoustic speed and coupling[17]. Another advantage of the single crystal form lies in terms of microstructural issues associated with polycrystalline ceramics, including grain size, porosity, etc. These can be also ignored removing scaling limitations, particularly relevant to high frequency transducers.

It is the objective of this work to systematically evaluate crystal structural property relationships and to present ongoing investigation on the theoretical designs using these single crystal materials. Based on the commonalties inherent to Relaxor-

PT systems[18,19] our research was limited to two representative systems of PZN-PT and PMN-PT. Though PMN-PT MPB crystals exhibit piezoelectric properties comparable with PZN-PT, more focus was given to the PZN system owing to its relatively lower PT content for MPB. This allows more uniform crystal growth of these solid solution materials. Details of crystal growth for these systems are given in references. [20,21]

2. DIELECTRIC AND PIEZOELECTRIC PROPERTIES OF RELAXOR-BASED SINGLE CRYSTALS

Dielectric, piezoelectric, and electromechanical coupling coefficients for the various crystals are reported in table 2 and table 3. Parameters relevant to transducer designs, including dielectric loss, frequency constant (N), elastic compliance (s_{ij}), mechanical Q etc., are also reported.

As reported in table 2, large coupling coefficients (k_{33}) and large piezoelectric coefficients (d_{33}) were found for PZN-PT crystals with MPB compositions, as previously reported by Kuwata[14]. It should be noted, however, that electromechanical coupling (k_{ij}) and piezoelectric coefficients (d_{ij}) equal to and larger than MPB crystal compositions were found for domain engineered rhombohedral crystals* as shown in Figure 2. PZN-4.5%PT and PZN-8%PT crystals were found to possess high k_{33} values of ~92% and 94%, respectively, for (001) crystal cuts. Low values of dielectric loss < 1% should also be noted.

As previously reported and given in table 3 and figure 2, large values of k_{33} are also found in the tetragonal region (PT>10%) and, as reported in table 3, a value of 63% and 62% k_T was detected for the PZN-11%PT and PZN-12%PT, respectively. High thickness coupling may be associated with the large anisotropy of the tetragonal crystals.

The dielectric constant was also found to be dependent on the crystal symmetry. Tetragonal crystals exhibited dielectric constants on the order of less than 1000 being significantly lower than rhombohedral crystals (3000~5000). Lower dielectric constants are also associated with both increased anisotropy and T_c. With similar coupling coefficients, the range of dielectric constants found in the PZN-PT system offer the flexibility in designing transducers with equivalent electrical impedance for a wide range of frequency and geometry. In following sections, transducer simulation using these material properties will be discussed.
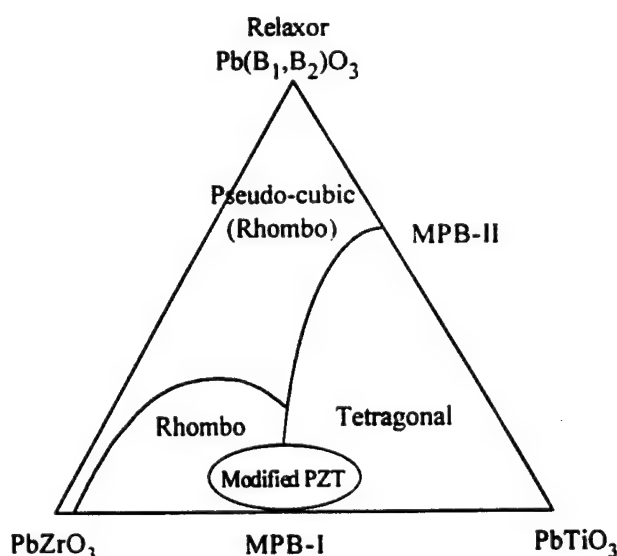

Figure 1 Ternary diagram depicting MPBs in PZT and Relaxor-PT systems for piezoelectric ceramics.
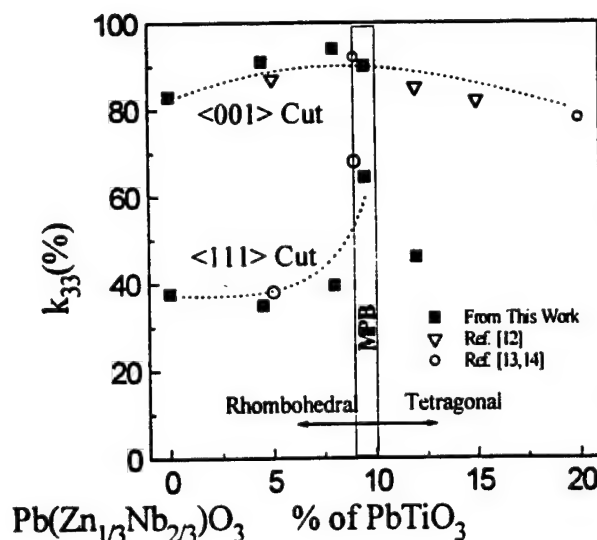
Figure 2 k_{33} as a function of composition and orientation in crystals of PZN-PT.

---

* Rhombohedral crystals oriented and poled along pseudocubic <001> direction. Crystallographically, polarization direction of rhombohedral crystal is pseudocubic <111> direction.

Table 2 Dielectric and piezoelectric properties of $Pb(A_{1/3}Nb_{2/3})O_3$ - $PbTiO_3$ crystals ($A=Zn^{2+}$, Mg^{2+}) - longitudinal (k_{33}) mode

Composition	T_{max} (°C)	Crystal Structure	Orient.	coupling	s_{33}^E ($10^{-12} m^2/N$)	K_3^T	loss	d_{33} (pC/N)	Nt (Hz m)
PZN	140	Rhom[1]	111	0.38	7.4	900	0.012	83	2058
			001	0.85	48	3600	0.008	1100	1521
PZN-4.5%PT	160	Rhom	111	0.35	9.0	1500	0.004	110	1961
			001	0.92	102	4000	0.004	2000	1344
PZN-8%PT	170	Rhom	111	0.39	7.4	2150	0.012	82	2205
			001	0.94	130	4200	0.012	2200	1401
PZN-9.5%PT	176	MPB[2]	111	0.64	10.4	4300	0.007	600	2240
			001	0.89	77	1600	0.004	1600	1403
PZN-12%PT	200	Tetra[3]	001	0.86		900	0.004	500	1296
PMN-24%PT	150	Rhom	001			3700	0.009	900	1608
PMN-33%PT		Rhom	001	0.94	79	4500	0.012	1700	1866
PMN-35%PT	160	MPB	001	0.92	67	3100	0.014	1240	1730

[1] Rhombohedral structure
[2] morphotrophic phase boundary composition
[3] Tetragonal structure

3. TRANSDUCER DESIGN

3.1 Arrays

Once the ideal polarization axis is defined, one must consider the geometry of the ultrasonic device to be fabricated. An acoustic array uses a different geometry, and thus a different vibrational mode, than a single element transducer or, for that matter, a k_{33} test sample. Consider first an array which consists of many tall, narrow elements. Each element utilizes a partially clamped k_{33} mode of vibration. A true k_{33} mode would be a rod poled through the long axis and driven parallel to the poling direction. The rod is not laterally clamped in any direction. An array element, however, is laterally clamped in the elevation direction. This geometry tends to reduce the coupling coefficient from the ideal k_{33}. The tall, narrow geometry also mandates a small surface area, and thus a low capacitance, which leads to a large electrical impedance and an electrical mismatch to standard 50 Ω transmit and receive electronics. The need to increase the capacitance of each element forces the designer to look for high dielectric constant materials. As discussed in the previous chapter, both a high k_{33} and a large free dielectric constant are found on the rhombohedral side of the MPB. However the large coupling coefficients leads to a low clamped, or high frequency, dielectric constants with respect to soft PZTs. The result of this lower clamped relative permittivity can be seen in the simulated pulse echo response in figure 5. While the <001> family is defined as the poling direction for an array element showing high coupling, it is now left to define a dicing direction along the surface of the crystal

Table 3 Dielectric and piezoelectric properties of $Pb(A_{1/3}Nb_{2/3})O_3$ - $PbTiO_3$ crystals ($A=Zn^{2+}$, Mg^{2+}) - thickness (k_T) mode

Crystal	Cut	Coupling	K_3^T	Loss	Qm	Nt (Hz m)
PZN	001	0.49	2732	0.013	40	2056
PZN-8%PT	001	0.48	4450	0.017	39.5	1831
PZN-9.5%PT	001	0.54	1553	0.024	31.3	1967
PZN-11%PT	001	0.64	890	0.024	16.6	1576
PZN-12%PT*	001	0.62	580	0.001	16.0	1926
PMN-30% PT	001	0.57	4739	0.014	43.7	2368
PMN-35%PT	001	0.54	4540	0.031	35.3	2305

* under bias of 100V (15kV/cm)

which will provide the optimum performance. Given crystal symmetry with the <001> family every 90 degrees, the [100] and [110] (45 degrees from <001>) directions have been investigated, as shown in Figure 3. Dicing parallel to the [100] axis yields three distinct modes, with the thickness or clamped k_{33} mode along the poling axis (at 880 KHz in the test sample of Figure 4) being the dominant mode. The low frequency mode at 228 KHz is the k_{31} mode, with the bar resonating in the length dimension perpendicular to the poling direction. The center mode has been attributed to a flexural length mode. The frequency constants (Nt measured in Hz m) of the present modes are such that it is fairly easy to move undesired modes and harmonics out of the main thickness mode to allow accurate measurement and efficient operation. The drop in k_{33} to what we call k_{bar} (for the clamped k_{33} or 'bar' mode) is minimal, from 94% to 90%. Dicing parallel to the [110] direction yields a more confusing picture. There is not a dominant mode present. The frequency constants of the various modes result in modal overlap in samples cut to approximate array dimensions, bleeding energy between modes and making accurate measurement and efficient operation impossible.

Up to this point we have defined the characteristics needed for an array element: A rhombohedral composition, poled parallel to <001> and diced, parallel to [100], to dimensions defined by the frequency constants to achieve a pure thickness vibrational mode over the final bandwidth of the transducer. It will be seen later that these single crystal materials can yield very wide bandwidth devices, so care must be taken when dimensioning the final transducer to avoid exciting unwanted modes.

3.2 Single elements

Transducer design for an application such as ultrasound backscatter microscopy (UBM) has requirements different than design for arrays. Since impedance of the piezoelectric resonator varies inversely with capacitance as in (1),

$$Z = \frac{1}{j\omega C} \qquad (1)$$

at high frequencies, large area, high frequency, single element transducers suffer from the opposite problem than array elements; low electrical impedance, offers a poor match to the 50Ω driving electronics. As before, a large coupling coefficient is desired to achieve a wide bandwidth. However, these elements operate in a true clamped thickness, or k_t, mode. Rhombohedral crystals, compositions with PT content below the MPB tend to have very efficient k_{33}, but k_t's only comparable to PZT.

Compositions above the MPB have low free dielectric constants characteristic as reported in table 3. In this tetragonal configuration, the crystal is very anisotropic with the polar axis at [001]. Evaluation of PZN-11%PT and PZN-12%PT crystals show $k_t \sim 63\%$ and 62% as reported in table 3, in comparison to PZT Navy Type VI at k_t of only 52%, potentially promising increased performance for single element transducers.
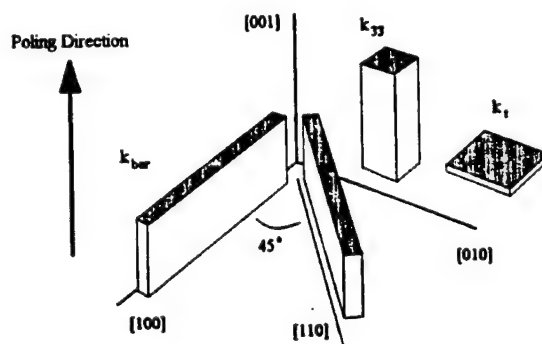

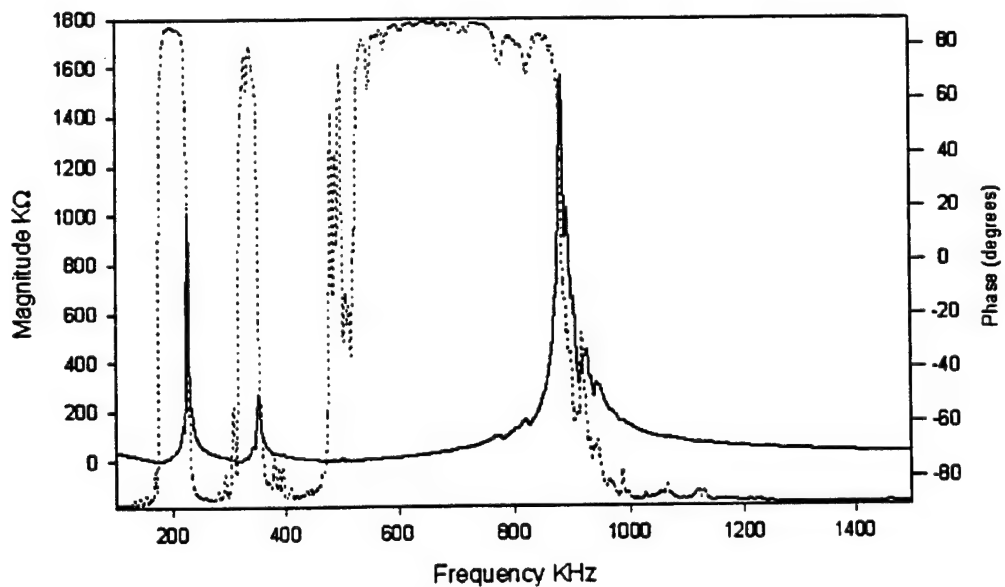Fig 3. Resonant samples prepared. k_{33} and k_t samples were not aligned in the 1 and 2 directions.

Figure 4 Impedance plot for a <001> poled and [100] aligned PZN-8%PT kbar sample. The low frequency mode is k_{31}.

4. TRANSDUCER SIMULATION

The second step in the design of a transducer is to optimize the required transducer response. For example, a Doppler transducer has different bandwidth requirements than an imaging transducer. Our goal herein is to construct very high resolution imaging transducers. Design was simulated using the KLM model[22] employed via an ABCD parameter approach encoded in MathCad[23].
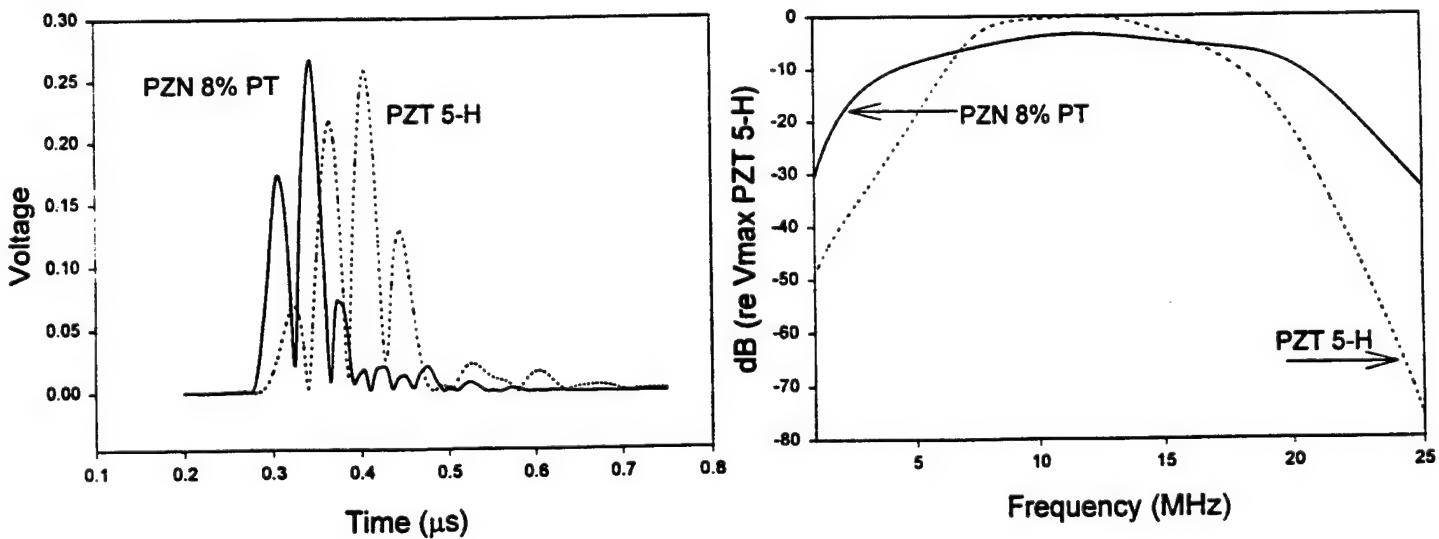

Figure 5 Simulated pulse/echo response of a 124% bandwidth PZN-8% PT array element at 10 MHz compared to 87% bandwidth PZT element of similar design.

Figure 6 Bandwidth comparison between PZN-8%PT 10 MHz array element vs. PZT-5H.

The pulse/echo waveform in figures 5 simulates a 125% bandwidth array element with a center frequency of 10 MHz. The bandwidth was measured at the -6dB points in the spectrum. Figure 6 shows bandwidth comparison between PZN-8%PT vs. PZT-5H. This simulation predicts results for an array fabricated from PZN 8% PT poled in <001> and diced parallel to [001]. A 10 Mrayl impedance backing was simulated and an idealized 2 layer matching scheme as described by Desilets et al. was used to achieve a maximally flat response[24]. An optimized array design of the same geometry constructed of Navy type VI PZT 5-H displays only a 87% bandwidth.

5. SUMMARY

The single crystal form of Relaxor-PT materials offers the possibility of dramatic improvements in transducer performance. Electromechanical coupling coefficients greater than 94% with non-MPB compositions as well as MPB compositions enables degree of freedom in designing transducers with broad bandwidth and/or improved sensitivity. A range of dielectric constants from ~600 to 5000 in the PZN-PT system offers designers dielectrics for optimum electrical impedance matching.

Transducer simulation was carried out using the KLM model. The pulse/echo response simulated a 124% bandwidth subdiced array element with a center frequency of 10 MHz. An optimized array design of the same geometry constructed of Navy type VI PZT 5-H displays a 87% bandwidth.

Dicing parallel to the (001) yields 90% of laterally clamped coupling (k_{bar}) out of 94% longitudinal coupling (k_{33}). On the other hand, samples diced parallel to (110) exhibited no dominant mode present. Thickness coupling (k_T) as high as 64% and low dielectric constant (K_3^T) < 800 with low loss (<1%) could be achieved using tetragonal crystals of (1-x)PZN-xPT and (1-y)PMN-yPT, where x>0.1 and y>0.4.

ACKNOWLEDGMENTS

REFERENCES

1. L. E. Cross, "Relaxor Ferroelectrics," *Ferroelectrics*, vol. 76, pp. 241-267, 1987.
2. Seung-Eek Park, Thomas R. Shrout, "Characteristics of Relaxor-Based Piezoelectric Single Crystals for Ultrasonic Transducers," in press *IEEE Trans. on Ultrasonics, Ferroelectric and Frequency Control Special Issue on Ultrasonic Transducers*, 1997.
3. D. A. Berlincourt, C. Cmolik, and H. Jaffe, "Piezoelectric Properties of Polycrystalline Lead Titanate Zirconate Compositions," *Proceedings of the IRE*, vol. 48, pp. 220 -229, 1960.
4. H. Jaffe and D. A. Berlincourt, "Piezoelectric Transducer Materials," *Proceedings of IEEE*, vol. 53 no. 10, pp. 1372-1386, 1965.
5. S. W. Choi, T. R. Shrout, S. J. Jang, and A. S. Bhalla, "Dielectric and Pyroelectric Properties in the $Pb(Mg_{1/3}Nb_{2/3})O_3$ -$PbTiO_3$ system," *Ferroelectrics*, vol. 100, 29-38, 1989.
6. H. Ouchi, K. Nagano, and S. Hayakawa, "Piezoelectric Properties of $Pb(Mg_{1/3}Nb_{2/3})O_3$ -$PbTiO_3$ - $PbZrO_3$ Solid Solution Ceramics," *Journal of American Ceramic Society*, vol. 48, no. 12, pp. 630-635, 1965.
7. J. F. Wang, J. R. Giniewicz, and A. S. Bhalla, "Soft Piezoelectric (1-x)$Pb(Sc_{1/2}Ta_{1/2})O_3$ - x$PbTiO_3$ Ceramics with High Coupling Factors and Low Qm," *Ferroelectric Letters*, vol. 16, pp. 113-118, 1993.
8. Y. Yamashita, "Improved Ferroelectric Properties of Niobium-Doped $Pb[(Sc_{1/2}Nb_{1/2})Ti]O_3$ Ceramics Material," *Japanese Journal of Applied Physics*, vol. 32, pp. 5036-5040, Nov. 1993.
9. Y. Yamashita, "Piezoelectric Properties of Niobium-Doped $[Pb(Sc_{1/2}Nb_{1/2})_{1-x}Ti_x]O_3$ Ceramics Material near the Morphotropic Phase Boundary," *Japanese Journal of Applied Physics*, vol. 33, no. 8, pp. 4562 -4656, August 1994.
10. S. T. Chung, K. Nagata, and H. Igarashi, "Piezoelectric and Dielectric Properties of $Pb(Ni_{1/3}Nb_{2/3})O_3$ -$Pb(Zn_{1/3}Nb_{2/3})O_3$ -$PbTiO_3$," *Ferroelectrics*, vol. 94, pp. 243-247, 1989.

11. S. Baumler, "The Dielectric and Piezoelectric Properties of PZN:PT:BT Ceramics," M. S. Thesis, The Pennsylvania State University, 1986.

12. T. R. Shrout, unpublished work.

13. J. Kuwata, K. Uchino, and S. Nomura, "Phase Transitions in the $Pb(Zn_{1/3}Nb_{2/3})O_3$ -$PbTiO_3$ System," *Ferroelectrics*, vol. 37, pp. 579-582, 1981.

14. J. Kuwata, K. Uchino, and S. Nomura, "Dielectric and Piezoelectric Properties of 0. 91$Pb(Zn_{1/3}Nb_{2/3})O_3$ -0. 09$PbTiO_3$ Single Crystals," *Japanese Journal of Applied Physics*, vol. 21, no. 9, pp. 1298-1302, Sept. 1982.

15. T. R. Shrout, Z. P. Chang, N. Kim, and S. Markgraf, "Dielectric Behavior of Single Crystals near the (1-x)$Pb(Mg_{1/3}Nb_{2/3})O_3$ - (x) $PbTiO_3$ Morphotropic Phase Boundary," *Ferroelectric Letters*, vol. 12, pp. 63-69, 1990.

16. Y. Yamashita and S. Shimanuki, "Synthesis of Lead Scandium Niobate - Lead Titanate Pseudo Binary Single Crystals," Materials Research Bulletin, in press.

17. J. M. Herbert, *Ferroelectric Transducers and Sensors*, London and New York: Gordon and Breach Science Publishers, 1982.

18. T. R. Shrout and J. Fielding, Jr. , "Relaxor Ferroelectric Materials," *in Proceedings of the 1990 IEEE Ultrasonics Symposium*, 1990, pp. 711-715.

19. C. A. Randall, A. S. Bhalla, T. R. Shrout, and L. E. Cross, "Classification and Consequences of Complex Lead Perovskite Ferroelectrics with regard to B-site Cation Order," *Journal of Materials Research*, vol. 5, no. 4, pp. 829-834, 1990.

20. M. L. Mulvihill, S. -E. Park, G. Risch, Z. Li, K. Uchino, T. R. Shrout, "The Role of Processing Variables in the Flux Growth of Lead Zinc Niobate-Lead Titanate Relaxor Ferroelectric Single Crystals," *Japanese Journal of Applied Physics*, vol. 35, no. 7, pp. 51-57, July 1996.

21. S. -E. Park, M. L. Mulvihill, G. Risch, and T. R. Shrout, "The Effect of Growth Condition on Dielectric Properties of $Pb(Zn_{1/3}Nb_{2/3})O_3$ Crystal," *Japanese Journal of Applied Physics*, Pt. 1, vol. 36, no. 3, March 1997.

22. R. Krimholtz, D. A. Leedom, and D. L. Matthaei, "New Equivalent Circuits for Elementary Piezoelectric Transducers," *Electr. Let.* ,vol. 6, pp 398-399, July 1971.

23. M. J. Zipparo, K. K. Shung, T. R. Shrout, "High Frequency Properties of Fine Grain PZT," *Proc. IEEE Ultrasonic Symposium*, vol. 1, pp. 601-604, November, 1995.

24. C. S. Desilets, J. D. Fraser, and G. S. Kino, "The Design of Efficient Broad-Band Piezoelectric Transducers," *IEEE Trans. on Sonics and Ultrasonics.* , vol. 25, no. 3, pp 115-25, May 1978.

APPENDIX 24

Pb(Zn$_{1/3}$Nb$_{2/3}$)O$_3$ / PbTiO$_3$ Single Crystal Piezoelectrics for Ultrasonic Transducers

Patrick D. Lopath[1], Seung-Eek Park[2], K. Kirk Shung[1] and T.R. Shrout[2]
The Whitaker Center for Medical Ultrasonic Transducer Engineering

[1]Bioengineering Department
[2]Materials Research Laboratory
The Pennsylvania State University
University Park, Pennsylvania 16802

ABSTRACT

The Pb(Zn$_{1/3}$Nb$_{2/3}$)O$_3$ (PZN) / PbTiO$_3$ (PT) solid solution has been grown in single crystal form. The dielectric and piezoelectric properties have been determined over a wide range of compositions. Longitudinal coupling constants in this system can be maintained at near 90% for a wide range of relative permittivities, allowing a 'designer dielectric' approach to ultrasonic transducer design. The piezoelectric transducer model developed by Kimholtz, Leedom and Matthaei (KLM) was employed to first optimize transducer design points, and then to study the behavior of these materials as operational transducers. Two types of transducers were modeled and contrasted to conventional materials: a 50 MHz single element designed for ultrasound backscatter microscopy and a 5 MHz phased array element. These two transducer designs are representative of the wide range of properties available in this system by carefully choosing a composition. Extremely high piezoelectric coupling coefficients (k_{33} > 94%) and a range of dielectric constants (3000-5000) have been observed in these systems on the rhombohedral side of the morphotropic phase boundary (MPB). Relatively low dielectric constants (~1000) and high thickness mode coupling (kt > 63%) were observed as typical of tetragonal formulations. A prototype single element transducer at 35 MHz was fabricated from PZN / 8% PT and compared, in pulse / echo mode, to a PZT-5H transducer similar design.

Keywords: ultrasonic transducers, single crystals, Pb(Zn$_{1/3}$Nb$_{2/3}$)O$_3$ / PbTiO$_3$ (PT)

1. INTRODUCTION

Modern ultrasound diagnostics require an ever broadening range of transducer designs to cover the complete spectrum of non or minimally invasive imaging. Current technology spans from the low frequency end between 2.5 and 10 MHz for transthoracic imaging, to around 100 MHz[1] for ultrasound backscatter microscopy. With this broad frequency range come demands on the transducer engineer to develop materials that will provide optimum properties for a specific application. Currently, many types of piezoelectrics are available for such applications. ranging from polycrystalline ceramics to piezo-polymers. Each material has its advantages as well its drawbacks in terms of the material properties offered to the designers.

In this work, a transducer material system is introduced which will avail many desirable properties over the standard frequency range. The lead zinc niobate / lead titanate, Pb(Zn$_{1/3}$Nb$_{2/3}$)O$_3$ / PbTiO$_3$ (PZN / PT), single crystal system displays properties which vary both crystallographically and compositionally over the range investigated[2] (from 4% PT to 12% PT). These variations can be exploited to meet the demands of vastly different types of transducers. Single crystal forms offer several other advantages over polycrystalline ceramics; high frequency transducers can be constructed free from the grain size effects which can plague high frequency ceramic transducers and crystallographic orientation can be exploited in dicing of arrays to move undesired modes out of the pass-band.

In order to explore the desirable material properties for various transducer designs, an extensive simulation routine was undertaken utilizing the KLM transmission line model[3]. Material parameters such as the coupling coefficients and clamped relative permittivities were varied over the range available in current single crystalline materials, while transducer responses such as sensitivity and bandwidth were evaluated. Compositional selection within the PZN / PT system was based on the optimum available points derived from these simulations.

Two transducer designs were selected to illustrate the advantages of the PZN / PT system representing the extremes of medical ultrasonic imaging: a 5 MHz phased array and a 50 MHz single element transducer. Typical 5 MHz phased array elements are very small (<100 μ wide), and thus have a low capacitance presenting a large impedance (>150 Ω) to the electronics. The high frequency single element transducers have the opposite problem, presenting a very low impedance (<50 Ω). These problems were addressed in simulation for the 5 MHz phased array case by using PZN / 4.5% PT which has a longitudinal coupling constant (k_{33}) of 92% and a relative clamped dielectric permittivity (ε_r^S) of 775. For the high frequency transducer, PZN / 12% PT was chosen with a 62% thickness mode coupling constant (k_t) and a clamped dielectric permittivity of 128. Both these designs are compared, in pulse echo simulation, to standard polycrystalline ceramics currently used for such designs.

To explore operational transducer designs and fabrication demands, a 35 MHz single element transducer from PZN / 8% PT was constructed. While this choice of material is not necessarily optimum for the type of transducer displayed, material selection was based on current availability, thus the potential pitfalls of single crystal transducer design could be explored. Additional advantages of the single crystalline form in regard to fabrication will be discussed.

2. MATERIAL PROPERTIES SIMULATION

At the heart of an ultrasonic transducer is the piezoelectric material. In the past, much transducer design was done from an acoustic engineering standpoint of applying existing piezoelectric materials to a specific design need, and living with that material's shortcomings. Recently, we have been looking at the problem of ultrasonic transducer design from a materials science standpoint, where, given a particular need, we try to design the piezoelectric material itself to solve the problem. Careful consideration of the material properties needed for a specific application will lead to a more effective transducer. To aid us in our material properties evaluation, we investigated the effect of varying both the coupling constant and the permittivity at differing acoustic impedances. Because k_{33} and ε_{33} are related by the following equation[4],

$$k_{33} = \frac{d_{33}}{\sqrt{s_{33}^E \varepsilon_{33}^T}} \tag{1}$$

our manipulation of these parameters allows $d_{33} / \sqrt{s_{33}^E}$ to float. We chose to vary k_{33} and ε_{33} because these two properties are probably the most commonly quoted with respect to a material suitable to medical transducers, and within the PZN/PT system, k_{33} can be held at elevated levels while ε_{33} is very easily manipulated with composition.

2.1 High frequency transducers
For our simulation of transducer response, we chose the KLM transmission line model T matrix approach implemented in MathCad[5]. Our first objective was to isolate crystal compositions which look promising for future development. Varying the chosen parameters systematically and plotting the results is processor time intensive, however the results from our model have, in the past, been shown to match up very well with experimental transducers[5].
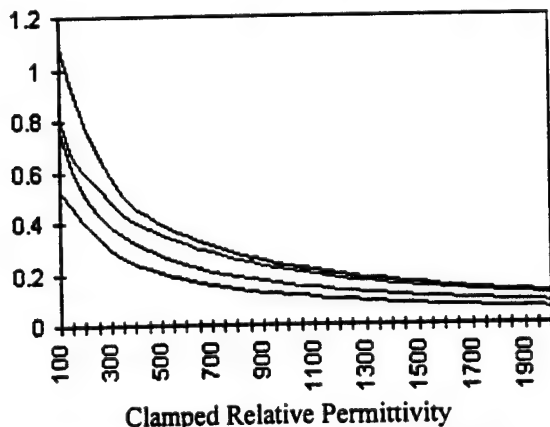

Fig. 1. Transducer sensitivity vs. relative permittivity and coupling constant for a 2 mm diameter 50 MHz transducer.
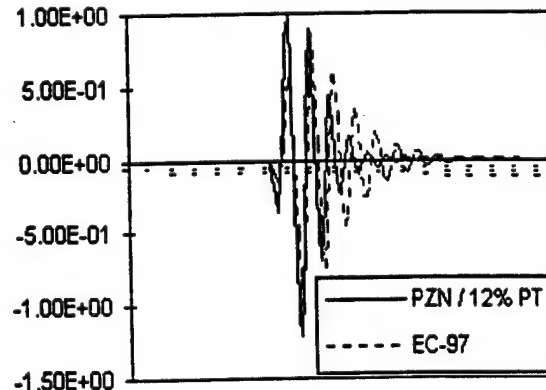

Fig. 2. Pulse / echo response comparison between PZN / 12% PT at 50 MHz and a commercial lead titanate

Figure 1 demonstrates graphically that transducers must be matched to their driving electronics. As the clamped permittivity of the active material is decreased in these high frequency transducers, the received voltage increases for a given excitation. This results from a better match to the 50 Ω driving electronics. Obviously, the sensitivity of the transducer also increases as the k_t increases. We can see the need to choose a material with as high a coupling constant as possible and a low relative permittivity. With conventional ceramics, a low dielectric constant is usually achieved with a lead titanate ceramic. Using measured values for a commercial PT material (EC-97, Edo Corporation, Salt Lake City, UT) and a single crystal of PZN / 12 % PT, the KLM simulation yields the time domain plot in Fig.2. for a set of lightly backed 50 MHz resonators One can immediately see the increased sensitivity and bandwidth due to the higher k_t of the PZN/PT (0.62 vs. 0.47) and the lower relative dielectric constant (128 vs. 200).

2.2. Array transducers

The use of low dielectric constant materials is a must for large area high frequency transducers, but the tiny elements of modern phased array imaging systems require materials with much higher dielectric constants in order to match into the 50 Ω electronics. The example of a 5MHz phased array is illustrative. In order to avoid grating lobes in the steered acoustic pattern of a 5MHz array, the elements of the sampled aperture must be placed no more than λ/2 apart, or 150 μm on center. Now, if this transducer has broad bandwidth (as is the goal), it will have significant energy carried in frequency components above 5MHz, which means that the elements should be placed even closer than 150 μm to avoid grating lobes at these frequencies. Assuming we space the elements 120 μm apart and dice a 20 μm kerf between elements, our array elements are 100 μm wide. Each element may be 5-10 mm long, leaving a very small capacitor, as capacitance varies with the following equation,

$$C = \frac{A\varepsilon_r\varepsilon_o}{t} \tag{2}$$

where C is capacitance, A is the area of the dielectric material, ε_r is the relative permittivity, ε_o is the permittivity of free space, and t is the thickness of the dielectric. Since impedance varies inversely with C, array elements tend to be very high impedance devices to drive with 50 Ω electronics. This problem is currently tackled by the use of high permittivity, soft PZTs such as 5H. The PZN/PT system aids the transducer engineer designing for 50 Ω electronics in two ways. First, the relative clamped dielectric constants are near those of soft PZTs (775 for PZN/4.5% PT vs 1100 for PZT-5H) and second, the extremely high coupling constants combined with a slow longitudinal sound velocity (2790 mm/μm vs. 4520 mm/μs for PZT-5H) mandate that the active material in a transducer be thinner than a material with a lower coupling constant and a higher sound velocity. The thinner material and relatively high clamped dielectric constant correlate to an overall higher capacitance element than PZT.
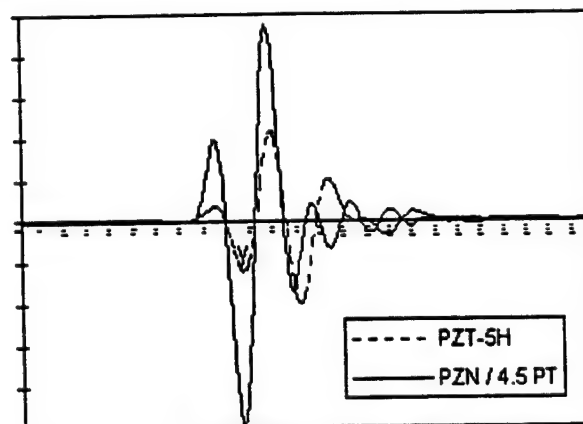
5MHz Phased Array Element Pulse / Echo

Fig. 3. Pulse / Echo of a 5MHz phased array element. Each element is moderately backed and a two layer maximally flat response matching scheme[6] is simulated. Note not only the increased signal amplitude afford by the PZN 4.5 % PT element, but also its shorter pulse ringdown time which corresponds to better axial resolution.

Figure 3 displays theoretically predicted responses of two different types of elements. The first simulation uses the industry standard PZT-5H parameters and the second uses measured values from PZN 4.5% PT. The increased signal amplitude arises from a number of sources. Most obviously, the bar mode coupling of this composition is approximately 87%, vs. 69% for the PZT 5H. Also, as mentioned earlier, the higher capacitance of the 4.5% PT element leads to an impedance which is less than half of that of the PZT element. Also, the single crystal material has a much lower acoustic impedance than the PZT due to the much slower longitudinal wave velocity. This provides an easier match to the simulated water load via the quarter wave transformers.

3. TRANSDUCER FABRICATION

In our previous work (Lopath, Park et. al)[2] we investigated the mechanical properties of some of these single crystal materials in regard to operational transducers. Most notably, we tediously optimized the poling and dicing procedures necessary to construct operational transducers. It was found that not only does the poling direction play a major role[7] in the measured properties. but, for an array geometry element, the surface dicing orientation with respect to the crystallographic axes can have a significant influence on modal interference. For this work we concentrated on easier to fabricate single element transducers. While the simulation results pointed our high frequency single element endeavors toward the 12% tetragonal crystals, current crystal availability forced us to design and fabricate a 35 MHz element from PZN 8% PT. As is characteristic of the rhomohedral side of the MPB in this system, 8% PT crystals display k_t only comparable to PZT; however the lower relative dielectric constant allows for a fairly well matched transducer at 2 mm in diameter.

Fabrication begins as the crystal is sliced parallel to the (001) plane and then lapped to the desired thickness. The pieces are then sputter coated with gold and backed with conductive epoxy. Following Lookwood et al.[8], the samples are turned at high speed in a lathe to the proper diameter and mounted in a SMA connector for evaluation. Gold is then sputtered onto the front face as a ground electrode and the piece is poled at 20 kV/cm for 10 minutes. Care must be taken to pole the ceramic using the same polarity field as the driving pulser, as the high voltage broadband spike can depole thin transducers if fabricated improperly. As a final step, a quarter wave transform can be applied with a parylene deposition system (Specialty Coating Systems. Indianapolis, In). Some compositions in this system must be poled before they are backed, as the unusually high strain levels (1.5% in the poling field, or orthogonal to it) can be damaging.
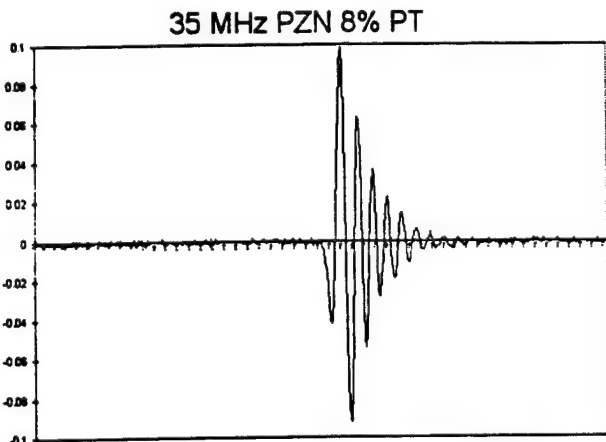

Fig 4. 35 MHz PZN 8% PT transducer pulse / echo response, unmatched into a water load. Target distance 11.7 mm.
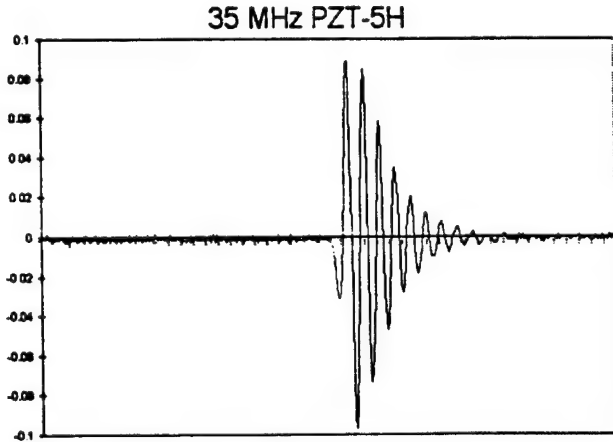
Fig. 5. 35 MHz PZT-5H transducer pulse / echo response, unmatched into a water load. Target distance 11.7 mm.

The pulses above were generated and received by 2 mm diameter single element transducers. On the left (fig. 4), is the pulse / echo from a 57% 6 dB bandwidth PZN 8% PT element operating at 35 MHz. Figure 5 is a comparable PZT-5H single element at 35 MHz. The bandwidth for the PZT is only 32%. Both responses could be improved by the addition of a quarter wave transformer matching layer, which is usually accomplished in our laboratory for high frequency samples by the application of an appropriate thickness paralene layer. The transducers were excited with a broadband pulse from a Panametrics 5900PR.

4. CONCLUSION

We have demonstrated in simulation that the PZN / PT single crystal system offers a wide variety of advantages to the ultrasonic transducer engineer. The variability in the clamped relative permittivity from 775 to 128, over the compositional range from 4.5% to 12% PT allows the fabrication of the entire spectrum of medical ultrasound devices. Other advantages of this family of piezoelectric materials include a lower acoustic impedance than most conventional materials, and, of course, high coupling constants. approaching 95% for some k_{33} samples. In the low frequency regime, the crystallographic direction can be exploited to assist properties of diced arrays while high frequency transducers are aided by a lack of grain size effects. From a fabrication standpoint, these materials have different requirements than ceramic transducers, in fact, transducer fabrication can be more time consuming. However we believe that potential rewards of a device using single crystal transducers may out weigh any difficulties in processing.

REFERENCES

[1] F. Stuart Foster. et al., "Principles and Applications of Ultrasound Backscatter Microscopy," *IEEE Trans. on Ultrasonic. Ferroelectrics and Frequency Control*, vol. 40, no. 5, pp. 608-616, September, 1993.

[2] P.D.Lopath, Seung-Eek Park, K. K. Shung, T. R. Shrout, "Ultrasonic Transducers Using Single Crystal Perovskites," to be published in *Proc. ISAF*, August, 1996.

[3] R. Krimholtz, D. A. Leedom, and D. L. Matthaei, "New Equivalent Circuits for Elementary Piezoelectric Transducers, *Electr. Let.*,vol. 6, pp 398-399, July 1971.

[4] Bernard Jaffe. William R. Cook, Jr., and Hans Jaffe, Piezoelectric Ceramics, R.A.N. Publishers (1971).

[5] M.J. Zipparo. K. K. Shung, T. R. Shrout, "High Frequency Properties of Fine Grain PZT," *Proc. IEEE Ultrasonic Symposium.* vol. 1, pp. 601-604, November, 1995.

[6] C. S. Desilets. J. D. Fraser, and G. S. Kino, "The Design of Efficient Broad-Band Piezoelectric Transducers," *IEEE Trans. on Sonics and Ultrasonics.*, vol. 25, no. 3, pp 115-25, May 1978.

[7] Seung-Eek Park, Thomas R. Shrout, "Characteristics of Relaxor-Based Piezoelectric Materials for Ultrasonic Transducers," in press *IEEE Trans. on Ultrasonics, Ferroelectric and Frequency Control Special Issue on Ultrasonic Transducers*, 1996.

[8] G.R.Lockwood, D.H. Turnbull. and F.S. Foster, "Fabrication of High-Frequency Spherically Shaped Ceramic Transducers", *IEEE Trans. Ultrason., Ferroelect., Freq. Contr.*, vol. 41, no 2, pp.231-235, March 1994.

[9] Jun Kuwata. Kenji Uchino, and Shoichiro Nomura, "Phase Transitions in the $Pb(Zn_{1/3}Nb_{2/3})O_3$-$PbTiO_3$ System". *Ferroelectrics*, vol. 37, pp. 579-582, 1981.

[10] Jun Kuwata. Kenji Uchino, and Shoichiro Nomura, "Dielectric and Piezoelectric Properties of $0.91Pb(Zn_{1/3}Nb_{2/3})O_3$ - 0.09PbTiO3 Single Crystals," *Japanese Journal of Applied Physics*, vol. 21, no. 9, pp. 1298-1302, September, 1982.

[11] U.S. Patent Number 5402791, "Piezoelectric Single Crystal, Ultrasonic Probe, and Array-Type Ultrasonic Probe" Toshiba. April, 1995.

[12] Shoichiro Nomura, Takashi Takahashi, Yuji Yokomizo, "Ferroelectric Properties in the System $Pb(Zn_{1/3}Nb_{2/3})O_3$-$PbTiO_3$." *J. Phys. Soc. Japan*, vol. 27, pp. 262, 1969.

[13] T. R. Shrout, J. Fielding, "Relaxor Ferroelectric Materials", *Proc. IEEE Ultrasonics Symposium* ,1990.

[14] K. K. Shung, "General Engineering Principles In Diagnostic Ultrasound," *IEEE Eng. Med. Biol. Magazine*, pp 7-13, Dec 1987.

[15] W. A. Smith, "Piezocomposite Materials for Acoustical Imaging Transducers", *Proc. International Symposium on Acoustical Imaging*, 1994.

APPENDIX 25

RELAXOR BASED FERROELECTRIC SINGLE CRYSTALS FOR ELECTRO-MECHANICAL ACTUATORS

Seung-Eek Park and Thomas R. Shrout
Materials Research Laboratory
The Pennsylvania State University
University Park, PA 16802

ABSTRACT

The piezoelectric properties of relaxor based ferroelectric single crystals, such as $Pb(Zn_{1/3}Nb_{2/3})O_3$ - $PbTiO_3$ (PZN-PT) and $Pb(Mg_{1/3}Nb_{2/3})O_3$ - $PbTiO_3$ (PMN-PT) were investigated for electromechanical actuators. In contrast to polycrystalline materials such as $Pb(Zr,Ti)O_3$ (PZT's), morphotropic phase boundary (MPB) compositions were not essential for high piezoelectric strain. Piezoelectric coefficients (d_{33}'s) > 2200 pC/N and subsequent strain levels up to >0.5% with minimal hysteresis were observed. Crystallographically, high strains are achieved for <001> oriented rhombohedral crystals, though <111> is the polar direction. Ultrahigh strain levels up to 1.7%, an order of magnitude larger than those available from conventional piezoelectric and electrostrictive ceramics could be achieved, possibly being related to an E-field induced phase transformation. High electromechanical coupling (k_{33}) > 90% and low dielectric loss <1%, along with large strain make these crystals promising candidates for high performance solid state actuators.

Keywords : Relaxor ferroelectrics, single crystal, actuator, piezoelectrics, hysteresis.

INTRODUCTION

Electromechanical actuators directly transform input electrical energy into mechanical energy. Of the many types of actuator materials including, magnetostrictive, photostrictive, and shape memory alloys, piezoelectric and electrostrictive ceramics are widely used in applications requiring high generative force, high frequency operation, accurate displacement, quick response time, or small device size [1]. Generally, among the material properties determining actuator performance, the electric field (E-field) induced strain is the most important parameter for actuators. This is demonstrated by strain energy density which is a measure of the energy per unit mass an actuator can deliver,

$$e_{max} = 1/\rho \cdot 1/4 \cdot (1/2 \cdot E(s_{max})^2) \qquad (1)$$

where e_{max} is the strain energy density, E is the actuator's elastic modulus, s_{max} is the maximum field induced strain, and ρ is the actuator's density. [1] 1/4 is the appropriate factor for an actuator impedance related to its surroundings. In designing an actuator, the maximum strain energy density should be as high as possible. In electroactive ceramics, density and elastic modulus vary little from material to material, therefore, the level of strain and maximum strain achievable with a reasonable electric field (<50kV/cm) dominates the energy density. The piezoelectric coefficient

(d_{ij}), determining the level of induced strain at a given electric field, is the most widely used parameter describing actuator performance. Currently, $Pb(Zr,Ti)O_3$ (PZT) polycrystalline ceramics are used with piezoelectric coefficients (d_{33}) ranging from 200 to 750 pC/N, the later limited by hysteresis. Electrostrictive ceramics such as $Pb(Mg_{1/3}Nb_{2/3})O_3$ offer effective d_{33}'s > 700pC/N, but only over a narrow range of E-field.

It is the objective of this paper to report ultrahigh piezoelectric coefficients (d_{33}) and remarkably high strain levels with low hysteresis observed for single crystals of $Pb(Zn_{1/3}Nb_{2/3})O_3$ - $PbTiO_3$ (PZN-PT) and $Pb(Mg_{1/3}Nb_{2/3})O_3$ - $PbTiO_3$ (PMN-PT). Strain behavior as a function of E-field will be discussed with respect to crystal structure, orientation, and anticipated actuator performance.

MORPHOTROPIC PHASE BOUNDARY CERAMICS

$Pb(Zr_{1-x},Ti_x)O_3$ (PZT) ceramics have been the mainstay for high performance actuator applications. Compositionally, PZT ceramics lie near the morphotropic phase boundary (MPB) between the tetragonal and rhombohedral phases as shown in figure 1. MPB compositions exhibit anomalously high dielectric and piezoelectric properties as a result of enhanced polarizability arising from the coupling between two equivalent energy states, i.e. the tetragonal and rhombohedral phases, allowing optimum domain reorientation during the poling process. Alternate MPB systems can be found in Relaxor-$PbTiO_3$, also as shown in figure 1. Lead based relaxor materials are complex perovskites with the general formula $Pb(B_1B_2)O_3$, ($B_1=Mg^{2+}$, Zn^{2+}, Ni^{2+}, Sc^{3+} ..., $B_2=Nb^{5+}$, Ta^{5+}, W^{6+} ...). Characteristic of relaxors is a broad and frequency dispersive dielectric maxima [2].
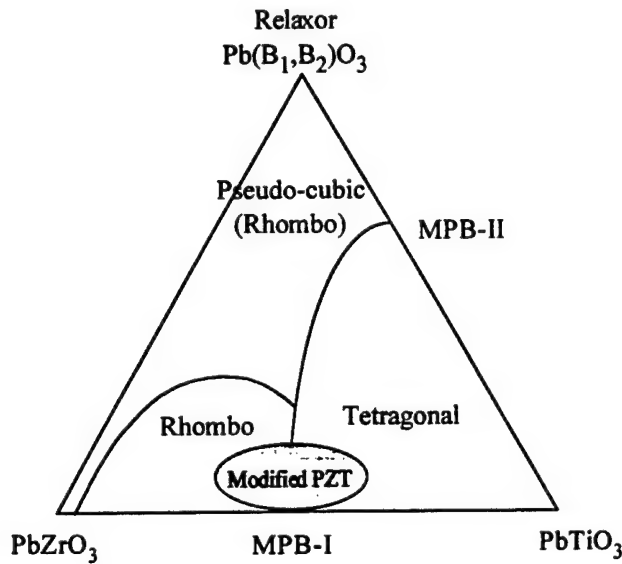

Figure 1 Ternary diagram depicting MPBs in PZT and Relaxor-PT systems for piezoelectric ceramics.

To achieve a high piezoelectric coefficient, MPB-based ceramics are further engineered by compositionaly adjusting the Curie temperature (T_c) downward relative to room temperature. The effect of transition temperature (T_c) on the piezoelectric properties is clearly evident in figure 2. As shown, the room temperature values of d_{33} are plotted as a function of T_c for a variety of modified PZT ceramics, including Relaxor-PT systems. Enhanced piezoelectric activity of MPB-based ceramics is achieved by compositionaly adjusting Tc downward relative to room temperature resulting in 'soft' piezoelectric ceramics. This enhanced piezoelectric effect, therefore, comes with the expense of more temperature dependent properties, and less polarization stability, i.e. aging and loss of piezoelectric activity. Further details on the relationship between dielectric/piezoelectric properties and Curie temperature (Tc) of piezoelectric ceramics can be found in the article by S.-E. Park et al. [3]

Most importantly, a consequence of increased piezoelectric activity for these "soft" ceramics is large hysteresis in the strain vs. E-field behavior as a result of domain motion. Strain vs. E-field behavior for PZT-5H (Navy type -VI) is shown in figure 3 as an example. Though the piezoelectric coefficient (d_{33}) of PZT-5H ceramics is in the range of ~600 to 700 pC/N [4] (implying ~0.06 to 0.07% strain at 10 kV/cm), strain as high as 0.1% can be observed at 10kV/cm. This enhanced nonlinear strain is the result of domain motion, and therefore, accompanied by significant hysteresis, resulting in poor positioning accuracy. Area within the strain vs. E-field curve or dielectric loss results in significant heat generation during operation. Heat generation combined with a decreased temperature usage range, results in poor temperature stability and limits these ceramics to low frequency applications.
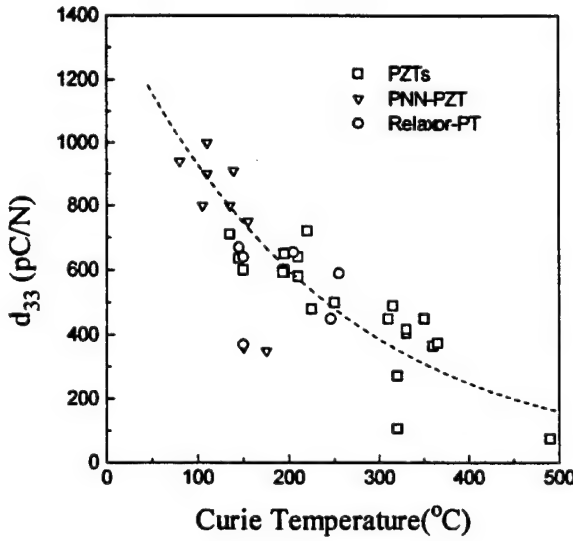

Figure 2 Piezoelectric coefficient d_{33} as a function of transition temperature (Tc) for piezoelectric ceramics, including PZT, modified PZTs, and Relaxor-PT systems.
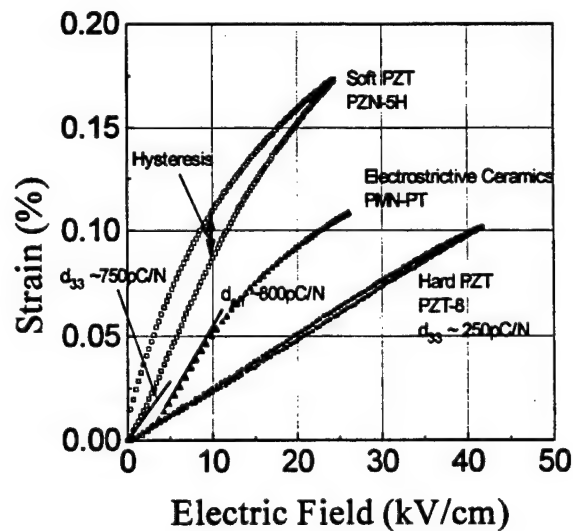
Figure 3. Strain vs. E-field behaviors for various electromechanical ceramics

Strain vs. E-field hysteresis can be minimized with the use of the "hard" piezoelectric ceramics. Hard piezoelectric ceramics such as PZT-8 (Navy type III) offer very low hysteresis as shown in figure 3. However, the reduction in hysteresis and loss comes at the expense of d_{33} and subsequent strain level. Typically d_{33} values, for 'hard' PZTs range from ~200 to 300 pC/N [4].

Another category of ceramic materials used in commercial actuators are electrostrictors. Electrostrictive strain is proportional to the square of polarization. A few materials such as PMN and its solid solution with PT exhibit significant electrostrictive strain (> 0.1%) with virtually no hysteresis as shown in figure 3. Effective d_{33} 's > ~800 pC/N calculated directly from the strain vs. E-field curve can be achieved, but only over a very narrow range of E-field. For hard piezoelectric and electrostrictive ceramics, strain level with low hysteresis does not exceed 0.15%. This limitation originates from the material's dielectric breakdown strength and polarization saturation.

In summary, piezoelectric and electrostrictive ceramics offer strain levels up to ~ 0.15%. Soft PZT's, exhibiting piezoelectric coefficients (d_{33}) as high as 750 pC/N, are inherently limited due to hysteresis caused by domain motion. Hysteresis can be minimized with the use of hard piezoelectric ceramics, but d_{33} values of only ~200 - 300 pC/N are available. Even though electrostrictive ceramics offer effective d_{33} 's~ 800 pC/N, maximum strain level is limited by its dielectric breakdown strength and polarization saturation. To achieve E-field induced strain levels > 0.15%, electroactive materials should possess high piezoelectric coefficients (d_{33} >1000pC/N) and high dielectric breakdown strength.

SINGLE CRYSTAL PIEZOELECTRICS

Single crystal piezoelectrics such as quartz (SiO_2), lithium niobate ($LiNbO_3$), and the analogue lithium tantalate ($LiTaO_3$) are widely employed in specific applications that include oscillators, surface acoustic wave (SAW) devices, and in optics. In contrast to PZT ceramics, however, these single crystals offer inferior piezoelectric properties, with d_{33} 's< 50 pC/N.

Attempts to grow single crystals of MPB PZTs have been made by numerous researchers, resulting in crystallites too small to allow adequate property measurements [5,6,7,8,9]. In contrast to PZT crystal growth, relaxor-PT materials can be readily grown in single crystal form. This key distinction was first realized by Nomura and co-workers for the PZN and PZN-PT systems [10,11] and later by Shrout for the PMN-PT [12]. In general, most $Pb(B_1,B_2)O_3$-PT crystals can be grown by high temperature solution growth using Pb-based fluxes.[13,14]

Piezoelectric coefficients as high as ~ 1500 pC/N have been reported [11,12] for MPB Relaxor-PT crystals. However, it should be noted that piezoelectric coefficients are generally determined using low field (< 0.1kV/cm) techniques such as the resonance method (IEEE standard) [15]. Therefore, direct observation of the strain vs. E-field behavior is essential in order to investigate hysteresis and maximum levels of strain, key experiments to directly confirm actuator performance. In relation to actuators, several questions arise, 1) How do the high d_{33} values determined using low field techniques correlate to direct measurements? As for piezoelectric and electrostrictive ceramics, will the strain level saturate with increased E-field? 2) How much hysteresis accompanies the strain?, 3) Is morphotrophy essential for enhanced piezoelectric properties?, 4) Are there optimum crystallographic cuts as in the case of the other piezoelectric crystals? In the following sections, we will attempt to answer many of these questions, reporting piezoelectric properties and direct observation of strain behavior as a function of crystallographic orientation and electric field for Relaxor-PT single crystals.

DIELECTRIC AND PIEZOELECTRIC PROPERTIES
OF RELAXOR BASED SINGLE CRYSTALS

In this section, the dielectric and piezoelectric properties of Relaxor-PT systems as a function of crystal composition and orientation are summarized. Commonalties inherent to Relaxor-PT systems have been discussed in reviews by Shrout [16] and Randall [17]. Based on these commonalties, our research was limited to two representative systems, PZN-PT and PMN-PT. Though PMN-PT MPB crystals exhibit piezoelectric properties comparable with PZN-PT, more focus was given to the PZN system owing to its relatively lower PT content for MPB, allowing more uniform crystal growth of these solid solution materials. Experimental procedures are briefly summarized including crystal growth, crystal alignment, dielectric and piezoelectric measurements using direct observation of strain as a function of electric field as well as low field property measurements using the IEEE resonance technique. [15]

CRYSTAL GROWTH, SAMPLE PREPARATION AND PROPERTY MEASUREMENTS

High purity (>99.9%) powders of Pb_3O_4, ZnO, $MgCO_3$, Nb_2O_5 and TiO_2 were used as starting material. Raw powders were weighed with desired molar ratio with excess Pb_3O_4 as a flux. The powders were dry mixed for a desired period of time using a tumbling mill. The mixed powders were loaded into a Platinum crucible, which was placed in an alumina crucible sealed with an alumina lid and alumina cement to minimize PbO volatilization. The crucible and powder were placed in a tube furnace and held at soak temperatures (1100 to 1200°C), followed by slow cooling (1 to 5°C/hr). The crucible was then furnace-cooled to room temperature. Hot HNO_3 is used to separate the crystals out of the rest of the melt. Typically crystal size ranged from 3 to 20 mm. Further details on the flux growth technique of these crystals can be found in ref. [13,14].
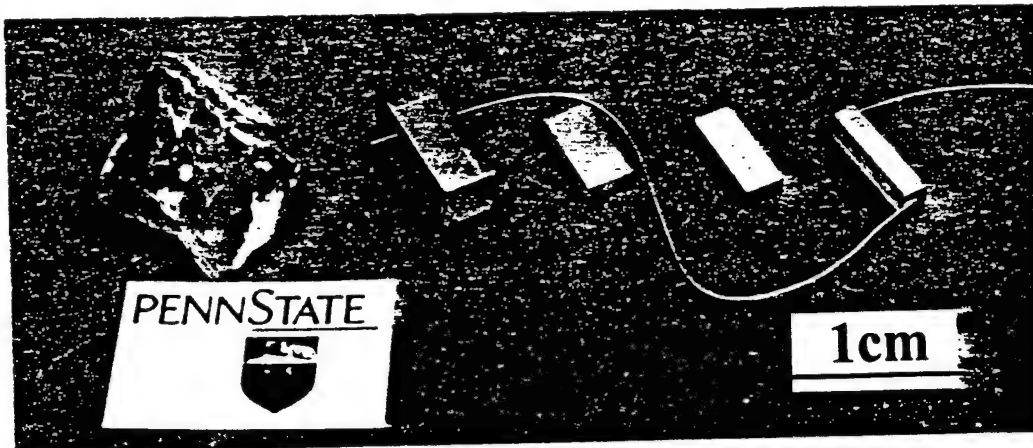

Figure 4. As grown crystal, an aligned sample using the Laue camera, a cut and polished sample, an electroded sample for direct strain observation as well as for low field planar mode resonant sample, and a low field longitudinal mode resonant sample, for PZN-9.5%PT, (from left to right).

Individual crystals were oriented along their pseudocubic <001> and the <111> axis using a Laue back reflection camera. For electrical characterization, samples were prepared by polishing with silicon carbide and alumina polishing powders to achieve flat and parallel surfaces onto which gold electrodes were sputtered. High-field measurements included polarization and strain hysteresis using a modified Sawyer-Tower circuit and linear variable differential transducer (LVDT) driven by a lock-in amplifier (Stanford Research Systems, Model SR830). Plate shape samples with thickness ranging from 0.2 mm to 0.5 mm were used. Electric fields as high as ~140 kV/cm were applied using an amplified unipolar wave form at 0.2 Hz, using a Trek 609C-6 high voltage DC amplifier. During testing the samples were submerged in Fluorinert (FC-40, 3M, St. Paul, MN), an insulating liquid, to prevent arcing. For piezoelectric coefficient(d_{33}) determination, bar shape samples with lengths ranging from 3 mm to 5 mm were tested. Samples were poled either by field cooling (10kV/cm) from temperatures above the dielectric maximum temperature (T_{max}) or by applying 40kV/cm at room temperature. Figure 4 presents, from left to right, a representative of an as grown crystal, an aligned sample using the Laue camera, a cut and polished sample, an electroded sample for direct strain observation as well as for low field planar mode resonant sample, and a low field longitudinal mode resonant sample, for PZN-9.5%PT, respectively.
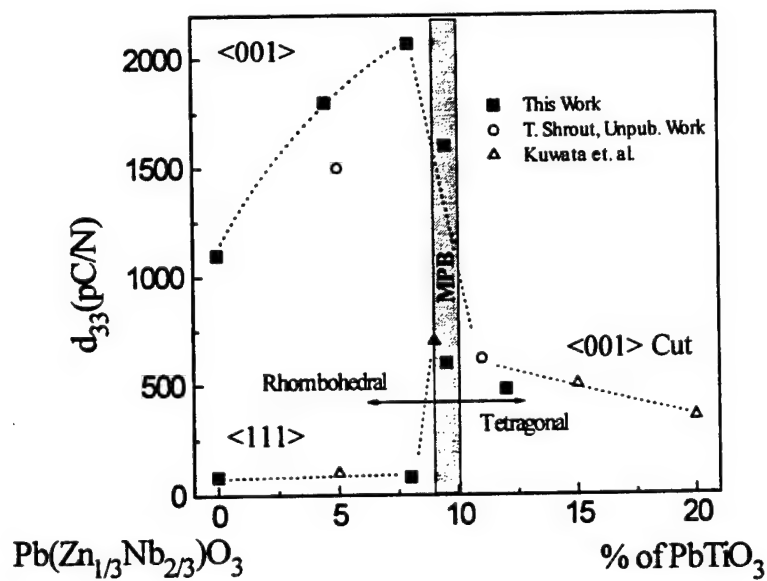

Figure 5 d_{33} as a function of composition and crystallographic orientation in crystals of PZN-PT.

LOW FIELD MEASUREMENTS

Piezoelectric coefficients as a function of composition and crystal orientation for PZN-PT, calculated based on IEEE standards, are presented in figure 5. As shown, large piezoelectric coefficients (d_{33} ~ 1600 pC/N) were found for PZN-PT with MPB compositions (9.5% PT), as previously reported by Kuwata [11]. PMN-PT crystals with MPB

compositions (PMN-35% PT) also exhibited large piezoelectric coefficients ($d_{33} \sim 1500$ pC/N).[3] It should be noted, however, that all rhombohedral crystals oriented along their psuedocubic <001> direction exhibited large piezoelectric coefficients. As shown in figure 5, d_{33} increased with increased amount of PbTiO$_3$ for <001> oriented rhombohedral crystal. Maximum d_{33} values of ~2200 pC/N were determined with domain engineered rhombohedral crystals[*]. In contrast to PZT's, d_{33} dramatically decreases at MPB to levels ~ 500pC/N for tetragonal composition. Though <111> is the polar direction in rhombohedral crystals, such cuts exhibited low piezoelectric coefficient, believed to be associated with domain instability. Further details on domain motion and crystal anisotropy are reported elsewhere. [18] Dielectric loss value < 1% and electromechanical coupling constant values (k_{33}) > 90% were reported elsewhere. [3]

STRAIN VS. E-FIELD BEHAVIORS
FOR RELAXOR BASED SINGLE CRYSTALS

Though high piezoelectric coefficients (d_{33}) were determined, high field measurements are more indicative of actuator performance. The following observations will clearly show the potential of relaxor based ferroelectric single crystals, for applications as actuators.

Strain as a function of electric field for various <001> oriented rhombohedral crystals (pure PZN, PZN-4.5%PT, PZN-8%PT, and PMN-24%PT) are presented in figure 6. Also E-field induced strains of various electromechanical ceramics such as soft PZT (PZT-5H), hard PZT (PZT-8) and electrostrictive ceramics (PMN-PT) are compared. Piezoelectric coefficients (d_{33}) directly calculated from the slope of strain vs. electric field curves confirmed the piezoelectric coefficients determined by the low field resonance method. Strains as high as 0.58% were observed with low hysteresis for these crystals, significantly larger than that for polycrystalline ceramics. The limitation of achievable strain for polycrystalline ceramics is the result of polarization saturation and subsequent saturation on strain and breakdown strength. However, as shown in figure 6, strain did not saturate with increased E-field for <001> oriented rhombohedral crystals. This remarkable strain vs. E-field behavior with low hysteresis is believed to be related to the engineered domain state. Although crystallographically <111> is the polar direction, low piezoelectric coefficients (d_{33}) < 100 pC/N were determined as shown in figure 5. This inferior piezoelectric activity was found to be related to domain instability after poling. Details on mechanisms are presented elsewhere. [18]

Saturation of E-field induced strain behavior for <001> oriented rhombohedral crystals was investigated until dielectric breakdown as presented in figure 7. Far from saturation, the strain abruptly increased with strain levels as high as 0.8% being achieved for all crystals tested. Strain levels >1.2% for the PZN-4.5%PT crystal were the result of higher breakdown voltage. The E-field induced strain behavior observed is believed to be associated with an E-field induced rhombohedral-tetragonal phase transition. This phase transition behavior is more apparent in figure 8 presenting the E-field induced strain behavior of the <001> oriented PZN-8%PT crystal. At ~120kV/cm, the induced strain along with high dielectric breakdown strength resulted in a strain level as high as 1.7%. The piezoelectric coefficient (d_{33}) ~ 480 pC/N calculated directly from the slope of strain vs. E-field in the high field region corresponded to the tetragonal phase (between 40 and 120 kV/cm in figure 8) coincides with a d_{33} value (~500 pC/N) of tetragonal PZN-12%PT crystal. Although phase transition is a likely explanation for the ultrahigh strain level, direct observation of phase transition using in-situ XRD is required.

---

[*] * Rhombohedral crystals oriented and poled along pseudocubic <001> direction. Crystallographically, polar direction of rhombohedral crystal is pseudocubic <111> direction.
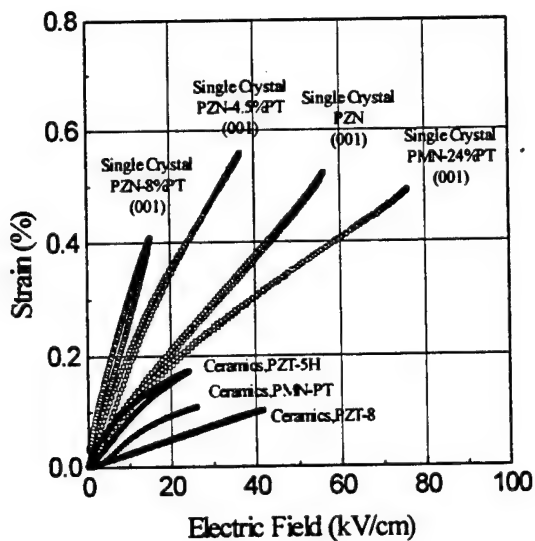
Figure 6 Strain vs. E-field behaviors for crystals of PZN-PT and PMN-PT, and for various electromechanical ceramics.
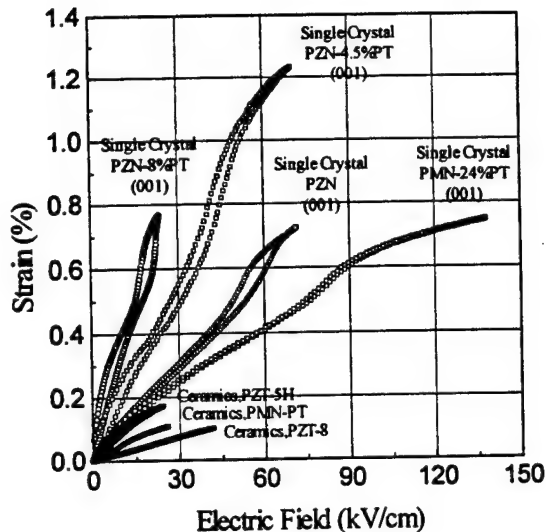

Figure 7 Strain vs. E-field behaviors for crystals of PZN-PT and PMN-PT, and for various electromechanical ceramics till breakdown.
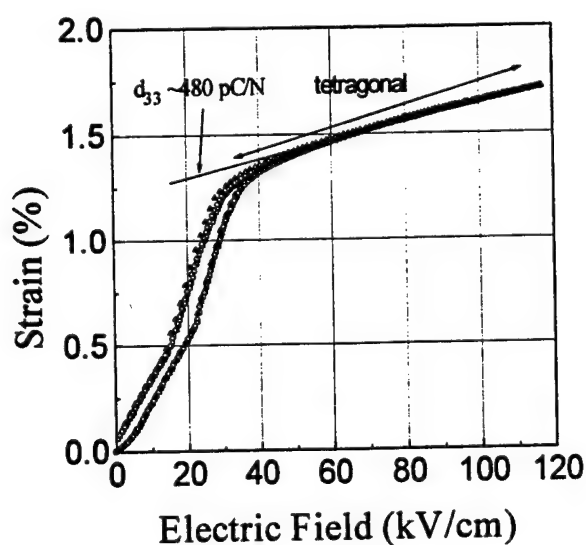

Figure 8 Strain vs. E-field behaviors for <001> oriented PZN-8%PT crystal

CONCLUSION

Pseudocubic <001> oriented relaxor based rhombohedral crystals such as (1-x) PZN-x PT (x<0.09) and (1-x) PMN-xPT (x<0.35) exhibited actuation levels not available with current piezoelectric ceramics. Ultrahigh piezoelectric coefficients (d_{33}) > ~2200 pC/N and strain levels up to 0.58% with low hysteresis were observed. Ultrahigh strain levels up to 1.7% could be achieved for relaxor based ferroelectric single crystals as a result of E-field induced rhombohedral-tetragonal phase transition. Other relaxor based rhombohedral crystals are expected to exhibit similar strain vs. E-field behavior. Textured polycrystalline ceramics is also believed to exhibit high strain behaviors. Though clearly promising candidates for high performance actuators, further investigations in crystal growth and prestress testing are required for single crystal piezoelectrics to become the next generation material of actuators.

ACKNOWLEDGMENT

REFERENCES

1. V. Giurgiutiu, Z. Chaudhry, and C. A. Rogers, "Energy-based Comparison of Solid-State Actuators," Report No. CIMSS 95-101, Virginia Polytechnic Institute and State University, Sept. 1995.
2. L. E. Cross, *Ferroelectrics*, **76**, 241 (1987)
3. S.-E. Park, T. R. Shrout, in press *IEEE Trans. UFFC Special Issue on Ultrasonic Transducers*, 1997.
4. H. Jaffe and D. A. Berlincourt, *Proc. of IEEE*, **53**, 1372 (1965).
5. S. Fushimi and T. Ikeda, *J. Amer. Ceram. Soc.*, **50**, 129 (1967).
6. V. A. Kuznetzov, *J. Cryst. Growth*, **34**, 405 (1968).
7. R. Clarke and R. W. Whatmore, *J. Cryst. Growth*, **33**, 29 (1976).
8. T. Hatanaka and H. Hasegawa, *Jap. J. Appl. Phys.*, **34**, 5446 (1995).
9. K. Yanagisawa, H. Kanai, and Y. Yamashita, *Jap. J. Appl. Phys.*, **34**, 536 (1995).
10. J. Kuwata, K. Uchino, and S. Nomura, *Ferroelectrics*, **37**, 579 (1981).
11. J. Kuwata, K. Uchino, and S. Nomura, *Jap. J. Appl. Phys.*, **21**, 1298 (1982).
12. T. R. Shrout, Z. P. Chang, N. Kim, and S. Markgraf, *Ferroelectric Lett.*, (12), **63** (1990).
13. M. L. Mulvihill, S. -E. Park, G. Risch, Z. Li, K. Uchino, T. R. Shrout, *Jap. J. Appl. Phys.*, **35**, 51 (1996).
14. S. -E. Park, M. L. Mulvihill, G. Risch, and T. R. Shrout, *Jap. J. Appl. Phys.*, **36**, (1997).
15. IEEE Standard on Piezoelectricity, American National Standards Institue, 1976.
16. T. R. Shrout and J. Fielding, Jr. , *Proc. 1990 IEEE Ultras. Sym.*, 1990,711-715.
17. C. A. Randall, A. S. Bhalla, T. R. Shrout, and L. E. Cross, *J. Mat. Res.*, **5**, 829 (1990).
18. S.-E. Park and T. R. Shrout, unpubilished work.

APPENDIX 26

Characteristics of Relaxor-Based Piezoelectric Single crystals for Ultrasonic Transducers

Seung-Eek Park and Thomas R. Shrout

Whitaker Center for Ultrasonic Imaging, The Pennsylvania State University
University Park, PA 16802

Abstract - For ultrasonic transducers, piezoelectric ceramics offer a range of dielectric constants (K~1000-5000), large piezoelectric coefficients (d_{ij}~200-700pC/N), and high electromechanical coupling ($k_T \cong 50\%$, $k_{33} \cong 75\%$). For several decades, the material of choice has been polycrystalline ceramics based on the solid solution $Pb(Zr_{1-x},Ti_x)O_3$ (PZT), compositionally engineered near the morphotropic phase boundary (MPB). The search for alternative MPB systems has led researchers to revisit relaxor-based materials with the general formula, $Pb(B_1,B_2)O_3$ (B_1:Zn^{2+}, Mg^{2+}, Sc^{3+}, Ni^{2+}..., B_2:Nb^{5+}, Ta^{5+}...). There are some claims of superior dielectric and piezoelectric performance compared to that of PZT materials. However, when the properties are examined relative to transition temperature (Tc), these differences are not significant. In the single crystal form, however, Relaxor-PT materials, represented by $Pb(Zn_{1/3}Nb_{2/3})O_3$ - $PbTiO_3$ (PZN-PT), $Pb(Mg_{1/3}Nb_{2/3})O_3$ - $PbTiO_3$ (PMN-PT) have been found to exhibit longitudinal coupling coefficients (k_{33})>90%, thickness coupling (k_T)>63%, dielectric constants ranging from 1000 to 5000 with low dielectric loss <1%, and exceptional piezoelectric coefficients d_{33}>2000pC/N, the later promising for high energy density actuators. For single crystal piezoelectrics to become the next generation material of ultrasonic transducers, further investigation in crystal growth, device fabrication and testing are required.

INTRODUCTION

Innovations in transducer design continues to be the driving force for the development of new piezoelectric materials. Electromechanical coupling (k_{ij}), dielectric constant (K) and acoustic impedance (Z) are the most important parameters which determine the performance of an ultrasonic imaging system. Material characteristics associated with the design of imaging devices have been reviewed by Gururaja [1] and Smith [2]. Piezoelectric ceramics are currently the material of choice offering relatively high coupling, a wide range of dielectric constants, and low dielectric loss. These merits translate into transducer performance in the form of relatively high sensitivity, broad bandwidth and minimal thermal heating. Two approaches have been taken to couple
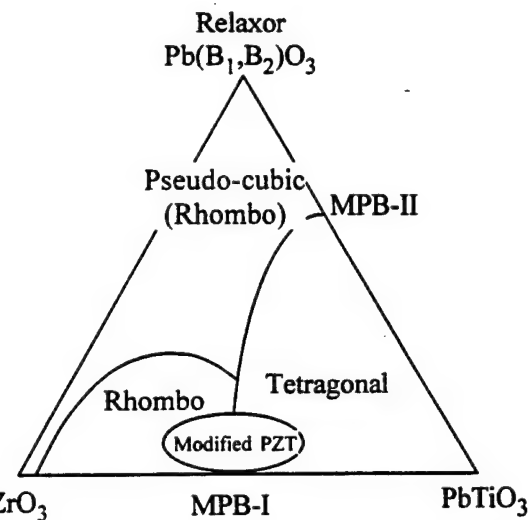

Figure 1 Ternary diagram depicting MPBs in PZT and Relaxor-PT systems for piezoelectric ceramics [27].

acoustic energy from high acoustic impedance (Z=30-36 MRayls) piezoelectric ceramics to the human body(Z=1.5 Mrayls); (1) multiple quarter wavelength matching layers and/or (2) lower impedance composite comprised of piezoelectric ceramic with a passive polymer. Although the properties can be tailored to meet various device requirements, it is the volume ratio of the piezoelectric ceramic and its inherent properties that are critical to transducer performance.

$Pb(Zr_{1-x},Ti_x)O_3$ (PZT) ceramics have been the mainstay for high performance transducer applications. Compositionally, PZT ceramics lie near the morphotropic phase boundary (MPB) between the tetragonal and rhombohedral phases, as depicted in Figure 1. MPB compositions have anomalously high dielectric and piezoelectric properties as a result of enhanced polarizability arising from the coupling between two equivalent energy states, i.e. the tetragonal and rhombohedral phases, allowing optimum domain reorientation during the poling process. Further modifications using acceptor and donar dopants give us the wide range of piezoelectric compositions we have today. An excellent review on piezoelectric ceramics including both modified and undoped PZT ceramics is

Table 1 Morphotropic Phase Boundaries in perovskite $Pb(B_1B_2)O_3$-PT systems

Binary System	PT content on MPB	T_c (T_cs of end compounds)	Ref
(1-x) $Pb(Zn_{1/3}Nb_{2/3})O_3$ - x $PbTiO_3$ (PZN-PT)	x ≅ 0.09	~180°C (140°C- 490°C)	28
(1-x) $Pb(Mg_{1/3}Nb_{2/3})O_3$ - x $PbTiO_3$ (PMN-PT)	x ≅ 0.33	~150°C (-10°C - 490°C)	29,30
(1-x) $Pb(Mg_{1/3}Ta_{2/3})O_3$ - x $PbTiO_3$ (PMT-PT)	x ≅ 0.38	~80°C (-98°C - 490°C)	8
(1-x) $Pb(Ni_{1/3}Nb_{2/3})O_3$ - x $PbTiO_3$ (PNN-PT)	x ≅ 0.40	~170°C (-120°C - 490°C)	30
(1-x) $Pb(Co_{1/3}Nb_{2/3})O_3$ - x $PbTiO_3$ (PCN-PT)	x ≅ 0.38	~250°C (-98°C - 490°C)	31
(1-x) $Pb(Sc_{1/2}Ta_{1/2})O_3$ - x $PbTiO_3$ (PSN-PT)	x ≅ 0.45	~205°C (26°C - 490°C)	32
(1-x) $Pb(Sc_{1/2}Nb_{1/2})O_3$ - x $PbTiO_3$ (PST-PT)	x ≅ 0.43	~250°C (90°C - 490°C)	33,34
(1-x) $Pb(Fe_{1/2}Nb_{1/2})O_3$ - x $PbTiO_3$ (PFN-PT)	x ≅ 0.07	~140°C (110°C - 490°C)	8
(1-x) $Pb(Yb_{1/2}Nb_{1/2})O_3$ - x $PbTiO_3$ (PYN-PT)	x ≅ 0.50	~360°C (280°C - 490°C)	8
(1-x) $Pb(In_{1/2}Nb_{1/2})O_3$ - x $PbTiO_3$ (PIN-PT)	x ≅ 0.37	~320°C (90°C - 490°C)	35
(1-x) $Pb(Mg_{1/2}W_{1/2})O_3$ - x $PbTiO_3$ (PMW-PT)	x ≅ 0.55	~60°C (39°C - 490°C)	36
(1-x) $Pb(Co_{1/2}W_{1/2})O_3$ - x $PbTiO_3$ (PCW-PT)	x ≅ 0.45	~310°C (32°C - 490°C)	37
(1-x) $PbZrO_3$ - x $PbTiO_3$ (PZT)	x ≅ 0.48	~360°C (230°C - 490°C)	3

given by Jaffe, Cook, and Jaffe [3], published in 1971.

RELAXOR-BASED PIEZOELECTRICS

The search for alternative MPB systems other than that found in PZT have led researchers to investigate relaxor-based ferroelectrics and their solid solution with $PbTiO_3$ (PT). Lead based relaxor materials, discovered by Soviet researchers [4,5] in 1950s, are complex perovskites with the general formula $Pb(B_1B_2)O_3$, ($B_1=Mg^{2+}$, Zn^{2+}, Ni^{2+}, Sc^{3+} ..., $B_2=Nb^{5+}$, Ta^{5+}, W^{6+} ...). Characteristic of relaxors is a broad and frequency dispersive dielectric maxima [6]. These relaxor materials and their solid solutions with $PbTiO_3$ have been compiled by Landolt-Börnstein [7] with numerous MPB systems reported.

Early investigations of Relaxor-PT ceramics in the 60s and 70s were plagued with inadequate process controls resulting in piezoelectric ceramics of marginal interest. With the advent of the columbite precursor method and an overall better understanding of perovskite-pyrochlore phase relationship and corresponding structure-property relationships, a renewed interest in the Relaxor-PT MPB systems came about. The wide range of Relaxor-PT MPB systems have been recently reviewed, including relevant dielectric and piezoelectric properties [8].

Several of the Relaxor-PT systems are summarized in Table 1 and schematically shown in the $PbZrO_3$–$PbTiO_3$–$Pb(B_1B_2)O_3$ ternary system in Figure 1. In contrast to the PZT system, the amount of PT associated with Relaxor-PT MPB is in general less than that for PZT varying from 7% for PFN-PT to 50 mole% for PYN-PT. In PZT, the MPB is relatively insensitive to temperature. However, in

Relaxor-PT systems, the MPB compositions are strongly temperature dependent.

In recent articles on Relaxor-PT compositions, including new MPB systems, e.g. PYN-PT [8], modified PSN-PT [9], and materials processed using hot pressing [10], there are claims of compositions with superior dielectric and piezoelectric properties compared to that of PZT ceramics. As reported in Table 2, these claims appear to be valid, with Relaxor-PT ceramics* offering relatively high dielectric constants (K_S), large piezoelectric coefficients (d_{ij}), and superior electromechanical coupling coefficients (k_{ij}). In the following section, however, it will be shown that such claims are misleading and must be analyzed with respect to the ferroelectric materials transition temperature. This temperature

Figure 2 Piezoelectric coefficient (d_{33}) as a function of transition temperature (T_c) for piezoelectric ceramics, including PZT, modified PZTs, and Relaxor-PT systems. Data were compiled from references, commercial brochures and internal investigations.

---

* The term "relaxor ferroelectric" is used herein to represent all complex perovskite $Pb(B_1B_2)O_3$ systems. In actuality, relaxor dielectric behavior only occurs for those systems which possess short range chemical ordering as classified by Randall et al. [24] In general, however, classical relaxor behavior occurs within certain compositional limits for all $Pb(B_1B_2)O_3$ -PT systems.

Table 2 Reported Dielectric and Piezoelectric Properties for selected PZT and Relaxor Binary Systems

Form	Materials	k_P	k_t*	k_{33}	d_{33} (pC/N)	K_3^i	Tc (°C)	Ref.
Ceramics (poly-crystalline)	**PZT-MPB Composition**							
	PZT 53/47	0.52		0.67	220	~800	360	36
	Modified PZTs							
	PZT-4 (Navy I)	0.58	0.51	0.70	289	1200	330	39
	PZT-8 (Navy III)	0.50	0.44	0.70	220	1000	300	39
	PZT-5 (Navy II)	0.60	0.49	0.70	400	2000	360	39
	PZT 5H (Navy VI)	0.65	0.50	0.75	590	3500	190	39
	Relaxor-PT MPB Compositions							
	0.7PMN-0.3PT	0.50			670	5000	145	29
	0.67PMN-0.33PT	0.63		0.73	690	5000	160	29
	0.60PMN-0.40PZT(40/60)	0.50			-	2370	170	40
	0.55PST-0.45PT	0.61		0.73	655		205	32
	0.575PSN-0.425PT	0.66	0.55	0.74	389	1550	260	9
	0.575PSN-0.425PT (1%Nb doped)	0.69	0.52	0.76	504	2540	248	9
	0.575PSN-0.425PT (2% Sc doped)	0.63	0.53	0.72	359	1480	260	9
	0.58PSN-0.42PT	0.71	0.56	0.77	450		260	41
	0.5PNN-0.5PZT(35/65)	0.45	-		370		150	42
	0.87PZN-0.05BT-0.08PT	0.52	0.49		640	5200	150	43
Single Crystals	95PZN-5PT			0.86	~1500	4000	160	44
	91PZN-9PT			0.92	~1500		190	18,19
	89PZN-11PT			0.92	620	1000	200	44
	70PMN-30PT				~1500	4000	150	20
	60PMN-40PT				~1500		170	20

designated by T_c, is the temperature at which the material transforms from the prototypical non-ferroelectric to ferroelectric phase being associated with a spontaneous polarization and large dielectric anomaly. The importance of this transition temperature with respect to transducer fabrication, piezoelectric activity, etc., will also be discussed.

COMPOSITIONAL ENGINEERING OF PIEZOELECTRIC CERAMICS

Among the important material parameters mentioned previously, electromechanical coupling (k_{ij}), dielectric constant (K) and associated piezoelectric coefficient (d_{ij}) are the key parameters to be compositionaly engineered. In general, the piezoelectric properties of a ferroelectric ceramic can be expressed using the simplistic term,

$$d_{ij} \sim 2Q_{ij}K\varepsilon_0 P_i \qquad (1)$$

where d_{ij} is the piezoelectric coefficient, P_i the remnant polarization on poling, K the dielectric constant, ε_0 the permittivity of free space, and Q_{ij} the electrostriction coefficient. Since both Q_{ij} and P_i exhibit little dependence on composition or temperature below T_c in ferroelectric ceramics such as PZT, the piezoelectric coefficient d_{ij} and dielectric constant K are interrelated,

i.e., a ceramic with high piezoelectric coefficient also exhibits a large dielectric constant. To achieve a high dielectric constant or piezoelectric coefficient, MPB-based ceramics are further engineered by compositionaly adjusting the Curie temperature (T_c) downward relative
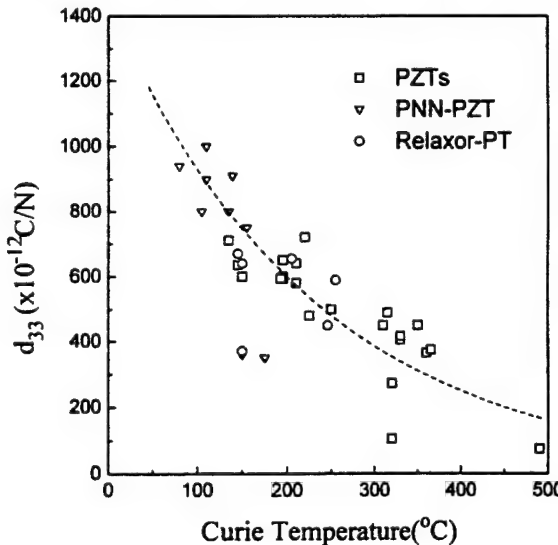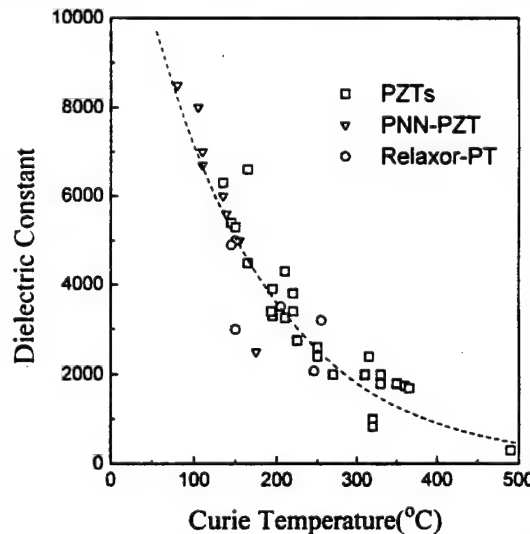

Figure 3 Dielectric Constant (K) as a function of transition temperature (T_c) for piezoelectric ceramics, including PZT, modified PZTs, and Relaxor-PT systems. Data were compiled from references, commercial brochures and internal investigations.

Figure 4 Longitudinal coupling coefficient (k_{33}) as a function of transition temperature (T_c) for piezoelectric ceramics, including PZT, modified PZTs, and Relaxor-PT systems. Data were compiled from references, commercial brochures and internal investigations.
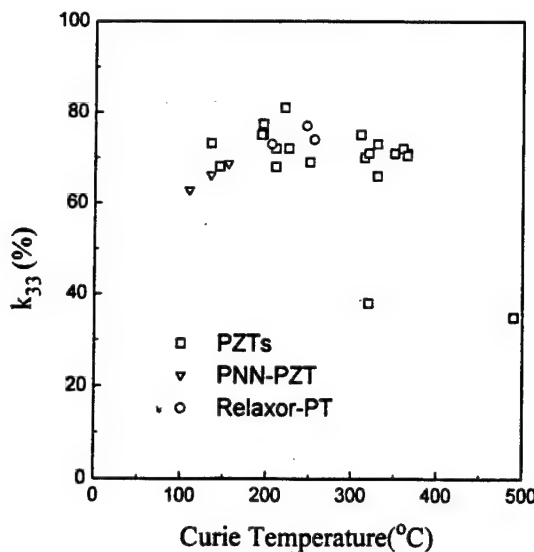
to room temperature. The effect of transition temperature (T_C) on the dielectric and piezoelectric properties is clearly evident in Figures 2 and 3. As shown, the room temperature values of both d_{ij} and K are plotted as a function of T_C for a variety of modified PZT ceramics, including Relaxor-PT systems, rather than a tabulation of properties, the methodology frequently available in company brochures, review articles, etc. To achieve both
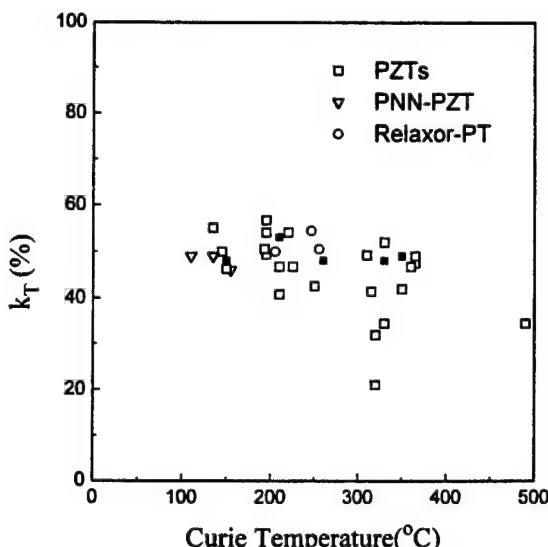

Figure 5 Thickness coupling coefficient (k_T) as a function of transition temperature (T_c) for piezoelectric ceramics, including PZT, modified PZTs, and Relaxor-PT systems. Data were compiled from references, commercial brochures and internal investigations.

high dielectric constant and corresponding piezoelectrically "soft" materials generally used in ultrasonic imaging, requires materials with relatively low T_C. However, high piezoelectric coefficients and dielectric constants with correspondingly low T_Cs come with the expense of more temperature dependent properties, and less polarization stability, i.e. aging and loss of piezoelectric activity. As a general rule of thumb, piezoelectric materials can be safely used to approximately 1/2 T_C, without significant reduction in piezoelectric activity. This can restrict the working range of the device or limit fabrication techniques. During the fabrication process of transducers, the piezoelectric material may experience excessive temperature due to cutting/dicing, polymer curing, or the attachment of acoustic matching/backing materials. Therefore, not only must the dielectric and piezoelectric properties of a transducer material be considered, but also their T_C.

Electromechanical coupling factor (k_{ij}) is often referred to as the key material parameter for transducer design because it measures the true strength of the piezoelectric interaction once the elastic and dielectric response of the medium are normalized [11,12]. In addition, high coupling factor corresponds to a broad bandwidth response, which offers better axial resolution, deeper penetration, and most importantly, a degree of engineering freedom with the potential of operating the transducer at a narrow frequency regime for enhanced sensitivity.

Electromechanical coupling factor, piezoelectric coefficient and dielectric constant are interrelated by following equation,

$$k_{ij}^2 = \frac{d_{ij}^2}{K\varepsilon_0 s_{ij}} \qquad (2)$$

where d_{ij} is the piezoelectric coefficient, K the dielectric constant, ε_0 the permittivity of free space, and s_{ij} the elastic compliance. The question arises, since both d_{ij} and K are strongly dependent on T_C, what is the dependence of coupling k_{ij}? Figure 4 presents room temperature values of k_{33} (longitudinal coupling) as a function of T_C. Important for high frequency ultrasound back scattered microscopy (UBM) and single element transducers, k_T (thickness) coupling values are given in Figure 5. As observed for both coupling coefficients, no relationship with T_c was evident. It is noted that the most widely used material in the ultrasonic imaging industry has a Tc ~ 210°C owing to the materials relatively high dielectric constant and coupling coefficient with providing good temperature stability.

In summarizing the observations presented above, the dielectric and piezoelectric properties of piezoelectric ceramics are strongly related to the transition temperature T_C. Upon direct comparison, *no one type of material*,

Table 3 Dielectric and Piezoelectric Properties of Pb(A$_{1/3}$Nb$_{2/3}$)O$_3$ -PbTiO$_3$ crystals (A=Zn, Mg) from this work.

Longitudinal mode

Crystal	Cut	Tmax (°C)	Dielectric Constant (Loss)	Coup-ling	s_{33}^D (× 10^{-12} m^2/N)	d_{33} (pC/N)	Nt (Hz m)
PZN	001	~140	3600 (0.008)	0.852	13.2	1100	1521
PZN-8%PT	001	~165	4200 (0.012)	0.938	15.5	2070	1401
PZN-9.5%PT	001	~176	1400 (0.004)	0.894	15.5	1600*	1403
PMN-30%PT	001	~150	2890 (0.014)	0.808	11.6	730	1608
PMN-35%PT	001	~160	3100 (0.014)	0.923	10.2	1240	1730

* values determined by Berlincourt d$_{33}$ meter.

Table 3 Continue.

Thickness mode

Crystal	Cut	Coupling	K_3^T	Loss	Qm	Nt (Hz m)
PZN	001	0.493	2730	0.013	40	2056
PZN- 8%PT	001	0.481	4450	0.017	39	1831
PZN- 9.5%PT	001	0.541	1550	0.024	31	1967
PZN-11%PT	001	0.638	890	0.024	17	1576
PMN-30% PT	001	0.568	4740	0.014	44	2368
PMN-35%PT	001	0.541	4540	0.031	35	2305

whether PZT-based or Relaxor-PT, offer significant advantages in overall transducer performance. *The question arises, are there opportunities for new piezoelectric materials with enhanced properties?*

To answer the question above, one must look to the single crystal form of piezoelectric materials, the topic of the following section.

SINGLE CRYSTAL PIEZOELECTRIC MATERIALS

Single crystal piezoelectrics such as quartz (SiO$_2$), lithium niobate (LiNbO$_3$), and the analogue lithium tantalate (LiTaO$_3$) are widely employed in specific applications that include oscillators, surface acoustic wave (SAW) devices, and in optics. In contrast to PZT ceramics, these single crystals offer inferior dielectric and piezoelectric properties. However, the single crystal form of high performance PZTs has been the research interest for many materials scientists. Attempts to grow single crystals of PZTs have been made by numerous researchers, resulting in crystallites too small to allow adequate property measurements [13,14,15,16,17]. Though Relaxor-PT ceramics were not shown to offer enhanced dielectric and piezoelectric properties comparable to PZT ceramics of similar T$_C$s, they can be readily grown in single crystal form. This key distinction was first realized by Nomura and co-workers for the PZN and PZN-PT systems [18,19]. Following this ground-breaking work, single crystal growth of PMN-PT[20] and PSN-PT[21], etc., followed. In general, most Pb(B$_1$,B$_2$)O$_3$-PT crystals can be grown by high temperature solution growth using Pb-based fluxes.

Dielectric and piezoelectric properties for several Pb(B$_1$B$_2$)O$_3$-PT crystals are reported and compared to their polycrystalline counterparts in Table 2. As presented, piezoelectric coefficients and coupling coefficients are significantly higher, with d$_{33}$ and k$_{33}$ values greater than 1500 pC/N and 90%, respectively, found for MPB compositions in both the PZN-PT (x-0.09) and PMN-PT (x=0.35) systems. Though the Curie temperature (T$_C$) of these materials are relatively low < 200°C, the significance of these values becomes evident by directly comparing their values in relation to T$_C$ in Figures 2~5.

Although ultra high coupling and piezoelectric properties of the PZN-PT system, first reported in 1981 and later in the PMN-PT system (1989), have been known for several years, their potential for high performance bio-medical ultrasound transducer and related devices has only been recognized recently. Serious efforts on the development of Pb(B$_1$B$_2$)O$_3$-PT crystals for high performance transducers includes investigations at Toshiba Co. and at the Pennsylvania State University.

Merits of the single crystal form itself include the possibility of "optimum" crystallographic cuts as analogous in the 35.25° rotated Y-cut in quartz crystals for a zero temperature coefficient of resonance, and X-cut in LiTaO$_3$ or 128° rotated Y cut in LiNbO3 crystals for
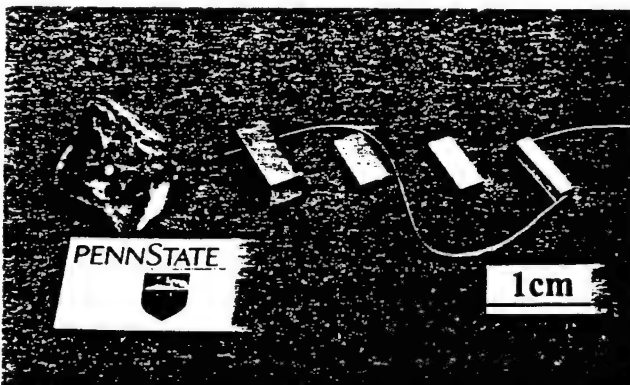

Figure 6 Sequence of sample preparation based on IEEE standards (PZN-9.5%PT (001) cuts). From left, as grown crystal, oriented sample using Laue back reflection camera, cut and polished sample, k$_{31}$ sample electroded gold sputtering, and k$_{33}$ sample.
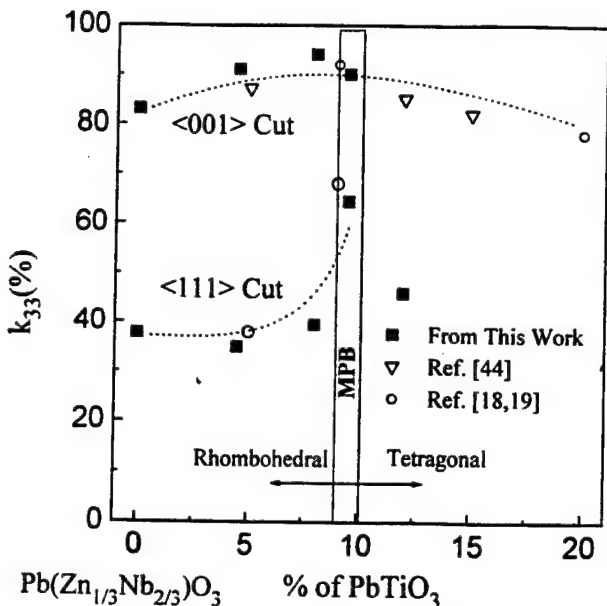
Figure 7 k_{33} as a function of composition and orientation in crystals of PZN-PT.

optimum conditions including surface acoustic speed and coupling [22]. Another advantage of the single crystal form lies in terms of microstructural issues associated with polycrystalline ceramics, including grain size, porosity, etc. These can be also ignored removing scaling limitations, particularly relevant to high frequency transducers.

As stated above, the merits of using single crystals for high performance transducers is clearly evident, but few systematic studies have yet to be made. In the following section, preliminary results based on the author's ongoing investigation are presented.

CRYSTAL STRUCTURAL PROPERTY RELATIONSHIPS

Commonalties inherent to Relaxor-PT systems have been discussed in reviews by Shrout [23] and Randall [24]. Based on these commonalties, our research was limited to two representative systems of PZN-PT and PMN-PT. Though PMN-PT MPB crystals exhibit piezoelectric properties comparable with PZN-PT, more focus was given to the PZN system owing to its relatively lower PT content for MPB. This allows more uniform crystal growth of these solid solution materials. Details of crystal growth for these systems are given in references [25,26]. Compositions investigated include the rhombohedral PZN end member, MPB compositions (PT $\cong$ 9%) and tetragonal phases (> 10% PT).

High quality crystals (maximum size 1×1×1 cm) grown using PbO-based fluxes were characterized and samples prepared in accordance with IEEE standards. Figure 6, shows an example of the sequence of sample preparation

starting with an as-grown PZN-9.5%PT crystal.

Dielectric, piezoelectric, and electromechanical coupling coefficients for the various crystals are reported in Table 3. Parameters relevant to transducer designs, including dielectric loss, frequency constant (N), elastic compliance (s_{ij}), mechanical Q etc., are also reported.

As reported in table 3, large coupling coefficients (k_{33}) and large piezoelectric coefficients (d_{33}) were found for PZN-PT crystals with MPB compositions, as previously reported by Kuwata [19]. Electromechanical coupling (k_{ij}) and piezoelectric coefficients (d_{ij}) equal to and larger than MPB crystal compositions were found for domain engineered rhombohedral crystals[#] as shown in Figure 7. Both pure PZN and PZN-8%PT crystals were found to possess high k_{33} values of ~85% and 94%, respectively, for (001) crystal cuts. Low values of dielectric loss < 1%, significantly less than their polycrystalline counterparts, should also be noted. The role of domains and their stability on the dielectric and piezoelectric properties of single crystals is the topic of further investigation, and further details is beyond the scope of this work.

As previously reported and given in figure 7, large values of k_{33} are also found in the tetragonal region (PT>10%) and, as reported in table 3, a value of 63% k_T was detected for the PZN-11%PT. High thickness coupling may be associated with the large anisotropy of the tetragonal crystals.

The dielectric constant was also found to be dependent on the crystal symmetry. Tetragonal crystals exhibited dielectric constants on the order of less than 1000 being significantly lower than rhombohedral crystals (3000~5000). Lower dielectric constants are also associated with both increased anisotropy and T_c. With similar coupling coefficients, the range of dielectric constants found in the PZN-PT system offer the flexibility in designing transducers with equivalent electrical impedance for a wide range of frequency and geometry.

SUMMARY

The single crystal form of Relaxor-PT materials offers the possibility of dramatic improvements in transducer performance. Electromechanical coupling coefficients greater than 90% with non-MPB compositions as well as MPB compositions enables degree of freedom in designing transducers with broad bandwidth and/or improved sensitivity. A range of dielectric constants from ~1000 to 5000 in the PZN-PT system offers designers dielectrics for optimum electrical impedance matching. Ultrahigh piezoelectric strain coefficient d_{33}>2000pC/N clearly warrants further investigations in relation to high

---

[#] Rhombohedral crystals oriented and poled along pseudocubic <001> direction. Crystallographically, polarization direction of rhombohedral crystal is pseudocubic <111> direction.

energy density actuators. Microstructurally, single crystal transducers are not limited by grain size or porosity, offering high performance at very high frequencies.

Though clearly promising, the commercialization and growth of single crystals must be demonstrated and anticipated difficulties in fabrication and processing such as dicing, attaching matching layers and etc., must be overcome if single crystal piezoelectrics are to become piezoelectric materials for the next generation of ultrasound transducers.

ACKNOWLEDGMENT

REFERENCES

[1] T. R. Gururaja, "Piezoelectrics for Medical Ultrasonic Imaging", *American Ceramic Society Bulletin*, vol. 73, no. 5, pp. 50-55, May 1994.

[2] W. A. Smith, "New Opportunities in Ultrasonic Transducers emerging from Innovations in Piezoelectric Materials," 1992 SPIE International Symposium, July 21-22, 1992.

[3] B. Jaffe, W. R. Cook, Jr., and H. Jaffe, *Piezoelectric Ceramics*, London and New York: Academic Press, 1971.

[4] G. A. Smolenskii, V. A. Isupov, A. I. Agranovskaya, and N. N. Kainik, "New Ferroelectrics of Complex Composition. IV," *Soviet Physics - Solid State*, vol. 2 no. 11, pp. 2651-2654, May 1961.

[5] G. A. Smolenskii, V. A. Isupov, A. I. Agranovskaya, S. B. Popov, "Ferroelectrics with Diffuse Phase Transitions", *Soviet Physics - Solid State*, vol. 2, no. 11, pp. 2584-2594, May 1961.

[6] L. E. Cross, "Relaxor Ferroelectrics," *Ferroelectrics*, vol. 76, pp. 241-267, 1987.

[7] Landolt-Börnstein, *Ferroelectric and Antiferro-electric Substances*, vol. 19, Group III, Berlin: Springe Verlag, 1981.

[8] Y. Yamashita, "Pb(B'B")O$_3$-PbTiO$_3$ Materials," *The 7th US-Japan Study Seminar on Dielectric and Piezoelectric Ceramics*, Tukuba, 1995, pp. 181-185.

[9] Y. Yamashita, "Improved Ferroelectric Properties of Niobium-Doped Pb[(Sc$_{1/2}$Nb$_{1/2}$)Ti]O$_3$ Ceramics Material," *Japanese Journal of Applied Physics*, vol. 32, pp. 5036-5040, Nov. 1993.

[10] N. Kim, *Grain Size Effect on the Dielectric and Piezoelectric Properties in Compositions which are near the Morphotropic Phase Boundary of Lead Zirconate-Titanate Based Ceramics*, Ph. D. Thesis, Pennsylvania State University, 1994.

[11] J. F. Nye, *Physical Properties of Crystals, Oxford University Press*, Oxford: Clarendon Press, 1957.

[12] D. A. Berlincourt, D. R. Curran and H. Jaffe, *Piezoelectric and Peizomagnetic Materials and Their Function in Transducers*, New York: Academic Press, 1964, p169 in Physical Acoustics, Volume 1A, edited by W. P. Mason.

[13]. S. Fushimi and T. Ikeda, "Phase Equilibrium in the System PbO-TiO$_2$-ZrO$_2$," *Journal of the American Ceramic Society*, vol. 50, no. 3, pp. 129-132, March 1967.

[14] V. A. Kuznetzov, "Crystallization of Titaium, Zirconium and Hafnium Oxies and Some Titanate and Zirconate Compounds under Hydrothermal Conditions," *Journal of Crystal Growth*, vol. 34, pp. 405 - 410, 1968.

[15] R. Clarke and R. W. Whatmore, "The Growth and Characterization of PbZr$_x$Ti$_{1-x}$O$_3$ Single Crystals," *Journal of Crystal Growth*, vol. 33, pp. 29-38, 1976.

[16] T. Hatanaka and H. Hasegawa, "Dielectric Properties of Pb(Zr$_x$Ti$_{1-x}$)O$_3$ Single Crystals Including Monoclinic Zirconia," *Japanese Journal of Applied Physics*, vol. 34, pp. 5446-5448, Sept. 1995.

[17] K. Yanagisawa, H. Kanai, and Y. Yamashita, "Hydrothermal Crystal Growth of Lanthanum-Modified Lead Zirconate Titanate," *Japanese Journal of Applied Physics*, vol. 34, pp. 536-538 Sept. 1995.

[18] J. Kuwata, K. Uchino, and S. Nomura, "Phase Transitions in the Pb(Zn$_{1/3}$Nb$_{2/3}$)O$_3$ -PbTiO$_3$ System," *Ferroelectrics*, vol. 37, pp. 579-582, 1981.

[19] J. Kuwata, K. Uchino, and S. Nomura, "Dielectric and Piezoelectric Properties of 0.91Pb(Zn$_{1/3}$Nb$_{2/3}$)O$_3$ - 0.09PbTiO$_3$ Single Crystals," *Japanese Journal of Applied Physics*, vol. 21, no. 9, pp. 1298-1302, Sept. 1982.

[20] T. R. Shrout, Z. P. Chang, N. Kim, and S. Markgraf, "Dielectric Behavior of Single Crystals near the (1-x)Pb(Mg$_{1/3}$Nb$_{2/3}$)O$_3$ - (x) PbTiO$_3$ Morphotropic Phase Boundary," *Ferroelectric Letters*, vol. 12, pp. 63-69, 1990.

[21] V. G. Smotorakov. I. P. Raevskii, M. A. Malitskaya, S. M. Zaitsev, Y. M Popov, and N. A. Strekneva, "Preparation and Properties of Single Crystals of Pb$_2$ScNbO$_6$," *Inorganic Materials*, vol. 19, pp. 105-108, 1983.

[22] J. M. Herbert, *Ferroelectric Transducers and Sensors*, London and New York: Gordon and Breach Science Publishers, 1982.

[23]. T. R. Shrout and J. Fielding, Jr., "Relaxor Ferroelectric Materials," *in Proceedings of the 1990 IEEE Ultrasonics Symposium*, 1990, pp. 711-715.

[24] C. A. Randall, A. S. Bhalla, T. R. Shrout, and L. E. Cross, "Classification and Consequences of Complex Lead Perovskite Ferroelectrics with regard to B-site

Cation Order," *Journal of Materials Research*, vol. 5, no. 4, pp. 829-834, 1990.

[25]. M. L. Mulvihill, S.-E. Park, G. Risch, Z. Li, K. Uchino, T. R. Shrout, "The Role of Processing Variables in the Flux Growth of Lead Zinc Niobate-Lead Titanate Relaxor Ferroelectric Single Crystals," *Japanese Journal of Applied Physics*, vol. 35, no. 7, pp. 51-57, July 1996.

[26] S.-E. Park, M. L. Mulvihill, G. Risch, and T. R. Shrout, "The Effect of Growth Condition on Dielectric Properties of $Pb(Zn_{1/3}Nb_{2/3})O_3$ Crystal," *Japanese Journal of Applied Physics*, in review.

[27] Y. Yamashita, "Large Electromechanical Coupling Factors in Perovskite Binary Material System," *Japanese Journal of Applied Physics*, vol. 33, Pt. 1[9B], pp. 5328-5331, 1994.

[28] S. Nomura, "Ferroelectric Properties in the System $Pb(Zn_{1/3}Nb_{2/3})O_3$ -$PbTiO_3$," *Journal of Physical Society of Japan*, vol. 27, p. 262, 1969.

[29] S. W. Choi, T. R. Shrout, S. J. Jang, and A. S. Bhalla, "Dielectric and Pyroelectric Properties in the $Pb(Mg_{1/3}Nb_{2/3})O_3$ -$PbTiO_3$ system," *Ferroelectrics*, vol. 100, 29-38, 1989.

[30] H. Banno et al., in *Proceedings of the 1st Meeting on Ferroelectric Materials and Their Applications*, 1975, F-14, p. 339.

[31] T. Kudo, T. Yazaski, F. Naito, and S. Sugaya, "Dielectric and Piezoelectric Properties of $Pb(Co_{1/3}Nb_{2/3})O_3$-$PbTiO_3$ -$PbZrO_3$ Solid Solution Ceramics," *Journal of American Ceramic Society*, vol. 53, pp. 326-328, June 1970.

[32] J. F. Wang, J. R. Giniewicz, and A. S. Bhalla, "Soft Piezoelectric $(1-x)Pb(Sc_{1/2}Ta_{1/2})O_3$ - $xPbTiO_3$ Ceramics with High Coupling Factors and Low Qm," *Ferroelectric Letters*, vol. 16, pp. 113-118, 1993.

[33] V. J. Jonson, M. W. Valenta, J. E. Dougherty, R. M. Douglass and J. W. Meadows, "$Pb(Sc_{0.5}Nb_{0.5})_xO_3$, Perovskite-Type Ferroelectric Solid Solutions Possessing Relatively Large Spontaneous Polarizations," *Journal of Physical Chemistry in Solids*, vol. 24, pp. 85-93, 1963.

[34] V. J. Tennery, K. W. Hang, R. E. Novak, "Ferroelectric and Structural Properties of the $Pb(Sc_{1/2}Nb_{1/2})_{1-x}Ti_xO_3$ System, *Journal of American Ceramic Society*, vol. 51, pp. 671-674, Dec. 1968.

[35] U. Kodama. M. Osada, O. Kumon, and T. Nishimoto, "Piezoelectric Properties and Phase Transition of $PbIn_{1/2}Nb_{1/2}O_3$-$PbTiO_3$ Solid Solution Ceramics," *American Ceramics Society Bulletin*, vol. 48, no. 12, pp. 1122 - 1124, 1969.

[36] A. I. Zaslavskii and M. F. Bryzhina, "An X-ray Structural Investigation of the Antiferroelectric Pb_2MgWO_6 and the System of Solid Solutions Pb_2MgWO_6 - $PbTiO_3$," *Soviet Physics-Crystallography*, vol. 7, no. 5, pp. 577-583, 1963.

[37] V. A. Isupov and L. P. Belous, "Phase Transition in the Antiferroelectric $PbCo_{0.5}W_{0.5}O_3$ and $PbCo_{0.5}W_{0.5}O_3$ - $PbTiO_3$ Solid Solutions," *Soviet Physics-Crystallography*, vol. 16, no. 1, pp. 129 - 133, 1971.

[38] D. A. Berlincourt, C. Cmolik, and H. Jaffe, "Piezoelectric Properties of Polycrystalline Lead Titanate Zirconate Compositions," *Proceedings of the IRE*, vol. 48, pp. 220 -229, 1960.

[39] H. Jaffe and D. A. Berlincourt, "Piezoelectric Transducer Materials," *Proceedings of IEEE*, vol. 53 no. 10, pp. 1372-1386, 1965.

[40] H. Ouchi, K. Nagano, and S. Hayakawa, "Piezoelectric Properties of $Pb(Mn_{1/3}Nb_{2/3})O_3$ - $PbZrO_3$ Solid Solution Ceramics," *Journal of American Ceramic Society*, vol. 48, no. 12, pp. 630-635, 1965.

[41] Y. Yamashita. "Piezoelectric Properties of Niobium-Doped $[Pb(Sc_{1/2}Nb_{1/2})_{1-x}Ti_x]O_3$ Ceramics Material near the Morphotropic Phase Boundary," *Japanese Journal of Applied Physics*, vol. 33, no. 8, pp. 4562 -4656, August 1994.

[42] S. T. Chung, K. Nagata, and H. Igarashi, "Piezoelectric and Dielectric Properties of $Pb(Ni_{1/3}Nb_{2/3})O_3$ -$Pb(Zn_{1/3}Nb_{2/3})O_3$ -$PbTiO_3$," *Ferroelectrics*, vol. 94, pp. 243-247, 1989.

[43] S. Baumler. "The Dielectric and Piezoelectric Properties of PZN:PT:BT Ceramics," M. S. Thesis, The Pennsylvania State University, 1986.

[44] T. R. Shrout, unpublished work.

APPENDIX 27

PIEZOELECTRIC PROPERTIES AND EQUIVALENT CIRCUITS OF FERROELECTRIC RELAXOR SINGLE CRYSTALS

B.M. JIN, RUYAN GUO AND A.S. BHALLA
Materials Research Lab, The Pennsylvania State University, University Park, PA, USA

Abstract   Temperature dependent piezoelectric properties of ferroelectric relaxor single crystals, particularly the Ce-doped strontium barium niobate $Sr_{0.6}Ba_{0.4}Nb_2O_6$:Ce (SBN60:Ce) crystals, were investigated by resonance and anti-resonance technique. Characteristic resonant frequencies (f_r-f_a, f_s-f_p, and f_m-f_n) were studied using equivalent circuit simulation. The piezoelectric resonance in a ferroelectric relaxor SBN60:Ce resonator was found to persist into temperatures much higher than T_m (temperature at which dielectric constant κ has a maximum at $1 kHz$), in contrast to a normal ferroelectric resonator such as TGS. The parameters in an equivalent circuit, however, are phenomenally different from that of a normal resonator like TGS, at near and above the transition temperature region. Experimental results pertaining to understanding the piezoelectric resonance characteristics in ferroelectric relaxors are reported.

INTRODUCTION

Temperature and frequency dependencies of the dielectric permittivity of a SBN ($Sr_{0.6}Ba_{0.4}Nb_2O_6$, SBN60) single crystal near the ferroelectric-paraelectric phase transition, as well as other compositions in this solid solution system [1-2], have been studied extensively [3-4]. At any specific temperature in a broad vicinity (several 10 or several 100°C) of its Curie point, a ferroelectric relaxor may still preserve its macroscopic chemical composition and crystalline symmetry; however its local chemistry may deviate from the global stoichiometry and its local symmetry may be lower than global symmetry, as a result of local polarization fluctuation due to microscopic chemical inhomogeneity [5-6].

It is well known that ferroelectric crystals are subspecies of a piezoelectric family. After proper poling, a macroscopic polarization is sustained in temperatures below the Curie temperature, parallel to the polar axis direction. Approaching to the Curie temperature, a centric prototype normal ferroelectric crystal undergoes a catastrophic depolarization phase transition from a ferroelectric (polar) state to a paraelectric (nonpolar) state, and the piezoelectricity vanishes. However, the spontaneous polarization in a relaxor ferroelectric does not suddenly vanish at a specific temperature, but gradually decays with increasing temperature. The diffuse nature of the transition has been postulated due to a partially disordered distribution of cations in a relaxor ferroelectric crystal, so that a mixture of ferroelectric islands (microphase) and paraelectric matrix exists over a wide temperature region. This paper studies the piezoelectric behavior of a typical relaxor single crystal SBN at near and above the Curie transition temperature, with particular interests on its piezoelectric behavior.

EXPERIMENT

The resonance and anti-resonance method was performed to measure the piezoelectric parameters of SBN60:Ce single crystal from room temperature to 200°C. An alanine-doped TGS single

crystal, for comparison purposes, was measured from room temperature to 100°C. Before piezoelectric measurement, SBN60:Ce sample was poled at 140°C for 15 min under 10kV/cm DC field, and cooled down to 50°C while maintaining the electric field. The d_{33} value measured using Burlincort d_{33}-meter was 158×10^{-12} C/N in a freshly poled sample.

Piezoelectric parameters, impedance ($|Z|$) and phase angle (θ), were measured with high precision to determine the characteristic resonant frequencies f_r-f_a, f_s-f_p, and f_m-f_n, respectively. Constant voltage measurement condition was maintained throughout the measurement. Based on the measured basic parameters, impedance ($|Z|$) and phase angle (θ) at each temperature, other necessary parameters are converted using IRE standard formalism [7].

The same sample was used in both dielectric and piezoelectric measurements for consistency of results. Sample dimension for both measurements was $3.71 \times 1.16 \times 0.77$ mm^3 (in a,c,b direction). All data was collected using a computer through an GPIB interface connected to a HP impedance analyzer (HP 4194A, USA).

RESULTS AND DISCUSSIONS

Fig. 1 shows the result of piezoelectric θ-Freq. characteristics measured by resonance and anti-resonance method from room temperature to 200°C for relaxor SBN60:Ce. Impedance peaks became undetectable at temperatures higher than 160°C for SBN60:Ce.
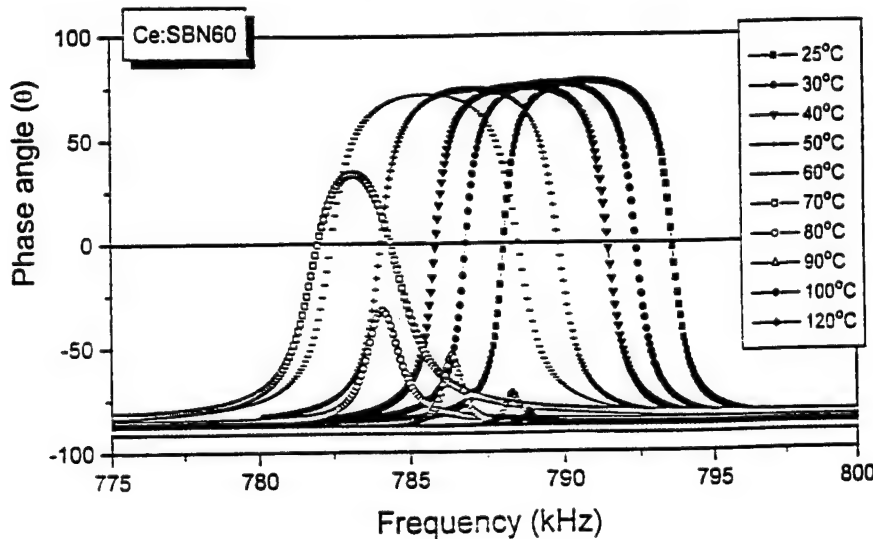

FIGURE 1. Phase angle variation of SBN60:Ce as a function of frequency around resonance at different temperatures.

If one defines diffusiness D as [(temp. at which piezo-peak disappears) / (temp. at which dielectric permittivity maximizes)], the D value for SBN and TGS are then found to be 2.1 and 1.2, respectively. This diffusiness reflects the degree of persistency of the piezoelectric characteristics above the dielectric maximum (T_m) temperature and seems to correlate with the ferroelectric relaxor nature. In the case of relaxor SBN, minimum impedance appears in between 780 kHz and 790 kHz depending on the temperatures. These minima shift to lower frequency in temperatures lower than T_m (76.02°C at 1kHz in dielectric measurement) and to higher frequency in temperatures higher than T_m, as temperature increases. This trend can not be accounted by taking into consideration of the thermal expansion ($x_{33}(T)$) because converse effects will be resulted from the c-axis dimensional change as function of temperature [6]. Elastic constant, s_{11}^E, however, shows maximum softness near the T_m therefore the shift of the resonant frequency is in

accordance with the trend of the mechanical susceptance. The phase angles reached to the zero values (a true resonance and anti-resonance condition) at the resonance frequencies for temperatures below T_m. However, at temperatures above T_m, phase angle maintained at a negative value through the resonance frequency range, even though the overall piezoelectric resonance appears persist well above the T_m.

Normal ferroelectric crystal TGS, on the other hand, has a much narrower impedance peak (smaller f_a-f_r). It's phase angle satisfy the resonance and anti-resonance condition (θ=0) in temperatures up to T_C. The frequency of its impedance peaks decreases in ferroelectric phase and decreases again in paraelectric region (after a minor increase at the immediate vicinity above the T_c).

Piezoelectric coefficient, such as k_{31}, s_{11}^B and d_{31} can be calculated using the following relations:

$$\frac{k_{31}^2}{1-k_{31}^2} = \frac{\pi f_a}{2f_r} \tan \frac{\pi \Delta f}{2f_r}, \qquad \text{where} \quad \Delta f = f_p - f_s$$

$$s_{11}^E = \frac{1}{4l^2 \, \rho f_s^2}, \quad \text{and}$$

$$d_{31}^2 = \kappa_{31}^2 \varepsilon_{33}^T s_{11}^E$$

Above the T_m, on the other hand, we could not obtain the actual coupling constant, k_{31} and the other piezoelectric coefficients because the resonance and anti-resonance conditions are not satisfied. The results are summarized in Fig. 2 showing s_{11}^E and d_{31}, respectively.

In Figure 2, the broken lines indicate that the s_{11}^E and d_{31} values above that temperature are hypothetical values taking assumption that $f_m \sim f_r$, and $f_n \sim f_a$. (at Z_{max} and Z_{min}). An impedance Cole-Cole plot around resonance frequency demonstrate this point more clearly as shown in Fig. 3. At 70°C locus, all the piezoelectric parameters, f_m, f_s, f_r, f_a, f_p and f_n can be determined because susceptance has a positive value, namely, f_r and f_a can be determined by the junction point of susceptance with zero line. At 80°C locus, all the data points were below zero line, so f_a and f_r can not be determined, neither the true piezoelectric parameters in piezoelectric resonant equivalent circuit. Therefore, there is no real piezoelectric resonance above T_m although it appears in a ferroelectric relaxor resonator that piezoelectric resonance persists to temperatures (~160°C) far beyond T_m (~76°C).

Even though the normal ferroelectric TGS also has an f_p and an f_n frequency up to 65°C – 15°C higher than its T_C (Curie temperature of TGS) – their magnitude is small comparing to that of the values below T_C. Therefore, in the case of TGS, f_p and f_n are almost negligible, hence impedance as a function of temperature shows near-second order transition behavior. On the contrary, impedance of SBN shows a very strong temperature dependence. The magnitude of impedance gradually decreases but persists into the polarization fluctuation state (ferroelectric local islands surrounded by paraelectric matrix). The significance of the diminishing temperature of piezoelectric resonance is not yet clear. Presumably, this temperature is related to the thermal energy that is critical for coherent interactions among the localized polarizations.

CONCLUSIONS

Piezoelectricity of relaxor ferroelectrics does not vanish at a specific temperature but decays over a certain temperature region. The resonance and anti-resonance conditions (zero-reactance), however, are no longer satisfied near and above a specific temperature (T_m). The piezoelectricity vanishes at a temperature when presumably the coherence or interactions of neighboring polar islands are critically broken.
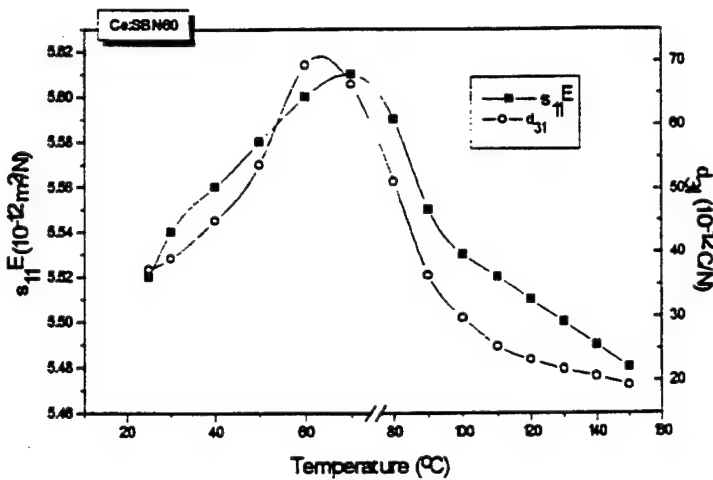
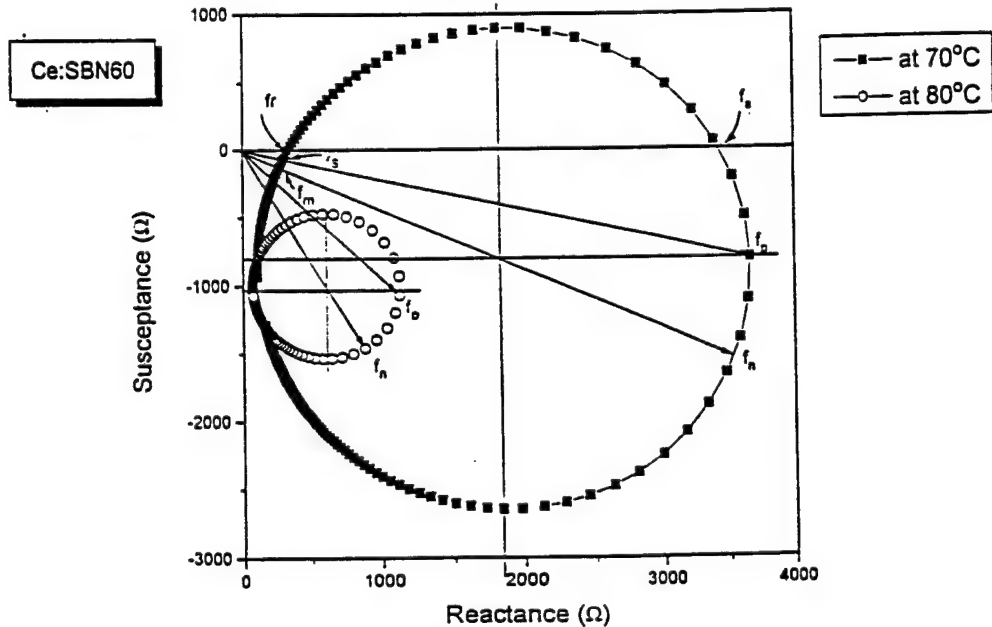FIGURE 2. s_{11}^E and d_{31} vs. temperature of SBN60:Ce

FIGURE 3.   Impedance Cole-Cole plot at 70°C and 80°C that are the temperatures just below and above T_m.

REFERENCES

[1] A.A. Ballman, H. Brown, *J. Cryst. Growth*, **1** (1967) 311

[2] M.F. Dubovik, Yu.N. Venevtse and A.A. Bush, *Izv. Akad. Nauk SSSR Neorg. Mater.*, **13** (1977) 2214

[3] G.A. Smolenskii, *J. Phys. Soc. Jpn., suppl.*, **26** (1970)

[4] L.E. Cross, *Ferroelectrics*, **76** (1987) 241

[5] R. Guo, A.S.Bhalla, C.A. Randall, and L.E. Cross, *J. Appl. Phys.*, **67** (1990) 6405

[6] A.S.Bhalla, R. Guo, L.E. Cross, G. Burns, F. Dacol, and R.R. Neurgaonkar, *Phys. Rev.*, **B36** (1987) 2030

[7] H. Jaffe et. al., *Proceedings of the IRE*, **14** (1957) 353.

APPENDIX 28

In-situ observation of the domain configurations during the phase transitions in barium titanate

By Maureen L. Mulvihill†, Kenji Uchino†, Zhuang Li‡ and Wenwu Cao†

†International Center for Actuators and Transducers (ICAT), Materials Research Laboratory, The Pennsylvania State University, University Park, PA 16802, USA
‡Materials Science Division, Argonne National Laboratory, Argonne, IL 60439, USA

ABSTRACT

Using a polarizing optical microscope in conjunction with a charged-coupled device camera system, the domain microstructural evolution with respect to temperature in all three phases of $BaTiO_3$ was studied. Along a (001) oriented section the domains in the tetragonal phase form 90° domain patterns in an 'a–a' configuration. The transition on heating and cooling between the cubic and tetragonal phases occurred near the same temperature, 125°C. On cooling, the domain structures in the orthorhombic phase appeared as a long continuous lamellar structure, while on heating the domains formed a 'patchwork' structure. This transition temperature showed a large thermal hysteresis. The final transition temperature from orthorhombic to rhombohedral was difficult to determine using this technique. The transition on cooling occurred at −134°C based on a colour change and the disappearance of all the domains. During heating, the domains reappeared at −110°C and remained in a patchwork structure throughout the orthorhombic phase.

§ 1. INTRODUCTION

1.1. *Background of BaTiO₃*

Since the discovery of the barium titanate ($BaTiO_3$) crystal in the early 1940s, many researchers have studied it due to its large dielectric, piezoelectric and elastic constants. $BaTiO_3$ is used in many applications such as capacitors (Buessem, Cross and Goswami 1966), electro-optic devices (Nakao, Tomomatsu, Ajimura, Kurosaka and Tominaga 1994) and memory devices (Merz 1954, Cudney *et al.* 1993). Domains, which are caused by multivariants in the spontaneous polarization and strain (Arlt and Sasko 1980), contribute greatly to the physical properties of $BaTiO_3$ (Arlt 1990).

A domain is a uniform volume of spontaneous electrical polarization (P_s) which can be formed on cooling from the paraelectric to ferroelectric (FE) phase or a transion between FE phases. Domains can be altered by temperature, pressure, electric field and past history of the mateial (Forsbergh 1949). Domains develop in various configurations to balance the stress in the material so that the overall elastic energy is minimized (Arlt 1987, 1990, Kim, Chung and Kim 1993). In some situations, certain kinds of domain patterns can be stabilized by defects (Cao 1995). The domain configurations depend on the crystallographic symmetry of the material. Domain structures are of basic importance in FE polycrystals since the struc-

tures determine the mechanisms of the polarization reversal process. The presence of domain walls also affects the dielectric, elastic and piezoelectric properties since the walls are mobile under an external field (Fousek and Janovec 1969).

BaTiO$_3$ (BT) has four phase stability regions as a function of temperature. The high temperature phase (greater than $\sim 120°C$) is a cubic perovskite. Merz (1949) reported the dielectric constant as a function of temperature for BT. BT transformed from (c)ubic [paraelectric] to (t)etragonal [ferroelectric] at 120°C, to (o)rthorhombic [ferroelectric] at −7°C, and to (r)hombohedral [ferroelectric] at −90°C. On heating, the phase transitions of r → o, o → t, and t → c occurred at slightly higher temperatures than on cooling, which signified the presence of latent heat and a first order transition (Kanata, Yoshikawa and Kubota 1987). The polarization axes in the ferroelectric phases are along the [001], [110] and [111] directions for the tetragonal, orthorhombic and rhombohedral, phases, respectively (Merz 1949, Cook 1956). Since the polarization axis in each phase changes, the domain configuration also varies as the structure changes with temperature.

As BT transforms from the cubic to the tetragonal structure, the c-axis elongates and the lattice constant c/a ratio increases to 1·01 (DeVries and Burke 1957). Strains develop and are relieved by the formation of domains with polarization alone one of the three principal crystallographic axes. Due to the degeneracy of $\pm P_s$, there are six possible orientations in the tetragonal phase. In the tetragonal phase 90° and 180° domains occur. The 90° domain walls orient along one of the {101} planes (DeVries and Burke 1957, Cao and Cross 1991). The domains with polarization vectors anti-parallel to each other are 180° domains. Optical microscopy cannot distinguish the 180° domains since the change of optical indices is only related to the strain and not direction.

As the temperature decreases below 0°C, BT transforms into the orthorhombic structure. The polarization axis changes to one of the twelve [101] directions and the domains can meet with polarization vectors forming 60°, 90° and 180° angles (Smolenskii 1982). As the temperature decreases even further to −80°C, BT transforms into the rhombohedral phase where the polarization axis goes to one of the eight [111] directions, and these are 71°, 109° and 180° domain structures. Experimentally, it was observed that in contrast to the tetragonal phase, birefringence occurred in both the orthorhombic and rhombohedral phases (Smolenskii 1982). Also, the actual changes in polarization were larger than expected in the orthorhombic and rhombohedral phases. It was suggested that the increase in polarization was possibly due to both the change in crystal axes and the change in the magnitude of polarization (Merz 1949).

1.2. *Microscopy techniques used to observe domain configurations*

A significant amount of research has been conducted on BT since 1943 using various techniques such as optical microscopy (OM), scanning electron microscopy (SEM) and transmission electron microscopy (TEM) in an attempt to understand the relationship between the domain structures and the properties of BT. Most of the research dealt with the effect of electric fields and compressive stresses on the tetragonal domain configurations. Owing to the low temperature necessary to observe the orthorhombic and rhombohedral domain configurations, their configurations have not been studied as frequently as the tetragonal phase configurations.

Regions in which all polarization directions are parallel to the surface of the section are called 'a' domains whereas regions perpendicular to the surface of the

section are called 'c' domains (Hooton and Merz 1955). Using polarizing optical microscopy the 'c' domains appear dark since the optic axis for a tetragonal phase is along the *c*-axis, whereas the 'a' domains are bright (Merz 1954). Hooton and Merz (1955), using optical microscopy were able to observe both 90° and 180° domains by etching BT samples with hydrochloric acid. They found that the positive end of the domain etched faster than the negative end of the polarization vector. Even though this technique proved successful for the observation of 90° and 180° domains, the method is destructive to the sample and not useful for dynamic studies.

, Electron microscopic techniques have been used to obtain high resolution information concerning the domains and domain boundaries (Merz 1949). Domain patterns must be etched to be observed using SEM. Due to the preferential etching, the 'a', '+c' and '−c' domains appeared grey, dark and bright, respectively (Hu, Chan, Wen and Harmer 1986). Park and Chung (1994) using SEM observed that the 90° and 180° domains formed a herringbone pattern when all three domains ('a', '+c' and '−c') were present. They also found that the spatial forms of the 90° and 180° domain boundaries formed irregular cross-sections which appeared cylindrical.

When optical microscopy was compared to TEM, it was reported that the domain widths were much larger for bulk than thin film materials. The measured domain widths for bulk samples were tens of micrometres whereas for thin film techniques the widths were between hundredths or even thousandths of micrometres (Merz 1949). It is believed that the bulk domains contain many smaller domains which were unobservable using optical microscopy.

In this study, domain creation and orientation changes for the three phase transitions in BT were observed as a function of temperature. The technique differs from previous studies because it is *in situ*, allowing domain configurations at each phase transition as well as in each ferroelectric phase to be observed in real time. Bulk domain behaviours can be determined without etching.

§ 2. EXPERIMENTAL PROCEDURE

The high quality BT single crystal used in this study was obtained from the Institute of Physics, Chinese Academy of Science, Beijing China. The crystal was grown by the top seed solution method. As received, it was optically clear, free of imperfections, and untwinned when examined under cross polarizers.

The Laué X-ray technique was used to precisely determine the [001] family of directions in the crystal. The crystal was then sliced parallel to the (001) plane, ground to a thickness of $100\,\mu m$, and polished with $0.5\,\mu m$ gamma-alumina in kerosene. The samples were gold sputtered on one side leaving a $400\,\mu m$ gap on the surface. Silver leads were attached to the electrodes with air dry silver paste. The samples were annealed above 200°C to remove any internal stresses in the material which were produced during the cutting and polishing operation.

A high resolution charged coupled device (CCD) camera attached to a Nikon transmission optical microscope was connected to a monitor and VCR as illustrated in fig. 1. The birefringence between the domains permitted the observation of the domains with the polarizing light microscope. Magnifications up to 1300× can be observed on the monitor. The temperature-controlled sample stage (Linkam Inc.) in conjunction with the deep focal point of the objective lenses allows the observation of domain behaviour as a function of temperature between +200°C and −185°C at a rate of $10°C\,min^{-1}$. The stationary and changing domains were instantaneously recorded by the VCR and observed on the monitor.

M. L. Mulvihill *et al.*

Fig. 1
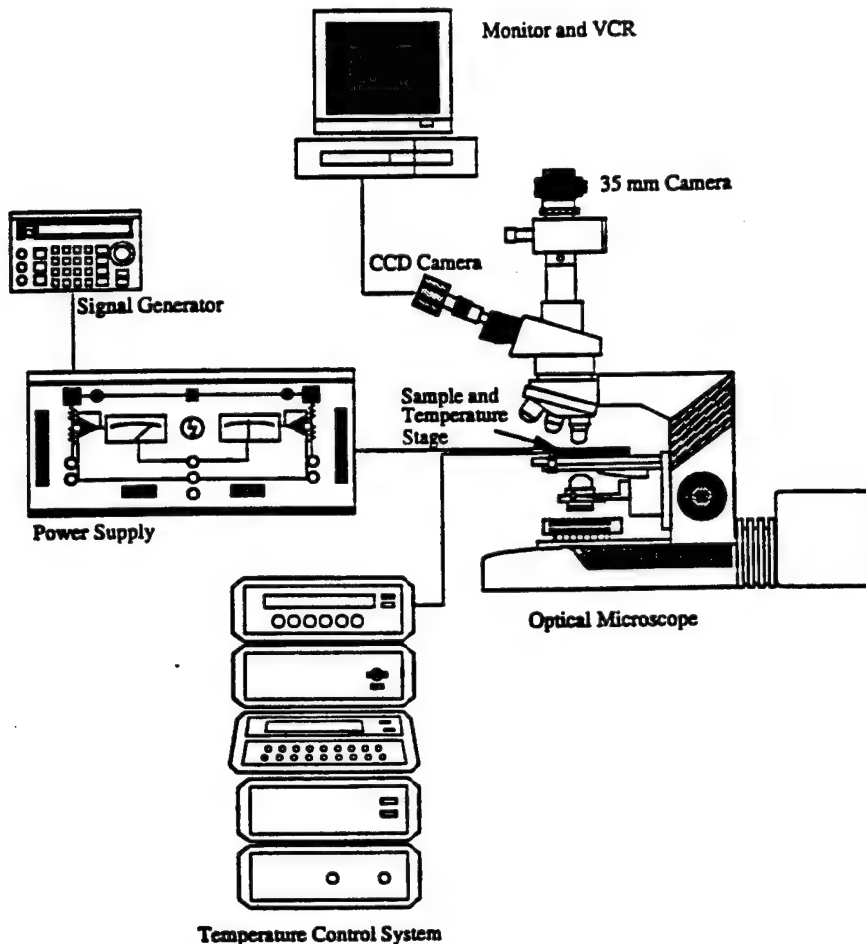
Experimental set-up of CCD microscope system used in this study.

For the dielectric constant versus temperature measurements, the crystals were cut and polished to 100 μm thick sections. Circular gold electrodes were sputtered on parallel surfaces with diameters of 1 to approx. 2 mm. The capacitance and loss of an unpoled crystal section were measured as functions of temperature and frequency in a computer controlled furnace system using a Hewlett Packard Programmable 4275A Multi-frequency LCR meter. The samples were measured on cooling from 200°C down to −160°C at 1°C min⁻¹, then heated back to 200°C at 1°C min⁻¹.

§ 3. Results and discussion

A high quality BT single crystal section with (001) orientation was measured under transmission optical microscopy (TOM) as a function of temperature during several temperature cycles to determine domain configuration changes through the three ferroelectric phase transitions. These phase transitions were observed by the changes in the domain configurations and then compared with the measured dielectric constant. The (001) section contains several directions, as illustrated in fig. 2.

Fig. 2
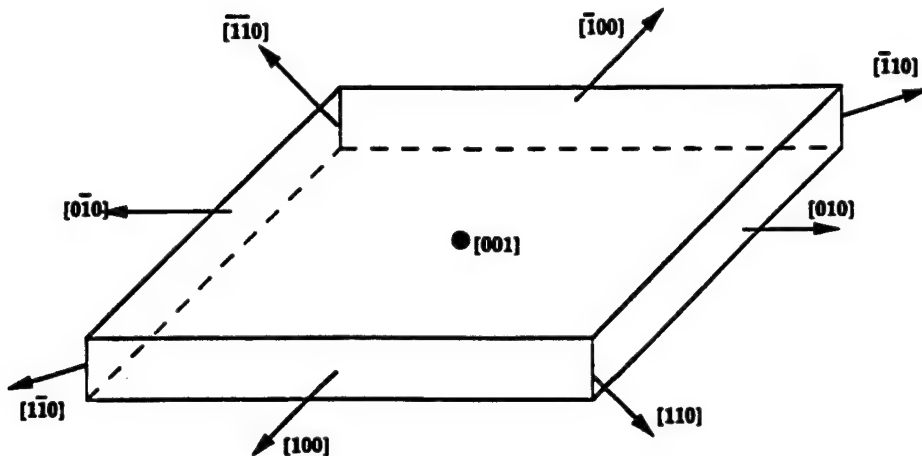
An illustration of the directions contained in the (001) section.

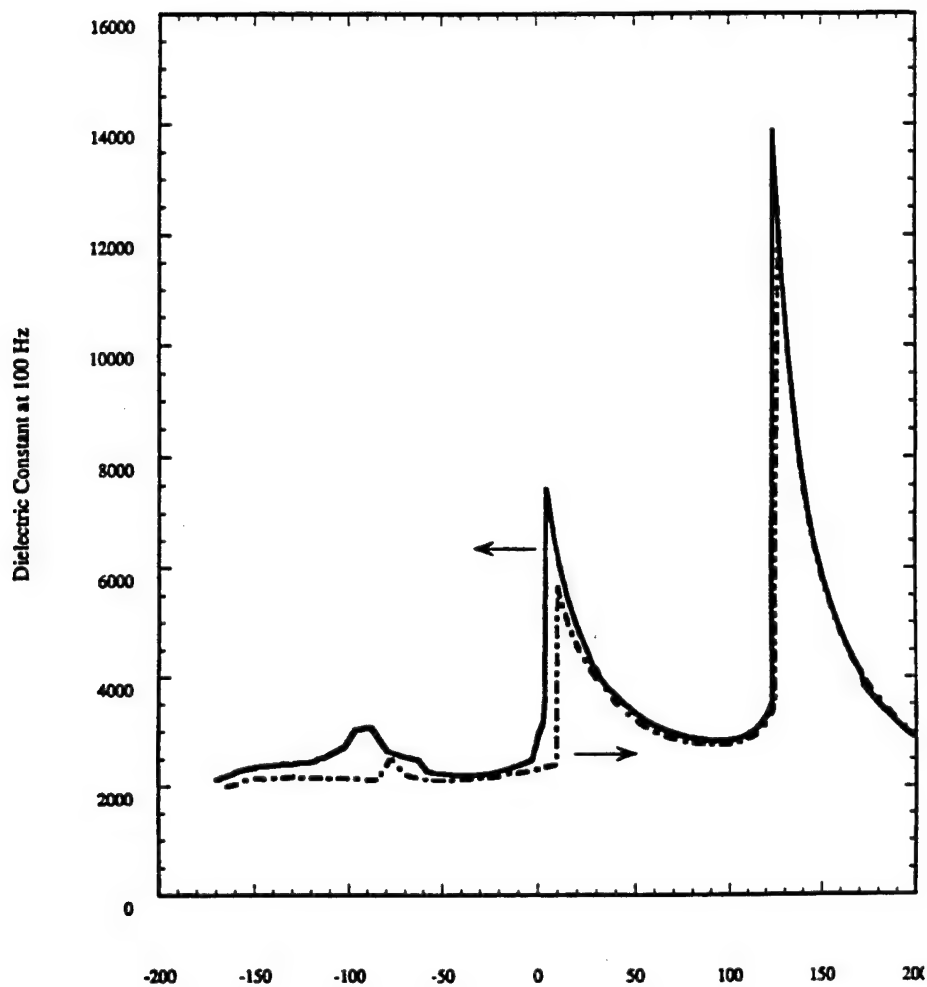### 3.1. *Measured dielectric constant as a function of temperature*

The dielectric constant as a function of temperature during heating and cooling for an unpoled BT single crystal measured along the [001] direction is shown in fig. 3. The phase transition temperatures of this crystal occurred at slightly higher temperatures than those measured by Merz (1949). In this experiment, the c → t phase transition occurred at 125°C on cooling while the t → c transition occurred at 127°C on heating (the c ↔ t phase transition reported by Merz was 120°C). The other two phase transitions, i.e. t ↔ o and o ↔ r showed larger thermal hystereses. The t ↔ o phase transitions occurred near 2·5°C on cooling and 10°C on heating, and the o ↔ r phase transitions occurred at −100°C on cooling and −90°C on heating.

3.2. *Optical observation of the cubic ↔ tetragonal phase transitions*

For each of the three thermal cycles, the cubic to tetragonal phases transition occurred at the same temperature of 125°C on cooling which was in agreement with the c ↔ t phase transition temperature of the measured dielectric constant shown in fig. 3. A small thermal hysteresis was observed as the sample was heated back through the tetragonal to cubic transition which occurred near 127°C.

In the cubic phase above 125°C, the sample appeared to be a uniform colour. On cooling, wedge-shaped domains appeared at 125°C as shown in fig. 4 (*a*). These wedge-shaped domains elongated and widened with further cooling as shown in fig. 4 (*b*) at 124·4°C. The isolated wedge domains grew into a more uniform twin band with domain walls oriented in [1̄10]. Another set of twin bands is formed with the domain walls oriented along the [110] direction. At 122·3°C the entire sample contains tetragonal 90° domains as shown in fig. 4 (*c*). One set of twin bands disappeared leaving only the twin band with domain walls oriented along [1̄10]. The lamellar domains had a wedge shape which travelled across the sample slowly as the temperature decreased until the entire sample was covered. Most of the domain growth occurred by 120°C. Afterwards, the domain width (1–5 μm) appeared to be saturated and did not change with temperature down to 2·4°C. The 90° domains

Fig. 3

The measured dielectric constant versus temperature for an unpoled BT single crystal.

formed an 'a–a' configuration on the plane. The sample contained a high density of the long and sharp 90° domains. The colours of domains alternated yellow and green.

On heating, the tetragonal to cubic phase transition began at 124°C, signified by the disappearance of some domains. At 125°C the domains became very difficult to distinguish. At 126°C a swift shift to cubic phase occurred and all domains disappeared in a sweeping motion. However, even at 127°C, the sample still shows some birefringence. Uniform colour appeared only at 128°C.

3.3. *Optical observation of the tegragonal ↔ orthorhombic phase transitions*

With further cooling down to 2·4°C the second phase transition started, which is from the tetragonal phase to the orthorhombic phase as shown in fig. 4 (*d*). This phase transition took place within 0·4°C. It was also in agreement with the t ↔ o phase transition temperature in fig. 3. The orthorhombic phase domains grew across the sample in a sweeping motion with a narrow but finite temperature interval as illustrated in figs. 4 (*d*), (*e*), and (*f*). The orthorhombic domains were long and well
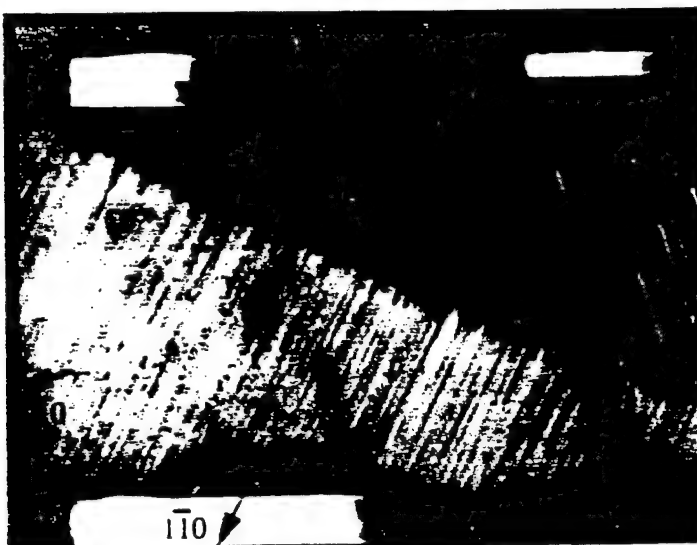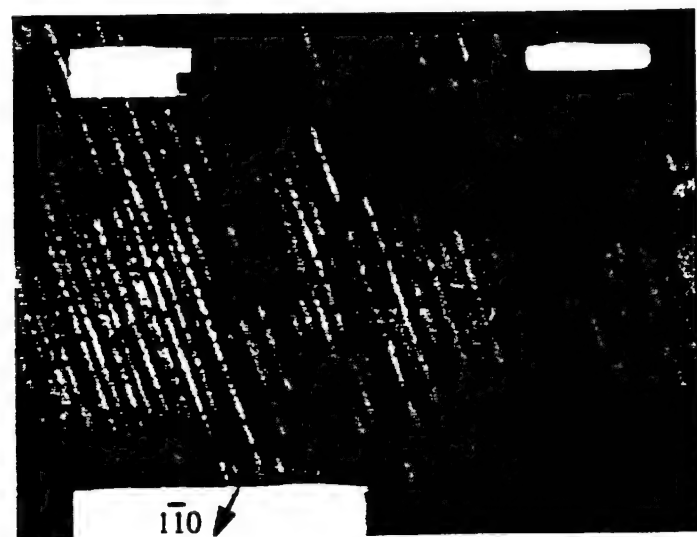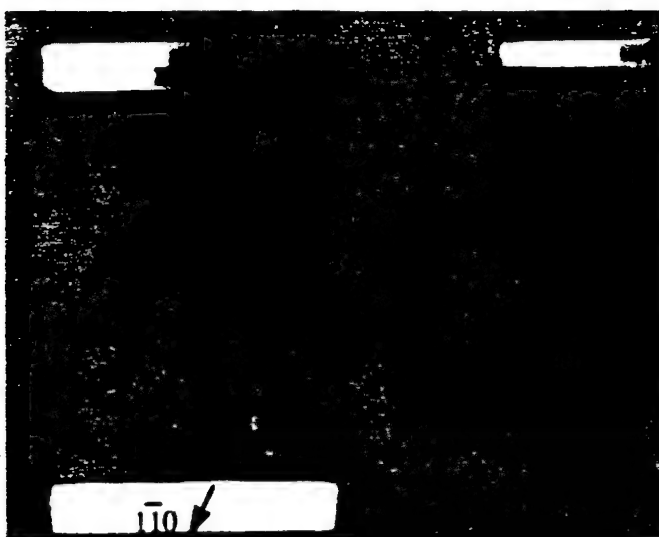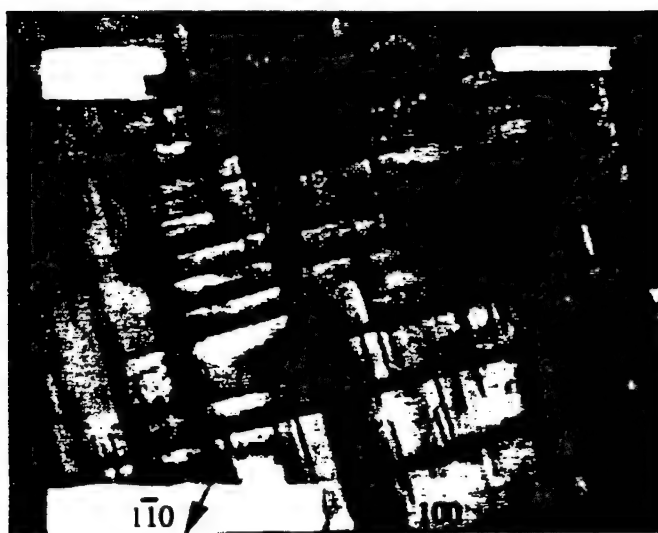
Fig. 4
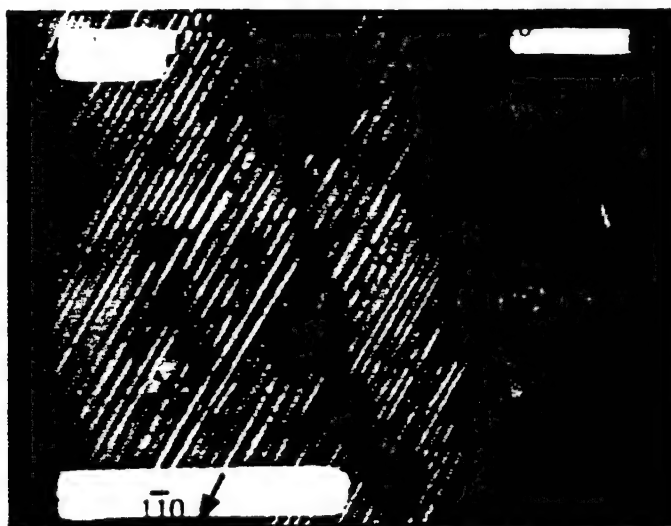
(d)

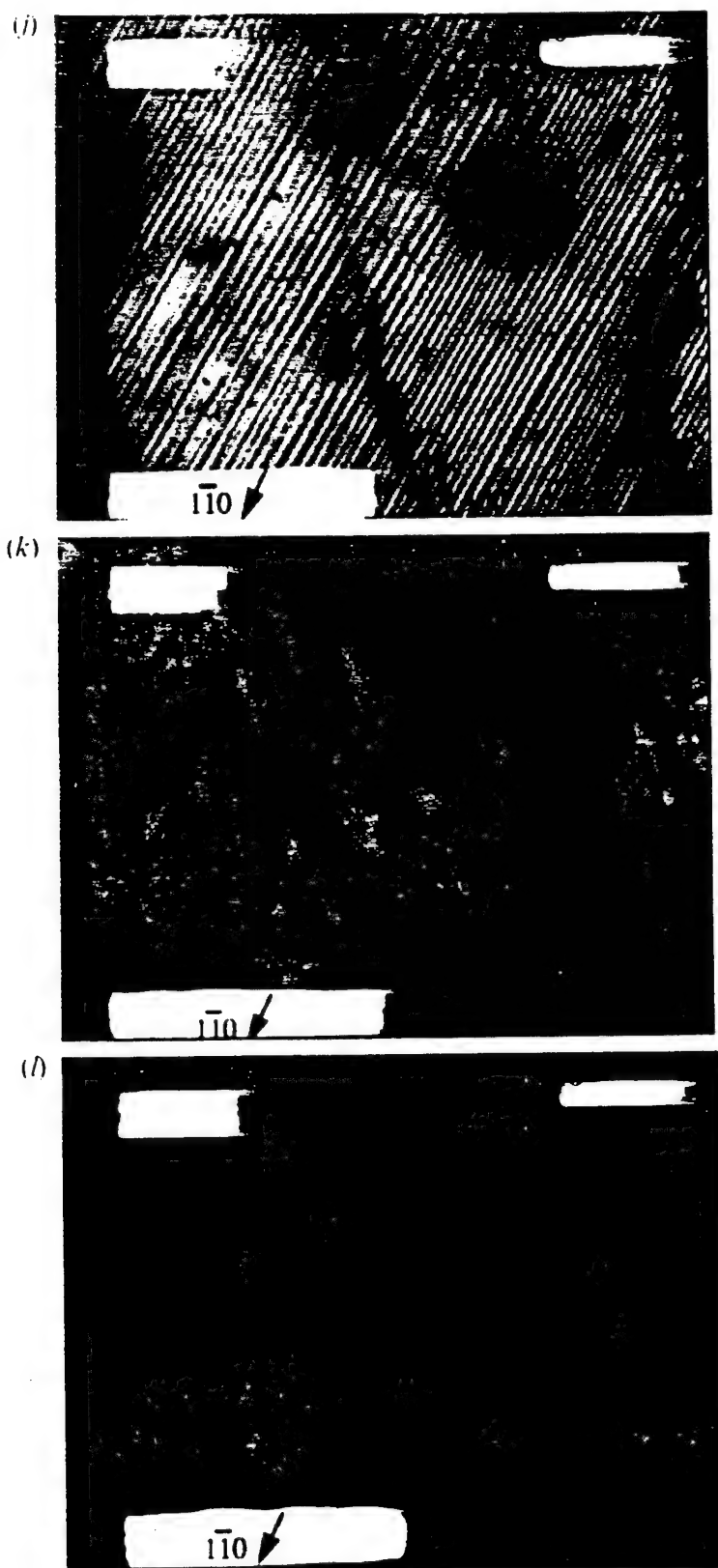$\bar{1}10$

(e)

0

$1\bar{1}0$

(f)

$1\bar{1}0$
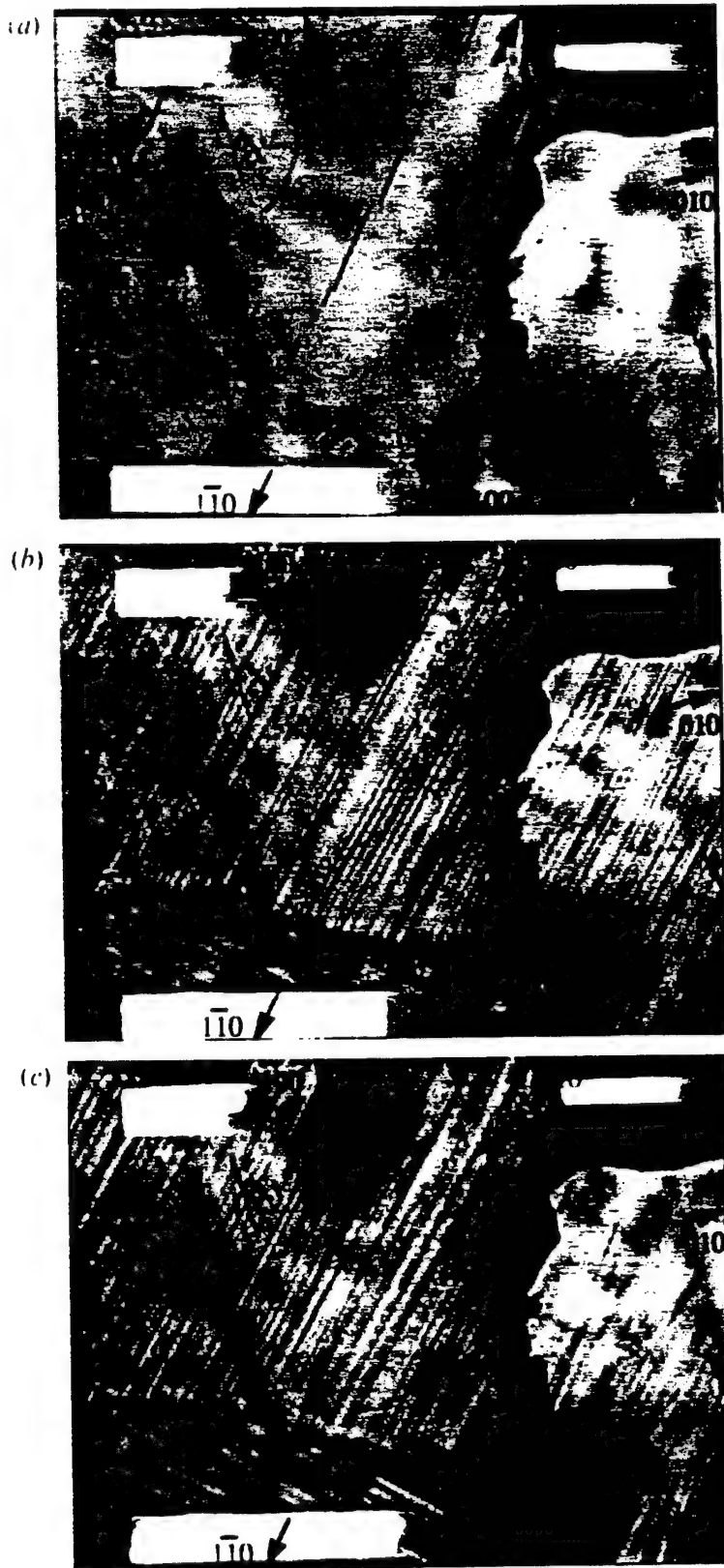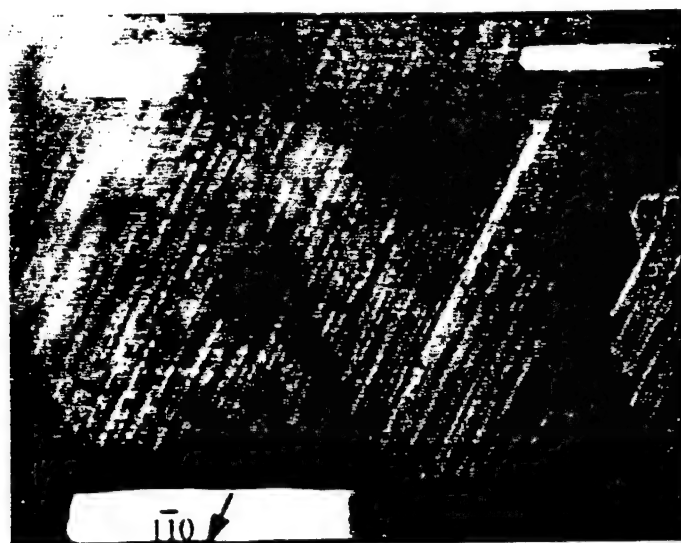
Domain structures of high quality 100% BT single crystal as a function of temperature: (*a*) 125°C. (*b*) 124·4°C. (*c*) 122·3 C. (*d*) 2·4 C. (*e*) 2·2°C. (*f*) 2·0°C. (*g*) −134°C. (*h*) 14·4 C. (*i*) 14·6 C. (*j*) 14·9°C. (*k*) −110·4 C and (*l*) −110·3°C.

defined. A single set of twin bands with domain walls oriented in the [010] evolved from the original tetragonal domains with domain wall oriented in [1$\bar{1}$0]. In effect, the domain walls rotated by 45°. The sample colour changed to warmer colours (red and orange). Taking into account the fact that the stripe period is similar in both the tetragonal and orthorhombic phases, this domain configuration change was to compensate the stress distribution.

On heating, the orthorhombic to tetragonal phase transition occurred at a much higher temperature, 14·4°C. The phase transition took place within 0·5°C as shown in figs. 4 (*h*) to (*j*). A moving interface perpendicular to the tetragonal domain walls swept across the sample, changing the domain wall orientation back to nearly the same configuration as before the t → o transition (fig. 4 (*c*)). The interface front which swept across the sample was not straight but slightly zigzagged. The period of this zigzag pattern corresponded roughly to that of a patchwork pattern. The recovered tetragonal phase consisted of long straight 90° domains similar to the 90° domains which appeared on cooling but with varying widths.

3.4. *Optical observation of the orthorhombic ↔ rhombohedral phase transitions*

The orthorhombic to rhombohedral phase transition temperature could not be clearly defined from the optical observation of the domain configurations. The observed phase transition temperatures varied from those shown in fig. 3. At −110°C the sample still contained long orthorhombic domains as in fig. 4 (*j*). At −123°C the sample darkened and the colours became less orange and red, but the pattern was the same as that in fig. 4 (*f*) in which the domain walls were oriented along the ⟨100⟩. The domains disappeared instantaneously at −134°C probably reflecting the orthorhombic to rhombohedral phase transition, as shown in fig. 4 (*g*). However, in the area near a crack, domains were still present. These domains are possibly caused by the residual strain of the crack (Cao and Krumhansl 1990). The sample stayed a uniform colour down to −185°C.

On heating to −110·4°C no domains were observed as shown in fig. 4 (*k*). At −110·3°C, a cross hatching of the twin bands or a 'patchwork' domain structure of purple colour was observed as shown in fig. 4 (*l*). The domain walls were oriented along both the [$\bar{1}$00] and [010] directions. The width of the patchwork squares was approximately 10–50 μm in size. This pattern may have originated from the rhombohedral domain period which has not been clarified in this work. At −5·3°C the brightness of the sample increased dramatically but the domain patterns remain the same as shown in fig. 4 (*h*). The patchwork domain patterns existed up to 14·6°C where the sample went through the orthorhombic-tetragonal phase transition, shown in fig. 4 (*i*).

§ 4. SUMMARY

A polarizing microscope in combination with a CCD camera system allowed the *in situ* observation of the phase transition in barium titanate and the associated domain structures for temperatures cycled between 200°C and −185°C. The domain configuration in each of the three phases had its own orientation and morphology. The transitions all appeared to be first order due to the existence of thermal hysteresis.

In the tetragonal phase, several twin bands were nucleated and later merged into a single set of twin bands with the domain walls oriented along the ⟨110⟩ directions. The width of the domains was in the range of 1–5 μm and did not seem to change

significantly with temperature. The orthorhombic domains were different when the system was transformed from the high temperature phase or from the low temperature phase. On cooling, the system transformed into a single set of twin bands from the twin bands of the tetragonal phase via a propagating habit plane perpendicular to the tetragonal domain walls. In contrast, a patchwork pattern formed on heating. The patchwork domain structure transformed to the tetragonal twin band via a zigzagged interface of an orientation near the [010]. No clear domain patterns were visible under TOM in the rhombohedral phase on this crystallographic section.

REFERENCES
ARLT, G., 1987, *Ferroelectrics*, **76**, 451; 1990, *Ferroelectrics*, **104**, 217.
ARLT, G. and SASKO, P., 1980, *J. appl. Phys*, **51**, 4956.
BUESSEM, W. R., CROSS, L. E., and GOSWAMI, A. K., 1996, *J. Am. Ceram. Soc.*, **49**, 33.
CAO, W., 1995, *Phase Transitions*, **55**, 69.
CAO, W., and CROSS, L. E., 1991, *Phys. Rev B*, **44**, 5.
CAO, W., and KRUMHANSL, J. A., 1990, *Phys. Rev. B*, **42**, 4334.
COOK, Jr., W. R., 1956, *J. Am. Ceram. Soc.*, **39**, 17.
CUDNEY, R. S., FOUSEK, J., ZGONIK, M., GÜNTER, P., GARRETT, M. H., and RYTZ, D., 1993, *Appl. Phys. Lett.*, **63**, 3399.
DEVRIES, R. C. and BURKE, J. E., 1957, *J. Am. Ceram. Soc.*, **40**, 200.
FORSBERGH, P. W., 1949, *Phys. Rev.*, **76**, 1187.
FOUSEK, J., and JANOVEC, V., 1969, *J. appl. Phys.*, **40**, 135.
HOOTON, J. A., and MERZ, W. J., 1955, *Phys. Rev.*, **98**, 409.
HU, Y. H., CHAN, H. M., WEN, Z. X., and HARMER, M. P., 1986, *J. Am. Ceram. Soc.*, **69**, 594.
KANATA, T., YOSHIKAWA, T., and KUBOTA, K., 1987, *Solid State Commun.*, **62**, 765.
KIM, S.-B., CHUNG, T.-J. and KIM, D.-Y., 1993, *J. Euro Ceram. Soc.*, **12**, 147.
MERZ, W., 1949, *Phys. Rev.*, **76**, 1221; 1954, *Phys. Rev.*, **95**, 690.
KAKAO, O., TOMOMATSU, K., AJIMURA, S., KUROSAKA, A., and TOMINAGA, H., 1994, *Ferroelectrics*, **156**, 135.
PARK, B.-M., and CHUNG, S.-J., 1994, *Ferroelectrics*, **157**, 27.
SMOLENSKII, G. A., 1982, *Ferroelectrics and Related Materials*, Vol. 3 (New York: Gordon and Breach), Chap. 7.

APPENDIX 29

DYNAMIC MOTION OF THE DOMAIN CONFIGURATION IN RELAXOR FERROELECTRIC SINGLE CRYSTALS AS A FUNCTION OF TEMPERATURE AND ELECTRIC FIELD.

MAUREEN L. MULVIHILL, L. ERIC CROSS, and KENJI UCHINO

International Center for Actuators and Transducers (ICAT), Materials Research
Laboratory, The Pennsylvania State University, University Park, PA, 16802,
USA, (814) 865-9931. Funding provided by the US Office of Naval Research.

Abstract Relaxor ferroelectrics exhibit unique characteristics such as a broad phase transition and frequency dispersion which may originate from the configuration of ferroelectric microdomains. In this study, the dynamic behavior of the macrodomains in $Pb(Zn_{1/3}Nb_{2/3})O_3$ single crystals was observed using an optical microscope in combination with a CCD camera system. Many domain characteristics such as changes in birefringence, transition between microdomains and macrodomains, and "freeze-in" temperature of the macrodomains were optically observed. These observations were then compared to measured dielectric properties in an attempt to clarify the relationship between the dielectric properties and the behavior of macrodomains.

INTRODUCTION

The observation of switching domains under an applied electric field and changing temperature has been difficult and limited research has been documented.[1-3] In this study, an optical technique was used to explore the growth of macrodomains from micropolar regions in the relaxor composition $Pb(Zn_{1/3}Nb_{2/3})O_3$ (PZN) as a function of temperature and applied electric field. Lead zinc niobate based single crystals were studied because of their large dielectric (K=56,000 along <111>) and piezoelectric (k^{*}_{33}=92% along <001>) properties which make PZN a potential material for actuator and transducer devices.[4] The measured dielectric constant and dielectric loss as a function of temperature for a poled and unpoled sample were compared to the optically observed domain behaviors to develop a fundamental understanding of the relaxor ferroelectric behavior in PZN.

EXPERIMENTAL PROCEDURE

Single crystals of PZN were grown using a flux method with excess PbO. The Laué x-ray technique was used to precisely determine the [111] directions in the crystals. The crystals were then sliced, ground to a thickness of 100 μm, and polished with diamond paste until a near-mirror finish was obtained on both surfaces. The PZN domain

configurations were observed through the single crystal along the <111> which is the spontaneous polarization direction of PZN. The electric field was applied as a triangular wave at 0.05 Hz up to ±10 kV/cm and the temperature was cycled between -185°C and 200°C. A high resolution CCD (Charged Coupled Device) camera was attached to a Nikon Transmission Petrographic Microscope which was connected to a monitor and VCR.[2,3] The temperature-controlled sample stage in conjunction with the deep focal point of the objective lenses allowed an electric field to be safely applied across the sample.

RESULTS AND DISCUSSION

Optical Observation

The CCD camera microscope system was used to observe macrodomain behaviors of PZN such as birefringence change, microdomain to macrodomain phase transition and "freeze-in" temperature. The color change due to the birefringence appeared under the applied electric field around the Curie temperature range (Tc≈140°C). The birefringence appeared at higher temperatures as the magnitude of the electric field increased, and was possibly caused by the microdomain alignment. The electric field caused the fluctuating microdomains to orient with the field leading to macroscopic birefringence in the crystal.

Still photographs of a 100% PZN single crystal at 100°C as the electric field increased are represented in Figures 1a through 1d. Macrodomains were not observed for the annealed state without the application of an electric field, but were first detected when the AC field was raised to 0.7 kV/cm. With an AC bias during field-cooling and field-heating, the phase transition from a ferroelectric (FE) microdomain to a macrodomain state occurred near 130°C.

As the temperature decreased, the domain motion ceased or "froze-in" at a temperature which was electric field dependent. Small frozen islands appeared randomly in the crystal which expanded with decreasing temperature.[3] This freezing phenomenon is not directly related to the coercive field and is not observed in normal ferroelectrics such as BaTiO$_3$. It was optically observed that the freezing temperature decreased as the electric field increased. On field heating, the thawing or "unfreezing" temperature took place at temperatures slightly higher than the freeze-in temperature, indicating a slight temperature hysteresis.

Dielectric Data

The dielectric constant and dielectric loss versus temperature at four frequencies for an unpoled and poled 100% PZN single crystal are shown in Figures 2 and 3, respectively. The dielectric constant and dielectric loss behavior exhibited above the transition temperature of ≈ 140°C were identical. The frequency dependent transition temperature
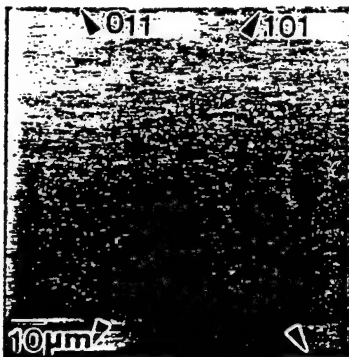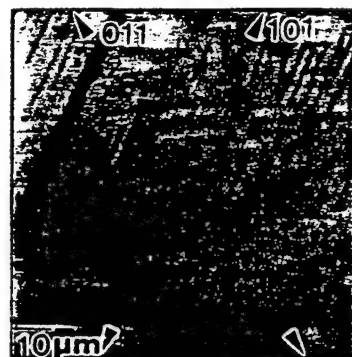
FIGURE 1a 100% PZN at 0 kV/cm.

FIGURE 1b 100% PZN at 1 kV/cm.

FIGURE 1c 100% PZN at 3.8 kV/cm.

FIGURE 1d 100% PZN at 6.3 kV/cm.

corresponds to the border between paraelectric and FE microdomain phases. As temperature decreased, the dielectric behavior of the poled and unpoled sample near 100°C diverged. The frequency dispersion exhibited in the unpoled sample did not occur in the poled sample. The temperature region where the dielectric constant had a nondispersive frequency behavior appeared as a "shoulder" in the poled sample, as shown in Figure 3. Also, the tanδ decreased drastically in this temperature region. The decrease in tanδ and the shoulder in the poled sample were caused by the alignment of the
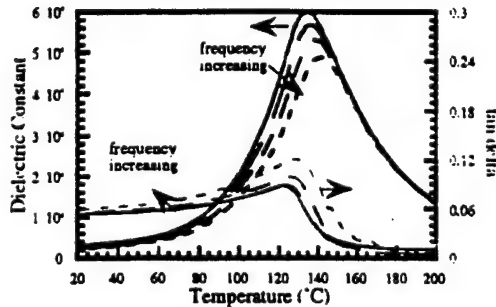

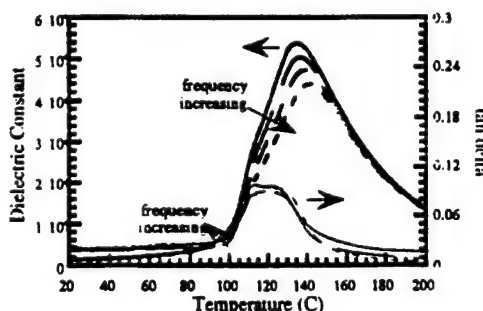FIGURE 2 Unpoled PZN single crystal.

FIGURE 3 Poled PZN single crystal.

microdomains by the +15kV/cm DC poling bias. However, in the unpoled sample the microdomains were not aligned and variation in the orientation of the microdomains caused the frequency dispersion in the dielectric data. This temperature range corresponds to the ferroelectric microdomain phase region. The shoulder corresponds to a critical temperature (T_{crit}) which is the phase border between FE microdomain and FE macrodomain.

Comparison of Optically Observed Domains and Dielectric Properties

The magnitude of the electric field as a function of temperature was plotted using the data from the optically observed characteristics and the measured dielectric properties, as shown in Figure 4. In conclusion, various trends in the data divided the figure into four phase regions as a function of temperature. Since the birefringence changes were caused by the induced micropolar alignment, it was assumed that the birefringence marked the first phase transition on decreasing temperature between paraelectric and FE microdomain phase regions. The second phase transition occurred at the temperature where the macrodomains appeared with field-cooling and disappeared with field-heating. This phase transition separated the FE microdomain phase from the FE macrodomain phase. The third phase transition occurred at the domain freeze-in temperature. This transition between the FE macrodomain phase and the FE frozen domain phase decreased to lower temperatures as the magnitude of the electric field increased.
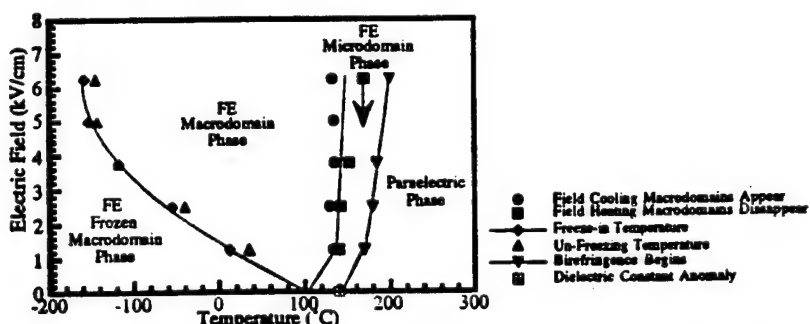

FIGURE 4 Optically observed behavior of the PZN macrodomains.

REFERENCES

1. K. Kato, K. Suzuki and K. Uchino, J. Ceram. Soc. Jpn., 98 840 (1990).
2. K.Y. Oh, K. Uchino, and L.E. Cross, J. Am. Ceram. Soc., 77 [11] 2809 (1994).
3. M. L. Mulvihill, L. E. Cross, and K. Uchino, J. Am. Ceram. Soc., accepted for publication.
4. J. Kuwata, K. Uchino and S. Nomura, Ferroelectrics, 37 579 (1981).

APPENDIX 30

Pergamon

PII S0025-5408(96)00035-9

CONVERSE METHOD MEASUREMENTS OF ELECTROSTRICTION COEFFICIENTS IN LOW-K DIELECTRICS

V. Sundar and R.E. Newnham
Intercollege Materials Research Lab.,
The Pennsylvania State University,
University Park, PA 16802

ABSTRACT

Methods for measuring electrostrictive coefficients are discussed and a set of converse method measurements on low-K dielectrics presented. The Q_{11} values measured in this work, in m^4/C^2, range from -0.49 for CaF_2 through smaller values like 0.34 for MgO up to 1.48 for BeO. Coefficients for BaF_2, SrF_2, $KMnF_3$, Al_2O_3, LiF, spodumene ($Li_2O \cdot Al_2O_3 \cdot 4SiO_2$) glass, and calcite ($CaCO_3$) are also presented. The separated Q_{ij} coefficients measured here are in good agreement with confirmed measurements available in the literature. Most of the non-cubic samples have been measured here reliably for the first time. A simple ion-chain model of electrostriction is also presented, and the results compared to experimental values of the hydrostatic electrostriction coefficient Q_h.

KEYWORDS: A. electronic materials, D. dielectric properties, D. piezoelectricity

INTRODUCTION

Phenomenology of Electrostriction. Electrostriction is the basis of electromechanical coupling in all insulators. While the phenomenology of electrostriction has been well established, accurate modeling of the phenomenon has been hampered by a lack of reliable and accurate data on the electrostriction coefficients.

Electrostrictive materials such as relaxor ferroelectrics find use in micropositioning applications that require reproducible deformations without hysteresis. Electrostriction is also the basis of piezoelectricity in that a ferroelectric material may be modeled as a biased lectrostrictor.

Electrostrictive stresses can cause breakdown of insulator materials used in microelectronics, where the small dimensions of the components lead to high applied fields. In high voltage insulating devices, breakdown may be initiated by electrostrictive strains, again due to the high fields present in them (1). In laser glasses, electrostrictive self-trapping of light can cause the initiation of damage in these glasses (2). Electrostrictive stresses have been correlated with optical Kerr effect phenomena and hydration effects in liquids (3). In dielectrics with thermal or dielectric discontinuities, electrostrictive stresses may play a significant role in the generation of pressure waves by microwave pulses (4).

From the Devonshire formalism of the thermodynamic phenomenology, that describes the coupling between dielectric and elastic properties of solids, three equivalent forms of the electrostrictive effect, one 'direct' and two 'converse' effect may be derived (5). From such an approach, the strain x_{ij} in a material may expressed as:

$$x_{ij} = s^E_{ijkl}X_{kl} + M_{mnij}E_mE_n$$

and

$$x_{ij} = s^P_{ijkl}X_{kl} + Q_{mnij}P_mP_n ,$$

where s_{ijkl} is the elastic compliance tensor under appropriate boundary conditions and X_{kl} the components of elastic stress. From these, the direct effect Q and M coefficients are defined as:

$$M_{mnij} = 1/2(\delta^2 x_{ij}/\delta E_m \delta E_n)_x$$

and

$$Q_{mnij} = 1/2(\delta^2 x_{ij}/\delta P_m \delta P_n)_x$$

Alternatively, by the application of Maxwell relations to the above expressions, the 'first converse' effect Q and M coefficients may be derived in terms of the dielectric susceptibility χ_{ij} and its inverse, the dielectric stiffness tensor η_{ij} as:

$$M_{mnij} = (1/2)(\delta\eta_{ij}/\delta X_{mn})_P$$

and

$$Q_{mnij} = (-1/2)(\delta\chi_{ij}/\delta X_{mn})_P$$

The second converse effect is the polarization dependence of the piezoelectric voltage coefficient g_{nij}, and may be expressed as:

$$Q_{mnij} = \delta g_{nij}/\delta P_m$$

and

$$M_{mnij} = \varepsilon_0(\varepsilon_{ij} - 1)^2(\delta g_{nij}/\delta P_m)$$

The M coefficients vary in order of magnitude from about 10^{-21} m²/V² in simple ionic solids to 10^{-15}m²/V² in perovskite actuator materials. The Q coefficients vary in an opposite way, from the order of 10^0 to 10^{-3} m⁴/C² for the same materials. The effects are comparatively large in oxide perovskite structures, due to their inherently large dielectric permittivities. When a field $E = 10$kV/m is applied to typical ferroelectric materials, strains $(x - ME^2)$ of the order of 10^{-5} are easily attained. In contrasting, simple oxides develop strains of the order of 10^{-11}, a very small value.

A brief review of the electrostriction constants measured and reported in the literature reveals that there exists a need to accurately determine these constants for materials other than the comparatively well documented perovskites. There are significant differences in the values determined for many materials, with disagreements even in the signs of these coefficients (6,7). Few measurements on crystal symmetries that are not cubic or isotropic are available.

This study was undertaken with the primary purpose of establishing reliable and accurate electrostriction coefficients for low-K dielectrics. It is felt that measurements confirmed by both the direct and converse methods would achieve this purpose. Some crystals with cubic symmetry, primarily fluoride perovskites, have been characterized in this way, but few non-cubic materials have been measured. As a result, the electrostriction coefficients of some important substrate materials such as Al_2O_3 and other electronic materials like perovskite glass ceramics remain unmeasured. It is hoped that this and subsequent studies will rectify this situation.

ELECTROSTRICTION MEASUREMENT TECHNIQUES

The direct and converse electrostriction effects are of importance in that they offer two independent and equivalent techniques of measuring electrostriction in a material:

a) by measuring the strains induced in materials in response to applied fields or induced polarizations, using the direct effect, and

b) measuring the change in permittivity (via the change in capacitance) under an appropriate stress using the converse effect.

These two routes to determining the electrostriction coefficients shall henceforth be referred to as the direct and converse methods respectively.

Direct Method Measurements.   Measurements of the direct electrostrictive coefficients require the ability to accurately measure very small strains or displacements. Widely used experimental techniques include the strain gauge method, the capacitance dilatometer (8,9), and laser ultradilatometers based on Michelson interferometers (10,11).

Converse Method Measurements.   Techniques for measuring the converse effect call for precision evaluation of dielectric properties. Other requirements are stable temperature control and the establishment of 'true' stress systems—completely hydrostatic if the hydrostatic Q_h coefficients are being measured and truly uniaxial stresses in compressometry (12).

A compressometric system was developed by Meng and Cross for the accurate evaluation of the separated components of the electrostriction tensor (13). This system is the basis for the design of the compressometer used in this work.

The system is designed for the application of a homogeneous stress on the sample surface from a completely uniaxial loading. Dead weights are used for this, in a direct loading scheme. A schematic of the compressometer system is shown in Fig. 1.The design for completely uniaxial loading is related to one of the advantages of this technique. The dielectric susceptibility changes linearly with applied stress, and inhomogenieties in applied stress, averaged out by a comparatively large sample diameter (2 cm approx., as contrasted to beam diameters of fractions of an mm in the interferometer) are further diluted by the linear relationship. In the interferometric method, inhomogenieties in the applied field are magnified by the fact that it appears as a squared term in the displacement-field relation.

The thermal mass of the compression jig is large enough to smooth out minor drifts in ambient temperature. The drift in the fractional change in capacitance is less than 7 ppm/min under quiet conditions.

The electrical stability of the system is also of high order. The capacitance of the sample holder itself is less than 20 aF. The intrinsic conductance is much lesser than 1×10^{-7} nS. Care is taken to ensure that the only capacitance path is through the sample itself, and all signal leads are coaxial and electrically guarded. The capacitance measurement is done in a three-terminal mode using a General Radio 1621 Capacitance Measurement System capable of measuring down to 0.1 aF.

The capacitance resolution is on the whole better than 1ppm, and the resolution in change in capacitance is less than 8 aF, even as estimated in a worst case analysis. This
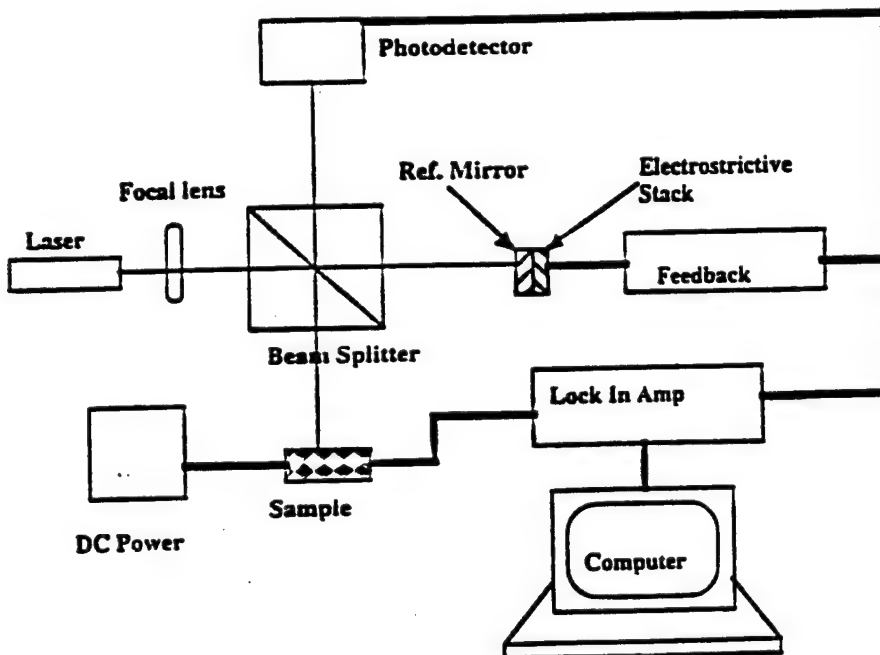

FIG. 1

Schematic of converse electrostriction measurement system.

system is a powerful technique to establish the signs and magnitudes of the electrostriction constants of even low permittivity, low M value materials (14).

Other Methods. More recent studies on quartz have used the change in resonant frequency of the vibration modes of the material caused by a dc field (15,16) , or the dc field induced variations in the transit times of ultrasonic pulses in the material (17). These methods are used to calculate combinations of the electroelastic and the electrostrictive constants of quartz, as well as the nonlinear piezoelectricity and the permittivity tensors. While the method yields accurate results for the piezostriction, the electrostriction values show poorer agreement with values in the literature. A significant intrinsic standard error also exists in the methods used. The second converse effect may also be used to measure electrostriction in a material. This is done by inducing piezoelectricity in the material using a bias field. The variation of the piezoelectric coefficients with the polarization induced is then measured to evaluate the Q coefficients.

EXPERIMENTAL PROCEDURE

Compressometry Equations. The equation for the capacitance of a parallel plate insulator, $C = \varepsilon_0 KA/d$, may be separated and differentiated with respect to stress applied to give:

$$\frac{\delta \ln K}{\delta X} = \left[\frac{|\Delta C/C|}{\Delta X} - \frac{\delta \ln(A/d)}{\delta X} \right] = [B_i(\text{measured}) - S_i(\text{from literature})]$$

where S_i are linear combinations of elastic compliances, and B_i pressure dependencies of the capacitance for the given cut. For a given cut of a cubic crystal, M' and Q', the coefficients for the cut for the first converse effect, are given by:

$$M' = (\varepsilon_0 K/2) [B_i - S_i]$$

and

$$Q' = [K/2\varepsilon_0(K - 1)^2] [B_i - S_i]$$

M' and Q' are related to crystal M and Q coefficients by using the equations for rotated cuts (12). We may use these equations to solve for Q_{11}, Q_{12}, Q_{44} (cubic crystals) by a least squares method, or use Q_h as additional input for an extra equation. In this work, the least squares method is used. Results in this study were verified by checking values for Q_h from the literature (6,10) and found to agree within 4%.

Sample Preparation. The samples used were well characterized chemically and dielectrically. Single crystals of orientations <100>, <110> and <111> were used for the cubic samples CaF_2, BaF_2, SrF_2, $KMnF_3$, and LiF. For MgO, Al_2O_3, BeO and calcite ($CaCO_3$), flat single crystals with <100> orientation were obtained. A disk shaped sample of spodumene ($Li_2O \cdot Al_2O_3 \cdot 4SiO_2$)glass was also measured.

The samples were polished down to thin discs with plane parallel faces. Using the fluorite samples as typical examples, sample dimensions are 2.3cm diameter and 0.8 mm

thickness. Gold electrodes were sputtered on samples polished to optical finishes, with a guard gap of 0.1 mm and 16mm across made on the low electrode.

Capacitance Measurements Under Stress.   All samples were characterized dielectrically before compressometry tests were performed on them. The dielectric constants of the samples were measured at room temperature using an HP 4270 LCR meter sensitive to 1 fF. All the capacitance measurements presented here were done at 1kHz.

As a check of the compressometry system, the samples were then placed in the compressometer stressing cell with no load applied, and their capacitances measured using the GenRad 1621 bridge, which is sensitive to 0.1aF. The capacitances were found to be in good agreement with the HP system measurements, taking into account the ± 0.001pF resolution limit for the less sensitive HP system.

A possible source of error was the effect of sample surface roughness under stress. If the sample is rotated about its own vertical axis (the axis of stressing) in the cell, surface roughness could produce variations in capacitance on the aF level for different orientations. This could give rise to irreproducibility and inconsistent capacitance measurements for such delicate measurements. The diametrical deformation, or barreling of disk shaped samples under stress is another source for concern. This nonuniform deformation is caused by the friction between the sample and the ram extender faces. It could destroy the axial symmetry of loading.

To check for surface roughness effects, measurements of capacitance changes with different axial orientations were made, for the same sample at low loads (0 and 1 kg) We found these measurements to be consistent to within 0.8%, which is acceptable in this range.

Diametrical deformation effects were checked by using a thin mylar film placed between the sample and the Plexiglas ram extenders to take up any surface unevenness.

$KmnF_3$ is a typical sample. To measure the separated electrostriction of cubic samples, <100>, <110>, and <111> oriented crystals were used. After dielectric measurements, they were placed in the compressometer cell, and small static loads of up to 4kg mass were applied in steps of 0.5 kg on the samples.

The change in capacitance for each step in load was measured during loading and unloading. The GenRad 1621 is an analog capacitance bridge. Capacitance measurement was done by iterative balancing of capacitive and loss components of the impedance under test. This was a time-consuming and involved process. However, the excellent sensitivity, resolution, and robustness of the system more than compensated for this.

The two changes (in loading and unloading) were averaged to give a net change in capacitance. This change ΔC was then used along with the measured capacitance measured before each loading step to calculate $\Delta C/C$. A plot of this fractional change in capacitance versus stress gives the factor B_i in the compressometry equations, for each orientation. This, along with elastic constant values from the literature (14,10) was used as input in calculating the separated electrostriction coefficients of the materials.

RESULTS AND DISCUSSIONS

Analysis of Change of Capacitance with Stressing.   The results for all the low-K dielectrics exhibits a good linearity for the $\Delta C/C$ vs. X plots, as shown in Fig. 2. This is an important verification of the method, since the premise is that the first converse effect is

a linear variation. A direct loading scheme at low loading (up to 4kg masses) is thus shown to be acceptable.

Differences in the sign of the capacitance change with stress are shown for different materials. For $KMnF_3$, the capacitance decreases with stressing for all orientations. This implies that fringing field effects are not dominant. For the fluorite family, the <100> cut shows increasing capacitance with stress, and the other two cuts show decreasing capacitance with stress. However, it has been shown in an earlier paper that such effects are consistent with the elastic anisotropy (18). For low-K dielectrics, the dielectric anisotropy is typically small in comparison to that for ferroic materials. We expect that the elastic anisotropy governs the electrostrictive anisotropy in these materials.

Tables 1 and 2 summarize the electrostrictive coefficients measured in this work. Measurements of electrostriction coefficients confirmed by both direct and converse methods exist in the literature (14) for fluorites and fluoride perovskites. This comparison is shown in table 1. It is seen that there is good agreement between the coefficients measured in this work and the confirmed Q_{ij} coefficients. The result for MgO is consistent with the Q_h value measured for this material (8). For most other noncubic materials, these are the first reliable measurements. The converse method measurements are being cross checked by interferometric techniques. Variation of Q values with frequency is very small in the range measured (100Hz–100kHz) for most low-K dielectrics.

Summary of Results for Low-K Dielectrics.   All values are measured at room temperature and 1kHz unless specified otherwise.
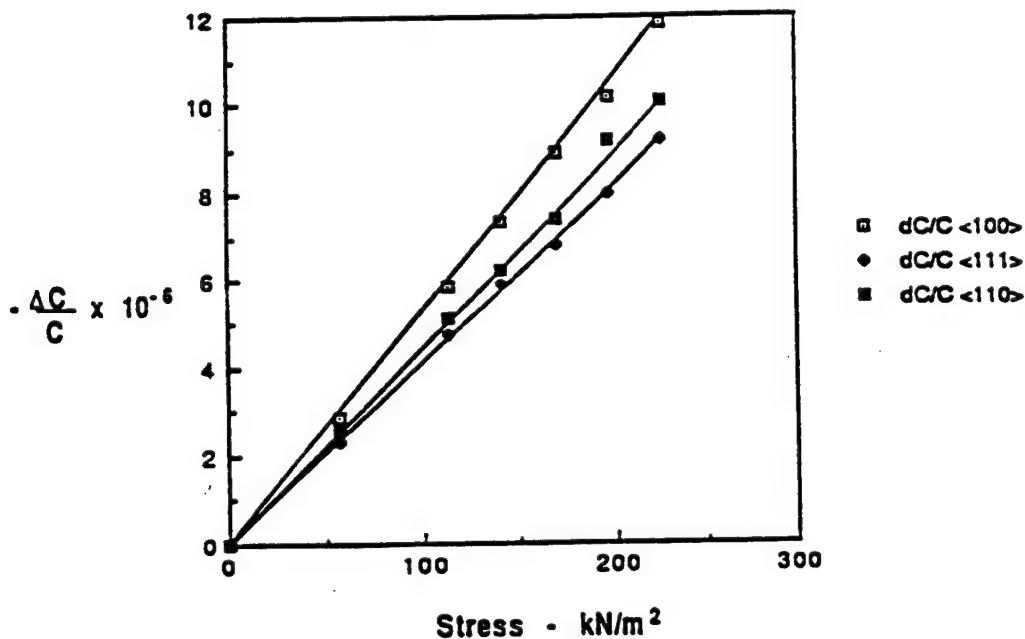
FIG. 2

Fractional change in capacitance with on stressing for the <100>, <110> and, 111> cuts of $KMnF_3$.

TABLE 1
Separated Q Coefficients – Q Values in m^4/C^2*

Material	Dielectric Constant	Q_{11}	Q_{12}	Q_{44}
$KMnF_3$	9.76	0.49 (+0.45)	-0.10 (-0.09)	1.15 (1.10)
CaF_2	6.79	-0.49 (-0.51)	-0.48 (-0.45)	2.01 (1.95)
BaF_2	7.36	-0.31 (-0.33)	-0.38 (-0.39)	1.88 (1.83)
SrF_2	6.46	-0.33 (-0.34)	-0.34 (-0.31)	1.60 (1.53)

*Values measured by Sun et al. (14) are given in parentheses, for comparison.

An Anharmonic Model for Electrostriction. A model based on the work of Uchino et. al. (19) is presented here and evaluated for the prediction of Q values in low-K dielectrics. The model is based on the rocksalt structure which has a coordination number N = 6.

We use a Born-Mayer potential function in an exponential form rather than an inverse power form to calculate the average potential energy U(x) per ion pair. For ions of charge +q and -q, with x as the distance between a cation and the neighboring anion,

$$U(x) = \frac{Mq^2}{x} + N\beta \exp(-x/\rho)$$

where M is the Madelung constant and ρ and β are potential constants. Setting $dU(x)/dx = 0$ gives us the equilibrium separation x_o. For small displacements Δx from x_o, the change ΔU in potential energy may be expressed as a function of Δx as follows:

$$U(x) - U(x_o) = \Delta U = f(\Delta x)^2 - g(\Delta x)^3,$$

where

$$f = \frac{Mq^2}{x_0^2}\left(\frac{1}{\rho} - \frac{2}{x_0}\right)$$

and

$$g = \frac{Mq^2}{6x_o^2}\left(\frac{1}{\rho^2} - \frac{6}{x_0^3}\right).$$

TABLE 2
Q_{11} Coefficients in m^4/C^2

Material	Dielectric Constant	Q_{11}
MgO (Periclase)	9.83	0.34
Al_2O_3	10.13	-0.48
Spodumene Glass	7.96	0.46
LiF	9.06	0.57
BeO	7.16	1.48
Calcite	8.42	1.19

An applied electric field E alters the potential energy to $\Delta V_{\pm} = \Delta U \pm qE\Delta x$. The subscript on V denotes the ion-pair positive and negative direction. The Boltzmann distribution is used to calculate the average equilibrium separation $\Delta x_{\pm}$ under a field E at a temperature T.

$$\Delta x_{\pm} \sim \frac{\int_{-\infty}^{\infty} \Delta x \, \exp\left(\frac{-\Delta V_{\pm}}{kT}\right) d\Delta x}{\int_{-\infty}^{\infty} \exp\left(\frac{-\Delta x_{\pm}}{kT}\right) d\Delta x} \sim (3gk/4f^2)T \pm (q/2f)E + (3gq^2/4f^3)E^2$$

The strain $(\Delta x_+ + \Delta x_-)/2x_0$ due to electric field alone, in the ion pair is then $(3gq^2/4f^3x_0)E^2$. The polarization $P = q\Delta x/2x_0^3$, where the denominator is the volume per ion pair. We may then write $P = q^2E/4fx_0^3$ and the longitudinal electrostriction coefficient Q_{11} as

$$Q_{11} = \frac{12gx_0^5}{fq^2}$$

and

$$Q_h \sim (1-2\sigma)Q_{11}$$

using the Poisson relation.

The averaged ionic valence $Z(q = Ze)$ value is 1 for halides, 2 for MgO and 1.5 for fluoride perovskites and fluorites. x_0 is approximated as half the lattice parameter. The value for the potential constant ρ is taken as 0.35Å (19).

For LiF, $x_0 = 2.15$Å, $g/f = 1/6[(r^{-2} - 6x_0^{-2})/(r^{-1} - 2x_0^{-1})] = 5.92 \times 10^9 m^{-1}$, $q^2 = 2.56 \times 10^{-38}C^2$, and $x_0^5 = 4.59 \times 10^{-49}m^5$. This gives $Q_{11} = 1.27 m^4/C^2$, and $Q_h = 0.53 m^4/C^2$.

Table 3 compares the results of the model to the values measured in this work, for representative cubic samples. There is no explicit dependence of Q coefficients on the constants M and N. The ionic valence and the cation-anion separation seem to be the determining parameters for the value of Q. The model significantly deviates from calculated results in two instances. For halides, this may be due to dislocations interfering with electrostrictive deformation. The fluorites do not have the rocksalt structure, and themodel deviates from observed values for these too. Better agreement is seen for other cubic structures including simple ferroelectric perovskites (19).

This model is efficient as a first order approximation. It also reflects relationships between electrostriction and other anharmonic properties (20). However, further modeling efforts will need to incorporate, among other parameters, local field effects, anisotropy, and crystal structure effects.

TABLE 3

Comparison of some cubic low-K dielectric $Q(m^4/C^2)$ values with those predicted by modeling

Material	x_0 Å	Q_h - observed	Q_h - calculated
LiF	2.15	0.36	0.53
CaF_2	2.73	0.47	0.63
MgO	2.10	0.18	0.16
$KMnF_3$	2.05	0.24	0.21

CONCLUSIONS

With this and in prior work, we have shown that compressometry is a reliable and accurate method to determine the electrostrictive constants of even low-K dielectrics. This implies that this is a technique that can be used to investigate electrostrictive properties over the entire range of size effects, from minute to large effects such as in relaxor ferroelectrics. The values for Q coefficients obtained by this method are in good agreement with prior vales measured by techniques of comparable accuracy. We are now measuring electrostriction coefficients for these materials using laser interferometric ultradilatometry. It is expected that accurate and reliable Q values for low K dielectrics, that have been confirmed by two independent techniques, will be very helpful for modeling and understanding this basic effect better.

ACKNOWLEDGMENTS

REFERENCES

1. R.E.Newnham, NIST Special Publication, **804**, 39, (1991).
2. R.M. Waxler, IEEE J. Quantum Electronics, QE-7, 4, 166 (1971).
3. P.B. McGrath and R.W. Bradish. IEEE Trans. on Electrical Insulation, **23**, 2, 189 (1989).
4. T.C. Guo and W.W. Guo, IEE Ann. Rept., Conf. on Elec. Insulation and Diel. Phenomena. IEEE, NY, 152 (1987)
5. A.F.Devonshire, Adv. Phys., **3**, 94 (1954).
6. K. Rittenmyer, Ph.D. Dissertation, The Pennsylvania State University, (1984).
7. Z.Y. Meng, Th. Kwaaital, W.M.M.M. van den Eijnden, J. Appl. Phys., **21**, 175 (1988).
8. K. Uchino, L.E. Cross, Jpn. J. App. Phys., **19**, L171 (1980).
9. L.Bohaty, S. Haussuhl, S. Acta Cryst., Sect. A, **33**, 114 (1977).
10. Q.M.Zhang, W.Y. Pan, L.E. Cross, J. Appl. Phys., **63**, 2492 (1988).
11. S.W. P. Sterkenburg, Th. Kwaaitaàl, W.M.M.M. van den Eijnden, Rev. Sci. Instrum., **61**, 2318 (1990).
12. P. Preu. S. Haussuhl. Sol. St. Comm., **45**, 619 (1983).
13. Z.Y. Meng, L.E. Cross. J. Appl. Phys., **57**, 488 (1985).
14. Y.M. Sun, Z.P.Chang, W.Y. Pan, W.W. Cao. L.E. Cross, J. Mat. Sci. Lett., **7**, 327 (1988).
15. K.K. Hruska, J. App. Phys., **68**, 41 (1990).
16. K.K. Hruska, R. Brendel, J. App. Phys., **67**, 1676 (1990).
17. E. Kittinger, J. Tichy, W. Friedel, J. Appl. Phys., **60**, 1465 (1986).
18. V. Sundar and R. E. Newnham, J. Mat. Sci. Lett., **13**, 799 (1994).
19. K. Uchino. S. Nomura. K. Vedam, R.E. Newnham and L.E. Cross, Phys Rev. B, **29**, 6921 (1984).
20. V. Sundar and R. E. Newnham. Ferroelectrics. **135**, 431 (1990).

APPENDIX 31

PII S0025-5408(96)00036-0

Pergamon

INTERFEROMETRIC EVALUATION OF ELECTROSTRICTION COEFFICIENTS

V. Sundar[1]*, J.-F. Li[2], D. Viehland[2] and R.E. Newnham[1]
[1]Intercollege Materials Research Lab., The Pennsylvania State University,
University Park, PA 16802
[2]Department of Materials Science and Engineering., The University of Illinois at Urbana-
Champaign, Urbana, IL 61801

ABSTRACT

A modified Michelson-Morley laser interferometer for measuring very small
(10^{-2} Å) electrostrictive displacements in low-K dielectrics is described. Prob-
lems specific to the evaluation of electrostrictive Q coefficients in low-K dielec-
trics, such as sample geometry, surface effects, sample warping, and Maxwell
stresses are discussed. This is a subresonant method, so the frequency limita-
tions (~ 160 kHz, upper limit) are established for typical ceramic samples. Mea-
surements of M_{ij} on fluorites (CaF_2, BaF_2,SrF_2), a fluoride perovskite ($KMnF_3$),
Al_2O_3, BeO, LiF, spodumene glass ($Li_2O \cdot Al_2O_3 \cdot 4SiO_2$), calcite ($CaCO_3$) and
MgO along with a glass ceramic sample (Corning Glass 888VE) and a relaxor
ferroelectric (3%Ca/PMN) are reported. Results from this method are compared
to a set of converse method measurements on these materials presented earlier.
Excellent agreement between the two methods is obtained for all samples except
the alkali halides. This establishes reliable and accurate values for the Q coeffi-
cients of these samples.

KEYWORDS: A. electronic materials, D. dielectric properties. D.
piezoelectricity

---

*To whom correspondence should be addressed.

INTRODUCTION

Electrostriction—The Direct Effect. Electrostriction is the basic electromechanical coupling mechanism in all insulators. Its effects can range from very minute in low-K dielectrics to very large effects in relaxor ferroelectrics. The thermodynamic phenomenology, of electrostriction has been well established, and helps define the effect and suggests methods of measurement (1). The elasto-dielectric contributions to the Gibbs free energy of an insulating crystal may be written as:

$$G = G_o(T) - 1/2s^E_{ijkl}X_{ij}X_{kl} - 1/2\varepsilon^x_{mn}E_mE_n - M_{mnij}X_{ij}E_mE_n$$

where s_{ijkl} is the elastic compliance tensor under appropriate boundary conditions and X_{kl} the components of elastic stress, and ε_{mn} the dielectric permittivities. Taking double partial derivatives, we may define the field related electrostriction coefficients for the direct and first converse effects as:

$$M_{mnij} = 1/2(\delta^2x_{ij}/\delta E_m\delta E_n)_X \qquad \text{and} \qquad M_{mnij} = 1/2(\delta\eta_{ij}/\delta X_{mn})_P$$

Polarization based Q coefficients, that better reflect the quadratic nature of the effect for materials where the permittivity changes with field applied may also be defined.

$$Q_{mnij} = 1/2(\delta^2x_{ij}/\delta P_m\delta P_n)_X \qquad \text{and} \qquad Q_{mnij} = -1/2(\delta\chi_{ij}/\delta X_{mn})_P$$

where χ_{kl} is the dielectric susceptibility and η_{kl} the dielectric stiffness.

The second converse electrostrictive effect is the polarization dependence of the piezoelectric voltage coefficient g_{jmn}, and may be expressed as

$$Q_{ijmn} = \delta g_{jmn}/\delta P_i$$

Typically, a low-K dielectric subjected to a high field of about 5 MV/m will develop an induced strain of the order of 10^{-5}. For a typical sample thickness of 1 mm, this involves resolving displacements of 10^{-2} Å at the very least. For the measurements using the first converse method, the limitation is aF level resolution of capacitance changes on stressing. It is evident that any technique used to measure these effects needs to be highly precise and accurate in resolving small displacements or changes in capacitance.

The difficulty of accurate measurements of these coefficients may be one reason why significant differences exist (even in signs of coefficients) for electrostriction values reported in literature (2,3). This work aims at partially rectifying this situation by measuring electrostriction coefficient by two independent techniques. The results of the direct method are reported here. The converse method results have been reported earlier, and the direct method results in this work are compared to those results. for verification of reliability. These are possibly the first such confirmed measurements for most of the noncubic samples reported in this work.

Interferometric Measurement Techniques. Measurements of the direct electrostrictive coefficients require the ability to accurately measure very small strains or displacements. Widely used experimental techniques include the strain gage method, the capacitance dilatometer (4,5), and laser ultradilatometers based on Michelson-Morley interferometers (6,7).
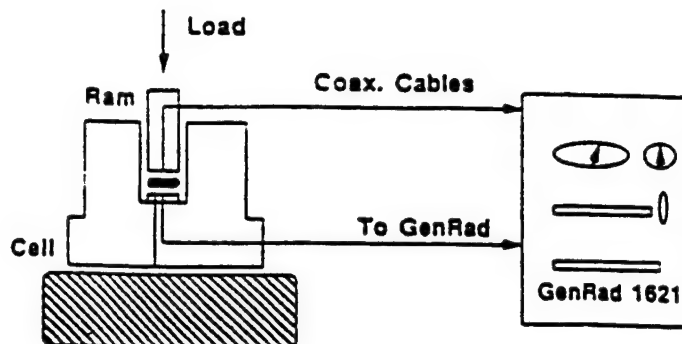
FIG. 1
Schematic of interferometer system.

Of these, the interferometric method offers the advantages of being a high-resolution (10^{-3} Å) non-contact method that does not require length calibration, and offers the possibility of interrogating points over the surface of a sample (8,9,10).

In the single-beam interferometric method, the sample under investigation is subjected to an ac field, and is interrogated with a polarized beam from a Helium-Neon laser. The path difference between the beam reflected from the sample surface and a reference beam produces interference, and resultant intensity variations that are sensed by a photodiode. The system requires isolation from noise sources in its operational frequency range of 1 kHz and less. At its most sensitive, its resolution is reported (6) at 10^{-4} Å.

Some single-beam systems may have a limited frequency range due to the possibility of sample 'back motion' at higher frequencies. Also, sample bending is a possible source of anomaly. These drawbacks are discussed in detail later, and may be overcome by using a system based on a double-beam interferometer (11).

The principles of measurement in the double beam (Mach-Zender) system are quite similar to those outlined above. However, both surfaces of the sample are interrogated with laser light in this system. Both beams are then combined with a reference beam to produce interference that is sensed with lock-in detection systems. This system is capable of a resolution of 10^{-2} Å, and is capable of measuring high-frequency piezoelectric and electrostrictive strains.

These systems have been used to measure electrostriction effects in various compounds, from large-striction perovskites to simple fluorites accurately (6).

THE INTERFEROMETRIC ULTRADILATOMETER

The interferometer used in this study was a very compact system with very light and rigid optical components. The optical path used was very small, which is of utmost importance in reducing noise. The entire system except for the body of the laser and the computerized detection systems were mounted in an acoustically and thermally shielded square box of about a meter on side. The system was mounted on a pneumatically supported table to reduce vibrations. A schematic of the system is shown in FIG. 1.

The laser used was a 2 mW polarized He-Ne laser (Uniphase). For monochromatic light such as a laser with a wavelength λ, interfering with a reference beam, the interference intensity detected may be expressed as:

$$I = Ip + Ir + 2\ Ip\ Ir\ \sin(4\pi\Delta d/\lambda)$$

where Ip and Ir and the intensities of the probe and reference beams.

The reference mirror, that reflects the reference beam, was mounted on an electrostrictive actuator stack connected to a feedback loop. This loop stabilizes the system at a point where the path difference is $\lambda/4$, the "$\pi/2$ point", where light intensity change is maximized for a small change in the displacement Δd of the sample surface. A full fringe shift was generated before any measurements, and I_{max} and I_{min}, the peak values of the interference pattern, were measured. It was then possible to hold the system at the $\pi/2$ point for the duration of the experiment.

For small displacements Δd about the $\pi/2$ point, we may rewrite the intensity detected as

$$I = 0.5(I_{max} + I_{min}) + 0.5(I_{max} - I_{min})\sin(4\pi\Delta d/\lambda)$$

A small sinusoidal displacement was obtained, giving interference intensity changes at the point of detection. The optical signal was converted to a voltage change by a biased photodiode (Motorola MRD500). The photocurrent was converted to a voltage using a high frequency current to voltage converter with a gain of 10^4 V/A. This voltage was detected by a lock-in amplifier (Stanford Research Systems 850) as V_{out} an rms value. The lock-in amplifier had high noise rejection and was used to amplify and filter out noise from the measurement signal, and to read the magnitude and phase of the resulting movements. For such small displacements, we may use $\sin(x) \sim x$. This implies the interference intensity change is linearly proportional to the induced displacement. The displacement may now be expressed as:

$$\text{displacement} = \left(\frac{\lambda}{\sqrt{2\pi}}\right)\left(\frac{V_{out}}{V_{p-p}}\right)$$

This displacement was then plotted against applied voltage to calculate the electrostriction coefficients.

EXPERIMENTAL PROCEDURE

Sample Preparation and Limitations. Oriented <100>, <110> and <111> single crystals of the cubic samples CaF_2, BaF_2, SrF_2, $KMnF_3$ were used in this study. For cubic LiF and MgO, <100> oriented samples were used. In noncubic symmetries, flat single crystals of trigonal Al_2O_3 and calcite ($CaCO_3$) with the surface perpendicular to the <100> axis of two fold symmetry were used. A hexagonal BeO crystal with the same <100> orientation was also tested. For more complex compositions, one sample of spodumene glass ($Li_2O \cdot Al_2O_3 \cdot 4SiO_2$), one of Corning glass ceramic 888VE, with a composition 86 wt% ferroics (50% $PbMn_{1/3}Nb_{2/3}O_3$, 50% $BaTiO_3$)14 wt% zinc aluminosilicate, and a relaxor ferroelectric composition of PMN ($PbMn_{1/3}Nb_{2/3}O_3$) with 3% calcium modification to shift the T_{max} down to -39°C were tested. The relaxor is thus well over its T_{max} and completely paraelectric at room temperature where all testing was done.

One of problems that has been reported in interferometric measurements is the possibility of non-uniform deformation of the sample. Local electric field differences can generate strain

differences that are not averaged out over the bulk of the sample. This is especially important in electrostrictors where the strain is proportional to the square of the applied field. To minimize sample warping, extreme geometries such as rods (bending) and disks (potato chip-like warping) were avoided. Instead, the samples were all cut into bulk cubic samples 1mm on side. This geometry has been shown to best minimize variations of displacement values across the surface of a sample.

Reference mirrors were made out of slip covers sputtered with gold, cut into suitable shapes, and epoxied on to the surface of the sample to provide an optically reflective front surface, along with silver electrode wires. The sides of the samples were then varnished to prevent air breakdown around the sample. This method of preparation also reduced the problem of charge buildup on the front surface of the sample. Such a charge buildup has been shown to introduce error in path length measurements by changing the density of the air near the front surface. The sample was then glued with conductive epoxy on to a relatively massive specially shaped brass disk and placed in a compact and rigid optical mount.

System Limitations. Limitations have been discussed in detail in an earlier work (12) and are summarized here. The frequency range of the system as determined by the system electronics has been calculated to be 10 Hz to 100 kHz. Between 2 Hz and 100 kHz, the displacement resolution for the system was better than 10^{-4} Å. Below this frequency, extraneous sources such as acoustically induced vibrations and air currents are possible sources of near-linear decrease in resolution. The wavelength stability of the system is very high, and the intensity stability was good over a period of a few hours. Displacement linearity has been established using x-cut quartz for the range of 10^{-14} to 10^{-8} m.

It is assumed that the back surface of the sample is stationary in these measurements. This may not hold true at higher frequencies. Here, the center of mass of the sample is held in place by inertia. This implies that either the epoxy holding the back surface to the brass disk is deformed or the brass disk as such is deformed. For a very large bonding layer thickness of 100 μ, the resonant frequency is calculated to be 167 kHz. A first approximation calculation for the resonant frequency arising from brass displacement gives 178 kHz. Both these frequencies are conservative estimates, and are both above 100 kHz, the high-frequency limit of the system.

Corrections for Maxwell Strains. The attractive coulombic forces between the free charges on the electrodes of the sample causes a change in dimension in the sample. While normally insignificant, this strain has to be corrected for in measurements of the delicacy and accuracy performed here. For a parallel plate capacitor with a uniform charge distribution, the attractive stress between the electrodes is given as (13):

$$X_m = -0.5 \, K_{11} \varepsilon_0 E^2$$

This stress is always compressive. It is proportional to the square of the applied field, and produces a negative strain. To correct for this, we need to add a corresponding value to the measured strain. This implies that the true electrostriction M'_{11} in any crystal direction is given by:

$$M'_{11} = M'_{11} \text{ (measured)} + 0.5 \, \varepsilon_0 s'_{11} K_{11}$$

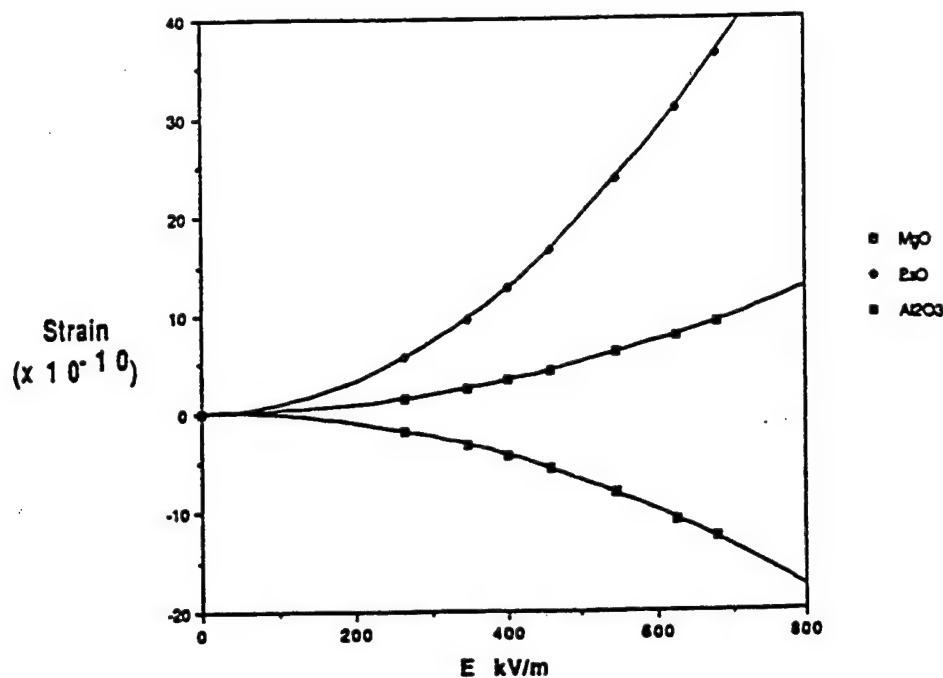This correction was performed on all the samples measured.

FIG. 2
Some strain vs. electric field results prior to Maxwell stress corrections.

MEASUREMENTS

The samples were coated with varnish on the sides, and mirrors were epoxied on to the front surfaces. They were then cured for 12 hours on a hot plate to set the mirrors and the electrode wires.

At the beginning of the measurements, the laser was allowed to stabilize over an hour, and then the peak to peak voltage was measured. Samples were then measured individually by increasing the applied voltages in small steps. The magnitude and the phase of the output voltage were recorded. Phase information was used to determine the sign of the M coefficient measured. Electrostrictive strain was observed at twice the frequency of the applied field. This is an important aid in ensuring that non-electrostrictive strains are not measured. For all samples, the lock-in amplifier was used to check for any odd harmonics. None of the samples displayed any odd harmonics. This ensured that no piezoelectric contributions were present in the ferroic samples such as the glass ceramics or the relaxors. The second harmonics for all samples gave an easily and accurately measurable output voltage. For the glass ceramic and relaxor ferroelectric samples, fourth and sixth harmonics were measurable. For BeO, calcite, Al_2O_3, LiF and the <111> cuts of the fluorites, the fourth harmonics were measurable, but not the sixth harmonics. This indicates that interferometry may be sufficiently sensitive to calculate even the higher order coupling terms such as the sixth rank coupling Φ_{ijklmn} for some samples.

The phase of the relaxor 3% Ca/PMN was noted as a reference, since it is known to have a large positive M_{33} coefficient. The phases of the fluorite samples for M_{11} and M_{12} and the phase of M_{11} for the alumina sample were 180° out of phase with the relaxor, thus establishing their signs as negative.

TABLE 1
Comparison of M_{11} Values as Measured and Corrected for Maxwell Stresses

Sample	K-dielectric constant	M_{11}–corrected, $\times 10^{-21} m^2/V^2$	M_{11}– as measured, $\times 10^{-21} m^2/V^2$
BaF$_2$	7.36	-1.04	-1.54
KMnF$_3$	9.76	3.08	2.66
CaF$_2$	6.79	-1.25	-1.54
SrF$_2$	6.46	-1.16	-1.44
LiF	9.06	4.02	3.57
MgO	9.83	2.02	1.85
BeO	7.16	4.31	4.23
Calcite	8.42	5.17	4.74
Spodumene glass	7.96	1.63	0.686
Al$_2$O$_3$	10.13	-3.20	-3.30
Materials with higher dielectric constants			
Corning 388VE glass ceramic	296.8	5.55×10^{-19}	5.53×10^{-19}
3% Ca-modified PMN	3943.5	3.52×10^{-18}	3.52×10^{-18}

Quadratic curves were fitted to the strain versus electric field results. Fig. 2 shows the strain vs. electric field plots for MgO, BeO, and Al$_2$O$_3$ prior to corrections for Maxwell stresses. Much lower fields were used for the glass ceramic (10 kV/cm max) and relaxor ferroelectric (0.8 kV/cm max) were used, because of the large electromechanical coupling expected. The samples showed quadratic strain responses in this region. Using the method of least squares, a parameter R^2 was calculated to evaluate the exactness of the quadratic curve fitting to the data. All samples had an R^2 value of 0.97 or better, with $R^2 = 1$ being the value for a perfect fit. This is also important in determining the true electrostrictive nature of the strain.

M coefficients for the samples, both corrected for Maxwell stresses and uncorrected, along with their dielectric constants, are given in Table 1. The uncorrected values are of interest particularly in electronic engineering applications. They represent the total measurable electromechanical response of these materials under an applied field, and not just the purely electrostrictive component.

In comparing the results from this method to those from converse method measurements, M_{ij} coefficients have been converted to the polarization related Q_{ij} coefficients for consistency with earlier work (14,15). The Q coefficients better reflect the quadratic nature of electrostriction especially for ferroic materials, where the dielectric constant changes with the field. The results of these measurements are summarized in Table 2.

It may be seen in the tabulation that all results agree in sign with the results from the converse measurement (16). The only serious discrepancy in magnitude is observed for the alkali halide LiF. Inaccuracy in measurements of electrostriction in these materials has been attributed to the release of charge from charged dislocations. This enhances Maxwell stresses and induces larger elastic strains and plastic deformation. The nonuniformity of the electric field in the sample may also be enhanced.

CONCLUSIONS

It is seen that interferometric measurements of electrostriction coefficients yield accurate and reliable values for the coefficients that are in excellent agreement with results independently

TABLE 2
Comparison of Direct and Converse Method Results

Material		Direct Q_{11} m^4/C^2	Converse Q_{11} m^4/C^2
BaF$_2$	Q_{11}	-0.33	-0.31
	Q_{12}	-0.39	-0.38
	Q_{44}	1.86	1.88
Al$_2$O$_3$		-0.49	-0.48
Spodumene Glass		0.43	0.46
KMnF$_3$	Q_{11}	0.51	0.49
	Q_{12}	-0.09	-0.10
	Q_{44}	1.16	1.15
CaF$_2$	Q_{11}	-0.48	-0.49
	Q_{12}	-0.48	-0.46
	Q_{44}	1.99	2.01
LiF		0.79	0.57
888 VE Corning Glass Ceramic		0.081	0.079
MgO		0.33	0.34
BeO		1.45	1.48
SrF$_2$	Q_{11}	-0.33	-0.33
	Q_{12}	-0.36	-0.34
	Q_{44}	1.64	1.60
3% Ca / PMN		2.89×10^{-3}	3.33×10^{-3}
Calcite		1.20	1.19

obtained by the converse method technique of compressometry. The high displacement resolution of the instrument makes it especially useful in this application. This confirmation also validates compressometry as a powerful technique for studying electrostrictive effects. Efforts are under way to study ferroic materials using these and other measurement techniques to evaluate them as electrostrictive actuators and assess the changes in electrostriction with grain size variations.

ACKNOWLEDGMENTS

REFERENCES

1. A.F. Devonshire. Adv. Phys., 3, 94 (1954).
2. K. Rittenmyer, Ph.D. Dissertation. The Pennsylvania State University. (1984).
3. Z.Y. Meng. Th. Kwaaital, W.M.M.M. van den Eijnden. J. Appl. Phys., 21, 175 (1988).
4. K. Uchino. L.E. Cross. Jpn. J. App. Phys., 19. L171 (1980).
5. Bohaty, L.; Haussuhl, S.; Acta Cryst., Sect. A. 33, 114 (1977).
6. Q.M. Zhang. W.Y. Pan. L.E. Cross, J. Appl. Phys., 63, 2492 (1988).
7. S.W.P. Sterkenburg, Th. Kwaaitaal, W.M.M.M. van den Eijnden, Rev. Sci. Instrum., 61. 2318 (1990).
8. Allenworth. D.L., Rev. Sci. Instrum., 51, 1380 (1980).

9. T.R. Gururaja. W.A. Schulze. L.E. Cross. R.E. Newnham. B.A. Auld. J. Wang. IEEE. 32. 481 (1985).
10. B.J. Luymes. Rev. Sci. Instrum.. 54. 90 (1983).
11. W.Y. Pan.L.E. Cross. Rev. Sci. Instrum.. 60. 2701, (1989).
12. J-F Li, P. Moses. D. Viehland. Rev. Sci. Instrum., 65, 1089 (1994).
13. J. Grindley. Phys. Rev.. 160, 698 (1967).
14. V. Sundar and R. E. Newnham. J. Mat. Sci. Lett., 13, 799 (1994).
15. V. Sundar, K.WaGachigi. D. McCauley, K.A. Markowski, R.E. Newnham. IEEE Symposium Proc., ISAF-94. 689, (1994)
16. V. Sundar and R.E. Newnham, Mater. Res. Bull. 31 (1996), in press.

APPENDIX 32

The Effect of Doping and Grain Size on Electrostriction in $PbZr_{0.52}Ti_{0.48}O_3$

V Sundar, N. Kim*, C.A. Randall, R. Yimnirun, R.E. Newnham
Intercollege Materials Research Lab., The Pennsylvania State University, State College, PA 16803,
* Samsung Inc., Suwon, Korea.

Abstract - The electromechanical properties of undoped $PbZr_{0.52}Ti_{0.48}O_3$ (PZT 52/48) samples in a size range 0.7 - 14μ were studied as a function of the grain size. Internal bias fields were found to have significant effects on the dielectric and piezoelectric behavior of the samples. Strains from domain reorientation caused hysteresis in the strain vs. polarization curves. It was necessary to filter out these contributions in order to study the variation in Q_{33}, the average ceramic electrostriction coefficient, with grain size. Q_{33} varied from $2.44m^4/C^2$ at 14μ to $2.04m^4/C^2$ at 0.7μ. An apparent critical size of 2.4μ was observed for Q_{33}. The suppression of the maximum dielectric constant for PZT 52/48 at the Curie Temperature may be related to to the changes in grain size through the electrostrictive effects of clamping stresses.

I. INTRODUCTION

Electrostriction is the fundamental mechanism of electromechanical coupling in all insulator materials. It is a quadratic effect, that quantifies the coupling between the strain developed in a material and the polarization induced in it as a function of an applied electric field. It is defined in terms of field related M coefficients or polarization related Q coefficients as follows :

$$x_{ij} = M_{ijkl} E_k E_l$$
$$x_{ij} = Q_{ijkl} P_k P_l \quad (1)$$

In isotropic ceramic materials, the longitudinal effect may be expressed by the simpler quadratic relationship :

$$x_3 = Q_{33} P_3^2. \quad (2)$$

The polarization related Q coefficients reflect the quadratic nature of electrostriction even in materials that have dielectric properties that vary with the applied electric field [1]. As part of a study to explore the

effects of grain size on phyisical properties of ferroics, a suite of $PbZr_{0.52}Ti_{0.48}O_3$ (PZT 52/48) morphotropic phase boundary composition samples was chosen as the focus of this study. The samples had a grain size (gs) range 0.7 - 14μ, and were prepared by B-site precursor methods, followed by thermal profile variations for grain size control at grain sizes over 2.4μ, and by HIP and HUP for grain sizes of 2.4μ and below. This variation in processing proved to significantly affect the properties of the samples [2].

The objectives of this study are to gain a better understanding of how the electrostriction coefficient Q_{33} varies with grain size for this composition, and how this relates to the other property (such as the dielectric permittivity, or piezoelectricity) variations with grain size.

II. PROPERTY VARIATIONS WITH GRAIN SIZE

A. *Lattice Parameter and Domain Size*

The unit cell volume and tetragonality (c/a) were determined by X-ray analyses. The unit cell volume varies very little between 12μ (~67.3Å^3) and 2.4μ. In contrast, it decreases from 67.1Å^3 at 2.4μ to 66.1Å^3 at 0.8μ. The tetragonality ratio (c/a) correspondingly decreases from 1.0245 at 2.4μ to 1.022 at 1μ. Internal stresses could hinder domain formation at low grain sizes and thus affect ferroelectric properties. However, TEM studies verified the presence of distorted domain structures at grain sizes below 1μ [3].

B. *Dielectric Properties*

An apparent critical size of 2.4μ was observed for the dielectric constant (Fig.1).This behavior is similar to that observed by Webster and Weston [4]. The room temperature dielectric properties include 20-60% extrinsic contributions from mechanisms such as domain wall motion, piezoelectric coupling, and defect dipole motion. These extrinsic contributions were frozen out at low temperatures. Measurements of the dielectric proerties at 15K verified this effect.

C. Piezoelectric Coefficients (d_{33})

Fig. 2 shows the variation of the d_{33} coefficients with grain size. The d_{33} was observed to decrease steadily till 2.4μ and then increase. Similar low temperature behavior was observed, with lower magnitudes of d_{33} as a result of lower extrinisic contributions.

The internal bias field hypothesis may be used to explain the piezoelectric behavior of the PZT samples. Bias fields are very dependent on doping. Donor dopants such as La, Nb etc. give rise to very small bias fields. Acceptor dopants such as Fe, Al etc.are known to be common impurities even in undoped samples. Superoxidation effects can produce excess Pb site vacancies, causing defects that tend to fix domain walls. Defect dipoles and 'dirty' non ferroelectric grain boundaries can also ,increase bias fields in conventionally processed samples [5,6].

In conventionally processed samples, the domain switching is clamped by bias field effects. For fine grained samples with 'dirty' grain boundaries, the high level of clamping gives rise to low poling efficiencies. Hot pressing cleans up grain boundaries and causes fewer defects, as the superoxidation level decreases. The d_{33} thus increases for samples with a grain size of 2.4μ and less.

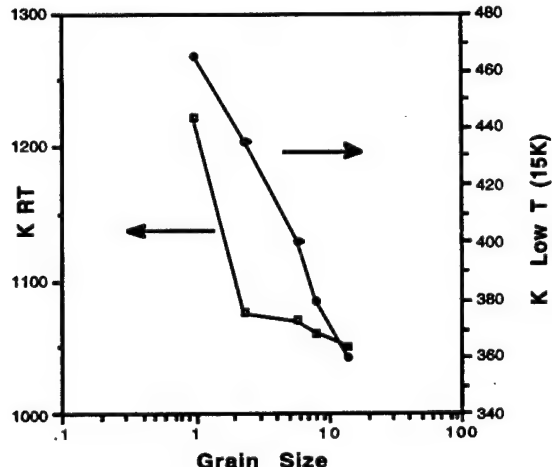## III. ELECTROSTRICTION MEASUREMENTS

A. Sample Preparation

The PZT 52/48 samples were prepared in the form of gold-electroded parallel plates with thicknesses of 0.4 - 0.8mm. The samples were depoled by heating to 500°C. No remanent piezoelectricity was observable in the samples after depoling.

B. Strain Measurement System

An automated LVDT based system capable of measuring polarization hysteresis and strain in ferroic samples was used to evaluate electrostriction. The system consists of a micrometer sample holder, a TREK 6090C-6 high voltage DC amplifier, and a Stanford SR830 DSP Lock-in Amplifier, connected through a data collection system to a personal computer. A schematic of the system is shown in fig. 3. The heart of the system is the Automated Polarization Measurement System (APMS). A measurement signal generated by activating the computer is amplified and applied to the sample. The resultant current is absorbed by the integrator circuitry of the APMS, converted to an output voltage.

The sample holder consists of a rigid steel frame. An 050-HR LVDT is mounted on the baseplate of the sample holder, with a sample mounting stage on its tip. The sample is held in a strain free state by a micrometer gage grip. Any strain in the sample may be monitored through strain outputs from the LVDT to the lock-in amplifier.

IV. RESULTS AND DISCUSSIONS

A. Size Effects in Electrostriction

Dielectric Constant Variation

Fig.1. RT and low temperature dielectric constants as a function of grain size.
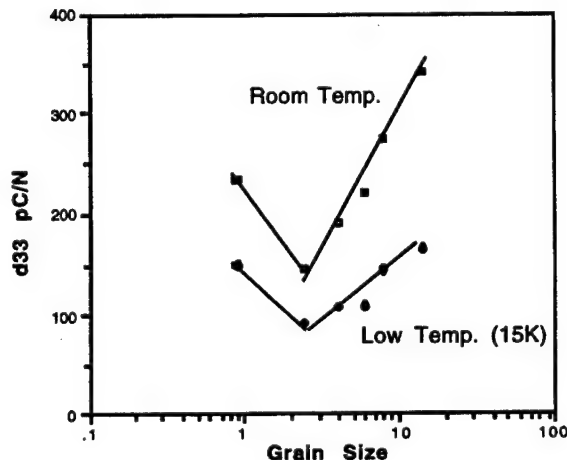
Piezo Properties

Fig.2. RT and low temperature d_{33} (pC/N) as a function of grain size.

The electrostriction in PZT 52-48 samples was measured in a grain size range from 14 - 0.7μ.

Fig. 4 shows a typical result for a sample with a grain size of 0.8μ. The unexpected hysteresis in the strain-polarization (x-P) quadratic plots is due to domain reorientation effects. Samples with large grain sizes (~14μ) showed very quadratic x-P plots. Hysteresis was observed at all other grain sizes, and decreased with the grain size down to 2.4μ. Hysteresis increased below 2.4μ consistent with the clamped domain hypothesis outlined in section II. To calculate the intrinsic electrostriction of the sample, the low-field regions of the x-P plots were analyzed and Q_{33} coefficients fitted to these curves. The results for the variation of Q_{33} with grain size for all samples are summarized in fig.5 overleaf.

The largest decrease in Q_{33} is observed again between 2.4 and 1.8μ. Since the d_{33} coefficients increase in this range, it may be concluded that domain reorientation and piezoelectric effects were completely filtered out and only the intrinsic electrostriction effects were measured.

B - Electrostriction and Dielectric Size Effects

The maximum dielectric constant for PZT 52/48 decreases as a function of grain size (Fig.6). Clamping stresses from the change in unit cell volume could act through the electrostriction to cause this suppression. For a grain size change from 14 to 0.9μ, the relative
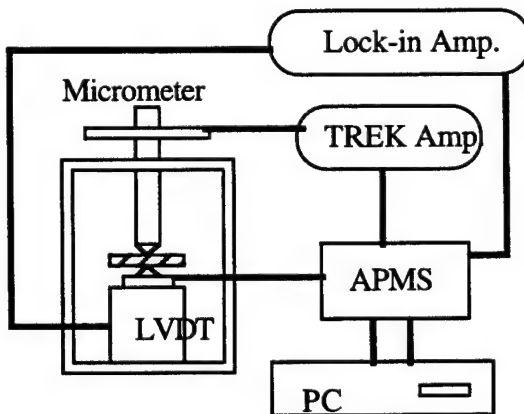

Fig.3. Schematic of Electrostriction Measurement System.
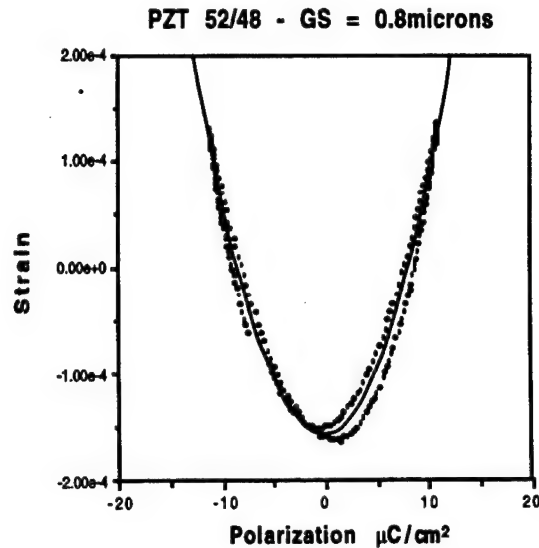

PZT 52/48 - GS = 0.8microns

Fig.4 Strain vs. Polarization results for PZT 52/48, grain size = 0.8 microns.

change in unit cell volume $\Delta V/V = 1.78 \times 10^{-2}$. Using the value of the volume compressibility $\beta v \sim 0.7 \times 10^{-11}$ Pa^{-1}, gives an equivalent hydrostatic clamping stress of 2.55 GPa. This clamping stress will be lower at T_c, the Curie temperature.

The corresponding change in inverse susceptibility, $\Delta \chi^{-1}$ is $(4.43 - 16.12) \times 10^6$. Using the relation $d\chi^{-1}/dp = 2Q_h$, with $Q_h \sim 0.005 m^4/C^2$ (@T_c, [2]), gives $\Delta p = 1.17$ GPa for stress. This is comparable to the clamping stress of 2.55 GPa. However, the corresponding shift in the Curie temperature T_c, predicted by $\Delta T_c / \Delta p = -2\varepsilon_0 C Q_h$ (C= 1.75×10^5, $\Delta T_c \sim -18°C$) is not observed.

V CONCLUSIONS

An apparent size effect was observed for electrostriction at a grain size of 2.4 microns. This corresponds to the largest decrease in tetragonality and unit cell volume The decrease in Q_{33} at 2.4μ demonstrates that the domain reorientation effects observed in the strain-polarization plots were filtered out, and intrinsic electrostriction was calculated. The clamping stresses from the change in unit cell volume could also contribute to the suppression of the maximum dielectric constant. A comparison of these effects in niobium doped PZT 52/48 could verify the aove conclusions.
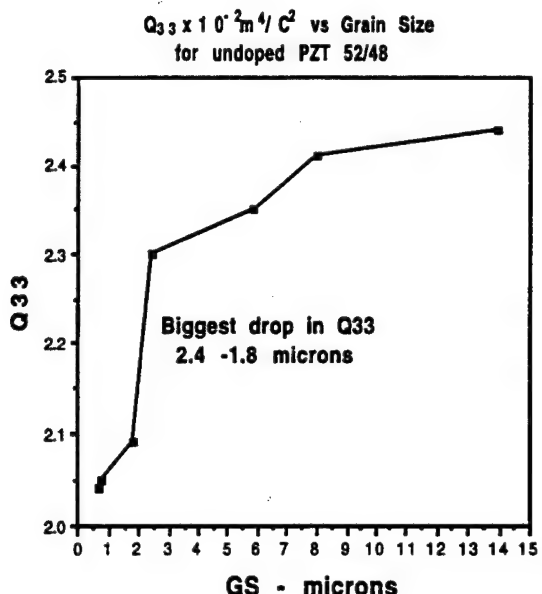
Fig.5. Variation of Q_{33} (m^4/C^2) with grain size for undoped PZT 52/48.

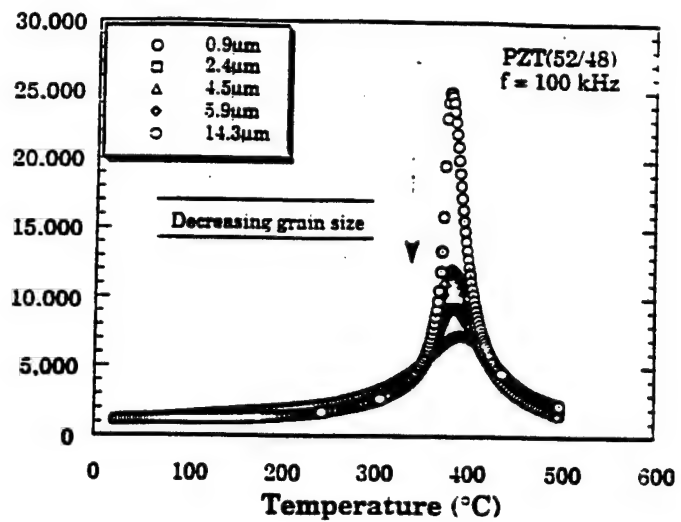Fig. 6. Suppression of the maximum dielectric constant for PZT 52/48.

ACKNOWLEDGMENTS

REFERENCES

[1] V Sundar, R.E. Newnham, *Ferroelectrics*, vol.135, p431, 1990..

[2] N. Kim, Ph.D. Thesis, The Pennsylvania State University, Univ. Park, PA 16802, 1994.

[3] W. Cao, C.A. Randall, *J. Phys. Chem. Solids*, in press.

[4] A. Webster, T. Weston, J. Canadian Ceram. Soc., vol. 37, p41, 1968.

[5] K. Carl, K.H. Hardtl, *Ferroelectrics*, vol.17, p473, 1978.

[6] G.H. Haertling, *Am. Ceram. Soc. Bull.*, vol.43, p875, 1964.

APPENDIX 33

Segregation and Inhomogeneities in Photorefractive SBN Fibers

S. Erdei [a], L.Galambos[b], I. Tanaka[c], L. Hesselink[b], F.W. Ainger[a],
L.E. Cross[a] and R.S. Feigelson[d]

a./ Intercollege Materials Research Laboratory, The Pennsylvania State University,
University Park, PA 16802, USA

b./ Department of Electrical Engineering, Stanford University, Stanford CA 95305,
USA

c./ Institute of Inorganic Synthesis, Faculty of Engineering, Yamanashi University
Miyame 7, Kofu, Yamanashi 400, JAPAN

d./ Center of Materials Research, Stanford University,
Stanford CA 95305, USA

Abstract

Ce doped and undoped $Sr_xBa_{1-x}Nb_2O_6$ (SBN) fibers grown by the laser heated pedestal growth (LHPG) technique in Stanford University were investigated by two dimensional scanning electron microprobe analysis (SEPMA). The SBN fibers grown along c [001] or a [100] axes often show radially distributed optical inhomogeneities (core effects) of varying magnitude. Ba enrichment and Sr reduction were primarily detected in the core which can be qualitatively described by a complex-segregation effect. This defect structure as a complex-congruency related phenomenon modified by the composition-control mechanism of LHPG system. Its radial dependence of effective segregation coefficient is described by the modified Burton-Prim-Slichter (BPS) equation.

Keywords: strontium barium niobate, SBN fibers, inhomogeneities in SBN, photorefractive fibers.

Strontium-barium niobate (SBN) $Sr_xBa_{1-x}Nb_2O_6$ ($0.25 \leq x \leq 0.75$) single crystals have a tetragonal (4mm) tungsten bronze structure are ferroelectrics and exhibit very large electro-optic, pyroelectric, piezoelectric effects [1-4]. SBN's excellent photorefractive properties make it a very promising real-time holographic data storage medium [5]. For this application high optical uniformity is required. In contrast to other oxides like $LiNbO_3$, $LiTaO_3$, YVO_4 etc. the SBN phase system has a huge solid-solubility region around $x = 0.61$, the congruent composition [6] in the $SrNb_2O_6$ (SN)--$BaNb_2O_6$ binary. This observation implies that no intrinsic precipitates and metastabilities are expected. However dopants like Ce or other rare-earth materials can induce deviations of the correct congruent composition and give rise to optical inhomogeneities. Furthermore the growth techniques can amplify (or reduce) these unwanted effects related to the phase diagram. In the widely used Czochralski (CZ) growth technique for instance, we can

minimize the typical microsegregated inhomogeneities like growth striations or facet induced inhomogeneities by applying very careful and precise temperature and diameter control, thermal symmetry, optimization and partial compensation of convection flows and by using very pure starting materials in the congruent composition [7]. Nevertheless the CZ growth essentially restricted to growth along the c-axis (i.e. [001] direction) due to significant anisotropy of the radial growth kinetics, but good crystals can be grown by low thermal gradient at 1510°C growth temperature [7] in Pt crucible. However the slight macrosegregation along crystal length cannot be eliminated by CZ technique.

Vertical floating zone techniques can offer a unique "composition controlling capability" for solid-solution crystals or doped crystals to eliminate the unwanted macrosegregation effects along crystals [8]. Utilizing this technique the composition of the molten zone will be automatically and gradually modified (enriched or decreased of components) to produce same composition at the growth interface which is feeding at the melting front. Consequently the modified composition of molten zone can offer macrosegregation-free crystal growth after characteristic length of material has been grown [8]. Among vertical floating zone

Fiber Growth

Single Crystal Fiber

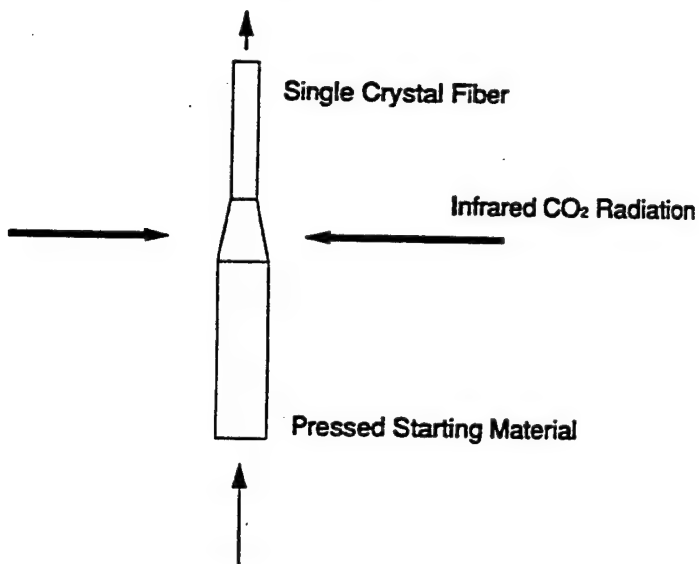Infrared CO_2 Radiation

Pressed Starting Material

Fig. 1 Schematic arrangement of Laser Heated Pedestal Growth (LHPG) system

techniques, the containerless laser heated pedestal growth (LHPG) technique provides the best solution for producing high quality SBN fibers for optical data storage systems. Fig. 1 shows a schematic arrangement of LHPG technique. The first efforts of SBN fiber growth were realized at the Center for Materials Research, Stanford University [9,10,12] and the Materials Research Laboratory of the Pennsylvania State university [11]. The importance of fiber configuration prepared for SBN growth by the LHPG technique for holographic application is emphasized by Hesselink and Redfield [12]. In addition special advantages for holographic data storage application were also observed in a-axis grown fibers. The first stable a-axis SBN fibers were grown by Wilde et al [13] and Sugiyama et al. [14] who even measured a better figure of merit in the a-axis than c-axis fibers.

In spite of these favorable characteristics special radially distributed optical inhomogeneities, in other words "core effects" can be found in SBN fibers. In the middle of the transverse cross-section of fibers Ba enrichment and a Sr reduction in concentration was already detected by scanning electron microprobe-analysis (SEPMA) in [15,8]. Figure 2 shows a typical concentration distribution profile of Ba in Ce:SBN fiber. During SBN fiber growth the molten zone will be enriched in Nb_2O_5 (Fig. 3a) and less BaO (Fig. 3b), SrO are observed. (The spherical end piece of the fiber represents the frozen molten zone in the Fig. 3). Utilizing these data it was considered that BaO has $k_{oBa} > 1$ equilibrium segregation coefficient while the Nb_2O_5 has a $k_{oNb} < 1$ coefficient. Recently we reported $1.04 < k_{oBa} < 1.34$ and $0.91 \leq k_{oNb} \leq 0.99$ coefficients estimated for Ba and Nb in [8,15]. Although we do not have direct evidences for k_{oCe}, it was concluded by indirect that it is less than unity.

To interpret observations and measurements of the above mentioned core effect (Fig. 2) we have to
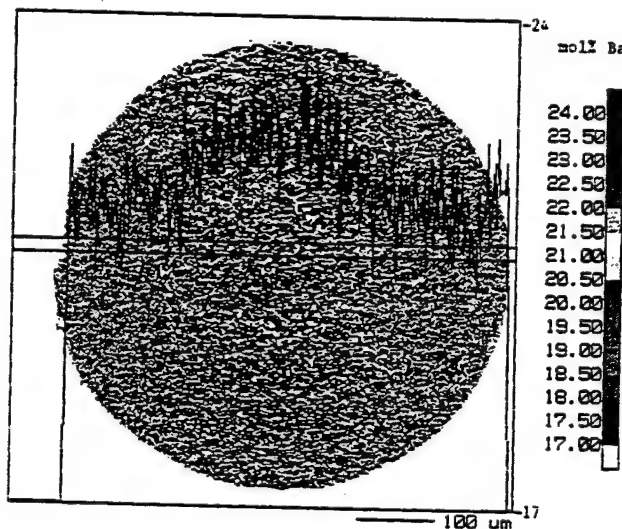
Fig. 2 Ba distribution in *c*-axis grown Ce:SBN fiber recorded by SEPMA in transverse section. The Ba concentration is recorded in mol% in the SrO-BaO-Nb_2O_5 system. (The nominal Ce concentration is 3 at% in $Sr_{0.60}Ba_{0.40}Nb_2O_6$ nominal fiber composition.)

consider and introduce the complex segregation coefficient described in detail in [8]. The modified composition of the molten zone will modify the equilibrium segregation coefficient of the different elements (Sr, Ba, Nb, Ce) which can influence each other. However, the distribution of different cations will primarily determine the effective complex segregation coefficient k_{effA} having a radial dependence. To qualitatively describe this radial dependence the classic BPS (Burton-Prim and Slichter [16]) equation can be utilized. (The exact mathematical description is not possible as analytic solution of the Fourier, Navrier-Stokes and Fick II complex partial differential equation system.) The LHPG crystallization is governed mainly by diffusion and thermally activated convection processes in close relation with the self-controlling zone mechanism and the complex segregation effects. The BPS equation gives a solution for

the one-dimensional steady-state diffusion equation allows us to express an effective segregation coefficient (k_{effA}) by Formula 1 as follows:

$$k_{effA}(r) = \frac{k_{0_A}}{k_{0_A} + \left(1 - k_{0_A}\right)e^{-\frac{f\delta_A(r)}{D_A}}} \qquad \text{Formula 1}$$

where D_A is the diffusion coefficient of the A component (element) in the solute at
        crystallization front

    f is the front growth velocity

    $\delta_A(r)$ is the radially depended diffusion boundary layer width of the A component (element)
        at the crystallization front in the molten zone (see more details of δ_A introduced by
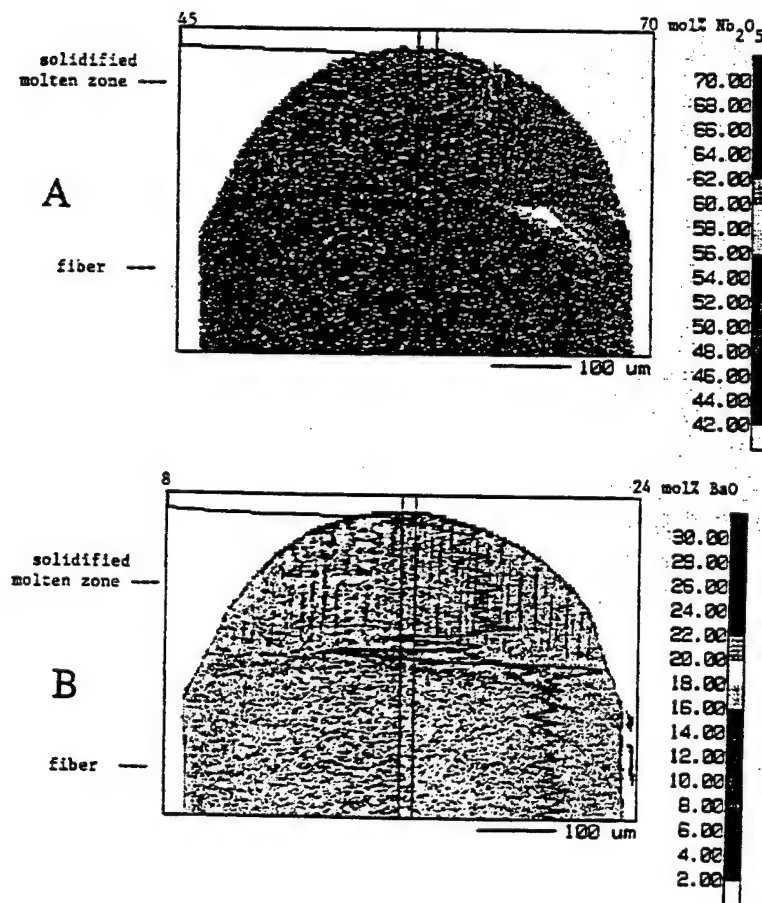   Tiller et al. in [17]).

Fig. 3 Nb (a.) and Ba (b.) distributions in Ce:SBN fibers ends recorded by SEPMA in longitudinal cross section. The approximately flat interface between fiber crystal and molten zone can also be seen on the pictures. (The nominal Ce concentration is 2 at.% in $Sr_{0.61}Ba_{0.39}Nb_2O_6$ nominal fiber composition)

The complex nonlinear cross coupling effects between above mentioned partial differential equations can be taken into account by the $\delta_A(r)$. The radial dependence of $\delta_A(r)$ will primarily determine the radial concentration distribution (optical inhomogeneities) in SBN fiber by Formula 2 as follows:

$$C_{SA}(r) = k_{effA}(r)C_{IA}$$
<div align="right">Formula 2</div>

where C_{SA} is the concentration of the A component (element) in the solidified fiber and
. C_{IA} is the concentration of the A component (element) in the floating zone

Consequently, the distribution of diffusion boundary layer width / $\delta(r)$ / depends on the complex segregation effect, the radial and axial thermal gradients in the molten zone and at the growth interface, the surface tension variation with the temperature distribution at floating zone surface (Marangoni effect [18]) and related convection flows generated by the laser source heating in the floating zone. During LHPG growth the inner section of the molten zone is the hottest place since the CO_2 laser beam is focused in the
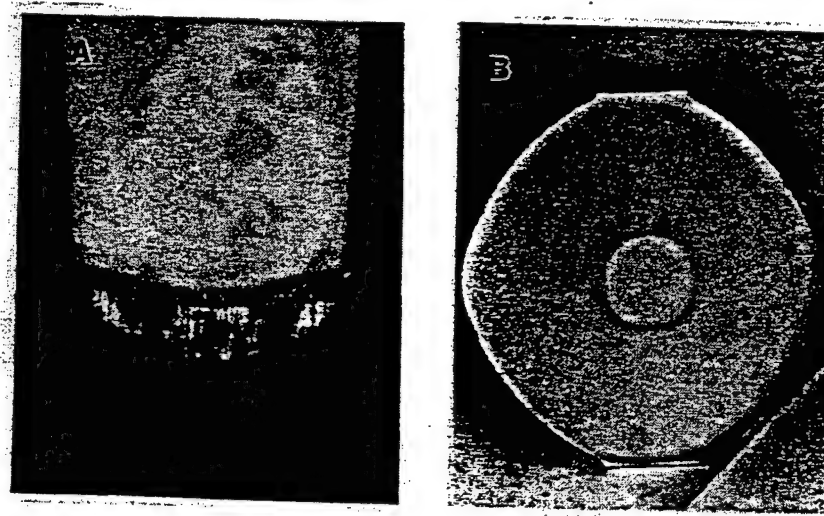

Fig. 4 Faceted growth interface of *a*-axis grown SNB fiber in longitudinal (a.) and transversal (b.) cross sections.

middle of the floating zone. Consequently, the major convection flow will be circulated up from the inner section to the peripheral region of the molten zone at the crystallization front. Ba enriched core effect (Fig. 2) results from a slightly Sr excess source in the rod composition doped by 3 at.% Ce where the k_{oBa} is more than unity ($k_{oBa} > 1$). In this case Ba poor floating zone will control the steady-state fiber growth, giving rise to an intensive convection of Ba poor melt which will decrease or minimize the $\delta_{Ba}(r)$ in the middle section of SBN fiber. Consequently the effective segregation coefficient (k_{effBa}) in the diffusion layer and the barium concentration in the fiber will be increased according to the BPS equation and Formula 2. In Ba rich SBN fibers for the $k_{oBa} < 1$ $Sr_{0.4}Ba_{0.6}Nb_2O_6$ composition, the intensive convection

as a substance carrier will build up a thicker $\delta_{Ba}(r)$ Ba enrichment is observed in the middle part of fiber (see further details in [8,15]). The dominance of thermal convection can be reduced by Marangoni convection [18], i.e. the core effect can be eliminated by reduction of fiber diameter which produces a relatively higher capillary convection effect. However this approach is not sufficient for the thicker (D > 500 μm) fibers typically required by holographic data storage systems.

Larger SBN fibers grown along the a-axis quickly lose their flat growth interface as seen in Fig. 4a. In this case a small flat facet with conical periphery is formed in the middle of the fiber. This facet growth will create a core with sharp contour (Fig. 4b) which has more contrast than the core observed in c-axis grown SBN fibers. The growth interface with facets indicates that the thermal gradient at the crystallization front is relatively small and unable to thermally reduce the equilibrium crystallographic planes(s) during growth along the a-axis. This is related to the critical axial and radial gradients which are strictly dependent on the growth orientation and on the actual composition of the molten zone especially in the diffusion boundary layer.

Acknowledgments

References:

[1]   J.R. Carruthers and M. Grasso, J. Electrochem. Soc., 117 (11) 142 (1970).
[2]   P.V. Lenzo, E.G. Spencer and A.A. Ballman, Appl. Phys. Letters 11, 23 (1967).
[3]   A.M. Glass, J. App.. Phys. 40, 4699 (1969).
[4]   R.R. Neurgaonkar and W.K. Cory and J.R. Oliver, Ferroelectrics 51, 3 (1983).
[5]   R.R. Neurgaonkar and W.K. Cory, J. Opt. Soc. Am. B3, 274 (1986).
[6]   K. Megumi, N. Nagatsuma, Y. Kashiwada, Y. Furuhata, J. Mat. Science 11, 1583 (1976).
[7]   R.R. Neurgaonkar, M.H. Kalisher, T.C. Lim, E.J. Staples and K.L. Keester, Mat. Res. bull., 15, 1235 (1980).
[8]   S. Erdei, L. Galambos, I. Tanaka, L. Hesselink, L.E. Cross, R.S. Feigelson. F.W. Ainger and H. Kojima, J. Cryst. Growth (accepted)
[9]   Initial work on fiber growth of SBN at Stanford began in 1985 as a collaborative effort between L. Hesselink and R.S. Feigelson. Contributions were made by W.L. Kway, F.M. Schellenberg and Y. Huang.
[10] R.S. Feigelson, in Materials for non-linear and Electro-Optics, Inst. Phys. Conf. Ser. 103, Part I, Ed. M.H. Lyons (Inst. Phys. , Bristol, 1989) 75.
[11] J.K. Yamamoto and A.S. Bhalla, Mat. Res. Bull. 24, 761 (1989).
[12] L. Hesselink and S. Redfield, Opt. Letters 13, 877 (1988).
[13] J.P. Wilde, D.H. Jundt, L. Galambos and L. Hesselink, J. Cryst. Growth 114, 500 (1991).
[14] Y. Sugiyama, I. Yokohama, K. Kubudesa and S. Yagi, IEEE Photonics Technol. Letters 3, 744 (1991).
[15] L. Galambos, S. Erdei, I. Tanaka, L. Hesselink, L.E. Cross, R.S. Feigelson, F.W. Ainger and H. Kojima, J. Cryst. Growth (accepted)
[16] J.A. Burton, R.C.Prim and W.P. Slichter, J. Chem. Phys. 21, 1987 (1953).
[17] W.A. Tiller, K.A. Jackson, F.W. Rutter, and B. Chalmers, Acta Met. 1, 428 (1953).
[18] D. Schwabe, A. Scharmann, F. Preisser and R. Oeder, J. Cryst. Grwoth 43, 305 (1978).

APPENDIX 34

Coherent Coupling in Ferroelectric Superlattices

Shaoping Li[1], Jeffy A. Eastman[1], J.M.Vetrone[1], R.E. Newnham[2] and L.E. Cross[2]

[1]Materials Science Division, Argonne National Laboratory
9700 South Cass Ave, Argonne, IL 60439
[2]Materials Research Laboratory, Pennsylvania State University, University Park, PA16802

Abstract—The phase transition and dielectric behavior of ferroelectric multilayers have been discussed. The coherent interaction between ultra-thin layers can be significantly strong, resulting in a broad diffuse phase transition. The thicknesses of layers and their spatial distributions hold the keys of enhancing dielectric properties in a broad temperature range.

I. INTRODUCTION

There is a fundamental interest in the study of ferroelectric superlattices because their mesoscopic structures drastically differ from bulk homogeneous materials. It has been expected that dielectric characteristics of ferroeletrics could be manipulated by controlling material's heterogeneity at the mesoscopic level(5-80nm)[1], leading to artificially engineering ferroelectric phase transitions and obtaining ferroelectric dielectrics with exceedingly larger dielectric coefficients.

Recently the experimental efforts of synthesizing ferroelectric superlattices or nanocomposites have been initiated by several groups[2] in order to produce ferroelectrics with novel dielectric properties through controlling their heterogeneities. While, on the other hand, the dielectric properties of ferroelectric superlattices and ferroelectric multilayers have also been theoretically examined in several aspects[3,4]. Schwenk et al. first employed the Ginzburg-Landau theory[3] to examine the dielectric properties of ferroelectric superlattices, such as $PbTiO_3/BaTiO_3$ superlattice with the first-order phase transition. More recently, Qu et al.[4] also analyzed the polarization and static dielectric susceptibility in ferroelectric superlattices for some special case. However, all these efforts overlooked a critical aspect: the heterogeneity in ferroelectrics with the diffuse phase transition is inhomogeneous in nature. From the phase transition point of view, the inhomogeneous heterogeneity is crucial for causing the dielectric anomalies in ferroelectrics. As well known, in normal systems, the spatial correlation length of order parameters (such as polarization) diverges at the Curie point, resulting in the dielectric singularity in ferroelectrics. While in inhomogeneous systems, the situations are quite different. The phase transitions in these situations tend to be confined in the localized regions from few nanometers upto a submicon level in scale. Additionally, the correlation lengths of local order parameters are limited by the physical sizes or dimensions of heterogeneities. More precisely, the soft modes will not propagate beyond the physical scale of heterogeneities. Another important feature in these cases is that localized transition points are virtually determined by the physical sizes of heterogeneities. Thus the phase transition in the system with mesoscopic inhomogeneities will be no longer a temperature point but a continuum temperature range as the physical sizes of heterogeneities form a continuum distribution.

Although it has long been known that most of inhomogeneous systems exhibit the diffuse phase transitions, it is still lacking a quantitative connection between the heterogeneity and dielectric coefficient in inhomogeneous systems. In this paper, we for the first time report a theoretical evaluation of dielectric phase transition behavior for a multilayer system with designed heterogeneity, based on an extended Ginzburg-Landau model. Our numerical results predict that a giant dielectric susceptibility may be obtained in ferroelectric superlattices or ultra-thin multilayer structures with the desirable heterogeneity.

II. MODEL

The Landau theory has long been successfully used to explain the phase transition behavior of ferroelectrics, and it has been proved to be a good description of the phase transition behavior in ferroelectrics because the smoothly varying coulomb force is responsible for establishing the polar phase. Recently it has been extended to study the surface and size effect on nanostructured ferroelectrics[5].

Following the expressions of the free energy in the literature[3,5], we now consider an O_h-C_{4v} proper ferroelectric phase transition in a superlattice system with different localized polarizations as order parameters. For simplicity, by assuming that the polarizations are always oriented along the z-axis, i.e., P={0, 0, P(z)}, and the superlattice dimensions along x-axis and y-axis are infinite, the free energy of the superlattice system with alternating slabs of a_n and b_n can be written as,

$$\Phi = \frac{F}{S} = \int_{-L/2}^{L/2} \left\{ \Phi_{ao} + \Phi_{bo} + \frac{\xi_1}{2}(\nabla P_a)^2 + \frac{\xi_2}{2}(\nabla P_b)^2 + \frac{1}{2}\alpha P_a^2 + \frac{1}{4}\beta P_a^4 \right.$$

$$+\frac{1}{6}\gamma P_a^r + \frac{1}{2}Q_1 P_a^2 \delta\{z \pm a_{n+1} + [\sum_n 2(a_n + b_{n+1}) - b_1 + a_{n+1}]\} + \frac{1}{2}AP_b^2$$

$$+\frac{1}{4}BP_b^4 + \frac{1}{6}CP_b^6 + \frac{1}{2}Q_2 P_b^2 \delta(z \pm b_{n+1} + [\sum_n 2(a_n + b_{n+1}) - b_1 + b_{n+1}])\bigg\}dz \qquad (1)$$

where S is the surface area of the superlattice with plane surfaces at $z = \pm L/2$; Φ_{a0} and Φ_{b0} denote the thermodynamic potential of layer A and layer B in paraelectric phase state. α, β, γ, A, B and C are normalized free energy coefficients, in which elastic coefficients and other relevant coupling parameters are tacitly included. Especially $\alpha = \alpha_0[T-T_1]$ and $A = A_0[T-T_2]$. T_1 and T_2 are phase transition temperatures in the bulk materials of layers A and B respectively. The subscripts of 1 and 2 indices describe two different layers. $T_2 > T_1$ is assumed in the present study. ξ_1 and ξ_2 are the gradient terms of order parameters, describing the polarization inhomogeneity. Q_1 and Q_2 are defined as the coherent coupling coefficients, which characterize the coherent coupling at the interface between different regions. Physically the coupling terms can be related to the stored elastic and electrostatic energy caused by coherency coupling. $\delta(z)$ is a delta function which describes the coordinates of the interface between two layers.

The integral of Eq.(1) is over all space since the order parameters vary spatially. The local order parameters $P_a(z)$ and $P_b(z)$ are the functions of space coordinates, which is illustrated in Fig.1. The spatial distribution of the polarization can be obtained by solving the Euler-Lagrange equations,

$$\xi_1 \frac{d^2 P_a}{dr^2} - (\alpha P_a + \beta P_a^3 + \gamma P_a^5) = 0 \qquad (2a)$$

$$\xi_2 \frac{d^2 P_b}{dr^2} - (A P_b + B P_b^3 + C P_b^5) = 0 \qquad (2b)$$

with following coherent boundary conditions at the interfaces,

$$P_a(z) = P_b(z)\big|_{z=[\sum 2(a_n + b_{n+1}) - b_1]} \qquad (3a)$$

$$P_a(z) = P_b(z)\big|_{z=[\sum 2(a_n + b_n) - b_1]} \qquad (3b)$$

$$\left[\frac{dP_a}{dz} + \frac{P_a}{d_1}\right]_{z=[\sum 2(a_n + b_n) - b_1]} = 0 \qquad (3c)$$

$$\left[\frac{dP_a}{dz} - \frac{P_a}{d_1}\right]_{z=[\sum 2(a_n + b_{n+1}) - b_1]} = 0 \qquad (3d)$$

$$\left[\frac{dP_b}{dz} + \frac{P_b}{d_2}\right]_{z=[\sum 2(a_n + b_{n+1}) - b_1]} = 0 \qquad (3e)$$

$$\left[\frac{dP_b}{dz} - \frac{P_b}{d_2}\right]_{z=[\sum 2(a_n + b_n) - b_1]} = 0 \qquad (3f)$$

Here $d_1 = -d_2$, and $d_1 = \xi_1/Q_1$, $d_2 = \xi_2/Q_2$, which are the extrapolation lengths, measuring the strength of surface effect[5]. The coherency is defined by the requirement that the local order parameters from one subsystem to another subsystem is continuos across all interfaces.
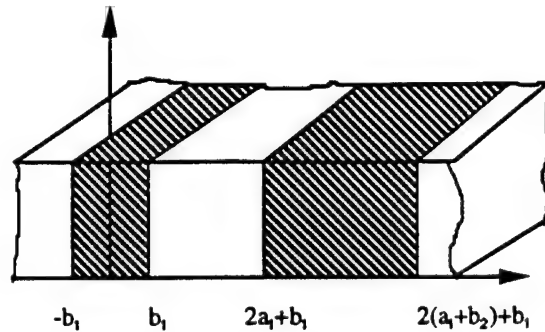

Fig.1. Model of the superlattice structure described in the text. Here a_n and b_n are the thicknesses of different layers.

III. LOCAL PHASE TRANSITION

The nontrivial solutions of Eqs.(2) can be derived exactly, although, in general, they are quite cumbersome. For brevity, only focusing on the temperature region from $T_2 < T < T_1$, the general solutions in the case of $a_n \approx \overline{b_n}$ can be approximately expressed as,

$$P_b = P_{b0} \cos(\kappa_2 \eta) \qquad (4a)$$
$$(\eta = z \pm \sum 2(a_n + b_{n+1}) - b_1 - b_{n+1})$$

$$P_a = \frac{P_{b0} \cos(\kappa_2 b_{n+1})}{\cosh(\kappa_1 a_{n+1})} \cosh(\kappa_1 r_2) \qquad (4b)$$
$$(r_2 = z \pm \sum 2(a_n + b_{n+1}) - b_1 + a_{n+1})$$

with

$$P_{b0} = \pm\left\{-\frac{B}{2C}\left[1 + \sqrt{1 - \frac{4A_0 C}{B^2}(T - T_{2c})}\right]\right\}^{1/2}$$

(in the case of the first order phase transition) $\qquad (4c)$

$$P_{b0} = \pm\left\{-\frac{B}{2C}\left[1 - \sqrt{1 - \frac{4A_0 C}{B^2}(T - T_{2c})}\right]\right\}^{1/2}$$

(in the case of the second order phase transition) $\qquad (4d)$

2

$$\kappa_1 = \sqrt{\alpha_0(T - T_1)/\xi_1} = 1/|d_1|\tanh(\kappa_1 a_{n+1}) \qquad (4e)$$

$$\kappa_2 = 1/|d_2|\tan(\kappa_2 b_{n+1}) \qquad (4f)$$

and

$$T_{2c} = T_2 - (\xi_2\kappa_2^2/A_0) \qquad (4g)$$

where κ_1 and κ_2 are defined as the characteristic lengths, which reflect the correlation radius of the order parameters and describe the breath of polarization fluctuation in two types of layers. For the first order phase transition, from Eq.(4c) the size induced phase transition point can be written as

$$T_2^* = T_2 + (3B^2/16A_0C) - (\xi_2\kappa_2^2/A_0). \qquad (4g)$$

Eqs.(4) describe the spatial variations of local order parameters of the superlattice system. Two important features from Eqs(4) are apparent: (i) The phase transition temperature of each layer is intimately related to its physical size and the associated coherent coupling at the interfaces. (ii) The layers with higher Curie points, i.e., the B type of layers, can induce the polarization in the peripheries of the A type of layers, even though the temperature is above the original local Curie temperature of the layers with lower Curie points. In other words, the local polarization $P_a(r)$ occurring in the A type of layers is caused by the coherent coupling from the B type of layers. As expected, the ferroelectric phase transition can be nucleated in the regions, which are intrinsic paraelectric states. In this case, the polarization occurring in the A type of layers is extrinsic in nature. According to Eqs.(4), the polarization in the B type of layers is plotted as a function of temperature and their physical size in Fig.2. In addition, the spatial profile of polarization P_a in the A type of layers is also numerically plotted as the functions of both the normalized coordinate and temperature in Figs.3. Quite clearly, at the exact interface, the local Curie point is the transition temperature of B types of layers, and then it decreases quickly as a function of the space coordinates.

IV. DIFFUSE PHASE TRANSITION

One of the most important properties for ferroelectrics is their static susceptibility $\chi(T)$ near the Curie range. Next we examine the static dielectric anomalies in our superlattice system. The *average* inverse susceptibility of the superlattice can be expressed as

$$\left\langle \chi^{-1} \right\rangle = \frac{1}{\sum 2(a_{n+1} + b_{n+1})}\left[\frac{\partial^2\Phi}{\partial P_i^2}\right] \ (i = a, b) . \quad (5)$$

Now we construct a multilayer with 60 alternating layers of SrTiO₃/PZT, in which PZT layers are specified as the B type of layers, and they have a designed distribution for their thickness[6]. The thinnest is 6nm, while the thickest is 14.6nm. The overall temperature dependence of the average dielectric susceptibility and the spontaneous polarization of the multilayer system are numerically plotted in Fig.4. and Fig.5, respectively.
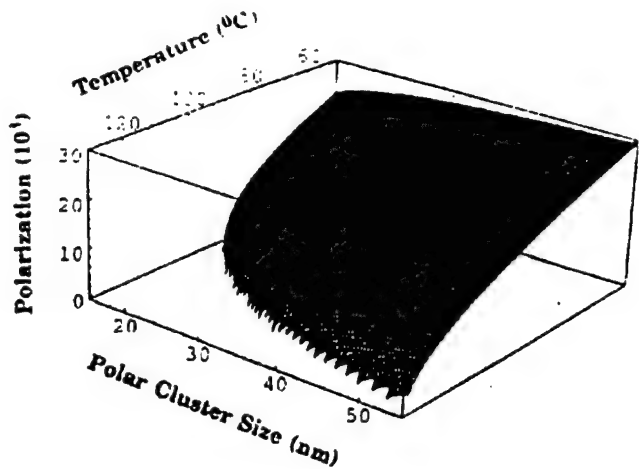

Fig.2. Calculated polarization in the layer B as functions of both temperature and its physical sizes. For the calculation, we take $A_0=10^{-5}$; $B=10^{-12}$; $C=10^{-24}$, $\alpha_0=10^{-4}$; $\beta=10^{-12}$; $\xi_1=10^{-16}$, $T_2=150°C$, $T_1=0°C$ and $a_n=100nm$.
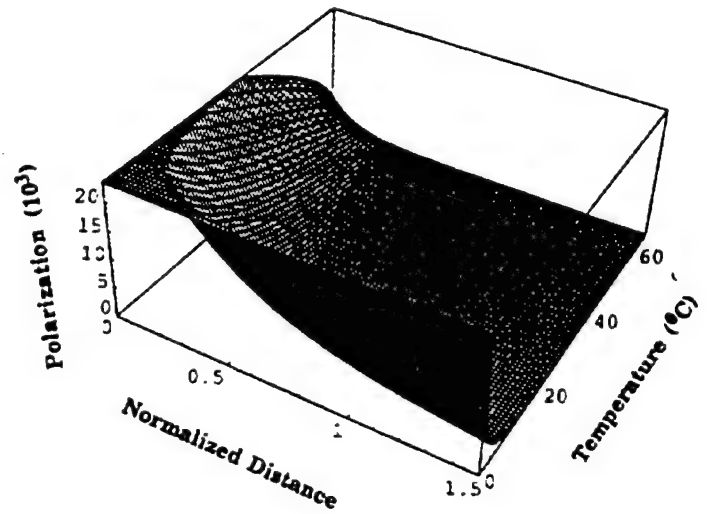

Fig.3. The view of the induced polarization in the A type of layers as functions of both temperature and the normalized distance away from the interfaces. All parameters for the calculation have the cgs unit unless specified.

Fig.4 shows the temperature dependence of the mean polarization in the superlattice. It can be found that the polarization is gradually weakening and depressing, exhibiting a significant deviation from the normal ferroelectric behavior. Since the thicknesses of PZT layers have a distribution, the local phase transition points of the superlattice will spread out in a temperature range, and these local phase transitions are

3

superposed in some degree so as to keep the entire superlattice system on the verge of structural instability under a broad temperature range.
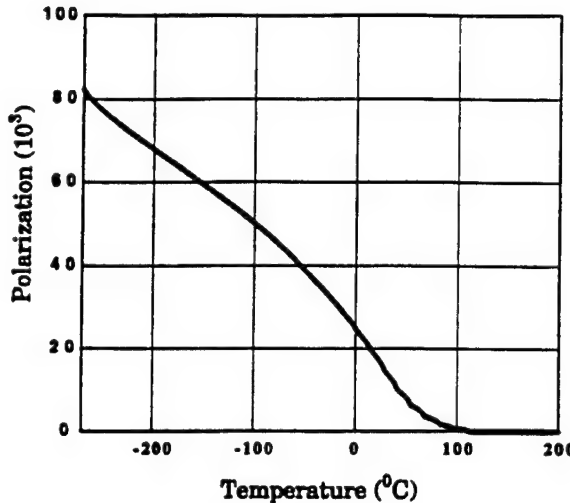

Fig.4. The temperature dependencies of the mean polarization of the PZT/STO superlattice with a total thickness of 0.573μm. $a_s=a_{s+1}=10nm$.
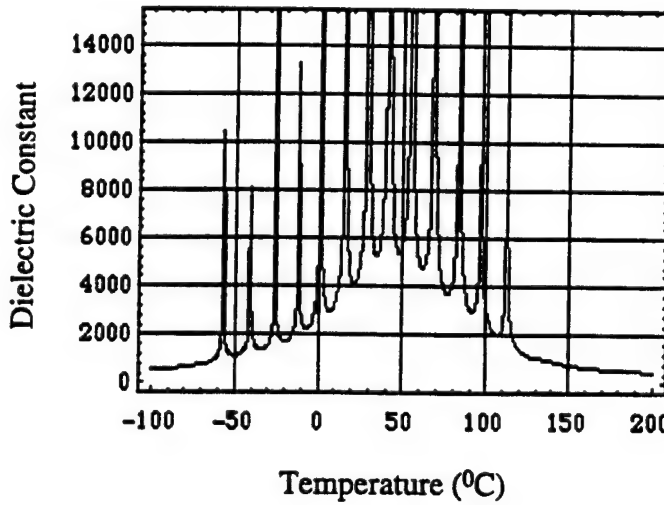

Fig.5. The temperature dependence of the mean susceptibility of the PZT/STO superlattice.

Fig.5. shows the dielectric constant of the superlattices can be well above 4,000 around the room temperature, and it illustrates a salient feature of dielectric behavior in ferroelectric superlattice with inhomogenous heterogeneties: a set of localized phase

transitions, arising from an intrinsic size effect, slightly superpose together and coherently form a giant dielectric response over a very broad temperature range. In other words, there exists a distribution of localized correlation lengths at different temperatures in the superlattice, and a set of localized dielectric singularities in a broad range of temperature together create a giant dielectric (pyroelectric) response. The overall dielectric coefficients in this case can be exceedingly larger than those suggested by the LST relation[7], or the conventional mean field theories. It can been also clearly seen in both Fig.4 and Fig.5 that the local polarization can exist well above the temperature, at which the dielectric constant exhibits its maximum.

V. CONCLUSIONS

A calculation of the dielectric behavior of ferroelectric supelattices with inhomogeneous heterogeneties has been performed. The coherent coupling between different layers can lead to an exceeding enhancement of dielectric properties in a broad temperature range. The overall dielectric response in the superlattice is controlled by the distribution of thicknesses of the PZT layers, i.e., the heterogeneity, as well as the associated coherent coupling effect.

REFERENCES

1. L.E. Cross, Ferroelectric Ceramics, edited by N.Setter and E.L. Colla (Birkhams Basel, 1993). p15
2. E. Wiener-Avnear, Appl. Phys. Lett. 65, 1784 (1994); H. Tabata, et al., Appl. Phys. Lett. 65 1970 (1994); I. Kanno, et al, Appl.Phys. Lett. 68, 328 (1996); T.Tsurumi, et al., Jpn. J. Appl. Phys. 33, 5192 (1994); Y.Ohya, et al., Jpn. J. Appl. Phys. 33, 5272 (1994); T. Hayashi et al., Jpn. J. Appl. Phys. 34, 5100 (1995); and H.-M Christem, et al. Appl. Phys. Lett. 68, 1488 (1996).
3. D. Schwenk, F. Fishman, and F. Schwabl, J. Phys. C2, 5409, (1990).
4. B. Qu, W. Zhong, and P. Zhang, Jpn. J. Appl. Phys. 34, 4114, (1995).
5. D.R. Tilley, and B.Zeks, Solid State Comm. 49, 823 (1984).
6. Shaoping Li, et al., to be published.
7. G. Burns and E. Burstein, Ferroelectrics 7, 297, (1973).

APPENDIX 35

Space Charge Enhanced Electromechanical Response
in Thin Film Polyurethane Elastomers

J. Su[1] and Q. M. Zhang[1,2]*

[1]Materials Research Laboratory and [2]Electrical Engineering Department

The Pennsylvania State University, University Park, PA 16802

R. Y. Ting

Naval Undersea Warfare Center, Naval Research Laboratory, Orlando, FL 32856

Abstract:

We show that the large electrical field induced strain response observed in certain polyurethane elastomers is a thin film effect. Based on the frequency dispersion of the strain response in samples with different thickness and the thermally stimulated discharge current on samples with different processing conditions, we suggest that the charge injection, an interface effect, which results in a non-uniform space charge distribution and hence, a non-uniform electric field distribution across the sample thickness, is responsible for the enhanced electromechanical response in thin polyurethane samples.

* Corresponding author

1

Due to many advantages of polymeric materials, there is a constant effort to develop high performance electroactive polymers for electromechanical applications.[1] Recently, it has been observed that in certain polyurethane elastomers, a large electric field induced strain can be achieved with a moderate external field, hence in the electric field biased state the material exhibits a large effective piezoelectric response, comparable to that in lead zirconate titanate piezoceramics.[2] This make the material very attractive for a wide range of electromechanical applications such as mechanical sensors, actuators, and microelectromechanical systems (MEMS). In earlier publications, we have shown that both the electrostriction and Maxwell stress effect (Coulomb interaction) contribute to the electromechanical response in the material.[3,4]

It was found recently, however, that the electric field induced strain response of the material exhibits a marked dependence on the sample thickness. As shown in figure 1(a), with a fixed field, the strain S_3, which is measured in the direction parallel to the applied electric field E, of a 0.1 mm thin film is much higher than that in a 2 mm thick sample although the strain-field relationship in both samples follows $S_3 = R E^2$, where R is the strain coefficient. Data presented in figure 1(b) summarizes this thickness dependence behavior. Since the elastic compliance of the polymer is much higher than that of the gold electrode, the electrode will impose mechanical clamping on the polymer and reduce the measured strain response, especially in thin film samples.[5] In the figure, the data for the corrected strain response, which takes the electrode clamping effect into consideration, are also shown. Apparently, the high strain sensitivity of the material reported is a thin film effect and in thick samples, the strain sensitivity of the material is not very high. In addition, the frequency dispersion of a 0.1 mm film is also much stronger than that from a 2 mm thick sample as presented in figures 2(a) and 2(b), respectively.

All the samples used in this investigation were made by the solution casting method from Dow 2103-80AE polyurethane. The electrodes were sputtered gold film of 300 Å thick. The strain measurement was made with a high sensitivity bimorph cantilever based dilatometer specially designed for characterizing the strain response in soft and thin polymer films.[6]

In searching for possible mechanisms for the large strain response in thin polyurethane films, we note that the dielectric constant and elastic compliance of the material do not show much change with thickness and their frequency dispersions are also much weaker than the strain dispersion from a 0.1 mm thick film. The observed thickness and frequency dependence of the strain response, hence, indicate the existence of other factors contributing to the high strain sensitivity in thin films and it is likely to be related to the electrode-polymer interface effects. In insulating polymers, one of the most commonly observed interface effects is the charge injection under external fields.[7,8] These charges can be from electrons and holes injected from the electrodes and/or impurity ions in the samples, and can be trapped in the interface and interphase regions, as well as other defect sites, resulting in a non-uniform space charge distribution which usually has a strong thickness and frequency dependence.

In order to investigate this possibility, samples were made from filtered solution (using a Fisher-P5 filter) in an attempt to remove some of the impurities from the original material. As shown in figure 3(a), there is a significant reduction in the strain response in the filtered films, where the data were taken from solution casting films of 0.1 mm thick. While in thick samples, there is not much difference in the strain response in filtered and non-filtered samples. Correspondingly, the thickness dependence of the strain response in the filtered samples is significantly reduced. Accompanying the strain reduction, the frequency dispersion of the strain response in filtered samples of 0.1 mm thickness also becomes nearly the same as that of a 2 mm thick sample as illustrated in figure 3(b).

The thermally stimulated discharge current (TSDC) method, a technique widely used to characterize the charge injection in polymeric materials, was employed to study the charge injection in these samples.[9] In this method, a sample was subjected a high DC electric field (E= 4 MV/m) at a high temperature (here at 80 °C) for 5 minutes, and then cooled down under the field to a low temperature (here at -70 °C). In this paper, these samples are termed as charged samples. TSDC data were collected for both non-filtered and filtered films where the samples were heated at a rate of 4 °C/min without external bias field.

3

As presented in figure 4, for non-filtered sample, there are four significant peaks in the temperature range measured. By comparison with the dielectric constant data, it can be identified that the peak 1 (at -35 °C) and peak 3 (at 45 °C) are related to the glass transition of the soft segments and "glass transition" in the hard segments, respectively.[3,4] Both peaks are followed by a discharge peak, i.e., peak 2 (near 10 °C) and peak 4 (near 70 °C).[10,11] In analog to other polymer systems, these discharge peaks can be identified as related to the non-uniformly distributed space charges in the soft segment region and the hard segment region, respectively. Hence, TSDC data confirm the existence of the non-uniform space change formation due to charge injection.

When the curve of the filtered film is examined, it is clear that there are marked changes in the TSDC data between the non-filtered and filtered samples. Although the peak related to the glass transition of the soft segments does not show much change, the peak area underneath the peak 2 is reduced by about half, indicating a reduction of the trapped space charges in the filtered sample in the interface region. In addition, the peak 3 is significantly reduced while the following discharging peak becomes barely visible. These results imply that the contributors which can trap the space charges to form a non-uniform space charge distribution in the sample have been significantly reduced by filtering.[12,13] Since the mesoscopic morphology of a polyurethane elastomer consists of hard segments embedded in a soft segment matrix, the interfaces between the soft segment and hard segment will act as space charge trapping sites. The change in the hard segments as revealed by the change in the peak 3 due to the filtering will likely change the energy levels at these trap sites and hence, the trap modulated space charge mobility and charge injection process.[11,14,15] The observation here also provides explanation of a recent experimental result in which the strain response in a phase segregated sample, where the hard segments form agglomerate, becomes much smaller than that of a phase mixed one.[16]

Based on these results, we suggest that the enhanced strain response in thin polyurethane films is a consequence of the change injection which results in a non-uniform space charge distribution across the thickness direction. From the Poisson's equation, it can be deduced that

4

such a charge distribution will produce a non-uniform local electric field across the thickness direction, especially in the electrode-polymer interface.[12] Hence, the effect is not significant in thick samples. For the polymer studied here, the electric field induced strain locally is proportional to the square of the local field E(x) and hence, the total strain response of the sample is equal to

$$S = \frac{1}{t}\int_0^t S(x)dx = \frac{R}{t}\int_0^t E^2(x)dx$$

where we have assumed the strain coefficient R is nearly a constant in the sample. t is the sample thickness. It can be shown that for a fixed applied voltage $V = \int_0^t E(x)dx$,

$\int_0^t E^2(x)dx > (\int_0^t E(x)dx)^2/t$. That is, any non-uniform field distribution across the thickness direction will enhance the strain response if the coupling between the strain and electric field is through a square relationship such as the electrostriction and Maxwell stress effect. In fact, such an enhancement mechanism can also be generalized to other effects such as Kerr electro-optical effect to improve the sensitivity. In this scenario, in thick samples, the local electric field is not very different from the average field and there is no enhancement effect due to the interface space charge. As the film thickness is reduced, the local field becomes much higher than the average field, resulting in an enhanced electromechanical response. In an even thinner films where the two interface regions near the two electrodes start to overlap which reduces the non-uniform charge distribution, this enhancement effect is reduced as shown in figure 1.

Reference:

1. H. S. Nalwa, ed. "Ferroelectric Polymer" (Marcel Dekker, New York 1994).

2. M. Zhenyi, J. I. Scheinbeim, J. W. Lee, and B. A. Newman, J. Polym. Sci. Part B: Polym. Phys. 32, 2721 (1994).

3. Q. M. Zhang, J. Su, C. H. Kim, and R. Ting, J. Appl. Phys. 81, 2770 (1997).

4. J. Su, Q. M. Zhang, C. H. Kim, and R. Ting, To be published in J. Appl. Polym. Sci. (1997).

5. H. Wang, Q. M. Zhang, L. E. Cross, and A. O. Sykes, Ferro. 150, 255 (1993).

6. J. Su, P. Moses, and Q. M. Zhang, Submitted to Rev. Sci. Instruments (1996).

7. G. M Sessler, Ed, "Electrets", Topic in Appl. Phys., Vol. 33, (Springer-Verlag, Berlin 1980) Chap. 2.

8. W. Suzuoki, H. Muto, T. Mizutami, and M. Ieda, J. Phys. D: Appl. Phys. 18, 2293 (1985).

9. J. van Turnhout, "Thermally Stimulated Discharge of Polymer Electrets", (Elsevier Sci. Publishing Comp., Amsterdam 1975).

10. E. J. Kim and Y. Ohki, IEEE Trans. on Diel. and Elect. Insulation, 2, 74 (1995).

11. A. Thielen, E. Hendrick, J. Niezette, J. Vanderschueren, and G. Feyder, J. Appl. Phys. 75, 4069 (1994).

12. K. S. Suh, D. Damon, and J. Tanaka, IEEE Trans. on Diel. and Elect. Insulation, 2, 1 (1995).

13. Y. Li, T. Takada, H. Miyata, and T. Niwa, J. Appl. Phys. 74, 2725 (1993).

14. M. M. Perlman and A. Kumar, J. Appl. Phys. 72, 5265 (1992).

15. A. Hirao, H. Nishizawa, and M. Sugiuchi, J. Appl. Phys. 74, 1083 (1993).

16. Ed. Balizar, data presented at 1996 ONR Review on Transducer and Transducer Materials, The Pennsylvania State University.
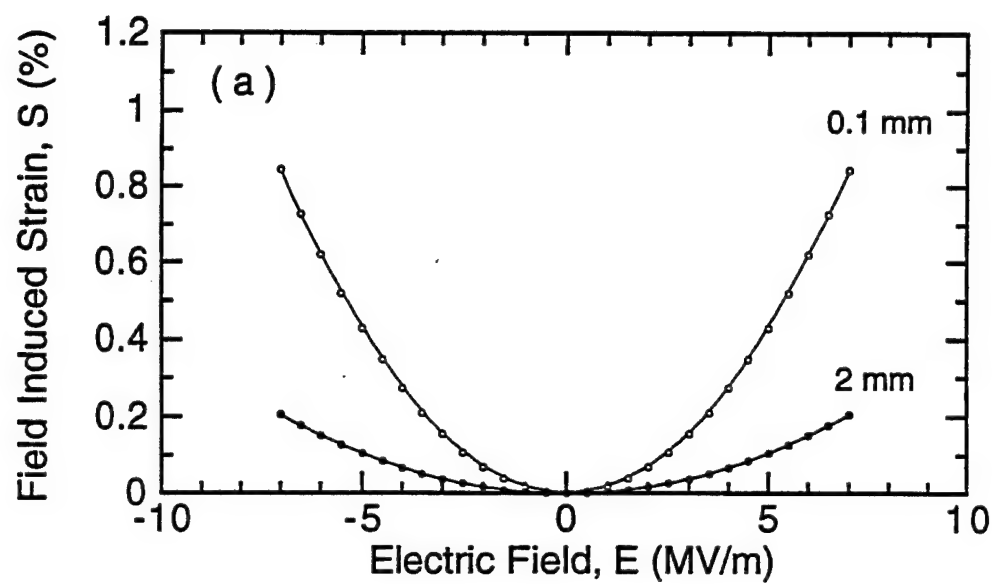
Figure captions:

Figure 1. (a) Comparison of the strain response, measured at 2 Hz, from a 0.1 mm thick and 2 mm polyurethane samples (Dow 2103-80AE). (b) The thickness dependence of the strain response in polyurethane elastomers (measured at 2 Hz). The black dots are the measured data and the open circles are those after the correction for the gold electrode mechanical clamping effect. Solid lines are drawn to guide eyes.
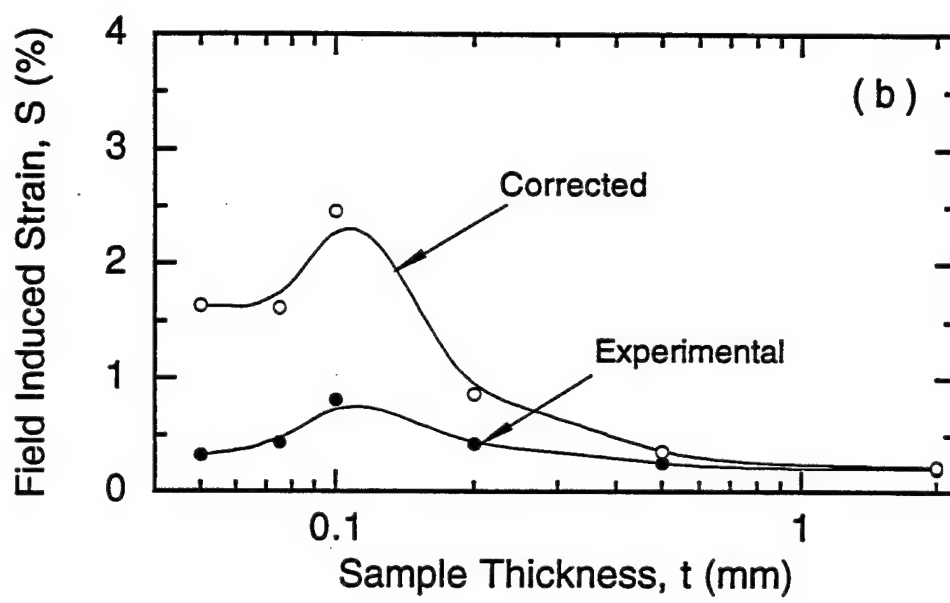
Figure 2. Frequency dispersion of the strain response of (a) 0.1 mm thick sample, and (b) 2 mm thick sample, respectively. The frequency dispersion of 2 mm thick sample is much smaller than that of 0.1 mm thick sample.

Figure 3. (a) Comparison of the strain response of unfiltered sample (uf) of 0.1 mm thick, filtered sample of 0.1 mm thick (f), and sample of 2 mm thick. For the 2 mm thick sample, there is very little difference in the strain responses between the filtered and unfiltered samples. (b) Comparison of the frequency dispersion of unfiltered sample of 0.1 mm thick (open squares), filtered sample of 0.1 mm thick (crosses), and 2 mm thick sample (black dots). The solid lines are drawn to guide eyes.
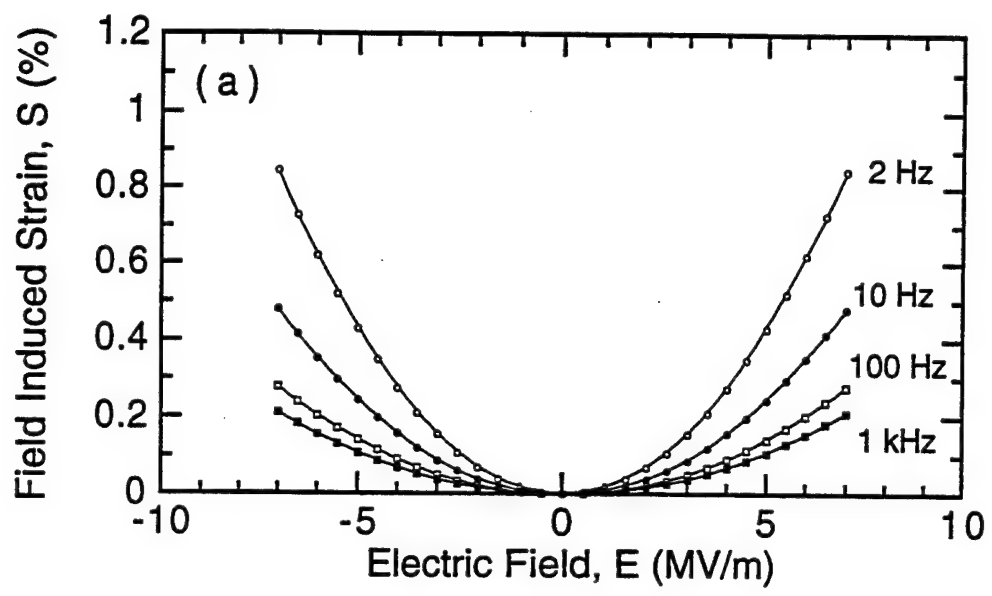
Figure 4. Thermally stimulated current data for both unfiltered and filtered samples. The thickness of the samples is 0.1 mm and area is about 1.2 cm^2.

7

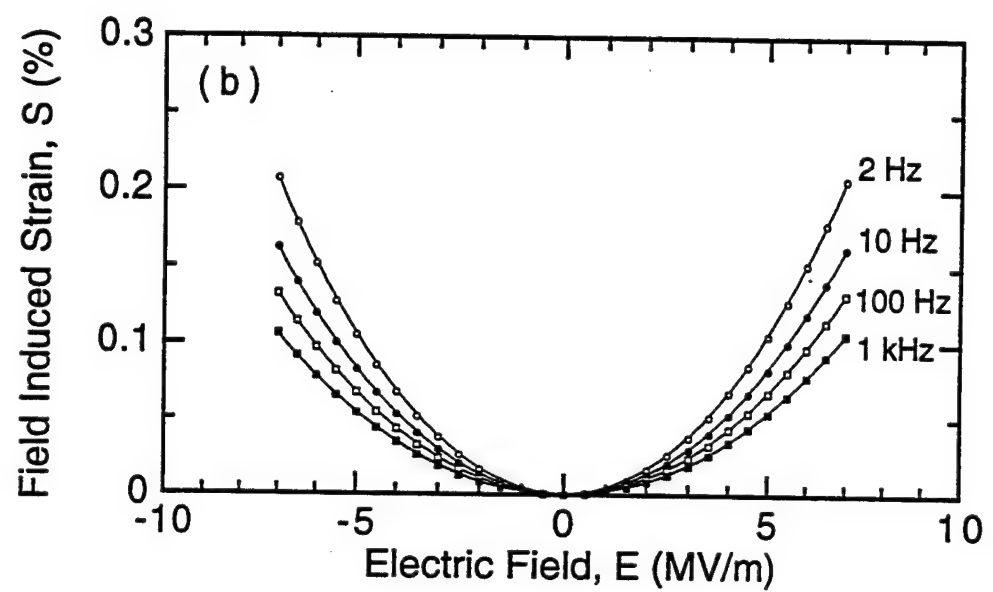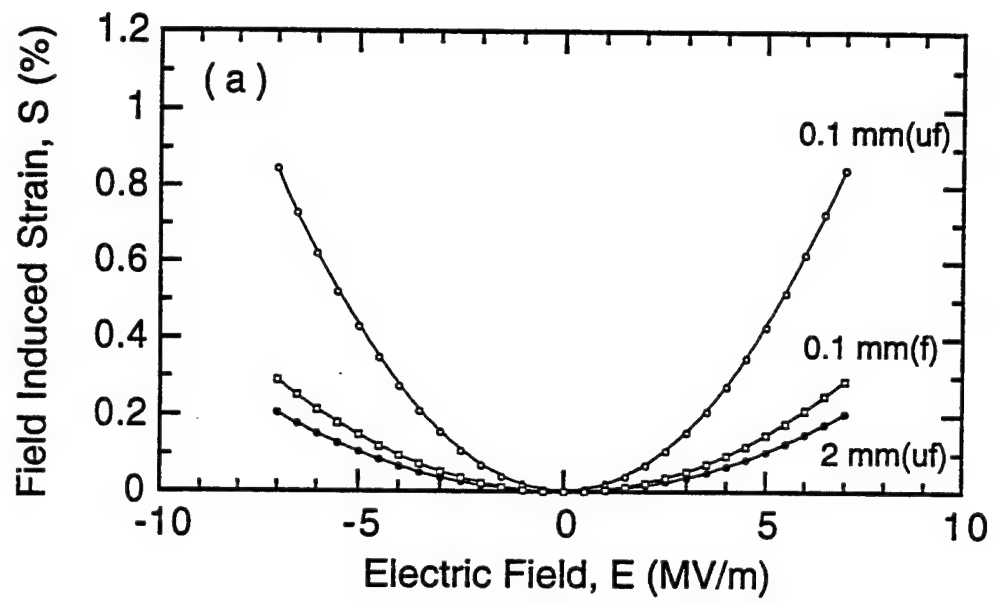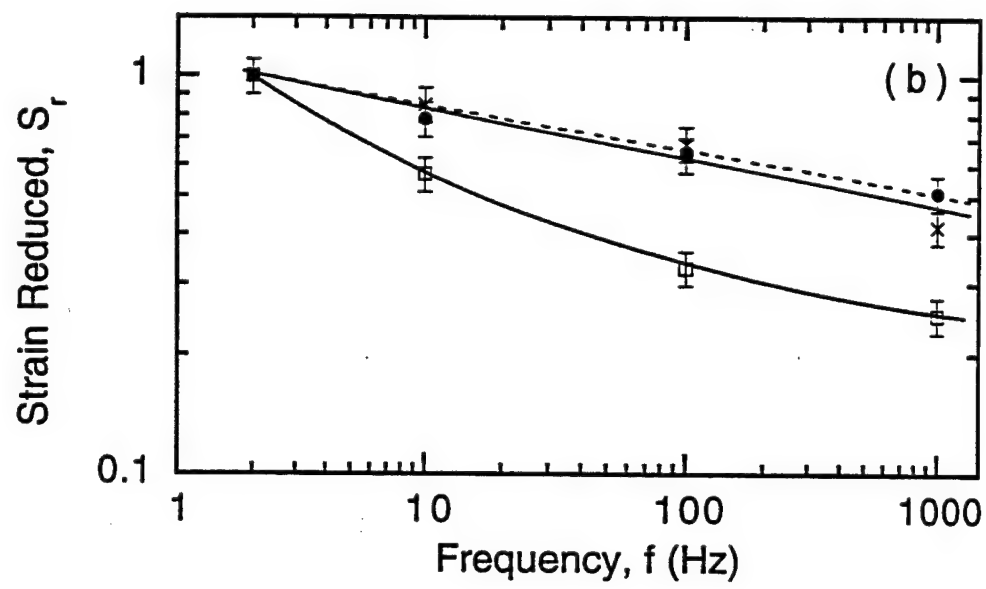Figure (a). Field Induced Strain, S (%) versus Electric Field, E (MV/m), with curves labeled 0.1 mm and 2 mm.

F. 1

F. 1

F.2

(b)

2 Hz
10 Hz
100 Hz
1 kHz

F.2

Figure (a): Field Induced Strain, S (%) versus Electric Field, E (MV/m), showing curves labeled 0.1 mm(uf), 0.1 mm(f), and 2 mm(uf).

F-3

(b)

Strain Reduced, S_r

Frequency, f (Hz)
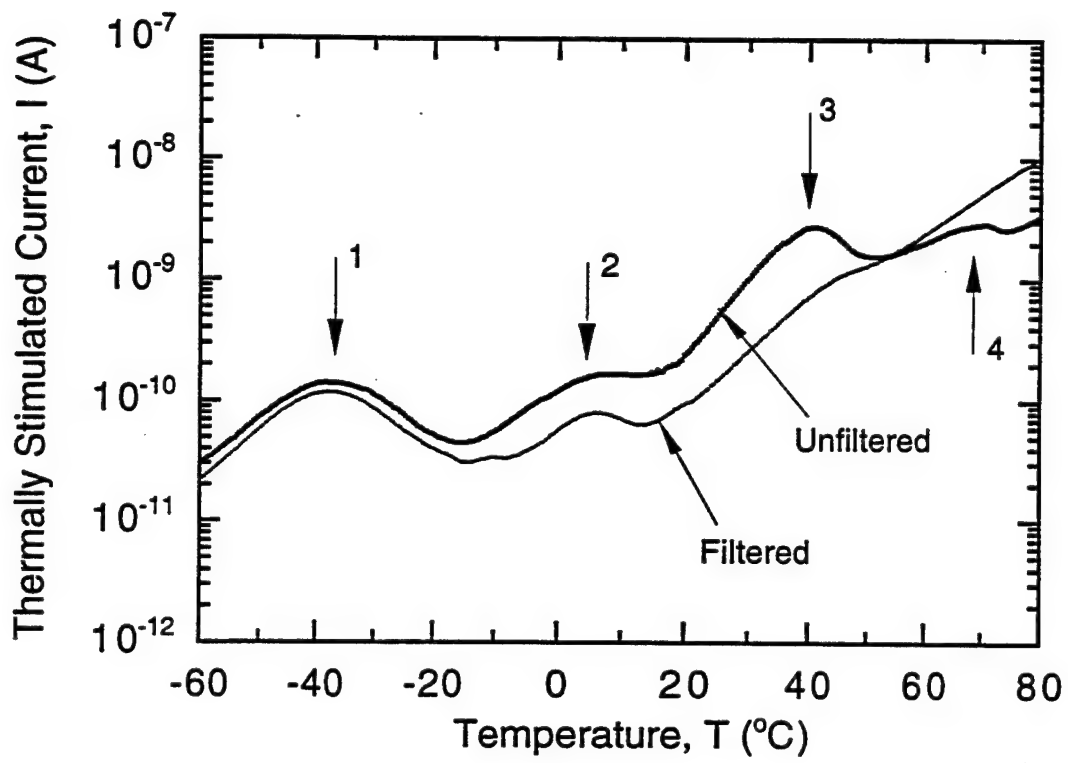
F·3

F. 4

APPENDIX 36

An experimental investigation of electromechanical responses in a polyurethane elastomer

Q. M. Zhang,[a] J. Su, and Chy Hyung Kim[b]
Materials Research Laboratory, The Pennsylvania State University, University Park, Pennsylvania 16802

R. Ting and Rodger Capps
Underwater Sound Reference Detachment, Naval Research Laboratory, Orlando, Florida 32856

The electromechanical response of a polyurethane elastomer was investigated at room temperature and in the temperature range near its glass transition. It was found that the Maxwell stress contribution to the strain response can be significant at temperatures higher than the glass transition temperature. In addition, the material exhibits a very high electrostrictive coefficient Q, about two orders of magnitude higher than that of polyvinylidene fluoride. It was also found that in a polymeric material, the chain segment motions can be divided into those related to the polarization response and those related to the mechanical response and the overlap between the two yields the electromechanical response of the material. In general, the activation energies for different types of motion can be different, resulting in different relaxation times in the dielectric, the elastic compliance, and the electrostrictive data, as observed in the polyurethane elastomer investigated. The experimental results indicate that at the temperatures investigated, the activation energy for the mechanical related segment motions is higher than that of nonmechanical related segment motions. © *1997 American Institute of Physics.* [S0021-8979(97)02406-7]

I. INTRODUCTION

Electromechanical coupling effects such as piezoelectricity and electrostriction have been widely utilized in many areas such as transducers and sensors.[1,2] Conventional electromechanical transduction materials include ceramics such as lead zirconate titanate (PZT) and lead magnesium niobate-lead titanate (PMN-PT) and single crystals such as quartz.[1,3] During the last three decades, electromechanical polymers have drawn much attention because they have high mechanical flexibility, low acoustic impedance, low manufacturing cost, and can be easily molded into desirable shapes.[4,5] However, the low electromechanical activity of the polymeric materials greatly limits their applications. For instance, the electromechanical coupling factor of the piezoelectric polyvinylidene fluoride (PVDF) and its copolymers with trifluoroethylene (TrFE), which possess the highest electromechanical activity among all the known electromechanical polymers, is less than 0.25.[6] In contrast, piezoceramic PZT has a coupling factor of 0.75.[3] Considering the fact that the energy conversion efficiency is proportional to the square of the coupling factor, the difference between the two is quite significant. Hence, there is constant searching for new polymeric materials with high electromechanical activity. Recently, it was reported that in certain polyurethane elastomers, a large electric field induced strain can be achieved and in the electric field biased state, the materials exhibit an effective piezoelectric coefficient higher than those of piezoceramic PZTs, which have stirred much excitement and interest in this class of materials.[7]

Since the discovery of this new class of materials, many experimental investigations have been conducted. It has been shown that the characteristics of the polarization response to applied electric fields indicate that the material is not a ferroelectric and the strain is proportional to the square of the applied electric field, in analogy to the electrostrictive effect.[6-8] Because of these features and the high elastic compliance of the material, which is in the range between 10^{-7} and 10^{-8} m^2/N, the question of whether the large electric field induced strain is caused by the Maxwell stress effect. i.e., the Coulomb interaction between the charges on the two electrodes of the specimen, is often raised. In fact, the Coulomb attraction between the charges on the two electrodes has been widely utilized to produce actuators and transducers such as those in the current microelectro-mechanical systems.[9] This possibility is reinforced by a recent experimental result which indicates that by increasing the elastic compliance of the polyurethane, the field induced strain was enhanced.[6] In addition, it was found that the electric field induced strain is very sensitive to the sample processing conditions and the thickness of the specimen.[6-8] The field induced strain by a unit external electric field increases as the film thickness is reduced. It was suggested that this increase is caused by a nonuniform electric field distribution across the thickness direction in the samples since for a strain response proportional to the square of the applied electric field, any nonuniform field distribution in a sample will increase the strain response. The most probable cause for such a thickness dependence behavior is the existence of a surface region and an interior region, which have different electric field strength in a specimen, and could be a result of charge injection and/or a nonuniform distribution of the material properties, as schematically drawn in Fig. 1(a).[6,10]

[a]Electronic mail: qxz1@psuvm.psu.edudrr
[b]Permanent address: Department of Chemistry, Chongju University, Chongji City, 360-764, Korea
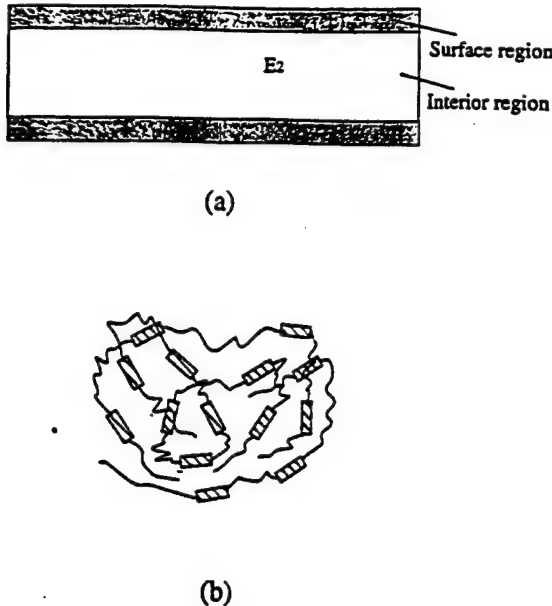
(a)

(b)

FIG. 1. (a) Schematical drawing of a polyurethane sample showing the surface region (hatched regions) and interior region. The electric fields E_1 and E_2 in the two regions may not be the same. (b) Schematic of the morphology of a polyurethane elastomer where the hard segments (hatched boxes) are embedded in the matrix of soft segments (thin lines).

The objective of this investigation is to provide an understanding of the possible mechanism for the observed electric field induced strain in this class of polyurethane elastomers. Through this process, we also intend to examine the nature or general features of electromechanical responses in nonferroelectric polymeric materials. Although the dielectric and elastic responses of polymeric materials have been investigated for many decades both experimentally and theoretically and are relatively well understood,[11] the investigation into the electromechanical response in polymeric materials, except those of piezoelectricity in PVDF and its copolymers, is much less extensive and consequently, the understanding of the elastoelectric properties of polymers is relatively poor.

II. EXPERIMENTAL

The polyurethane used in this investigation is produced by Deerfield Urethane, Inc. using a Dow polyurethane (Dow 2103-80AE). In previous studies, a large field induced strain response was reported in this material.[7] The sample was case and the thickness of the sample is 2 mm. As has been shown in an earlier investigation, for a sample of such thickness, the effect of surface regions in causing a nonuniform electric field distribution in the specimen is not significant and the observed response can be regarded as from a bulk material with approximately a uniform electric field distribution across the sample thickness direction.[6]

Polyurethane elastomer is a block copolymer with hard segments embedded in a soft segment matrix as schematically drawn in Fig. 1(b).[12] For the polymer investigated, the soft segment is poly(tetramethylene glycol) (PTMEG) with a molecular weight of about 1000. The hard segment is comprised of a di-isocyanate and a diol chain extender. The di-
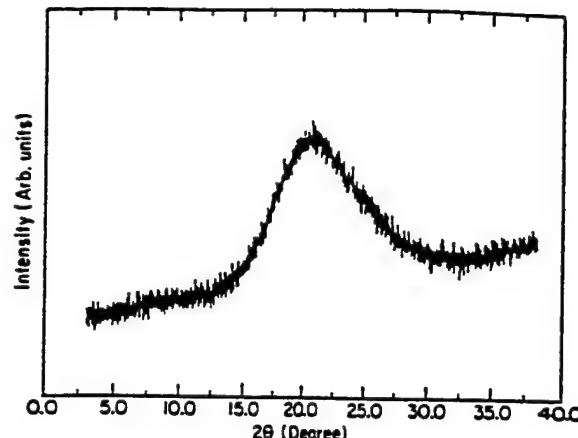

FIG. 2. X-ray diffraction data of the polyurethane elastomer at room temperature where the broad peak near 20° is the amorphous hola. No crystalline phase can be detected within the data resolution.

isocyanate is methylenedi-p-phenyl di-isocyanate (MDI) and the diol chain extender is 1,4-butanediol (BD). The mole ratio of the components is about

$$1.8 \text{ mol MDI}/0.8 \text{ mol BD}/1.0 \text{ mol PTMEG}.$$

Hence, the hard segment (MDI÷BD) is approximately 34% by weight in the sample.

The x-ray scattering result, shown in Fig. 2, reveals that both the hard segment and soft segment are in the amorphous phase and there is no detectable crystalline phase in the material within the experiment solution. In this investigation, the dielectric constant, the elastic compliance, and the electric field induced strain were characterized over a wide temperature and frequency range. In addition, Fourier transform infrared (FTIR) and the dependence of the dielectric constant on hydrostatic pressure were also investigated over a wide temperature range, which are reported on in another publication.[13]

The dielectric constant measurement was carried out by a HP LCR multimeter (HP 4274A), a HP impedance analyzer (HP 4192A), a capacitance bridge (General Radio 1616), and a lock-in amplifier (SR 850) depending on the capacitance value of the sample and the frequency range. The lock-in amplifier, which measures both the phase and amplitude of the voltage and current applied to the specimen, yielding the impedance and the capacitance of the specimen, was used in the frequency range from 1 mHz to 1 kHz. The capacitance bridge covers the frequency range from 100 Hz to 100 kHz, HP LCR meter in the frequency range from 1 kHz to 1 MHz, and HP impedance analyzer in frequency from 1 kHz to 10 MHz. For the specimens with a capacitance value below 100 pF, the capacitance bridge was utilized since the error from LCR meter and impedance analyzer is quite large in measuring capacitance of small value. The temperature control was provided by a Delta chamber interfaced with a HP computer.

The electric field induced strain measurement was conducted by a double beam laser dilatometer which is equipped with a temperature chamber in the temperature range from −100 °C to about 200 °C.[14] The operating frequency range

for the dilatometer is from 1 Hz to above 1 MHz. For the polymer specimens investigated, it was found that the spurious resonance existing at high frequencies made it difficult to carry out measurements to frequencies above 10 kHz.

The elastic modulus was measured by a dynamic mechanical analysis system which covers a wide frequency and temperature range.

III. RESULTS AND DISCUSSION

In general, in a nonpiezoelectric material such as the polyurethane elastomers investigated, the electric field induced strain can be caused by the electrostrictive and also by the Maxwell stress effects.[15,16] The electrostrictive effect is the direct coupling between the polarization and mechanical response in the material. It is the strain (S) or stress (T) change induced by a change in the polarization level (P) in the material which can be expressed as:

$$S = QP^2, \tag{1}$$

where Q is the electrostrictive coefficient of the material. For a linear dielectric where $P = \epsilon_0(K-1)E$, Eq. (1) can be written as

$$S = Q\epsilon_0^2(K-1)^2E^2. \tag{2}$$

K is the dielectric constant of the material and ϵ_0 is the vacuum dielectric permittivity. On the other hand, Maxwell stress, which is due to the interaction between the free charges on the electrodes (Coulomb interaction) and to electrostatic forces that arise from dielectric inhomogeneities, can also contribute to the electric field induced strain response. For the situation considered here, it is also proportional to the square of the applied electric field (E) and it can be shown

$$T = -\epsilon_0 K E^2/2. \tag{3}$$

Hence, the dimensional change due to the Maxwell stress is

$$S = -s\epsilon_0 K E^2/2, \tag{4}$$

where s is the compliance of the material. As can be seen, for a soft material, the strain induced by the Maxwell stress can be quite substantial. In order to identify the contributions from the different mechanisms, it is necessary to measure the dielectric permittivity, the elastic compliance, and the electric field induced strain simultaneously.

For a polymeric material, it is well known that most of the material properties such as the dielectric constant and elastic compliance are very dispersive even at low frequencies, reflecting relatively high activation energies for the motions of molecule units and chain segments.[11] Furthermore, the variation in the local environment and the length of the chain segments involved in the motion results in a broad distribution of the activation energy (broad relaxation time distribution). In dealing with the electromechanical response of a polymeric material, it is advantageous to divide the segment motions into those related to the dielectric response and those related to the mechanical response, and the overlap between the two, i.e., those related to both, yields the electromechanical response of the material. In addition, it is also conceivable that the activation energies for the motions of
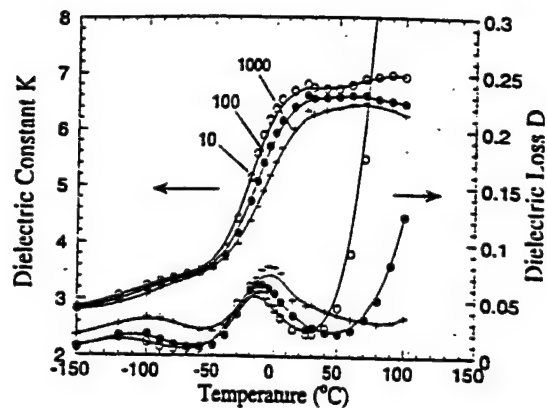

FIG. 3. Dielectric constant and dielectric loss as a function of temperature for the polyurethane elastomer where the measuring frequencies are 10 (open circles), 100 (solid circles), 1000 (plus signs) Hz.

molecular units and segments, which involve the strain and stress (mechanical) might be different from that for the motions of the segments, which involves little or no strain and stress. As will be discussed later in the article, such a difference in the activation energies between the two types of motions will have a direct effect on the electrostrictive response of a polymeric material. Therefore, dispersion characteristics of the dielectric and elastic responses of the sample will be analyzed in detail.

The dielectric constant as a function of temperature is presented in Fig. 3. A strong frequency dispersion was observed. In the temperature range investigated, there are three relaxation peaks. The one at temperature near 20 °C is related to the glass transition which is due to the freezing process of the soft segments from a rubbery state into a glass state (α-relaxation). The one at temperatures near -100 °C is the β-relaxation, which was suggested from the early studies on polyurethanes and polyamids to be related to the absorbed water molecules.[11] The nature of the relaxation at temperatures near 70 °C is unknown and is labeled as I-relaxation here. The results of a recent preliminary FTIR study suggests that it might be associated with the motion in the chain extenders.

The dielectric dispersion behavior was characterized over the frequency range from 0.01 Hz to 1 MHz and typical results are presented in Fig. 4(a). It was found that for the data at the temperature range from -80 °C to 20 °C, one can make use of the temperature-frequency superposition principal to construct a master curve as illustrated in Fig. 4(b) for the one at 0 °C where the data at temperatures other than 0 °C were shifted in the frequency by times a factor $a(t)$ [$a(t)\times f$, where f is the frequency], which is a function of temperature t.[11] For a dielectric relaxation with a broad relaxation time distribution, the Cole–Cole single relaxation time formula should be modified. In Fig. 4(b), the solid line is the fitting of the data with a modified Cole–Cole equation.

$$\epsilon^*(\omega) = \epsilon_u + \frac{\epsilon_R - \epsilon_u}{1 + (i\omega\tau_0)^\beta}, \tag{5}$$

which describes the dielectric dispersion with a broad distribution of the relaxation time centered at τ_0, where ω is the

Zhang *et al.*

FIG. 5. The elastic compliance s_{11} and elastic loss D as a function of temperature. The measuring frequencies are 0.3 Hz (open squares), 3 Hz (solid circles), and 30 Hz (crosses). The solid line at 30 Hz data is the fitting result.
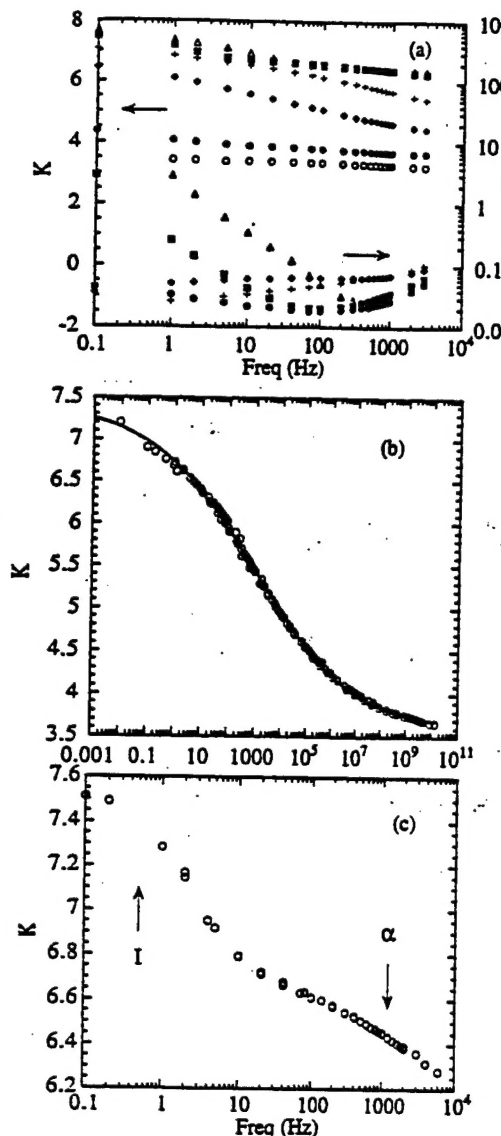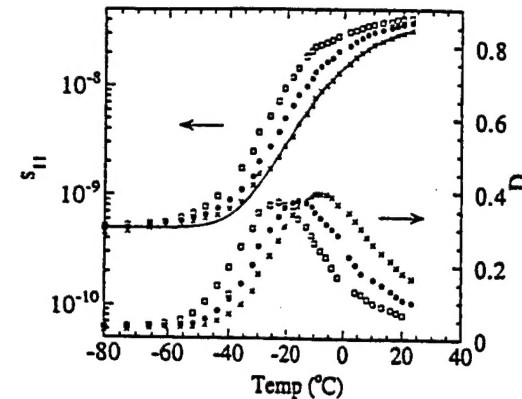
FIG. 4. (a) Dielectric constant (K) and dielectric loss (D) as a function of frequency at temperatures (from top to bottom): 80 °C (open triangles), 50 °C (solid squares), 5 °C (plus signs), −15 °C (solid diamonds), −40 °C (solid circles), and −80 °C (open circles). (b) Master curve of the dielectric constant at 0 °C where open circles are the data points and solid line is the fitting using Eq. (5). (c) Dielectric constant as a function of frequency at 60 °C which shows clearly two relaxation processes (labeled as I and α). The I-relaxation vanishes at temperatures below about 40 °C.

angular frequency. In Eq. (5), $0 < \beta \leqslant 1$ measures the width of the relaxation time distribution and when $\beta = 1$, Eq. (5) is reduced to the single relaxation time Cole–Cole equation and a smaller β corresponds to a broader distribution of the relaxation time. For the data in Fig. 4(b), the fitting yields $\beta = 0.22$ indicating the existence of a broad distribution of the relaxation in the material and the τ_0 at 0 °C is 2.2×10^{-4} s.

In addition, it was found that the shifting factor $a(t)$ follows the WLF relation[11]

$$a(t) = -\frac{c_1(t - t_g)}{c_2 + t - t_g},\qquad(6)$$

with $c_1 = 21.1$, $c_2 = 54.1$, $t_g = 220.0$ K. The glass transition

temperature t_g at 220 K $(= -53.15$ °C) is consistent with the data presented in Fig. 3. It should be pointed out that the parameters c_1 and c_2 obtained here are close to the universal constants c_1^g and c_2^g which have approximate values of 17.44 and 51.6, respectively.[11] At temperatures above 40 °C, there is a relaxation peak (I-relaxation) in addition to the α-relaxation as shown in Fig. 4(c). The temperature shifting factors for the two relaxations are different as they should be. Due to this fact, no attempt was made to generate a master dispersion curve in that temperature range.

The elastic compliance measured at temperatures about the glass transition is presented in Fig. 5. Apparently, there is more than one order of magnitude change in the elastic compliance of the material as it goes through the glass transition. Using the temperature-frequency superposition principle, the elastic compliance curve at 0 °C over a frequency range from about 10^{-2} Hz to above 10^3 Hz can be obtained as shown in Fig. 6(a). The elastic compliance changes by more than one order of magnitude in this frequency range. The shifting factor for the elastic compliance also fits well with the WLF relation as shown in Fig. 6(b) yielding $c_1 = 19.9$, $c_2 = 125.4$, and a glass transition temperature $t_g = 252.3$ K $(= -20.8$ °C). The higher glass transition temperature obtained from the elastic compliance data compared with that from the dielectric constant indicates that in the polyurethane elastomer investigated, for the α-relaxation (the glass transition), the activation energy for the chain segment motions related to the strain and stress is higher than that for the motions not strain and stress related (pure dielectric). We will come back to this point later in the article.

The data in Fig. 6(a) was also fitted with the relaxation equation (5) where the dielectric constant is replaced by the elastic compliance. The solid curve in Fig. 6(a) is the result of the fitting and apparently, the data can be described quite well by Eq. (5), which yields $\beta = 0.32$ and $\tau_0 = 6 \times 10^{-2}$ s. Compared with the parameters from Fig. 4(b) of the dielectric data (at the same temperature), the average relaxation time τ_0 is longer, which is consistent with the results presented in the preceding paragraph that the activation energies for the segment motions generating strain are higher than those of nonstrain related segment motions. From the fact
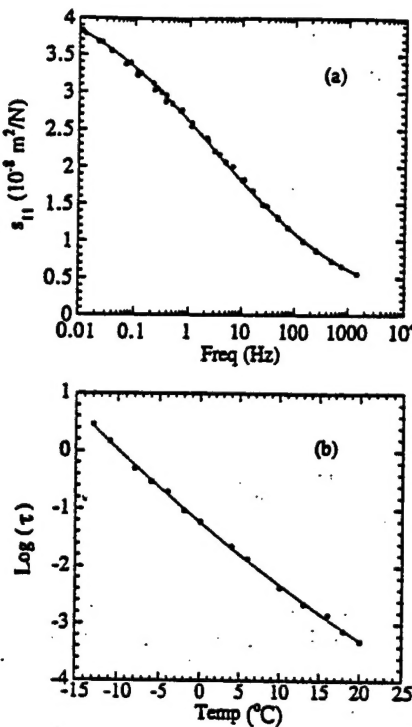
FIG. 7. R_{33} as a function of frequency at different temperatures (from top to bottom): 80 °C solid squares), 60 °C (open circles), 40 °C (open triangles), 30 °C (solid circles), 20 °C (open squares), 0 °C (crosses), −20 °C (solid circles), and −28.3 °C (open circles). The solid lines are drawn to guide eyes.

FIG. 6. (a) The master curve for the elastic compliance at 0 °C where the solid line is from the fitting and solid circles are the experimental data. (b) The change of the relaxation time τ with temperature, where τ is obtained from the elastic compliance data. Solid circles are the data points and solid line is the fitting using WLF relation.

that both Eq. (5) and the WLF relation describe the mechanical relaxation data rather well, we tried to combine Eq. (5) with the WLF relation

$$\log \tau_0 = \log \tau_g - \frac{c_1(t-t_g)}{c_2+t-t_g}$$

to fit the data in Fig. 5. Indeed, the data in Fig. 5 can be described well as demonstrated by the solid curve in the figure for the data at 30 Hz. The fitting yields $\beta=0.34$, $c_1=16.5$, $c_2=144$, and a glass transition temperature $t_g=255$ K. It is quite evident that the results of the fitting to the two sets of data are quite consistent with each other, especially the value of the glass transition temperature.

It has been shown that the electric field induced strain in the polyurethane samples is proportional to the square of the applied electric field. Hence, a parameter R_{33} is introduced to describe the sensitivity of the strain response of the material to an applied electric field

$$S_3 = R_{33}E^2.$$

In Fig. 7 R_{33} is a function of frequency characterized in the temperature range from −30 °C to 80 °C. R_{33} is always less than zero indicating that an applied electric field causes a contraction in the specimen in the direction parallel to the applied field. In analogy to the dielectric constant and elastic compliance, R_{33} also exhibits a strong frequency dependence. Making use of the dielectric constant and the elastic compliance data, the contribution of Maxwell stress to the total strain response in the material can be evaluated, which
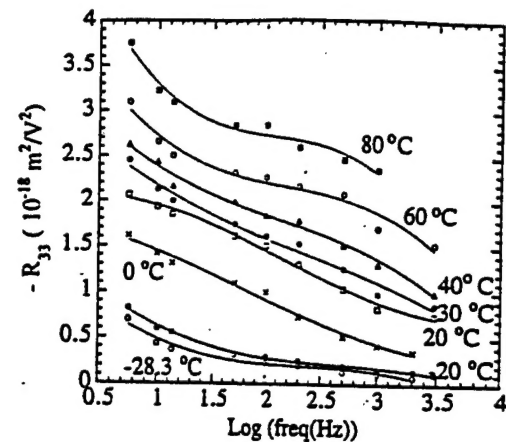
is shown in Fig. 8(a) along with the total strain response at 10 and 100 Hz, where the Maxwell stress term is $R_m = -s_{33}\epsilon_0 K/2$. Evidently, at temperatures above 20 °C, the contribution from Maxwell stress is significant. On the other hand, the non-Maxwell stress part or the contribution related to the true electrostriction, which is the difference in Fig. 8(a) between R_{33} and R_m, is also quite sizable. Based on Eq. (2), the electrostrictive coefficient for the material as a function of frequency and temperature is evaluated and presented in Figs. 8(b) and 8(c). Unlike the ferroelectric ceramic materials where Q is nearly independent of temperature and frequency, the electrostrictive coefficient for the polyurethane elastomer depends on frequency markedly and weakly on temperature in the temperature range investigated. The relatively large data scatter in Figs. 8(b) and 8(c) is caused by the fact that the data are obtained from three sets of data, i.e., R_{33}, K, and s_{33}, each of which contains data scatter. The decrease of the Q with frequency indicates that the component of the polarization motions of high frequency (short relaxation times) does not generate strain in the material and hence is pure dielectric.

In Table I, the electrostrictive coefficients Q_{11} from several commonly used ferroelectric materials are compared with that of polyurethane elastomer investigated. The Q for the polyurethane elastomer investigated is much larger than those of the other materials. Although the detailed mechanisms of the electrostriction in a material depends on the molecular bases generating it such as the ionic displacement and polarization orientation effect on which very little understanding exists, there exist empirical relationships which seem to be consistent with the experimental results on the electrostrictions from different materials. For instance, it has been observed that the electrostrictive coefficient Q is inversely proportional to the dielectric constant and proportional to the elastic compliance of the material.[16] As shown in Table I, these rules can qualitatively describe the data for PMN, PZT, and PVDF. However, for the polyurethane elastomer, in the temperature range from −30 to 20 °C, the elas-
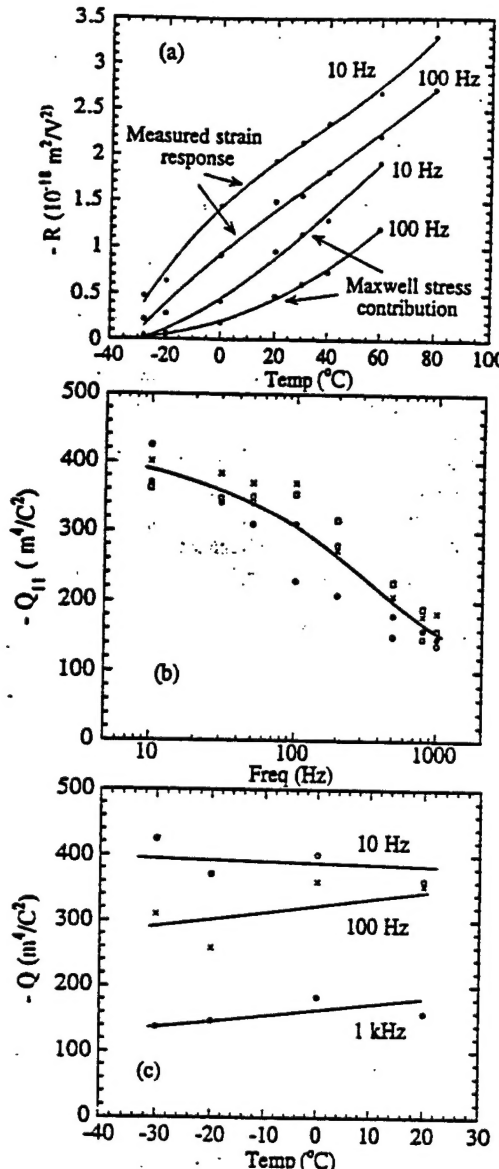
Zhang *et al.*

FIG. 8. (a) Comparison between the measured R_{33} and the contribution from the Maxwell stress effect R_m at 10 and 100 Hz. The solid lines are drawn to guide eyes. (b) The electrostrictive coefficient Q_{11} as a function of frequency at temperatures of −30 °C (open circles), −20 °C (solid circles), 0 °C (crosses), and 20 °C (open squares). The solid line is drawn to guide eyes. (c) The electrostrictive coefficient Q_{11} as a function of temperature in the temperature range from −30 °C to 20 °C: 10 Hz (open circles), 100 Hz (crosses), and 1 kHz (solid circles). The solid lines are drawn to guide eyes.

tic compliance reduces more than one order of magnitude (Fig. 5) while the change of Q in the same temperature range [Fig. 8(c)] is relatively minor, which seems inconsistent with the empirical rule between Q and compliance of the material.

The difference in the glass transition temperatures observed from the dielectric data and the elastic compliance data indicates that in the polyurethane elastomer investigated, the chain segment motions can be divided into those generating the mechanical response and those generating the dielectric and polarization response. The overlap between the two, i.e., those generating both the mechanical and polarization, yields the electromechanical response in the material. In addition, the dispersion of the electrostrictive coefficient Q,

TABLE I. Comparison of the electrostriction coefficients and related properties. Q_{11} is the longitudinal electrostrictive coefficient, K is the dielectric constant, and s is the elastic compliance.

Materials	Q_{11} (m⁴/C²)	K	$s(10^{-11}$ m²/N)
PMN-PT[a]	0.02	25 000	1.0
PZT[b]	0.096	2000	1.6
PVDF[c]	−2.0	9	30
Polyurethane	−150–450	4–8	5×10^2–5×10^3

[a]References 17 and 18.
[b]Reference 19.
[c]References 6 and 20.

i.e., the observed decrease of Q with frequency, indicates that the high frequency components of the polarization motions do not contribute to the strain response as much as the frequency components, which implies that the activation energies for the polarization motions generating strain response as higher than those for nonstrain related polarization changes. These are consistent with the facts that the glass transition temperature T_g from the elastic compliance data is higher than that from the dielectric data and that there is a large drop of the dielectric field induced strain response at temperatures near T_g of the elastic compliance data.

IV. SUMMARY

The electromechanical response of the polyurethane elastomer (Dow 2103-80AE) was investigated at room temperature and in the temperature range near the glass transition where the motions of the soft segments are frozen out. It was found that the Maxwell stress contribution to the strain response can be significant at temperatures higher than the glass transition temperature. In addition, the material also exhibits a very large electrostrictive coefficient Q, about two orders of magnitude higher than that of PVDF. It was also found that the Q shows little change in the glass transition temperature region, while the elastic compliance changes by more than one order of magnitude indicating that the inverse proportional relationship between the elastic compliance and the Q might not be universal.

The experimental results also show that for the polyurethane elastomer investigated, the temperature frequency superposition principle can be applied to both the dielectric and elastic data, while the change of the electrostrictive coefficient with temperature and frequency does follow this superposition principle. It was also found that in a polymeric material, the chain segment motions can be divided into those related to the polarization response and those related to the mechanical response. The overlap region between the two yields the electromechanical response of the material. In general, the activation energies for the two types of motions can be different, resulting in different relaxation times observed in the dielectric data, elastic compliance data, and the electrostrictive data, as observed in the polyurethane elastomer investigated. The higher glass transition temperature from the mechanical data and the decrease of the Q with frequency indicate that in the temperature investigated, the activation energy for the mechanical related segment motions

is higher than that of nonmechanical related segment motions.

[1] W. G. Cady, *Piezoelectricity* (Dover, New York, 1964).

[2] J. M. Herbert, *Ferroelectric Transducers and Sensors* (Gordon and Breach, New York, 1982).

[3] B. Jaffe, W. R. Cook, Jr., and H. Jaffe, *Piezoelectric Ceramics* (Academic, London, 1971).

[4] A. J. Lovinger, Science 220, 1115 (1983).

[5] H. R. Gallantree, IEE Proc. 130, 219 (1983).

[6] H. Wang, Ph.D. thesis, The Pennsylvania State University, 1994.

[7] M. Zhenyi, J. I. Scheinbeim, J. W. Lee, and B. A. Newman, J. Polym Sci. B Polym. Phys. 32, 2721 (1994).

[8] H. Wang, Q. M. Zhang, L. E. Cross, R. Ting, C. Coughlin, and K. Rittenmyer, Proc. Int. Symp. Appl. Ferro. 9, 182 (1994).

[9] I. Ladabaum, B. T. Khuri-Yakub, and D. Spoliansky, Appl. Phys. Lett. 68, 7 (1996).

[10] *Electrets*, edited by G. M. Sessler (Springer, Berlin, 1987).

[11] N. G. McCrum, B. E. Read, and G. Williams, *Anelastic and Dielectric Effects in Polymeric Solids* (Dover, New York, 1967).

[12] P. Wright and A. P. C. Cumming, *Solid Polyurethane Elastomers* (Gordon and Breach, New York, 1969).

[13] J. Su, C. Kim, V. Kugel, Q. M. Zhang, R. Ting, and R. Capps (unpublished).

[14] Q. M. Zhang, S. J. Jang, and L. E. Cross, J. Appl. Phys. 65, 2807 (1989).

[15] Y. Tada, Jpn. J. Appl. Phys. 1 34, 1595 (431).

[16] V. Sundar and R. E. Newnham, Ferroelectrics 135, 431 (1992).

[17] J. Zhao, Q. M. Zhang, N. Kim, and T. Shrout, Jpn. J. Appl. Phys. 1 34, 5658 (1995).

[18] E. A. McLaughlin, J. Powers, M. B. Moffett, and R. S. Janus, data presented at 1996 ONR Review on Transducer and Transducer Materials, The Pennsylvania State University, 1996.

[19] M. Haun, Ph.D. thesis, The Pennsylvania State University, 1983.

[20] T. Furukawa and N. Seo, Jpn. J. Appl. Phys. 1 29, 675 (1990).